Digital Signal Processing for Sensing in Software Defined Optical Networks

Maria Vasilica IONESCU

A thesis submitted to the University College London (UCL) for the degree of Doctor of Philosophy (Ph.D.)

Optical Networks Group
Department of Electronic and Electrical Engineering
University College London (UCL)

I, Maria Vasilica Ionescu, confirm that the work presented in this thesis is my own. Where information has been derived from other sources, I confirm that this has been indicated.

TO MY PARENTS AND JOHN.

Abstract

OPTICAL networks are moving from static point-to-point to dynamic configurations, where transmitter parameters are adaptively changing to meet traffic demands. Dynamic network reconfigurability is achievable through software-defined transceivers, capable of changing the data-rate, overhead, modulation format and reach. Additionally, flexibility in the spectral allocation of channels ensures that the available resources are efficiently distributed, as the increase in fibre capacity has reached a halt.

The complexity of such highly reconfigurable systems and cost of their maintenance increase exponentially. Implemented as part of digital signal processing of coherent receivers, sensing is an enabling technology for future software defined optical networks, as it makes possible to both control and optimise transmission parameters, as well as to manage faulty links and mitigate channel impairments in a cost-effective manner.

Symbol-rate is one of the parameters most likely to adaptively change according to existing fibre impairments, such as optical signal-to-noise ratio or chromatic dispersion. A single-channel symbol-rate estimation technique is demonstrated initially, yielding a sufficient accuracy to distinguish between different typical error-correction overheads, in the presence of dispersion and white Gaussian noise.

Further increasing the capacity over fibre to 1 Tb/s and beyond means moving towards superchannel configurations that employ Nyquist pulse shaping to increase spectral efficiency. Novel sensing techniques applicable to such information dense configurations, that can jointly monitor the channel bandwidth, frequency offset, optical signal-to-noise ratio and chromatic dispersion are proposed and demonstrated herein. Based on time-domain and frequency-domain functions derived from the theory of cyclostationarity, the performance of this joint estimator is investigated with respect to a wide range of parameters. The required acquisition time of the receiver is approximately 6.55 μs, three orders of magnitude faster compared to the round-trip time in core networks. The pulse shaping at the transmitter limits the performance of this estimator, unless the excess bandwidth is 30% of the symbol-rate, or more.

Acknowledgements

I AM greatly indebted to my supervisor, DR. BENN THOMSEN, who dedicated much of his time in guiding me in my research and was there for me when I needed to talk about the challenges I encountered. His trust, support and mentoring were paramount in putting this work together and achieving my goal.

I would also like to thank DR. SEB SAVORY for inspiring and ecouraging me to take the path of optical communications, as well as for guiding my early steps of research into this field. All my friends from the Optical Networks and Photonics groups have, in one way or another, helped shape my research experience. In particular, I would like to thank MASAKI SATO, DR. MILEN PASKOV and SEZER ERKILINÇ for their assitance in collecting experimental results and to DR. DAVID MILLAR and DR. JOSÉ MENDINUETA for mentoring and encouraging me when I first joined the group.

Thank you JOHN, for always being by my side when things got difficult and for believing in me. We have been on this journey together and I am grateful and lucky you have taught me so much during this important stage of my life.

And last but not least, I am grateful to my parents, CONSTANTIN and FILUŢA, for instilling in me the love of learning, making my education their priority and for teaching me the importance of perseverance from very early on. Everything that I have ever achieved was thanks to your dedication, love and support.

Contents

List of Figures

List of Tables

1 Introduction

1.1 Motivation

The early optical fibre communication systems of the late 1980s were simple point-to-point links based on On-Off Keying (OOK), transmitting single-carrier and single-polarisation signals, with a static and homogeneous traffic, and focusing mostly on voice services [Abbott, 2008]. The introduction of Synchronous Optical Networking/Synchronous Digital Hierarchy (SONET/SDH) standard in the 1990s was a turning point in the deployment of optical networks [Lee and Aprille, 1991], by providing a common ground for connecting optical equipment from different vendors and network domains, and by offering protection against failure with its self-healing ring mechanism.

As traffic demands started rising, the advent of wide-band optical amplifiers enabled the introduction of Wavelength Division Multiplexing (WDM) technology offering higher capacities and at a much lower cost than those required in the scaling of SONET/SDH systems [Wo et al., 1989]. Optical Transport Network (OTN) or "digital wrapper" technology was then introduced to combine the benefits of the SONET/SDH and WDM technologies, offering management for the WDM transport layer [ITU, ITU-T G.709]. The main functions provided by OTN were: transport, multiplexing, routing, management, supervision, and survivability. The ITU-T G.709 standard defining OTN, additionally proposed Forward Error Correction (FEC) limits for extending the reach of optical signals.

The increase in traffic required faster switching mechanisms that motivated the

transition from electrical to optical switches [Berthold et al., 2008]. The Optical-Electrical-Optical (O-E-O) switching architecture introduced in the mid-1990s was bulky, power inefficient and rendered scalability difficult. An alternative came in the form of optical bypass switches, such as Optical Add-Drop Multiplexers (OADMs) and later Reconfigurable Optical Add/Drop Multiplexer (ROADM), leading to transparent optical networks for the first time and to mesh as a new network topology.

These technological breakthroughs enabled higher capacities of the optical fibre to be readily available over longer distances and resulted in the explosive growth of data and video services. The introduction of narrow-band optical filtering enabled WDM systems with channel spacing of 50 GHz (renamed Dense Wavelength Division Multiplexing (DWDM) in the ITU-T G.694.1 standard), thus enabling an even higher increase in capacity. However, the available optical bandwidth had been completely saturated with the introduction of channel rates of 40 Gb/s using binary modulation and direct-detection in DWDM systems [Winzer, 2012]. The solution to further increasing the capacity has been relying on the deployment of spectrally efficient methods, such as higher order modulation formats with Polarisation Division Multiplexing (PDM). Optical coherent receivers employing Digital Signal Processing (DSP) for impairment mitigation, frequency and phase locking and polarisation demultiplexing have enabled signal rates of up to 100 Gb/s [Fludger et al., 2008].

At data rates of 100 Gb/s and higher, the capacity per channel is rapidly being pushed towards Shannon's limit [Roberts, 2012]. Limited by the slow increase in electronics speeds, in current optical networks, the available capacity increases at a slower rate than the traffic demand, with the latter expected to exceed the former by a factor of 10 in the next decade [Essiambre and Tkach, 2012]. New technological innovations are thus required in order to ensure that the traffic demands will continue to be met.

The efforts for increasing the capacity over fibre stimulated a wide range of modulation formats, coding schemes, data rates to be adopted. Networks are required to support a multitude of services simultaneously such as Internet Protocol (IP), SONET/SDH or OTN, each with their own performance advantages and specific applications [Berthold et al., 2008], and as a result, the networks face an increase in complexity in terms of operation and management. In addition, it is predicted [Monroy et al., 2011] that network operators would want to provide these services under different pre-established qualities, based on user requirements.

In the light of the increased complexity of current optical networks and higher bandwidth demands it is necessary to design autonomous, self-regulated and cognitive optical networks [Escalona et al., 2010; Monroy et al., 2011; Wei et al., 2012] that are able to adapt and maximise the utilisation of existing network resources and meet the Quality of Service (QoS) requirements. At the same time, it is desirable to find

cost-effective solutions that are scalable and can incorporate the already existing technologies. Software-Defined Optical Networks (SDONs) are therefore proposed, uniting programmable transmitters and digital coherent receivers as a single reconfigurable entity.

At the physical layer, the network needs to be able to identify and monitor transmission specific characteristics such as the symbol-rate, FEC rate, modulation format, wavelength or launch power and reconfigure and adapt these key parameters depending on the performance needs and the impairments present in the link at the time [Zervas and Simeonidou, 2010]. Sensing enabled through SDONs plays an essential role in the design of cognitive optical networks, forming a knowledge base that is necessary for the learning process of the network and also for making future predictions about the behaviour of the network [Monroy et al., 2011].

Digital coherent receivers with fast Analog-to-Digital Converters (ADCs) translate the signal linearly from the optical into the electrical domain, thus preserving information about amplitude, frequency and phase [Yamamoto and Kimura, 1981]. The full representation of the signal in the electrical domain enables DSP algorithms to compensate for linear and nonlinear impairments such as Chromatic Dispersion (CD), Polarisation Mode Dispersion (PMD), Polarisation Dependent Loss (PDL), Cross-Phase Modulation (XPM) [Kuschnerov et al., 2009]. Additionally, digital coherent receivers offer parameter estimation and performance monitoring, the latter providing information about the quality of the signal and of the service, as well as fault management.

As a result, sensing in SDONs can be performed through carefully selected DSP algorithms within digital coherent transceivers. As DSP is an integral part of any digital coherent receiver, the cost of this solution is greatly reduced. In addition, hardware programmability offers two main advantages: it makes scaling easy as software can be easily transferred between transceivers and it offers a common ground for integrating heterogeneous legacy networks. This work investigates sensing methods suitable for implementation within SDONs.

Future networks are likely to use Nyquist or Super-Nyquist superchannels, implemented as Root-Raised Cosine (RRC) filtered WDM signals, to further increase the spectral efficiency. It is therefore important to devise new joint monitoring techniques that could be applicable to such high information-dense signals, as previous sensing techniques investigated in the literature are not always applicable. The techniques presented in this thesis leverage on the programmability of the coherent receiver to implement SDON sensing techniques in its DSP, for Nyquist WDM superchannels.

1.2 Thesis outline

The rest of the thesis is organised as follows: Chapter 2 explains the basic concepts of SDONs and their constituent elements, namely programmable transmitters and digital coherent receivers. A synthesis of the main advancements in terms of high-capacity, high spectral efficiency obtained through Nyquist WDM superchannels is given. This chapter also describes previously proposed sensing techniques, focusing mainly on symbol-rate, Optical Signal-to-Noise Ratio (OSNR) and CD, and discusses their advantages, disadvantages and validity for SDONs.

Chapter 3 presents statistical and spectral properties of linearly modulated signals and noise, that are employed in this work to demonstrate novel sensing techniques. The main focus of this chapter is the theory of stationarity and cyclostationarity and the power spectral densities of signals with such properties.

Chapter 4 presents two new symbol-rate estimation techniques based on the power spectrum of coherently detected signals, that could be applicable to SDONs. The first method is based on a MMSE approach, comparing the received spectrum with test analytical spectra and finding the best match. The second method calculates the spectral standard deviation and computes the symbol-rate from a Look-up Table (LUT) by linear interpolation [Ionescu et al., 2013].

A novel joint estimator presented in Chapter 5, builds upon the theory of cyclostationarity and consists of time-domain and frequency-domain implementations of symbol-rate and CD estimators, as well as OSNR [Ionescu et al., 2014], frequency offset and roll-off factor estimators. These techniques are mainly directed towards Nyquist WDM superchannels.

Finally, Chapter 6 concludes the thesis with a discussion on the main findings of this work, in terms of the performance of the estimators and proposed future work for their improvement. A comparison between the existing and proposed estimators is also included in this chapter.

1.3 Original contributions

- Novel symbol-rate estimation technique based on the Power Spectral Density (PSD) of linearly modulated signals, and employing a scheme that reduces the impact of noise, is proposed and demonstrated. Its performance with respect to RRC roll-off factor, channel impairments, receiver bandwidth and sampling time is investigated.

- Novel joint estimation of symbol-rate (time and frequency domain), RRC roll-off factor, Intermediate Frequency (IF), CD (time and frequency domain) and OSNR based on the theory of cyclostationarity is presented here. The time-domain

symbol-rate and the OSNR estimators have been previously proposed in literature, but are here investigated in more detail and demonstrated experimentally. The implementations of the Spectral Correlation Function (SCF) and Cyclic Auto-correlation Function (CAF) presented here allow a continuous cyclic frequency, which enable a higher resolution. The impact of chromatic dispersion on the frequency-smoothed SCF implementation has been investigated for the first time and it is found that spectral correlation fading occurs. All of these estimators are investigated in turn, with respect to transmitted signal bandwidth, channel impairments, and receiver sampling time. This is one of the few joint estimators proposed thus far, that embeds both transmission and channel parameters.

1.4 List of publications

- "Cyclostationarity-based joint monitoring of symbol-rate, frequency offset, CD and OSNR for Nyquist WDM superchannels," Maria Ionescu, Masaki Sato, and Benn Thomsen, Opt. Express 23, 25762-25772 (2015).
- "In-band OSNR estimation for Nyquist WDM superchannels," Maria Ionescu, Masaki Sato, and Benn Thomsen, 40th European Conference on Optical Communication (ECOC 2014).
- "Novel baud-rate estimation technique for M-PSK and QAM signals based on the standard deviation of the spectrum," Maria Ionescu, Sezer Erkilinc, Milen Paskov, Seb Savory, and Benn Thomsen, 39th European Conference on Optical Communication (ECOC 2013).

2

Sensing methods for software defined optical networks

The introduction of WDM and coherent detection technologies have made possible the increase of capacity over optical fibres from 10 GBaud to 40 GBaud. To date, the finer frequency granularity of commercial DWDM systems, of 50 GHz or even 25 GHz, enables data-rates beyond 100 Gb/s and up to 400 Gb/s. A further capacity increase to 1 Tb/s and beyond will be made possible by employing flexible grid WDM superchannels, which allow more channels to be closely multiplexed. The spectral flexibility thus attained, can also enable adaptive on-demand data-rates, efficiently filling the available optical bandwidth.

The variability in data-rate and reach requirements will move the signal reconfiguration from the optical domain into the electrical domain, through programmable transceivers. Software-Defined Optical Networks can thus enable network reconfigurability according to traffic demands. Adaptively changing the symbol-rate, pulse shaping, FEC and modulation format at the transmitter, according to the existing channel impairments and transmission requirements, means that awareness of the state of the network configuration is needed, and this can be achieved through sensing.

Ideally, monitoring should be achieved blindly, with no prior knowledge of the transmitter parameters, nor by modifying the transmitter. Also, the response-time of the monitor needs to be comparable to the switching time of the existing network elements, keeping in mind the future evolution of such elements. Obtaining as many

estimates as possible from a single performance monitoring technique, is desirable, having the potential to significantly reduce the overall computational time. In terms of performance, the range and accuracy requirements depend on the parameter being estimated, and should both be maximised.

SDON is introduced in this chapter, discussing its programmable transceiver implementation and requirements and state-of-the art flexgrid superchannels. A synthesis of the current techniques for estimating some of the main parameters of interest, namely symbol-rate, OSNR and CD is contained herein. Existing joint estimators, usually incorporating a plethora of parameters, are also introduced.

2.1 Software-defined optical networks

There are similar trends in the evolution of radio technology to the evolution of optical networks, in terms of channel coding, modulation format and DSP [Glingener, 2011]. In radio, the migration towards higher order modulation formats, eventually limited by the Signal-to-Noise Ratio (SNR) requirements, have motivated the introduction of software-defined radio, making efficient use of the available spectral resources. Similarly, the role of SDON is to make efficient use of the optical spectrum, by providing adaptive bandwidth and dynamic wavelength reconfigurability [Wei et al., 2012]. In optical networks, parameters such as the symbol-rate, pulse shaping or modulation format can be adapted and controlled by software, to meet demand.

As Fig. 2.1 depicts, SDON is part of the cognitive optical networking paradigm [Zervas and Simeonidou, 2010], enabling the collection of information about the environment, in order to learn from it and consequently aid the allocation of resources strategically and intelligently. Through the perception-action cycle [Haykin, 2012], the cognitive system learns about the network. Firstly, it observes the network and collects information about it in a knowledge base or memory. The necessity for memory stems from the fact that the network changes dynamically with time. This implies that the cognitive system needs to continuously monitor the network and store the information in order to be able to make predictions about what are the expected responses to certain actions. Based on this knowledge, appropriate decisions and actions are taken. Both perception and action can readily be realised with software defined digital coherent transceivers, that can monitor the network as well as change signal parameters within the DSP. Attention is important in linking the allocation of resources and the existing strategies. Network intelligence unites perception, action, memory and attention for the purpose of making decision about the allocation of resources.

The introduction of SDON is currently being made possible as a result of a number of enabling technologies. WDM superchannels, programmable transmitters, digital coherent receivers are amongst the most important ones, and are treated next.

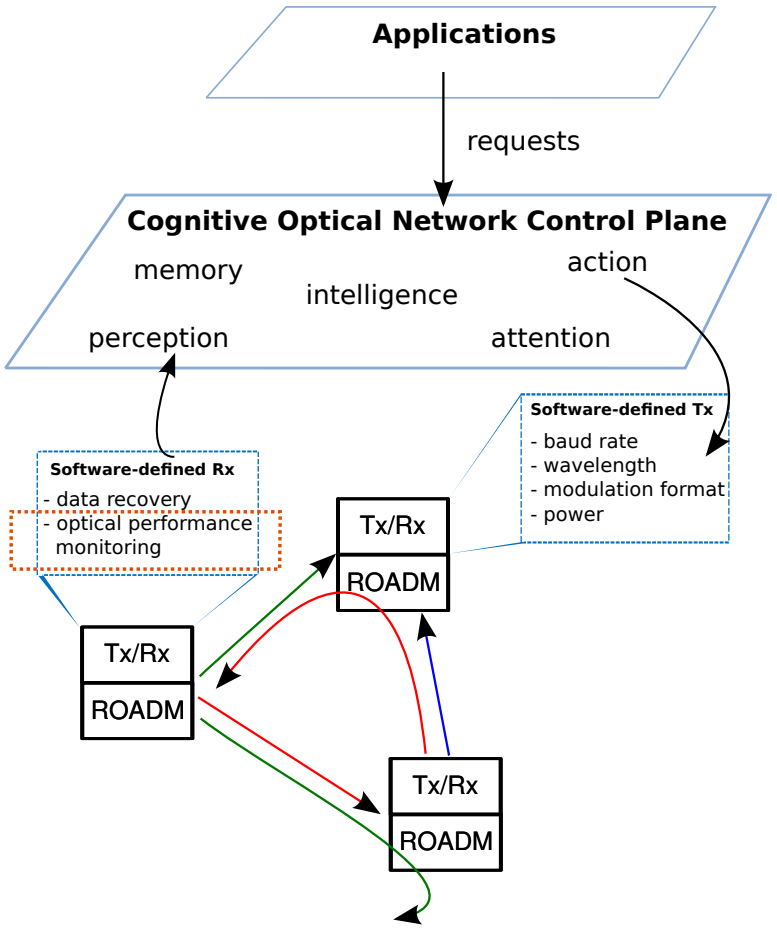

Figure 2.1: A software-defined cognitive optical network architecture.

2.1.1 Software defined transceivers

Software defined optical transceivers have emerged as a necessity to adapt from the static to the dynamic conditions of optical networks, including dealing with time varying impairments, achieving scalability, easy migration to higher capacities and reduced human interaction, by allowing flexible hardware to be controlled through software [Gringeri et al., 2013]. Flexible hardware is therefore a prerequisite to software-defined transceivers. This section presents the fundamental concepts behind the constituent parts of software-defined transceivers, namely programmable transmitters and digital coherent receivers, and gives a brief overview of the currently existing technologies.

Programmable transmitters

A flexible transmitter dynamically redefines parameters such as data-rate, modulation format, FEC schemes, pulse-shaping, number of subcarriers, through software in order to provide certain QoS or capacity requirements [Ji, 2012]. For instance, flexible modulation formats enable the adaptation of signal's bandwidth or capacity to different application-specific reach requirements [Eiselt et al., 2011]. An increase in the

order of the modulation format means that the constellation points are spaced more closely together, increasing the sensitivity to noise and distortions and thus limiting the transmission distance. For example Elbers and Autenrieth [2012] show that Binary Phase-Shift Keying (BPSK) is more suitable for submarine distances which exceed 5000 km, while Quadrature Phase-Shift Keying (QPSK) and 16-Quadrature Amplitude Modulation (QAM) are preferred for 100G and beyond metro applications, as they only allow transmission over 2500 km and 650 km respectively.

A variable modulation format transmitter can be realised with an IQ Mach-Zehnder Modulator (MZM) driven by a DAC with configurable input signals, as in Fig. 2.2. The amplitude levels of the Digital-to-Analog Converter (DAC)'s input signals dictate the modulation format order and are software-controlled. It is thus possible to greatly reduce the cost and complexity of future dynamic optical networks, by deploying a single flexible transceiver instead of multiple dedicated transceivers for each possible modulation format, with fixed transmission and reception capabilities. This type of transmitter implementation also allows variable pulse-shaping, such that the spectral efficiency can be optimised, within the limits of reach requirements.

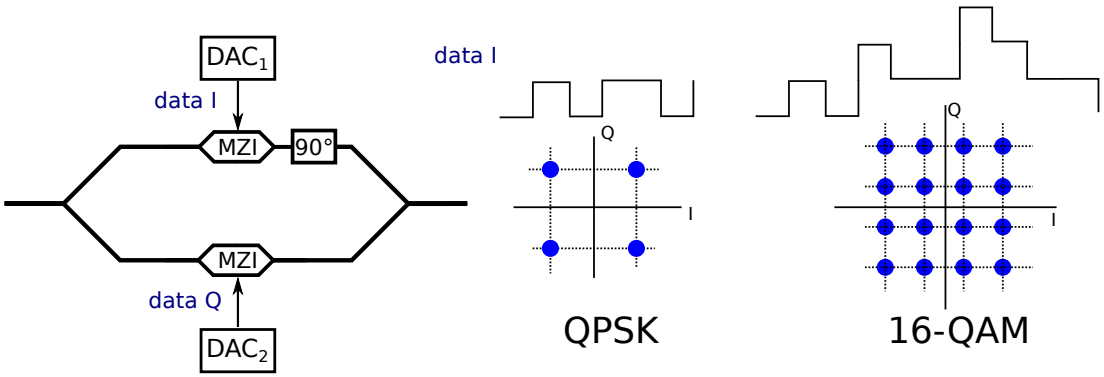

Figure 2.2: Modulation-flexible transmitter, where the format is selected via multi-level driving signals defined in software.

Given that the OSNR is continuously monitored in the network, a software-defined transmitter could additionally change the symbol-rate such that it can optimise the system operation at the Required Optical Signal-to-Noise Ratio (ROSNR) (Fig. 2.3). The symbol-rate can also be changed in response to the amount of cumulative dispersion on the transmission path, which suggests that CD also needs to be continuously monitored if the data-rate is to be optimised in accordance with the existing fibre impairments. These monitoring schemes will most effectively be implemented in the digital domain within the digital coherent receiver.

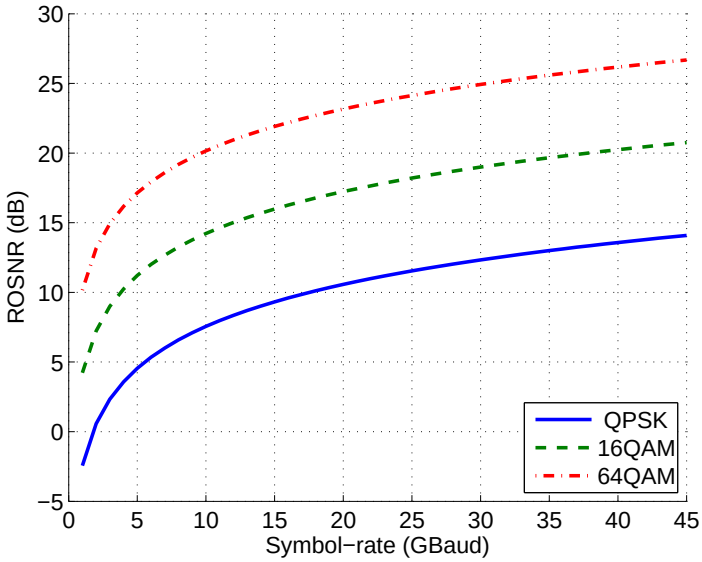

Figure 2.3: Required OSNR as a function of the symbol-rate and modulation format, for a target BER of $3.8 \cdot 10^{-3}$.

Digital coherent optical receivers

Digital coherent receivers have brought numerous advantages to optical communications, including shot-noise limited operation, phase and polarisation diversity and frequency tunability [Ryu, 1995]. Coherent detection enables the linearly mapping of the incoming signal from the optical domain into the electrical domain, thus allowing full compensation of fibre impairments through DSP [Ip et al., 2008; Savory, 2010], eliminating the need for expensive optics to fulfil the same task. Full data recovery is possible within 200 ns [Thomsen et al., 2011]. The schematic of Fig. 2.4, depicts the constituent algorithms and subsystems of digital coherent receivers.

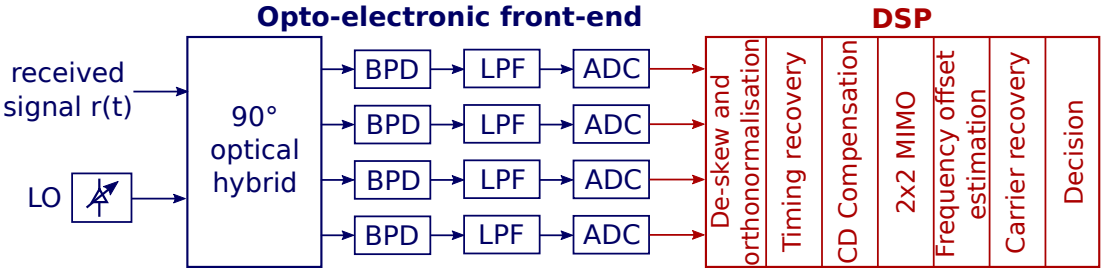

Figure 2.4: Digital coherent receivers comprise an opto-electronic front-end and programmable DSP stages for data recovery (ADC = Analog-to-Digital Converter, BPD = Balanced Photodiode, LPF = Low-pass filter, MIMO = Multiple-Input Multiple-Output).

After receiver front-end imperfections compensation, such as quadrature imbalance [Fatadin et al., 2008], clock timing recovery is required to adjust the sampling rate at the receiver to be an integer of the symbol-rate, such that the following 2x2 Multiple-Input Multiple-Output (MIMO) algorithm can be performed. Typically the timing recovery

algorithm is a Gardner [1993] interpolator and resamples the data at 2 samples per symbols, to speed the dynamic equalisation stage. Either placed prior or post CD compensation, this stage has knowledge of the symbol-rate, or alternatively, the symbol-rate has to be estimated within kHz accuracy and then the Gardner [1993] interpolator can be employed to further adjust the clock timing.

Digital compensation of the linear fibre impairments is performed, including CD and PMD [Ip and Kahn, 2007; Savory, 2008] compensation. CD occurs due to the difference in propagation speed of the different wavelengths components of the signal, whereas PMD is due to birefringence which leads to the difference in refractive index experienced by different polarisations, and hence to their different propagation speeds. These impairments severely limit the transmission over optical fibres, in particular at higher data-rates, and therefore require compensation. Generally, as dictated by the different nature of these impairments, the CD and PMD compensation stages are split into a static and a dynamic equaliser respectively, which are implemented as Finite Impulse Response (FIR) filters. Typically the CD equaliser is implemented in the frequency domain, whereas the PMD equaliser is implemented in the time domain as a 2x2 MIMO butterfly-structured filter, as Fig. 2.5 shows.

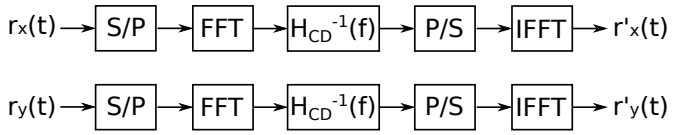

(a)

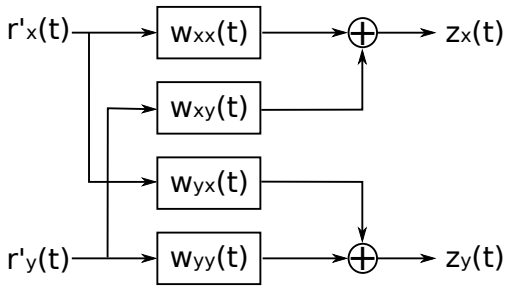

(b)

Figure 2.5: Static (a) and dynamic (b) equalisers employed in the DSP of coherent receivers. S/P = Serial to parallel; P/S = Parallel to serial. The FFTs and its inverse are performed blockwise.

Typically, a least-mean square algorithm such as the Constant Modulus Algorithm (CMA) is used to converge the filter taps to an optimum equalisation solution. The equalised signal is obtained by correlating the received signal $r(t)$ with the inverse of the channel impulse response, such that compensation of CD and PMD is achieved:

$$\begin{pmatrix} z_x(t) \\ z_y(t) \end{pmatrix} = \begin{pmatrix} w_{xx}(t) & w_{xy}(t) \\ w_{yx}(t) & w_{yy}(t) \end{pmatrix} \cdot \mathcal{F}^{-1} \left\{ H_{CD}^{-1}(f) \cdot \begin{pmatrix} R_x(f) \\ R_y(f) \end{pmatrix} \right\}. \tag{2.1}$$

In legacy static networks, it has been possible to fully compensate for CD, as the transmission distance and fibre type were known a priori. However, in reconfigurable networks, the CD is unknown at the receiver, thus the static equaliser requires feed-forward information from a CD estimator, integrated within the receiver's DSP. The static equaliser compensates for the bulk CD present in the received signal, whilst the subsequent dynamic equaliser can further compensate for the residual CD, resulting from imperfect CD estimation, in addition to the compensation of PMD and polarisation rotation impairments. The number of taps required for a CD compensating FIR filter implementation [Savory, 2010] increases linearly with the amount of dispersion to be compensated $D \cdot L$, and RRC roll-off factor r and quadratically with the symbol-rate F_b:

$$N_{taps} = D \cdot L \cdot F_b^2 \cdot (1 + r). \tag{2.2}$$

Intradyne coherent detection further imposes frequency offset estimation and correction. Frequency estimation is usually achieved based on a phase differential algorithm M-ary Phase-Shift Keying (M-PSK) [Morelli and Mengali, 1998]. The phase difference between consecutive symbols is measured, then the modulation format is removed by raising to the M^{th} power and finally averaging is performed to reduce the impact of noise. For 16-QAM signals the constellation is grouped into two (inner and outer) QPSK constellations which are the only ones used [Fatadin and Savory, 2011], as these have only one bit difference between adjacent symbols, giving a fixed phase difference. Frequency estimation based on spectral methods has also been demonstrated for M-ary Quadrature Amplitude Modulation (M-QAM) [Selmi et al., 2009] modulation formats. This is achieved by firstly raising the signal to the fourth power and then iteratively performing a spectral search of the carrier. The frequency offset proposed in Chapter 5 is compared against this conventional spectral approach.

The carrier recovery stage implies the estimation and compensation of the combined phase noise between the Local Oscillator (LO) and the incoming signal lasers [Taylor, 2009], before the information can be extracted from the recovered symbols. An increase in the order of the modulation format poses more stringent requirements on the LO linewidth [Seimetz, 2008]. Therefore, if employed as part of a flexible software-defined transceiver, the receiver has to be uniquely defined, independently of the modulation format which comes with individual LO laser linewidth requirements.

In a network where transmission parameters and fibre paths are changing, the classical coherent receiver's DSP implementation presented here would be modified to incorporate sensing techniques of the received signal and channel characteristics. The

following sections introduce some of these possible techniques, existing in literature, that are relevant to reconfiguration decision-making.

Current state-of-the-art software-defined transceiver

The current state-of-the-art software defined transceiver is WaveLogic 3 [Ciena, 2012] that brings a number of capabilities for the benefit of future cognitive and dynamic networks. By incorporating DSP at the transmitter, spectral pulse shaping can be employed, achieving increased bandwidth efficiency and independence of the different cascaded ROADM filters encountered along the optical path. Soft-decision FEC is preferred to hard-decision FEC as it enables higher capacities while maintaining the same reach requirements. Another feature of Wavelogic 3 is that it gathers fibre characteristics to populate routing tables and achieve dynamic optical path reconfigurability.

A fast switching time is necessary in future SDONs in order to ensure that the response-time of the network reconfiguration matches the application demands at high data-rates. A fast switching ($<$ 150 ns) burst mode coherent transceiver has been demonstrated to operate for a 24 channels DWDM system at 112 Gb/s Dual-polarised Quadrature Phase-Shift Keying (DP-QPSK) [Maher et al., 2012].

2.1.2 Flexible-grid superchannels

While there is no formal definition of a superchannel[1], a generally accepted description of the concept can be: a group of optical signals bundled up from transmission to reception and travelling together as a single entity [Liu and Chandrasekhar, 2014]. The concept of superchannels has arisen as a result of the electronic bottleneck which limits the per channel rates to 100 Gb/s. As a result, superchannels come as an enabling solution for higher channel capacity, through parallelising multiple "subcarriers" or "subchannels". The main aspects to be considered in the design of a superchannel are the channel bandwidth B, channel spacing Δf and modulation format. The overall data-rate of the superchannel depends on the individual symbol-rates of the constituent subchannels, and their underlying modulation formats.

Depending on the channel spacing to bandwidth ratio, superchannels can be classified [Kaminow, 2013, Chapter 3] as having:

- a fixed guard-band ($1 \leq \Delta f/B \leq 1.2$), in which case they are called "quasi-Nyquist" superchannels,
- no-guard band ($\Delta f/B = 1$) when the subchannels are contiguous and the bandwidth per channel is limited according to Nyquist frequency; such superchannels

[1]Conventionally, the term "super – channel " is employed to suggest the presence of a guard interval between the constituent sub-channels. For generality, in this thesis the term "superchannel" is used instead to refer to any of these three configurations and, in Chapter 5, all three possibilities are investigated.

are called “Nyquist-WDM”, or,

- faster-than-Nyquist or Super-Nyquist superchannels ($\Delta f/B < 1$).

By comparison, previously introduced WDM technology consisted of:

- coarse WDM, for $\Delta f/B > 50$,
- WDM, $\Delta f/B > 5$,
- DWDM, $1.2 < \Delta f/B \leq 5$.

Conventional DWDM systems designed at a fixed channel spacing of 50 GHz are insufficient for supporting data-rates higher than 100 Gb/s [Jinno et al., 2009]. A finer frequency granularity is thus required. The ITU-T G.694.1 standard defines the flexible-grid DWDM configuration to a minimum channel slot width of 12.5 GHz and a central frequency of 6.25 GHz. Flexible frequency grid DWDM allows the channel bandwidth to be mapped to the signal bit-rate, and thus maximises the use of available bandwidth. The spectral efficiency increase in a flexible-grid configuration is realised by closely packing together the existing channels, as seen in the example from Fig. 2.6 in designing a 1 Tb/s superchannel.

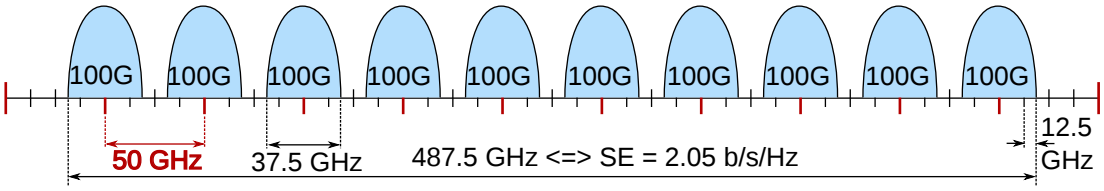

(a) 50 GHz frequency grid (DWDM technology).

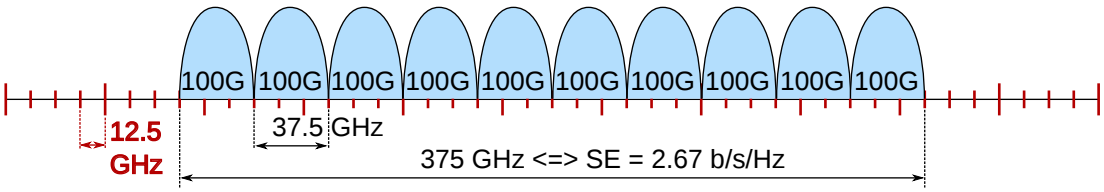

(b) Flexible grid WDM (superchannel technology).

Figure 2.6: 1 Tb/s superchannel gives a higher spectral efficiency if implemented on a flexible frequency grid, according to the ITU-T G.694.1 standard.

Nyquist pulse shaping is usually employed on each subchannel to improve the overall spectral efficiency and reduce the Inter-Channel Interference (ICI) together with Inter-Symbol Interference (ISI) [Pan et al., 2012]. Typically, a Raised Cosine (RC) filter is employed as a Nyquist filter, split between the transmitter and receiver as two RRC filters. Whilst the ideal roll-off factor of these filters should be zero, equivalent to no excess bandwidth beyond the Nyquist limit, its implementation is impractical

and roll-off factors below 0.1 [Bosco et al., 2010a] are typically used in pulse-shaping the individual subchannels. In order to design Nyquist WDM superchannels, it is thus required to have a flexible transmitter, capable of pulse shaping on a flexible grid. Superchannels can also be generated as Coherent Optical Orthogonal Frequency-Division Multiplexing (CO-OFDM), but this implementation has been demonstrated [Bosco et al., 2010b] to be less efficient in terms of bandwidth requirements and have less nonlinearity tolerance, compared to Nyquist-WDM.

Designing a superchannel of arbitrary data-rate is achieved by manipulating the number of subchannels, modulation format and symbol-rate. The spectral efficiency additionally depends on the spacing between the subchannels and the Nyquist pulse shaping employed. There are thus many design degrees of freedom, but each has its own limitation in terms of reach.

Taking as an example a 400 Gb/s superchannel, there are multiple implementation possibilities, three of which are shown in Fig. 2.7. If a higher spectral efficiency is desired and a compromise with respect to maximum reach is possible, dual-carrier 16-QAM modulated at 25 GBaud can be the solution. Its implementation has been demonstrated experimentally by [Buchali et al., 2012]. The main drawback of such a setup is that the maximum achievable reach is approximately 730 km of Standard Single Mode Fibre (SSMF), and as a result its applicability is limited only to metro-type networks. Switching to Dual-polarised (DP)-QPSK, whilst keeping the same symbol-rate, twice as many channels are needed in keeping the same overall data-rate of 400 Gb/s. Whilst the net spectral efficiency is halved, such super-channels can be transmitted over 2400 km [Chien et al., 2012] and are thus more suitable for core networks. Further, keeping DP-QPSK whilst lowering the symbol-rate to 10 GBaud, would increase the transmission distance even further, whilst the spectral efficiency is maintained. [Huang et al., 2012] equivalently demonstrated that 9 DP-QPSK channels modulated at 12.5 GBaud can be transmitted over 3560 km SSMF.

Comparing the last two examples based on DP-QPSK, the obvious difference lies in the number of channels and bandwidth per channel. In addition to that, the lower symbol-rate subchannels will travel over longer distances, as they are less affected by dispersion and by intra-channel non-linear effects [Poggiolini et al., 2011]. The first two examples demonstrate that there is a trade-off between reach and spectral efficiency, depending on the modulation format. There is an additional trade-off between reach and capacity, depending on the modulation format, as demonstrated by Bosco et al. [2011]. It may be concluded that 10 channels modulated with 10 GBaud DP-QPSK is the optimal superchannel design of the three, however, increasing the number of channels has a cost limitation as the number of required optical elements increases [Liu and Chandrasekhar, 2014]. Software-controlled transceivers will enable the ad-hoc superchannel configuration, according to existing impairments of the desired path,

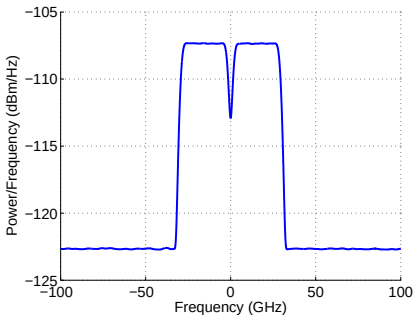

(a) 28 GBaud, DP-16-QAM.

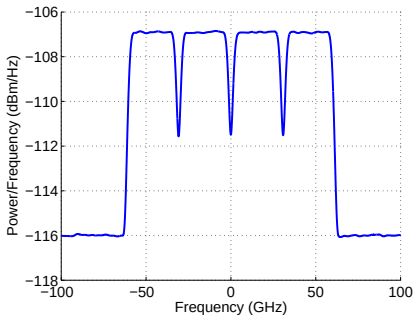

(b) 28 GBaud, DP-QPSK.

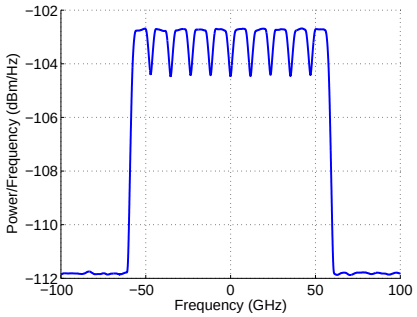

(c) 10 GBaud, DP-QPSK.

Figure 2.7: Different 400 Gb/s superchannel setups, all assuming Nyquist pulse shaping with a RRC filter of 10% excess bandwidth.

which it can additionally monitor.

A synthesis of the recent and outstanding advancements in superchannel capacity, spectral efficiency and reach can be found in table 2.1. While significant progress on increasing the capacity over SSMF employing Erbium Doped Fibre Amplifiers (EDFAs) has been made, but usually by sacrificing capacity for spectral efficiency [Zheng et al., 2013] and vice-versa [Dong et al., 2012], or reducing both capacity and spectral efficiency in favour of distance [Chandrasekhar et al., 2009]. Substantial increases in superchannel capacity up to 44.1 Tb/s [Foursa et al., 2013] and even 120.7 Tb/s [Takara et al., 2014] have been made possible by the use of specialised fibre and amplification.

At the time of publication, the real-time record of operating a Nyquist superchannel is held by NEC, for transmitting a 1 Tb/s superchannel over 7,200 km, achieved with the option of variable modulation format and FEC level transmitters and with digital coherent detection.

Table 2.1: Summary of some of the most prominent 400Gb/s and beyond flexible-grid superchannels that have so far been demonstrated experimentally and their setup. (F_b = Symbol-rate, SE = Spectral Efficiency, MCF = Multi-core Fibre, OFDM = Orthogonal Frequency Division Multiplexed, ROPA = Remote Optically Pumped Amplifier, (U)LAF = (Ultra) Large-Area Fibre)

Reference	Data-rate Tb/s	Distance km	SE b/s/Hz	Modulation	F_b GBaud	Channel spacing GHz	Bandwidth THz	Subcarriers	Fibre & amplifier
Cai et al. [2014]	54	9150	6.08	DP-16-QAM	32	33	9.125	272	Raman/EDFA
Raybon et al. [2014]	0.428	4800	3.3	DP-16-QAM	72	120	N/A	1 x 10	N/A
	1.28	3200	5	DP-16-QAM	107	200	N/A	2 x 5	N/A
Takara et al. [2014]	120.7	204	7.6	DP-32-QAM	11.5	12.5	2.25	180 x 7	MCF-ROPA + Raman/EDFA
Foursa et al. [2013]	44.1	9100	4.9	DP-16-QAM	20	20.3	9	441	LAF + Raman/EDFA
Zheng et al. [2013]	1.76	714	7.06	DP-16-QAM	5.6	6.25	0.25	40	SSMF + EDFA
Dong et al. [2012]	10	640	3.75	OFDM-DP-QPSK	12.5	25	2.825	112	SSMF + EDFA
Raybon et al. [2012]	1	3200	5.2	DP-16-QAM	80	200	1	2 x 5	N/A
Renaudier et al. [2012]	1	2400	5	OFDM-16-QAM	40	200	4.4	4 x 22	N/A
Liu et al. [2012]	1.5	5600	5.75	OFDM-16-QAM	30	32.8	0.263	8	ULAF + Raman/EDFA
Gavioli et al. [2010]	1.12	2300	N/A	DP-QPSK	56	61.6	0.616	10	SSMF + EDFA
Chandrasekhar et al. [2009]	1.2	7200	3.75	DP-QPSK	12.5	12.5	0.3	24	ULAF + Raman/EDFA

2.2 Symbol-rate estimation techniques

Symbol-rate estimation is a crucial step in blind equalisation and demodulation, automatic signal identification and classification problems. It is also an important problem that occurs in the design of future SDONs, that will perform spectrum sensing and, subsequently, adjust the transmitted signal symbol-rate on the fly, to optimize network performance in response to both traffic requirements and physical layer impairments [Monroy et al., 2011]. A fast response time is a desirable attribute for a symbol-rate estimation technique employed in adaptable and re-configurable networks. The accuracy of the estimators should be sufficiently high to distinguish between a set of symbol-rates and the FEC level. Given that traditional systems operate at 2.5, 10 and 25 GBaud, whereas typical FEC overheads range between $6.69\% - 25\%$ [Mizuochi, 2008], the maximum permissible errors should not exceed 6% of the symbol-rate, or more generally, 150 MHz.

Conventional symbol-rate estimation techniques can be broadly grouped into two categories:

- Signal-preserving techniques, which detect time domain or frequency domain features of the unmodified received signal, directly related to its clock speed.
- Signal-transforming techniques, which identify periodicities due to modulation after the signal has been manipulated through a transformation of some kind.

These techniques have been specifically proposed for radio applications. They are described next, together with their advantages and disadvantages, as applicable to optical communications.

2.2.1 Signal-preserving symbol-rate estimators

Early time-domain methods [Wegener, 1992], [Sills and Wood, 1996] detected the signal zero-crossings in order to estimate the symbol-rate. These methods are inaccurate when the signal is distorted by impairments such as high noise level, resulting in false transitions, or CD and PMD, resulting in symbols interfering with each other. As a result of these limitations, these techniques are not suitable in fast reconfigurable networks, as they cannot be used before equalisation in digital coherent receivers.

In the frequency domain, the signal's bandwidth is proportional to its symbol-rate. State-of-the-art Optical Spectrum Analyser (OSA) have spectral resolutions as high as 125 MHz (WaveAnalyzer 1500S by Finisar) or even 5 MHz (APEX AP2040 Series), which would be sufficient to give an accurate measurement of the signal symbol-rate from its PSD measurement. With coherent detection, the PSD is insensitive to CD. However, the presence of noise leads to ambiguity when measuring the zeros in a spectrum, and an improved approach would be needed to measure the spectral width.

2.2.2 Signal-transforming symbol-rate estimators

This class of estimators apply a type of transformation on the incoming signal that has the capability of inducing spectral tones equal to the symbol-rate. There are four main transformation types imposed on digitally modulated signals, that have been widely explored in literature, which can be grouped into: non-linear transformations, time-frequency transformations, and cyclostationarity.

Various non-linearity transformation estimators have been demonstrated, very early on, based on different approaches, including delay and multiply [Imbeaux, 1983], square law detector [Blachman and Mousavinezhad, 1990], or higher-order spectral analysis [Wickert and Staton, 1992]. Spectral peaks are induced at a frequency equal to the symbol-rate, by applying a non-linear transformation on the received signal (Figure 2.8(a)). The algorithm then performs a maximum peak search to estimate the symbol-rate. However, the spectral peak detectability is reduced when Nyquist pulse shaping is applied [Reed and Wickert, 1988], or under high noise conditions, limiting the performance of these methods. In addition, the peak power detectability suffers from fading under the impact of CD, due to the square law nonlinearity of the Photodiodes (PDs), as shown in Fig. 2.8(b).

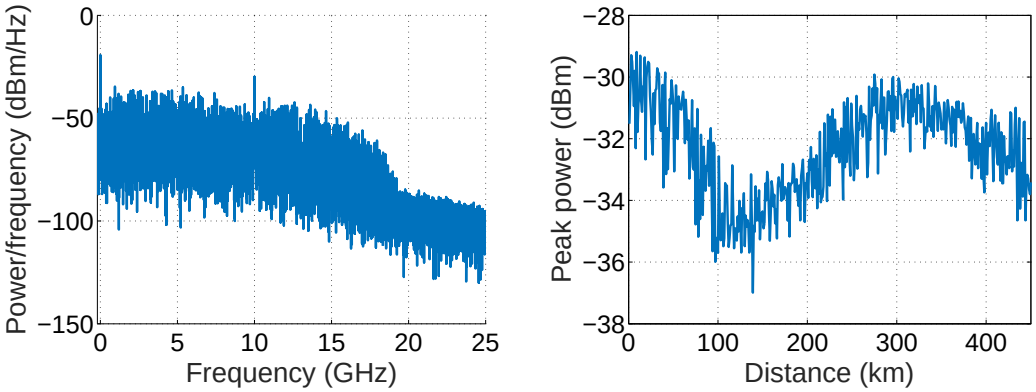

Figure 2.8: (a) 10 GBaud DP-QPSK signal with RRC roll-off of 0. The peak at the symbol-rate is induced by nonlinearity. (b) Spectrum power at the symbol-rate fading under the impact of CD.

The most widely employed types of time-frequency symbol-rate estimators are based on a wavelet transform approach. The method has been demonstrated for M-PSK [Chan et al., 1997], Frequency-Shift Keying (FSK) [Gao et al., 2012] and QAM [Barnes et al., 2009] modulation formats. Typically, a Haar wavelet transform is applied on the received signal in order to identify the time instances of symbol changes. Given a signal

$y(t)$, then the Wavelet Transform is defined as:

$$WT(a,\tau) = \frac{1}{\sqrt{a}} \int y(t) \psi^* \left(\frac{t-\tau}{a} \right) dt \tag{2.3}$$

where a is a scaling factor and the Wavelet function $\psi(t)$ is the Haar wavelet:

$$\psi(t) = \begin{cases} 1, -0.5 < t < 0 \\ -1, -0 < t < 0.5 \\ 0, otherwise \end{cases} \tag{2.4}$$

The magnitude of the transform contains peaks at the symbol transitions that occur periodically, with the period given by the symbol-rate. The symbol-rate is estimated from the wavelet transform magnitudes represented in the frequency domain, with a threshold applied in order to detect the peak locations, as depicted in Fig. 2.9. The detectability of the peaks is influenced by the choice of scaling factor, out-of-band noise and it requires a large signal bandwidth. Therefore, the main difficulties in the implementation of the wavelet transform method are the correct choice of scaling factor and threshold level. The method is sensitive to carrier frequency offset and it is unsuitable with RRC filtering at the transmitter [Holladay, 2004], limiting its applicability in practical situations.

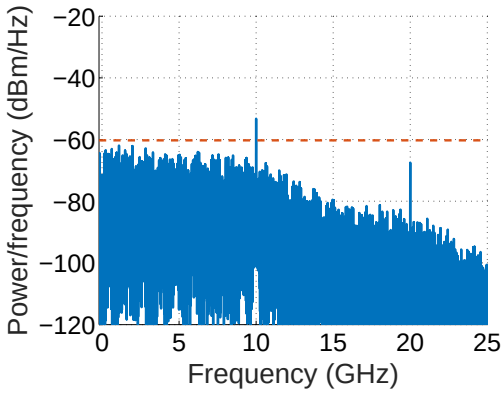

Figure 2.9: 10 GBaud estimation with Wavelet transform approach [Holladay, 2004].

Both the non-linear transformation and the wavelet transform methods are sensitive to CD (demonstrated in Chapter 4) and thus unsuitable for the initialization or control of subsequent DSP, which relies on a correct symbol-rate estimation.

Cyclostationary-based feature detectors have been proposed for the first time by Gardner [1988] in order to be used for symbol-rate, carrier frequency estimation and modulation format identification in radio applications. Cyclostationarity is the property of linearly modulated signals whereby their autocorrelation functions exhibit periodicity with the symbol-rate. As any periodic function, the autocorrelation has a Fourier series

decomposition, with tones at integers of the symbol-rate. The estimation problem thus reduces to finding the fundamental frequency of the autocorrelation function. A more detailed account of the theory of cyclostationarity is given in Chapter 3.

The cyclostationarity-based estimators will improve with an increase in number of samples used to estimate the symbol-rate, and it has been demonstrated to asymptotically converge at a fast rate of $N^{-3/2}$ [Ciblat et al., 2002], where N is the number of processed samples. These techniques have inherently high noise suppression capabilities, as noise sources have different statistical properties compared to digitally modulated signals. To the best of the author's knowledge, the impact of CD on the cyclostationarity linearly modulated signals, has not been investigated so far in the literature.

One major limitation of the cyclostationarity-based approach is that the symbol-rate tone strength reduces under narrow pulse shaping, such as RRC filtering of low excess bandwidths. Improvements to the original method involved a weighting matrix applied to the set of tones, such that the limitation due to excess bandwidths, roll-offs less than 0.5, is reduced [Mazet and Loubaton, 1999]. When 4000 samples are processed and the roll-off is 0.2, the accuracy improves from 0% to 99.808%. The current direction in the design of optical communications channels is to use roll-off factors much lower than 0.2, and therefore the cyclostationarity-based symbol-rate estimator would need further improvements.

2.3 Optical signal-to-noise ratio estimation techniques

The Bit Error Rate (BER), Q-factor and eye diagram are direct indicators of the signal quality. The measurement of these parameters in WDM systems firstly requires demultiplexing of the channels and then individual analysis of each channel, which is not always feasible [Gariépy and He, 2009]. On the other hand, the BER and the OSNR are directly deductible from each other, which means that the correct measurement of the OSNR is a good indicator of the system performance. [ITU, 2012] proposes that a good OSNR monitor should perform within 1.5 dB of the true value. An additional advantage of using the OSNR for performance monitoring purposes is that the OSNR is transparent to the modulation format or the data rate of the signal, making it particularly suitable for dynamic optical networks.

The simplest and most widely used way of measuring the OSNR is by using a linear interpolation technique, depicted in Fig. 2.10. The noise is measured out-of-band, between the channels, and then interpolated at the signal's wavelength. The OSNR is given by:

$$OSNR = 10log_{10}\left(\frac{P_{S+N} - P_N}{P_N} \cdot \frac{B_{res}}{B_{ref}}\right) \tag{2.5}$$

where

- P_{S+N} is the signal and noise power in Watts,
- $P_N = (P_{N_1} + P_{N_2})/2$ is the noise power in Watts, interpolated at the channel's wavelength,
- B_{res} is the resolution bandwidth of the measurement, and
- B_{ref} is the reference optical bandwidth, usually taken as 0.1 nm.

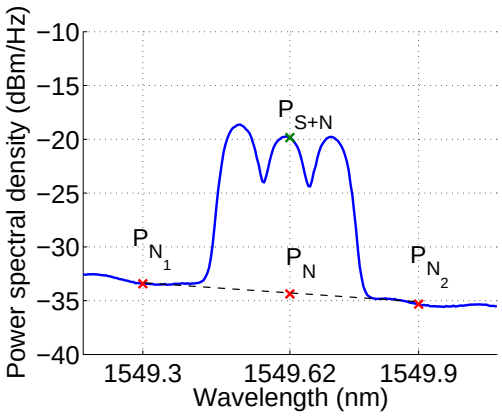

Figure 2.10: Out-of-band OSNR measurement.

In point-to-point links linear interpolation can work well since the noise spectrum can be almost flat. In dynamic networks however, channels can be added, dropped and cross-connected at any location within the network. Each channel has a different path history, over fibres of varying lengths, varying number of amplifiers and filters, leading to individual OSNRs per channel. Additionally, for superchannels with limited guard bands, it might not be possible to estimated the OSNR out-of-band, since the channels are contiguous or even overlapping. In such a case, only the in-band measurements of the OSNR are accurate. Different approaches to in-band OSNR measurement techniques have been proposed, exploring properties of modulated signals that distinguish them from noise.

Some of these techniques [Chan, 2010] are performed optically, and they require additional components. One example is the polarisation-nulling technique [Lee et al., 2006], that uses the assumption that the signal is highly polarised, while noise is completely unpolarised. Although highly accurate, this technique does not work in the presence of PMD or for polarisation multiplexed signals, affected by polarisation crosstalk. Another optical technique for measuring the in-band OSNR is based on detecting nonlinearities in the fibre, such as Four-Wave Mixing (FWM) which induce cascaded waves in a fibre optical parametric amplifier [Ng et al., 2005]. The main advantages of this method are that it is performed in the optical domain, and as a result it does not depend on fast ADCs in order to work with high bit rates and it is independent on the pulse shape of the signal. However, the optical parametric amplifier can be a costly addition to the existing networks.

In order to implement OSNR estimation at different nodes in the network, it would be advantageous to perform the measurements as part of the DSP in the digital coherent transceivers, because they are intrinsic to the current optical networks, and thus eliminate the need to have any additional hardware to perform OSNR measurements. Ideally, the OSNR monitor should be independent of CD and PMD, such that it could be implemented prior to the static and dynamic equalisers, for a reduced feedback time and resilience against possible failures of the two equalisation stages. In recent years, there have been a number of OSNR estimation techniques, designed for coherent receiver DSP.

One technique for measuring the OSNR as part of the DSP within a digital coherent receiver is based on the radial moments of the signal constellation [Ives et al., 2011; Zhu et al., 2012; Faruk et al., 2014]. It has been experimentally demonstrated to perform within 0.5 dB of the given OSNR for DP-QPSK signals. The limitation of this technique is that it is implemented after the equaliser and, as such, cannot be readily used to provide feedforward control information to the coherent transceiver, which makes it unsuitable for cognitive optical networks that require fast response times.

A similar approach, but based on the Error Vector Magnitude (EVM) measurements of symbol amplitude noise [Dong et al., 2012] was introduced to distinguish between linear and non-linear noise contributions on the OSNR measurement. This technique can in fact correct the OSNR underestimation, by estimating the non-linear noise from the correlation between adjacent symbols. This technique has to be applied after Carrier Phase Estimation (CPE) in order to work, which again, will seriously limit its utilisation in feedforward control.

Data-aided techniques have also been introduced, where training sequences based on Golay sequences [Do et al., 2013] or CAZAC sequences [Zhao et al., 2014] are sent between data frames in order to restore noise information. These techniques have been proven to be resilient to impairments such as CD or first order PMD, but they too require full or partial equalisation, which can limit the accuracy of the OSNR estimator.

A promising in-band OSNR estimation method [Grupp, 2010] exploits the fact that the modulated signal is a wide-sense cyclostationary random process, while the noise is wide-sense stationary. Therefore, it is possible to compute the SCF of received signals, which will consist of multiple spectra repeated periodically at the symbol-rate. The first of these spectra is the traditional PSD containing both signal and noise powers, whilst the others will be noise-free. Validated by simulation, this work suggests that RRC filtering will limit the number of spectra that will repeat periodically, but does not explore the limitations of the technique as a function of the roll-off factor. The impact of both linear and non-linear impairments on this technique also needs further investigation.

2.4 Chromatic dispersion estimation techniques

In a dispersive medium, such as an optical fibre, the different frequencies of a light pulse travel at different speeds due to the wavelength dependence on the refractive index. CD is a linear fibre impairment which has a quadratic phase response, described by the transfer function:

$$H_{CD}(f) = e^{j\psi f^2}, \tag{2.6}$$

where $\psi = -\frac{\pi\lambda^2 DL}{c}$, with D dispersion coefficient, λ the reference wavelength, L fibre length and c the speed of light in vacuum. Figure 2.11 shows the ideal phase response of a 1000 km SSMF with a dispersion coefficient of 16.78 ps/nm, where measurements were achieved by simulation. CD spreads the pulses in time, leading to ISI, but it has no impact on the optical power spectrum, provided coherent detection is employed.

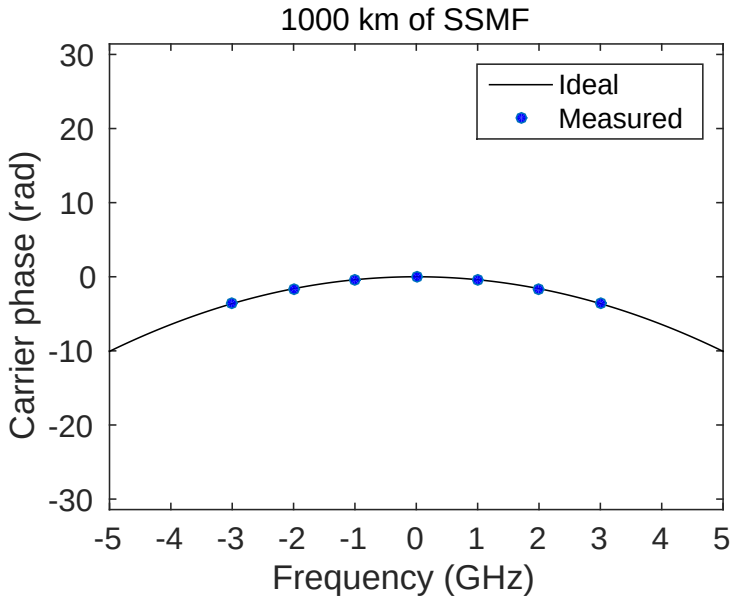

Figure 2.11: Quadratic phase response of Chromatic Dispersion.

CD estimation has been a widely researched topic in the realms of blind coherent detection and equalisation. Data-aided CD estimators [Kuschnerov et al., 2010] based on training symbols have been investigated, however, these have the disadvantage of increasing the transmission overhead. Two major blind (non-data-aided) CD estimators have been implemented within the digital coherent receiver, either based on the static or the dynamic equalisers output.

Static equaliser approach

In the first category, the estimator performs a best-match search on the static equaliser which minimises the residual dispersion based on a cost function [Kuschnerov et al., 2009; Hauske et al., 2011]. Referring back to Fig. 2.5(a), the spectrum of the received

signal $Y(f)$ is computed over blocks of length N_{FFT} and CD compensated, giving an approximation of the original signal spectrum $X(f)$:

$$\hat{X}_{N_{FFT},n}(t,f) = H^{-1}_{CD,n}(f) \cdot Y_{N_{FFT}}(t,f)$$

Multiple CD compensation trials are considered, scanning the possible transfer functions of the dispersive channel with arbitrary cumulative dispersion $\delta_n, n = \overline{1, N_{trials}}$:

$$H_{CD,n}(f) = e^{j\psi_n f^2} = e^{-\pi\lambda^2 \cdot \delta_n / c} \tag{2.7}$$

This technique then computes the circular autocorrelation of the spectrum at a given time, for each assumed dispersive channel, polarisation, and a given frequency lag Ω:

$$R_{X_{N_{FFT},n}}(t,\Omega) = \int \hat{X}_{N_{FFT},n}(t,f)\hat{X}^*_{N_{FFT},n}(t,f+\Omega)df \tag{2.8}$$

Finally, the best-match cost function can be defined as the averages of Eq. 2.8 in time and across all frequency lags Ω, not equal to the symbol-rate F_b:

$$J_{MIN}(n) = \sum_{\Omega \neq F_b} \int \left| R_{X_{N_{FFT},n}}(t,\Omega) \right| dt. \tag{2.9}$$

The minimum cost function indicates the best-match cumulative dispersion.

Soriano et al. [2011] alternatively shows that the cost function defined as the time average of the circular spectral autocorrelation at the frequency lag equal to the symbol-rate is optimum:

$$J_{MAX}(n) = \int \left| R_{X_{N_{FFT},n}}(t,\Omega = F_b) \right| dt. \tag{2.10}$$

Dynamic equaliser approach

The second most common approach to estimating the CD within the coherent receiver DSP is by making use of the adaptive equaliser taps to search for the minimum dispersion error using a gradient algorithm such as Least Mean Square (LMS) or CMA [Hauske et al., 2009]. The CD contributions is isolated from the time-varying impairments by operating on the tap filters:

$$arg\left\{H^{-1}_{CD}(f)\right\} = arg\left\{\sqrt{det(W(f))}\right\} = -\psi f^2. \tag{2.11}$$

where the Fourier Transform of the filter taps (Fig. 2.5(b)) after the convergence of the gradient algorithm is:

$$W(f) = \mathcal{F}\left\{ \begin{pmatrix} w_{xx}(t) & w_{xy}(t) \\ w_{yx}(t) & w_{yy}(t) \end{pmatrix} \right\}. \tag{2.12}$$

Optimum chromatic dispersion estimation

A comprehensive comparison between the two approaches [Soriano et al., 2011] reveals that the adaptive filter approach performs better, with a maximum residual dispersion error of ± 150 ps/nm, and a standard deviation of 30 ps/nm, up to an absolute cumulative dispersion of 900 ps/nm. Implemented with a 15-tap LMS, the adaptive CD estimator convergence can potentially be slow compared to the reconfiguration time of the network nodes, which is of the sub-μs order. Lowering the number of taps would be a serious limitation to the estimation range of this technique. This estimator requires timing-recovery and is modulation-format dependent.

By comparison, the best-match search approach, which gives a maximum residual dispersion error of ± 300 ps/nm, and a standard deviation of 76 ps/nm, for a much wider CD range, up to 32,000 ps/nm. These results were obtained from a total of $6,208$ captured samples, from which 6 spectra are computed with an FFT size is 2^{10} samples. The accuracy of the estimate depends on the CD search step and knowledge of the symbol-rate. This approach is modulation format independent and would be preferred in modulation-agnostic networks, despite the lower estimation accuracy.

To date, very little work has been done on estimating the CD of multi-carrier signals. Typically, the symbol-rate is known a priori, and the individual channels of a WDM signal are demultiplexed prior to CD estimation. As software-defined superchannels will travel together on the same optical path which is not necessarily fixed in time, a requirement for novel CD estimators that could be applied to the entire WDM superchannel arises.

2.5 Joint monitoring techniques

Joint estimation of transmission parameters and channel impairments is highly desirable, as it can reduce the estimation time from a single computational effort, together with the implementation cost. The three most prominent categories of joint parameters monitoring that have so far been investigated in the literature are time-domain sampling techniques that form asynchronous amplitude histograms, frequency domain Radio Frequency (RF) power measurements and techniques based on the equaliser taps. Other approaches have only been briefly investigated by the research community. Table 2.2 quantifies the performance of some of the main joint estimators in the literature. All of the listed techniques have been developed using direct detection and the majority for single channels. Employing direct detection looses phase and polarisation information, limiting the capability of such estimators. Also, there is a clear division between monitoring of channel impairments and monitoring of transmitter parameters, with very few focusing on both.

Table 2.2: Summary of prominent techniques for simultaneously estimating transmission parameters and channel impairments. AAH = Asynchronous Amplitude Histograms; ANN = Artificial Neural Networks; MFI = Modulation Format Identification; RF = Radio Frequency; BSF = Band-Stop Filter; PLL = Phase-Locked Loop; PM = Polarisation-Multiplexed; * = Root Mean Squared Error values.

Reference	Technique	Parameters	Range	Accuracy	Modulation	Data-rate	WDM	Drawbacks
Khan et al. [2014]	AAH & ANN	Bit-rate MFI	—	99.7%	RZ-OOK PM-RZ-QPSK PM-NRZ-16QAM	10/20 Gb/s 40/100 Gb/s 100/200 Gb/s	No	MFI dependent
Li et al. [2014]	RF tone	CD DGD	0-246.7 ps/nm 0-50 ps	N/A N/A	NRZ-DQPSK	80 Gb/s	No	BSF offset fixed to 10 GHz
Yi and Yu [2013]	AAH	CD OSNR	0-425 ps/nm 15-30 dB	20 ps/nm 1 dB	NRZ-DPSK DQPSK	10 Gb/s 20 Gb/s	No	CD limited (>425 ps/nm)
Wen et al. [2011]	Frequency down-conv. & PLL	Baud-rate CD OSNR	28 GBaud -40 – 40 ps/nm 18-36 dB	N/A N/A < 1 dB	NRZ-DQPSK	112 Gb/s	No	CD limited (>20 ps/nm)
Baker-Meflah et al. [2010]	RF tone	CD DGD OSNR	0-4742 ps/nm 0-200 ps 0-25 dB	± 100 ps/nm * ± 4 ps * ± 1dB *	NRZ-DPSK	40 Gbs	Yes	sensitive to filter detuning
Shen et al. [2010]	AAH & ANN	CD DGD OSNR	0-400 ps/nm 0-10 ps 10-30 dB	9.82 ps/nm * 0.92 ps * 0.43 dB *	RZ-DQPSK NRZ-16QAM	40 Gb/s	No	sub-second processing; complex training
Anderson et al. [2009]	AAH	CD DGD	0-700 ps/nm 0-20 ps	± 11 ps/nm * ± 0.75 ps *	NRZ-DPSK RZ-DPSK	40 Gb/s	No	sub-second processing
Hauske et al. [2008]	FIR filter coefficients	CD DGD OSNR	-2000-2000 ps/nm 0, 30, 60, 90 ps 12-24 dB	± 63 ps/nm * ± 4 ps * <1 dB	PDM-RZ-DQPSK	111 Gb/s	No	convergence time limited

2.5.1 Time domain sampling techniques

In the first category, [Anderson et al., 2009] proposed combining asynchronous delay tap sampling with statistical machine learning in order to estimate CD and Differential Group Delay (DGD). This monitor consists of a direct-detector, two slow ADCs of the order of kSa/s and a tunable delay-line. The incoming signal is sampled twice, such that the second set of samples are 1 bit delay apart from the first set. Plotted against each other, the pair of samples create a phase portrait of the waveform. Compared to an eye diagram, obtained through a singular sampling over a few bit periods to show the change in amplitude over time, the phase portrait shows the joint Probability Density Function (PDF) of the amplitude and slope of the signal with respect to time. This enriched capture of information is exploited to estimate a wide range of transmission impairments. OSNR, CD, PMD, interferometric crosstalk have different imprints on the phase portrait, and so they can simultaneously be extracted with pattern recognition based on statistical learning. This last stage is achieved by sweeping over a wide range of scenarios and "learning" the outcome of the phase portrait, but it is time-consuming process with up to 3 hours necessary to complete a training over 1200 scenarios. As this configuration stage can be done off-line, it is not a major limitation of the technique. On the other hand, the processing speed is of the sub-second order (<0.2 s), which is not sufficiently fast for burst-switched networks.

Demonstrated only for two level modulation formats (Return-to-Zero (RZ)- and Non-Return-to-Zero (NRZ)-Differential Phase-Shift Keying (DPSK)), the technique would encounter difficulties with higher order modulations, such as QPSK or 16-QAM. As the number of amplitude levels increases, the complexity of distinguishing them under the impact of a combination of impairments also increases. When additionally considering WDM signals, demultiplexing is required to apply this time-domain technique, which would further increase the complexity and lower the processing speed. [Khan et al., 2014] shows that the asychronous sampling method requires a resolution of about 12x12 bins such that the pattern of the two-dimensional phase portrait will be maintained, which can be easily achieved with existing ADC technology.

2.5.2 Frequency domain techniques

A spectral technique based on the RF power tone [Baker-Meflah et al., 2010] has been demonstrated by simulation and experimentally, having the capability to jointly and independently estimate multiple impairments such as OSNR, CD and DGD. The relative phases of a selected RF tones determine the CD and PMD effects, while the amplitude of the same tone with respect to the average signal power determine the OSNR. This technique is particularly sensitive to filter detuning, such that more than 2 GHz offset from the International Telecommunication Union (ITU) grid results in more than 1 dB

OSNR estimation error.

2.5.3 FIR filter coefficients techniques

The dynamic equaliser of digital coherent receivers implemented as an FIR filter provides a means to estimate the CD, DGD and OSNR [Hauske et al., 2008, 2009] after convergence is achieved. This joint estimator is robust and accurate (Table 2.2), but it relies on the convergence speed of the adaptive equaliser. Even though fast blind estimators that can converge within 200 ns have been demonstrated [Thomsen et al., 2011], most algorithms require up to 25 μs to fully converge. This technique could be applied to WDM signals, after demultiplexing and clock recovery of each channel.

2.6 Conclusions

A currently proposed solution for increasing the capacity of optical communications is by employing WDM superchannels. Whilst leveraging from legacy WDM transmission and reception systems, WDM superchannels require more tightly spaced sub-channels, achievable through flexible grid technology and narrow Nyquist pulse-shaping. SDON comes as a means to enable the operation of WDM superchannels, as well as enabling application-specific transmission characteristics. Section 2.1 of this chapter presented the motivation behind SDON, with specific examples of what transmission parameters are likely to be modified in software. The configuration of programmable transmitters and receivers have been discussed, with their specific constituent components. A synthesis of the breakthrough development of flexible-grid superchannels is also given.

The second part of this chapter focused on monitoring techniques for optical networks, a broad subject of discussion, as the necessity of ensuring effective transmission of information over fibre has for long been acknowledged. As the conditions of the SDONs are dyanmic, existing channel impairments estimation techniques are not always applicable. Firstly, not all past monitors are performed digitally, although this is currently the most promising solution allowing the cheap integration of multiple estimators in the already existing digital coherent receivers. The reconfiguration time of coherent transceivers and the time required for the DSP to recover the data is of the μs order, thus setting a similar time-limit for future monitoring techniques.

This chapter introduced some of the most common symbol-rate, OSNR, CD and joint monitoring techniques and discusses their issues regarding their applicability to SDONs. Previous approaches for estimating the symbol-rate (such as the Wavelet transform, time-domain zero crossing or nonlinearity induced spectral peaks) can be implemented within the DSP, but they are sensitive to CD and PMD. For Nyquist or Super-Nyquist WDM superchannels it is preferred to estimate the OSNR in-band

rather than out-of-band in order to avoid the issues associated with small guard bands and filtering effects. As coherent receivers translate the optical signal linearly into the electrical domain, preserving its phase and polarisation information, means that CD estimators are naturally suitable to be implemented within their DSP. Such techniques have successfully been demonstrated based on the channel equalisers, however they require demultiplexing of the individual sub-channels. Joint monitors are usually robust and more cost efficient, but these have been mainly specialised to parameters belonging to either the transmission setup or the optical channel.

Novel estimators suitable for software-defined Nyquist-WDM superchannels, to be implemented within the coherent receiver DSP are therefore required, preferably performed jointly as part of a single computational effort. The next chapter constitutes the theoretical background behind the monitoring techniques proposed in this work.

3

Statistical and spectral properties of digitally modulated optical signals

Spectral analysis is a powerful tool in the investigation of properties of signals, particularly when these are corrupted by noise. This chapter describes statistical and spectral properties of digitally modulated optical signals, from which a few novel practical spectral techniques will be derived in the subsequent chapters, for the purpose of signal characterisation and channel estimation. The PSD is traditionally employed for measuring the OSNR, but can also be used within the digital coherent receiver to estimate the symbol-rate of the signal, as it will be demonstrated in Chapter 4. The SCF, a generalisation of the PSD, further exploits the cyclostationarity property of linearly modulated signals, to help distinguish their underlying periodicities, when these are hidden in the PSD. The time domain counterparts of the PSD and SCF are the autocorrelation and the CAF respectively, which are also explained here. Chapter 5 will explore cyclostationarity for the estimation of a number of parameters. The present chapter, sets the background knowledge required for the understanding of the techniques demonstrated in this thesis. Established practical implementations of the SCF are also presented. Both the continuous and the discrete signal representations are being considered.

To illustrate these concepts, a simple transmission model is assumed, as depicted in Fig. 3.1: a linearly modulated signal $x(t)$, of symbol-period T_b, undergoes pulse shaping at the transmitter and is corrupted by noise arising from optical amplification

during transmission over L km of optical fibre. The signal is subsequently detected by a coherent receiver, in which the ADCs sample at F_s rate and N_{ADC} number of samples are captured, corresponding to Δt observation time interval.

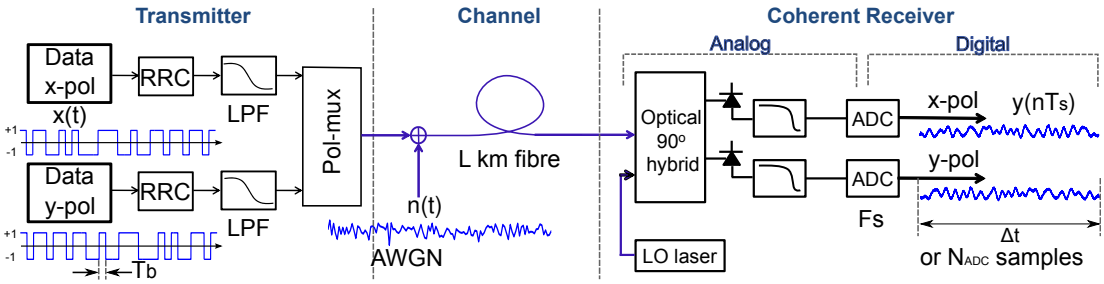

Figure 3.1: Simple transmission model assumed for the exemplification of the concepts in this chapter. The modulation format can be any M-PSK or M-QAM types (here BPSK is depicted).

The Amplified Spontaneous Emission (ASE) noise is modelled as Additive White Gaussian Noise (AWGN) and has different statistical properties from the signal. AWGN is a *wide-sense stationary process*, as its mean and autocorrelation are time-invariant. Signals that have an underlying periodicity due to modulation, multiplexing and/or sampling will be *wide-sense cyclostationary* [Gardner et al., 2006], meaning that their mean and autocorrelation are periodically time-variant, but stationary within their cycle.

This chapter is structured in four sections, as follows. The first section explains and exemplifies by contrast the stationarity and cyclostationarity properties. The definitions of the autocorrelation and Cyclic Autocorrelation Functions are also given here. Their frequency domain counterparts, the PSD and SCF are presented in the following two sections. Finally, the impact of the Nyquist pulse shaping filter on the SCF is discussed in the last section. For reference, the definitions of these signal properties are also given in Appendix D.

3.1 Autocorrelation function of stationary and cyclostationary processes

The autocorrelation function measures how much the complex field of a signal sampled at two time instances, which are separated by a fixed delay τ are correlated to (or resemble) each other. The parameter τ is called the time lag of the autocorrelation. Two alternative models of the autocorrelation are possible: either based on the assumption that the signal is a stochastic process, or that the signal is a time-series function [Gardner, 1991]. This section introduces the cyclostationarity property in terms of the stochastic and non-stochastic definitions of the CAF.

3.1.1 Stochastic definition

A stochastic model assumes multiple realisations of a process, such as those shown in Fig. 3.2, for a binary modulated signal and AWGN, for example. Ideally, all possible realisations are considered. However, as this is not the case in practice, due to a limited number of available measurements, an estimate is obtained instead.

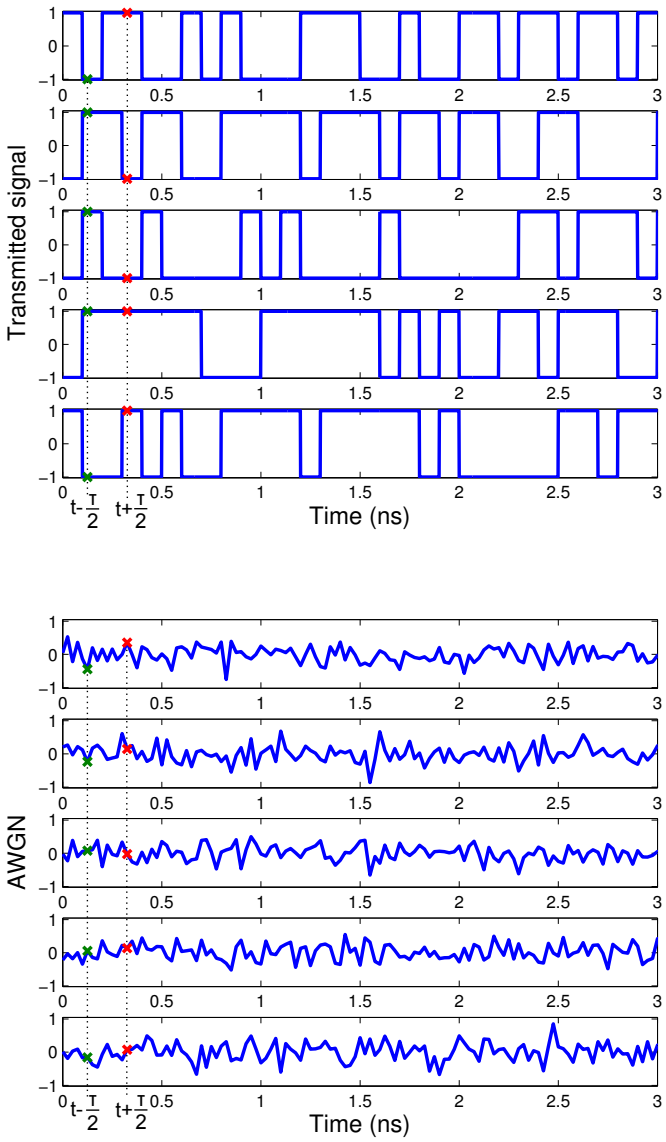

Figure 3.2: Multiple realisations of a zero-mean binary modulated signal (top) and AWGN of zero-mean and 0.25 standard deviation (bottom). Two samples, delayed from each other by τ, as indicated, are to be correlated across the whole ensemble.

The first and second order statistical properties (i.e. the mean and autocorrelation respectively), are obtained through ensemble averages:

$$\hat{\mu}_x = E\left[x(t)\right], \tag{3.1}$$

$$\hat{R}_x(\tau) = E\left[x(t+\frac{\tau}{2}) \cdot x^*(t-\frac{\tau}{2})\right]. \tag{3.2}$$

Conventional notations are used: $\hat{x}$ to indicate the estimated value of x, x^* for the complex conjugate of x, and E for the expectation operator, which gives the ensemble average.

The mean of a wide-sense stationary process is time-independent while the autocorrelation depends only on the time lag. In the majority of the optical communications literature, modulated signals have been assumed as wide-sense stationary processes, along with noise. However, as introduced in the seminal works of Hurd [1969] and Gardner [1972], linearly modulated signals have an autocorrelation function that is periodic with time, and therefore are not stationary in the wide-sense. These are instead defined as *wide-sense cyclostationary*, as the autocorrelation retains its stationarity within a fixed cycle.

The two examples considered previously demonstrate these statements. The mean values of both the binary modulated signal and the AWGN process are clearly zero. The autocorrelations on the other hand, exhibits different properties depending on the process considered, as Fig. 3.3 shows. Based on a large number of different realisations of a binary signal, Fig. 3.3(a) shows that the autocorrelation function will be cyclic in time, and the correlation is non-zero provided that the two samples which are to be correlated fall within the same clock interval. By contrast, the autocorrelation of a wide-sense stationary process as a function of both time and time lag is depicted in Fig. 3.3(b). Here, there is clearly no time-dependence and there is no correlation for any $\tau \neq 0$, because the different samples of a random process are independent from each other and therefore they do not correlate.

Therefore, under the cyclostationarity theory, the autocorrelation function will depend on two parameters: the time instant t, when the measurement is performed, and the time lag τ. The mathematical notation of the autocorrelation of the cyclostationary signal $x(t)$ becomes $\hat{R}_x(t,\tau)$, instead of $\hat{R}_x(\tau)$ as before, to underline its time-dependency.

These conclusions lead to the formal stochastic definition of cyclostationarity,which states that a signal is *wide-sense cyclostationary* (or cyclostationary of the second order) if its autocorrelation function is periodic with time:

$$R_x(t,\tau) = R_x(t+T_b,\tau). \tag{3.3}$$

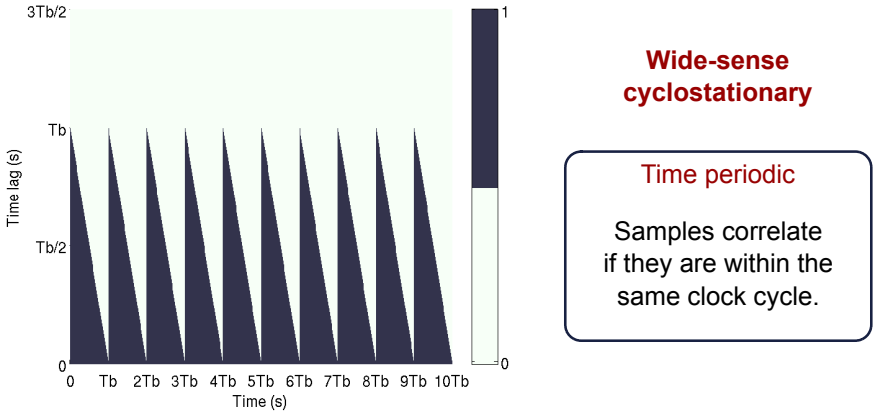

(a)

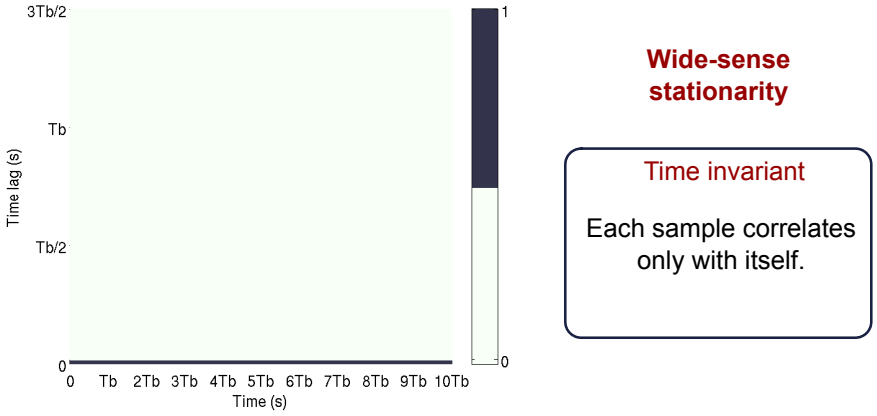

(b)

Figure 3.3: The autocorrelation function of binary modulated signals is cyclic in time, demonstrating that these are wide-sense cyclostationarity processes (a), while AWGN is time-invariant, as it is a wide-sense stationary process (b).

As a periodic function, the autocorrelation therefore has a Fourier series expansion, which is given by:

$$R_x(t,\tau) = \sum_{n=-\infty}^{+\infty} R_x^{\frac{n}{T_b}}(\tau) \cdot e^{j2\pi\frac{n}{T_b}t}, \tag{3.4}$$

where:

- $R_x^{\frac{n}{T_b}}(\tau)$ constitute the Fourier series coefficients of the autocorrelation function, called the *Cyclic Autocorrelation Functions*,
- $\alpha = \frac{n}{T_b}, n \in \mathbb{Z}$ are the Fourier series frequency components, which are called the *cyclic frequencies*, and
- T_b is the both the symbol period and the autocorrelation period.

Fig. 3.4 shows in more detail, the inherent periodicity of the autocorrelation function with time, for a fixed lag value. The duration over which the autocorrelation is not

identically zero, decreases as the lag parameter increases. For any lag value higher than the symbol period T_b, the autocorrelation will be zero, as consecutive symbols are uncorrelated (they are assumed independent and identically distributed).

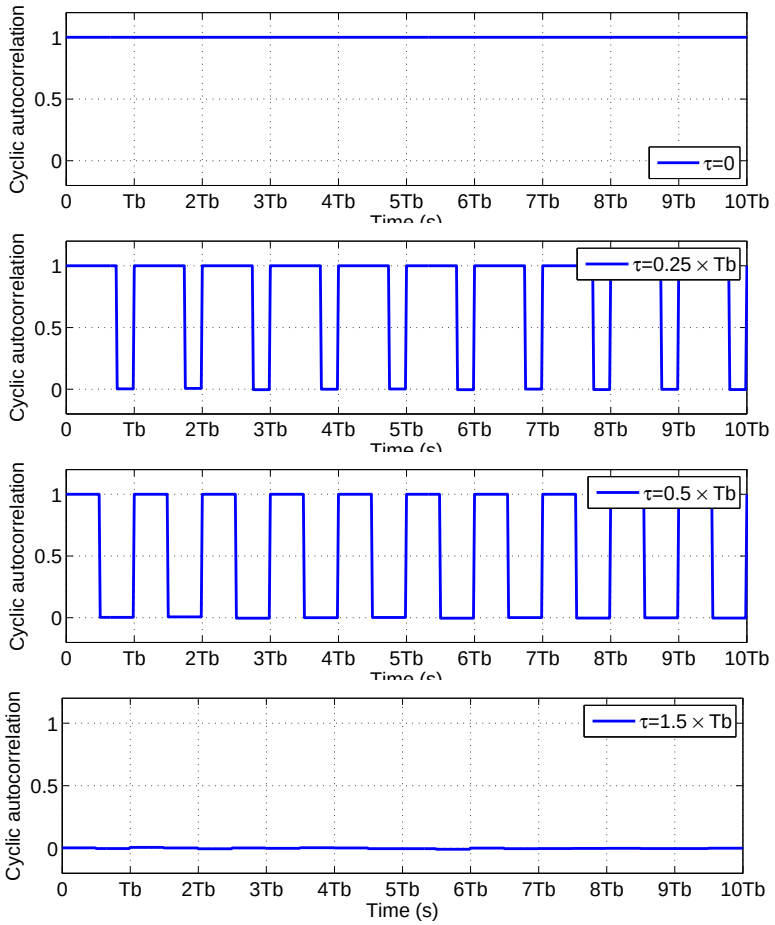

Figure 3.4: The autocorrelation of a modulated signal is cyclic in time, for a fixed time lag τ. The autocorrelation period is equal to the symbol period.

3.1.2 Deterministic definition

A deterministic definition implies a time average over the entire signal, which is regarded as a single time-series measurement. This is a direct consequence of the ergodicity property of stationary processes, for which the ensemble average is equal to the time average. Thus, the mean of $x(t)$ is:

$$\hat{\mu}_x = \lim_{T\to\infty} \frac{1}{T} \int_{-\frac{T}{2}}^{\frac{T}{2}} x(t)dt \tag{3.5}$$

and the autocorrelation is given by:

$$\hat{R}_x(\tau) = \lim_{T\to\infty} \frac{1}{T} \int_{-\frac{T}{2}}^{\frac{T}{2}} x(t+\frac{\tau}{2})x^*(t-\frac{\tau}{2})dt \tag{3.6}$$

The stochastic and deterministic (non-probabilistic) definitions are equivalent to each other, as the ensemble averaging is replaced by time averaging [Gardner, 1994]. When dealing with single time-series measurements of a signal, that cannot be modelled as realisations of a process, such as it is the case in a fibre optics transmission system as the one described previously in Fig. 3.1, it is more appropriate to use the deterministic model. This assumption and the following deterministic definitions of the CAF, and later the SCF, are used subsequently in Chapter 5 of this thesis.

In deterministic terms, the signal $x(t)$ is defined as *second-order cyclostationary* if there exists a quadratic time-invariant transformation that, when applied to the signal, it induces finite-strength additive sine-wave components, that were not contained in $x(t)$ before the transformation [Gardner, 1986a]. Linearly modulated signals are second-order cyclostationary, as there is such a second order transformation, namely the lag product $z(t) = x(t+\frac{\tau}{2})x^*(t-\frac{\tau}{2})$, that contains sine-wave components at frequencies α proportional to the symbol-rate. These components are the CAFs and the frequencies are called *cyclic frequencies*.

The CAF is, more simply, defined as the time average of the autocorrelation lag product weighted at a frequency component α (in other words, the sine-wave components of the lag product function):

$$\hat{R}_x^{\alpha}(\tau) = \lim_{T\to\infty} \frac{1}{T} \int_{-\frac{T}{2}}^{\frac{T}{2}} x(t+\frac{\tau}{2})x^*(t-\frac{\tau}{2})e^{-j2\pi\alpha t}dt \tag{3.7}$$

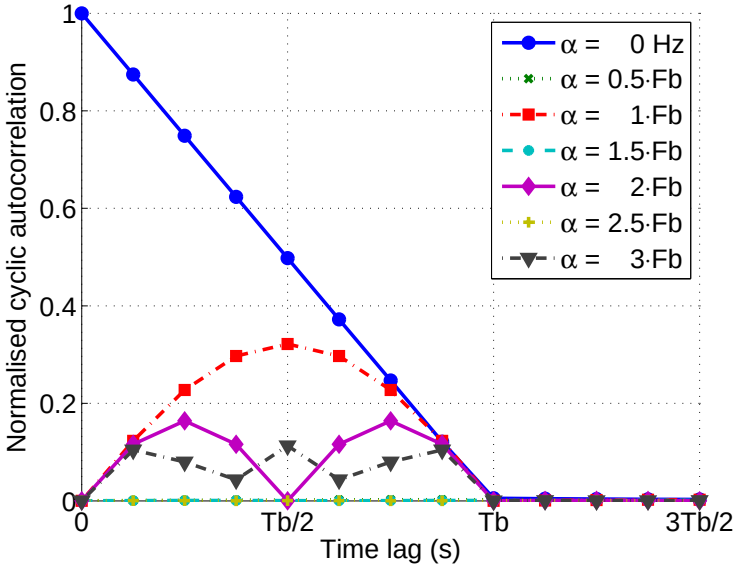

Figure 3.5: The Cyclic Autocorrelation Function is not identically zero only for cyclic frequencies which are multiples of the symbol-rate. Here, square pulses with no low-pass filtering are assumed.

Fig. 3.5 shows the CAF, as a function of the time lag τ and the cyclic frequency α. For linearly modulated signals, the cyclic frequency α is defined over a set $A_y = \{m \cdot F_b \mid m \in \mathbb{Z}\}$, where F_b is the symbol-rate and the inverse of the symbol period T_b. Over this set, the Cyclic Autocorrelation Functions constitute the Fourier coefficients of the autocorrelation, which is thus given by:

$$\hat{R}_y(t,\tau) \triangleq \sum_{\alpha \in A_y} \hat{R}_y^{\alpha}(\tau) \cdot e^{j2\pi\alpha t} \tag{3.8}$$

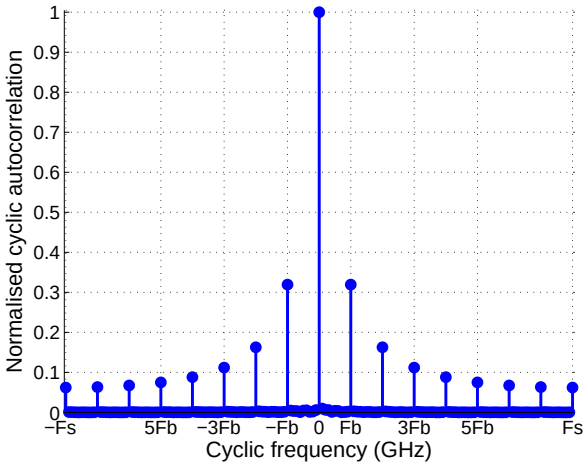

(a) QPSK signals are wide-sense cyclostationary as their autocorrelation contains frequency components at cyclic frequencies multiple of the symbol-rate.

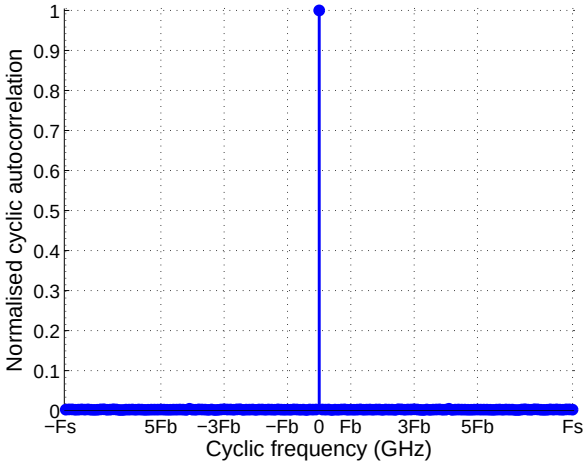

(b) AWGN is wide-sense stationary as each frequency component correlates only with themselves ($\alpha = 0$)

Figure 3.6: Cyclic frequencies components of the autocorrelation function, called the Cyclic Autocorrelation Functions.

The DC component of the lag-product $z(t)$, when $\alpha = 0$, is simply the ordinary autocorrelation function (from Eq. 3.6). In general, when $\alpha = m \cdot F_b$, for any non-zero

integer m, the $R_x^{\alpha}(\tau)$ is the m^{th} harmonic of the autocorrelation function. The presence of these harmonics indicates a cyclostationary process, as Fig. 3.6(a) shows for a QPSK signal, where the frequency components of $\hat{R}_x(t,\tau)$ exist only at integer multiples of the symbol-rate and are identically zero otherwise. Stationary processes do not have any harmonics within their autocorrelation, as demonstrated by Fig. 3.6(b) for AWGN.

It can be easily proved that the CAF of $x(t)$ is equivalent to the cross-correlation of two signals $u(t) = x(t) \cdot e^{-i\pi\alpha t}$ and $v(t) = x(t) \cdot e^{i\pi\alpha t}$ [Gardner, 1986a]:

$$\hat{R}_x^{\alpha}(\tau) = \hat{R}_{uv}(\tau) = \lim_{T\to\infty} \frac{1}{T} \int_{-\frac{T}{2}}^{\frac{T}{2}} u(t+\frac{\tau}{2}) v^*(t-\frac{\tau}{2}) dt. \tag{3.9}$$

The cyclic autocorrelation should not be confused with the circular autocorrelation. The former, as presented in this section, measures the presence of harmonics in the autocorrelation function of a cyclostationary signal, (with fundamental frequency equal to the symbol-rate when linearly modulated), hence the term *cyclic*. The latter, as described in [Oppenheim and Schafer, 2010], simply indicates the implementation of the autocorrelation function of a stationary signal by circularly shifting the signal in time to obtain different lags, hence the term *circular*.

3.2 Power spectral density

Through spectral analysis, a signal is decomposed into its constituent frequencies to measure the power distribution over these frequencies. This measurement represents the PSD of the signal, which can be used in a myriad of ways for signal analysis. One such use for example, is in the OSNR measurement using the OSA approach, as described in Section 2.3.

As an ideal PSD measurement is not possible in practice, due to the limited sampling rate and measurement time, different techniques have been devised in order to estimate the PSD of a signal, as accurately as possible. Some of the simplest and most effective techniques are directly derived from the Fourier transform of the signal.

To account for the fact that the signal is observed over a finite time interval, we use here the Short-Time Fourier Transform (STFT) in order to inspect the spectral content of the signal. The STFT is a FFT performed at time t over a window of arbitrary interval T, or in other words, it measures the spectral content with respect to time:

$$X_T(t,f) = \int_{t-\frac{T}{2}}^{t+\frac{T}{2}} x(\gamma) e^{j2\pi f\gamma} d\gamma \tag{3.10}$$

Equation 3.10 holds under the assumption that the window is rectangular. The periodogram is the most commonly used PSD estimate, and it is obtained by applying the STFT over the entire measured signal. Analytically, the PSD is given by the squared

magnitude of the STFT, inversely scaled by the measurement time interval, T (in this particular case $T = \Delta t$):

$$\hat{S}_{x_T}(t,f) = \frac{1}{T}\left|X_T(t,f)\right|^2 \tag{3.11}$$

The periodogram is a good estimate of the PSD provided that the SNR is high and the measurement time is sufficiently long. If this is not the case, the PSD will exhibit high variance (low estimation reliability).

An alternative approach to PSD estimation is Welch's method, which averages multiple periodograms over shorter intervals $T = \frac{1}{\Delta f}$, within the entire signal interval Δt:

$$\hat{S}_x(f) = \lim_{\Delta f \to 0} \lim_{\Delta t \to \infty} \frac{1}{\Delta t} \int_{t-\frac{\Delta t}{2}}^{t+\frac{\Delta t}{2}} S_{x_{1/\Delta f}}(\xi, f) d\xi \tag{3.12}$$

The averaging operation will thus reduce the variance due to noise, when the SNR is low.

According to the Wiener-Khinchin relation, the PSD of a stationary random signal is obtained from the Fourier Transform of the autocorrelation[1] of the signal:

$$\hat{S}_x(f) = \mathfrak{F}\left\{\hat{R}_x(\tau)\right\} = \int_{-\infty}^{+\infty} \hat{R}_x(\tau) e^{-j2\pi f\tau} d\tau \tag{3.13}$$

3.3 Spectral correlation function

Similarly to the autocorrelation function, which measures the correlation between time-domain samples separated by a time lag, the SCF measures the density of the correlation between the spectral components separated by a cyclic frequency α. This correlation is measured in both amplitude and phase. Since a cyclostationary signal exhibits time periodicity in its autocorrelation, with period equal to the symbol-period T_b, then its SCF exhibits periodicity with a fundamental frequency equal to the symbol-rate $F_b = \frac{1}{T_b}$. Parallels between the SCF and PSD are drawn here, in order to explain the basic cyclostationarity concepts in the frequency domain. A few digital SCF implementations have been proposed in the literature and are discussed here. The SCF is sometimes referred to as the *Spectral Correlation Density Function* or *cyclic spectra*. In the work presented in Chapter 5, the slice of SCF at $\alpha = F_b$ is specifically referred to as the *cyclic spectrum* and the process of obtaining it, spectral correlation.

Firstly, the Wiener-Khinchin theorem (Eq. 3.13) can be extended for cyclostationary signals, to the more general relation called the *Cyclic Wiener Relation* [Gardner, 1987] which states that the SCF is the Fourier Transform of the CAF:

[1] Using the notation for a wide-sense stationary process, as described in Section 3.1.

$$\hat{S}_x^{\alpha}(f) = \mathfrak{F}\left\{\hat{R}_x^{\alpha}(\tau)\right\} = \int_{-\infty}^{\infty} \hat{R}_x^{\alpha}(\tau) \cdot e^{-i2\pi f\tau} d\tau \tag{3.14}$$

The SCF is therefore defined on a bi-frequency plane, along the ordinary frequency f and the cyclic frequency α. If the two frequency axes are normalised to the sampling-rate, then the bi-frequency plane is uniquely defined along the ranges $f \in \left[-\frac{1}{2}, \frac{1}{2}\right]$ and $\alpha \in [-1, 1]$.

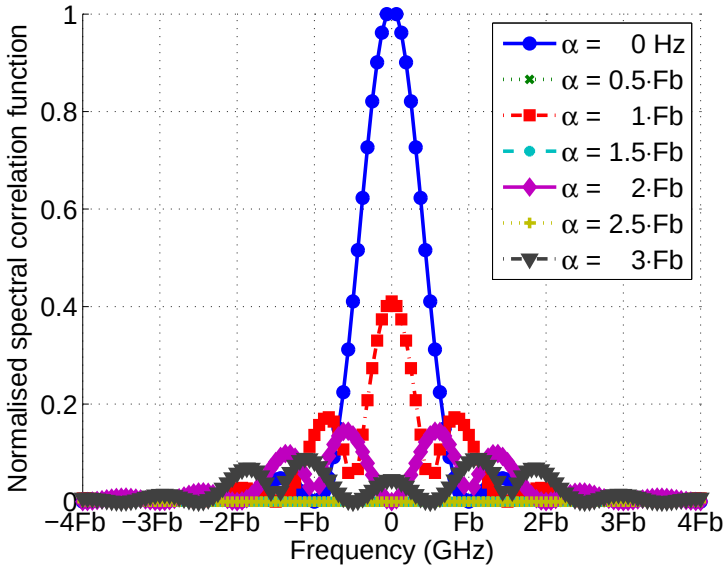

Figure 3.7: The SCF is the Fourier transform of the CAF and is not identically zero only for cyclic frequencies which are multiples of the symbol-rate. Here, square pulses with no low-pass filtering are assumed.

Referring back to Fig. 3.5, the Fourier Transform of the CAF is depicted in Fig. 3.7. The ideal SCF of a purely cyclostationary signal will exhibit periodicity only for cyclic frequencies equal to the symbol-rate and will be identically zero otherwise. The 3D representation of the SCF in Fig. 3.8 helps to better visualise the difference between wide-sense cyclostationary and wide-sense stationary signals. The cyclic spectra is periodic along the cyclic frequency with period equal to the symbol-rate, for signals modulated with a linear modulation format, such as M-PSK or M-QAM. On the other hand, AWGN is wide-sense stationary, so its SCF is identically zero for all cyclic frequencies, except for the special case when $\alpha = 0$.

Similarly to the periodogram of stationary processes (Equation 3.11), the SCF can be simply approximated by the *cyclic periodogram* $\hat{S}_{x_T}^{\alpha}(t, f)$, measured within an arbitrary observation time T, as given by:

$$\hat{S}_x^{\alpha}(f) \approx \hat{S}_{x_T}^{\alpha}(t, f) = \frac{1}{T} X_T(t, f + \frac{\alpha}{2}) \cdot X_T^*(t, f - \frac{\alpha}{2}). \tag{3.15}$$

which also suffers from high variance at low SNRs and when the observation time is

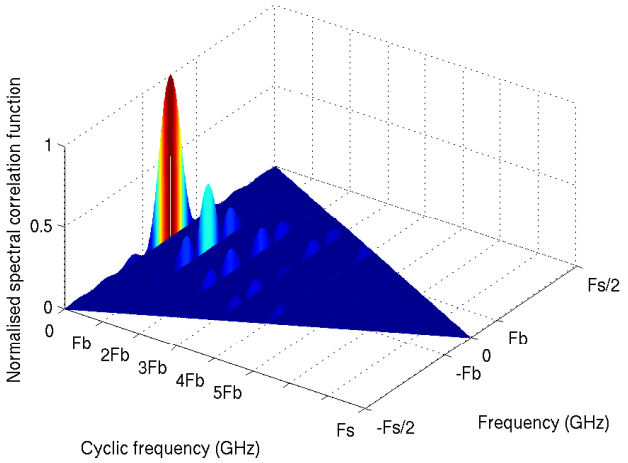

(a) QPSK signals are wide-sense cyclostationary as their SCF consists of cyclic spectra repeating periodically at cyclic frequencies multiple of the symbol-rate F_b.

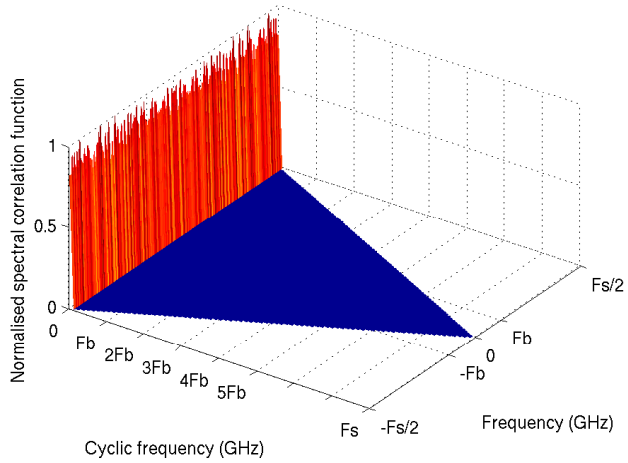

(b) AWGN is wide-sense stationary as only one spectrum exists at cyclic frequency $\alpha = 0$.

Figure 3.8: SCF of cyclostationary (a) and stationary (b) signals.

restricted.

An alternative, but equivalent, mathematical expression of the SCF is the Cross-Power Spectral Density (CPSD) of signals $u(t) = x(t) \cdot e^{-j2\pi\frac{\alpha}{2}t}$ and $v(t) = x(t) \cdot e^{j2\pi\frac{\alpha}{2}t}$, which can be introduced in Eq. 3.9 to give:

$$\hat{S}_x^{\alpha}(f) \approx \hat{S}_{uv}(t,f) = \frac{1}{T} U_T(t,f) \cdot V_T^*(t,f). \tag{3.16}$$

From these two last expressions arises the interpretation of the SCF as the complex correlation (in both amplitude and phase) of all frequency components of $x(t)$, separated by an arbitrary cyclic frequency α. When $\alpha = 0$, we are correlating each frequency with itself and the cyclic spectra simply reduces to the PSD, whilst the cyclic periodogram

(Eq. 3.15) reduces to the conventional periodogram (Eq. 3.11). Because the correlation is performed as a complex operation, the resulting SCF is complex for all $\alpha \neq 0$ and is real otherwise.

According to Gardner [1986b], the ideal SCF of a continuous-time signal $x(t)$ can be more efficiently estimated either as a temporally smoothed or as a spectrally smoothed cyclic periodogram. The difference between the two smoothing approaches is given not only by the domain onto which the averaging operation is performed, but also by the time intervals T over which the STFT is computed (i.e. in Eq. 3.15).

Temporal smoothing

Temporal smoothing is achieved by averaging multiple STFTs obtained over fractional time intervals of the measured signal ($T = \frac{1}{\Delta f}$).

$$\hat{S}_x^{\alpha}(f) = \lim_{\Delta f \to 0} \lim_{\Delta t \to \infty} \frac{1}{\Delta t} \int_{t-\frac{\Delta t}{2}}^{t+\frac{\Delta t}{2}} S_{x_{1/\Delta f}}^{\alpha}(\xi, f) d\xi \tag{3.17}$$

A graphical representation of the temporal smoothing technique is shown in Fig. 3.9. The captured signal of total time duration Δt is divided into shorter segments of duration $T = \frac{1}{\Delta f}$. Multiple cyclic periodograms are first computed over these different time slots, having a spectral resolution equal to Δf. The individual periodograms are subsequently averaged in time. In the cyclostationarity theory, the time-smoothing SCF is the equivalent of the Welch method for obtaining an improved PSD estimate, by reducing the impact of random effects through averaging. As a confirmation to this statement, when $\alpha = 0$, Eq. 3.17 becomes Eq. 3.12.

The spectral estimation variance can therefore be lowered, by increasing the number of averages. In order to do so, the total observation time must greatly exceed the duration of the time segments:

$$\Delta t >> T = \frac{1}{\Delta f} \tag{3.18}$$

Additionally, the segments could be overlapping in order to increase the number of averages, for a fixed Δt. However, increasing the number of averages has the disadvantage of increasing the computational complexity of the technique, when implemented in the digital domain. Several methods have been proposed for implementing the temporal smoothing approach, with differing levels of complexity.

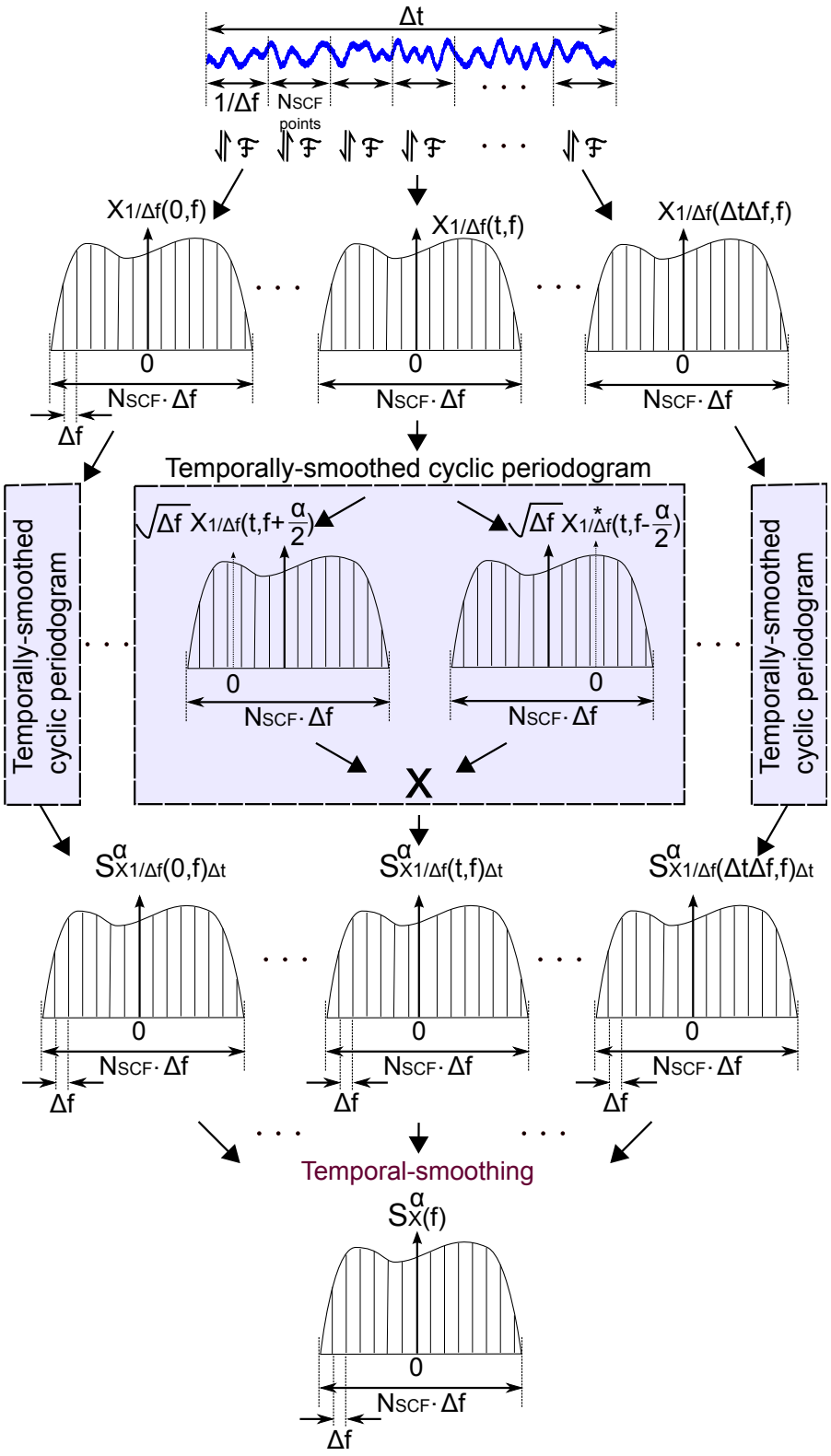

Figure 3.9: Schematic of the temporal smoothing technique to calculate the cyclic spectrum.

The discrete-time temporally smoothed SCF [Tom, 1995] is given by:

$$\hat{S}_x^{\gamma}(k) \approx \frac{1}{M \cdot N_{SCF}} \sum_{m=0}^{M-1} X_{N_{SCF}}(n+mL, k+\frac{\gamma}{2}) \cdot X_{N_{SCF}}^{*}(n+mL, k-\frac{\gamma}{2}) \tag{3.19}$$

where:

- γ is the discrete cycle frequency, the equivalent of the continuous α.
- k is the discrete ordinary frequency, across which each spectral slice is measured.
- n is the time index.
- M is the number of individual temporal segments.
- N_{SCF} is the number of samples within each segment, and the FFT size.
- L is the number of samples that are skipped when moving from one segment to another, and it indicates the amount of overlap.

The downconverted Discrete Fourier Transform (DFT) of the digital signal segment $x_{N_{SCF}}(n)$, filtered with $a_{N_{SCF}}(n)$ data tapering function, here assumed to be an ideal rectangular window, is:

$$X_{N_{SCF}}(n+mL, k) \stackrel{\Delta}{=} \sum_{n=0}^{N_{SCF}-1} a_{N_{SCF}}(n) x(n+mL) e^{-j2\pi k(n+mL)/N_{SCF}} \tag{3.20}$$

After the multiplication the term $e^{-j2\pi\nu mL/N_{SCF}}$ arises from the time-shift of the sliding window that extracts each data segment and contributes to the computation of the SCF by ensuring the segments are in phase.

In order to double the cyclic frequency granularity, the time segments of size N_{SCF}, are padded with zeros such that the total time interval is twice as long: $2N_{SCF}$. To cover the entire bi-frequency plane as shown in Fig. 3.10, $2N_{ADC}N_{SCF}$ cells are computed in total.

The brute-force approach involves the calculation of Eq. 3.19, cell-by-cell and is the least effective. It has a complexity dominated by the temporal averaging operation, which comprises of two multiplications for each cell: frequency-shifted spectra multiplications and time exponential multiplications.

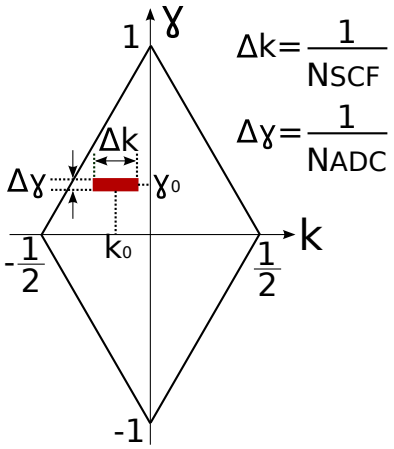

Figure 3.10: Bifrequency plane showing the width and length of a single cell. Its total area can be filled with $2 \cdot N_{SCF} \cdot N_{ADC}$ cells. The two frequency axes are normalised by the sampling frequency.

Operation	Number of complex multiplications
$2\,N_{SCF}$ - point FFT	$M\,N_{SCF}\,(1+log_2(N_{SCF}))$
Temporal averaging for all cells	$2\,M\,N_{ADC}\,N_{SCF}$

Table 3.1: Implementation complexity of the brute-force time smoothed SCF.

Two well established digital implementations of the time-smoothing method, with improved computational performance, are the FFT Accumulation Method (FAM) and the Strip Spectrum Correlation Algorithm (SSCA). Both algorithms use an extra FFT stage instead of averaging in order to improve the resolution along the cyclic frequency axis. Whilst detailed investigation of these approaches does not constitute the scope of this thesis, they are treated in [Roberts et al., 1991] and [Brown and Loomis, 1993] .

Frequency smoothing

The STFT computed over the entire measured signal ($T = \Delta t$):

$$\hat{S}_x^{\alpha}(f) = \lim_{\Delta f \to 0} \lim_{\Delta t \to \infty} \frac{1}{\Delta f} \int_{f-\frac{\Delta f}{2}}^{f+\frac{\Delta f}{2}} S_{x_{\Delta t}}^{\alpha}(t,\nu) d\nu \tag{3.21}$$

A graphical representation of the spectral smoothing approach, for the computation of the SCF, is shown in Fig. 3.11. Spectral smoothing is performed on a single periodogram, obtained from the entire measured signal ($T = \Delta t$, where Δt is the total observation time interval of $x(t)$). The averaging operation for reducing random effects is performed in the frequency domain, over fixed frequency bins, such that the final resolution of the cyclic spectrum is Δf.

To better reduce the effects of randomness causing a high estimation variance, the number of averages is increased, which in this case it is equivalent to the bandwidth of

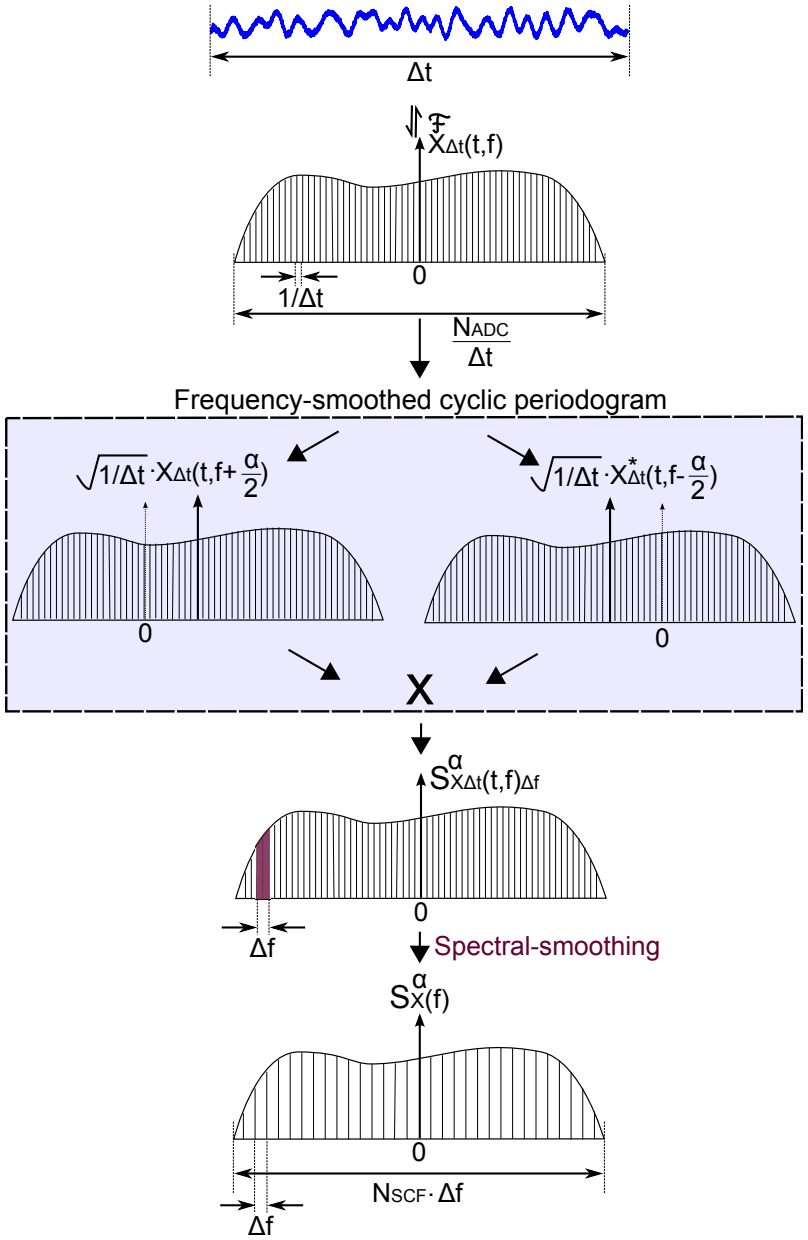

Figure 3.11: Schematic of the spectral smoothing technique to calculate the SCF Schematic of the spectral smoothing technique to calculate the cyclic spectrum.

averaging bins greatly exceed the frequency resolution of the periodogram:

$$\Delta f >> \frac{1}{T} = \frac{1}{\Delta t} \tag{3.22}$$

In the case of the digitized signal, $\Delta t = \frac{N_{ADC}}{F_s}$, while $\Delta f = \frac{F_s}{w}$, where w is the number of samples used for frequency averaging in Eq. (3.21). The frequency-smoothed SCF is thus defined over $N_{SCF} = \frac{N_{ADC}}{w}$ points. The condition 3.22 means that the frequency smoothing window w should be significantly less than the total sample size N_{ADC}, for an increase in number of averages and, thus, a decreased variance.

The discrete-time spectrally smoothed SCF [Tom, 1995] is given by:

$$\hat{S}_x^{\gamma}(k) \approx \frac{1}{w \cdot N_{ADC}} \sum_{l=-\frac{w-1}{2}}^{\frac{w-1}{2}} X_{N_{ADC}}(n, k+\frac{\gamma}{2}+l) \cdot X_{N_{ADC}}^{*}(n, k-\frac{\gamma}{2}+l) \tag{3.23}$$

where

$$X_{N_{ADC}}(n,k) \stackrel{\Delta}{=} \sum_{m=0}^{N_{ADC}-1} a_{N_{ADC}}(m) x(n+m) e^{-j2\pi k(n+m)/N_{ADC}}$$

is the downconverted DFT of the digital signal $x(n)$, and:

- γ is the discrete cycle frequency, the equivalent of the continuous α.
- k is the discrete ordinary frequency, across which each spectral slice is measured.
- n is the time index.
- N_{ADC} is the total number of samples captured by the ADC and the FFT size.
- $a_{N_{ADC}}(n)$ is a data tapering function, here assumed to be an ideal rectangular window.

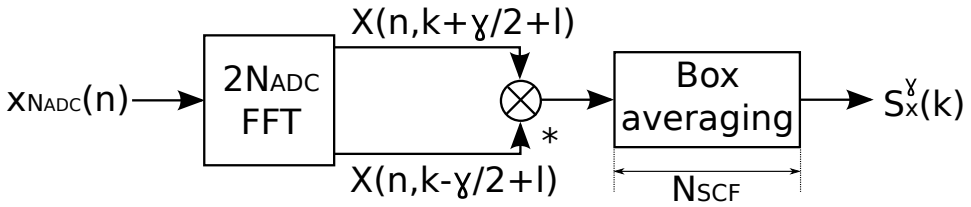

Figure 3.12: Brute-force method to digitally implement the calculation of the SCF, with a single FFT and a box averaging to perform frequency smoothing.

Digitally, the brute-force method for the estimation of the SCF by frequency smoothing can be implemented with a single FFT and a box-average filter along the frequency k as depicted in Fig. 3.12 and demonstrated by Brown and Loomis [1993]. In order to double the cyclic frequency granularity, the signals, are padded with zeros such that the total sample size is twice the initial sample size: $2N_{ADC}$. To cover the entire bi-frequency plane, $2N_{ADC}N_{SCF}$ cells are computed in total. The brute-force method implements Eq. 3.23 cell-by-cell, and has a complexity dominated by the FFT operation (Table 3.2).

Operation	Number of complex multiplications
$2\,N_{ADC}$ - point FFT	$N_{ADC}(1+log_2(N_{ADC}))$
Frequency averaging for all cells	$2\,w\,N_{ADC}\,N_{SCF}$

Table 3.2: Implementation complexity of the brute-force frequency smoothed SCF.

Reliability and resolution trade-off

A spectrum estimate is *reliable*, or it has a low variance, if the random amplitude and phase components corrupting it are reduced insofar as the measurement becomes time-independent. As discussed previously for the two averaging approaches, this can be achieved by increasing the number of averages performed, as Equations 3.18 and 3.22 described previously. These conditions are united under the *Grenander's Uncertainty Condition* [Gardner, 1986b], which states that for a reliable spectral estimation, the product between the temporal and spectral resolutions should be much greater than unity:

$$\Delta t \Delta f >> 1 \tag{3.24}$$

or, for digital signal representations, the number of samples used in the estimate should be much greater than the number of samples used to represent the final spectrum:

$$\frac{N_{ADC}}{N_{SCF}} >> 1. \tag{3.25}$$

By contrast, if the SCF would simply be approximated by the cyclic periodogram (Eq. 3.15), then $\Delta t \cdot \Delta f = 1$. However, when smoothing is performed, increasing the number of averages is equivalent to a reduced temporal resolution $\Delta t >> 1/\Delta f$ when temporal smoothing is employed, and a reduced spectral resolution $\Delta f >> 1/\Delta t$ when spectral smoothing is employed. It is not possible therefore, to maintain a high temporal or spectral resolution, as the reliability of the spectrum estimate increases.

The Grenander's condition can also be expressed in terms of the *cycle resolution* $\Delta\alpha = \frac{1}{\Delta t}$, which indicates how finely the cyclic frequencies could be distinguished:

$$\frac{\Delta f}{\Delta\alpha} >> 1 \tag{3.26}$$

Because the cycle resolution is the inverse of the temporal resolution and from Grenander's condition, the granularity of the cyclic frequency is much finer compared to the granularity of the ordinary frequency, in the bi-frequency plane (Fig. 3.10).

In an ideal measurement, $\Delta f \to 0$ and $\Delta\alpha \to 0$, meaning that the capability to distinguish ordinary and cyclic frequencies is infinite. As the number of samples and the sampling frequency are finite in practice, *spectral leakage* and *cycle leakage* are

limiting effects of the spectral measurement. A more detailed account of all of these concepts can be found in [Gardner, 1986b].

Temporal and spectral smoothing approaches comparison

The two smoothing approaches are equivalent to each other, as Gardner [1986b] proves, provided that the observation interval is sufficiently large ($\Delta t >> 1/\Delta f$), such that the impact of random effects on the estimate is diminished and the cycle resolution is increased ($\Delta\alpha = 1/\Delta t$). The temporal-smoothing approach is more computationally efficient if the entire SCF is required, for a multitude of ordinary and cyclic frequencies, whereas, frequency smoothing is more computationally effective if the number of cyclic frequencies of interest is limited [Roberts et al., 1991]. The work presented in this thesis focuses on the frequency smoothing approach, because the computation of the SCF for specific cyclic frequencies is needed.

3.4 Nyquist pulse shaping

When propagating through fibre, optical pulses experience spreading under cumulative dispersion. As the distance travelled increases, the adjacent pulses will start interfering, effect called ISI. A low-pass filter that satisfies the Nyquist ISI criterion can be employed to mitigate this distortion.

Nyquist pulse shaping additionally increases the spectral efficiency of the transmission by limiting the signal's bandwidth, whilst maintaining the same symbol-rate. The most commonly employed Nyquist pulse shaping filter is the RC filter, split between the transmitter and receiver into two RRC filters as shown in Fig. 3.13, for improved noise suppression.

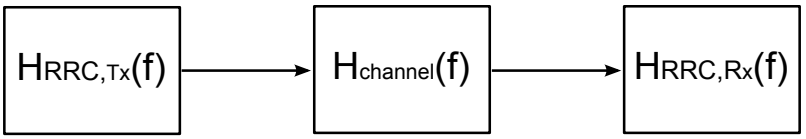

Figure 3.13: Two RRC matching filters are split between the transmitter and receiver, to give an overall RC filter response.

The overall RC filter frequency response is:

$$H_{RC}(f) = \sqrt{H_{RRC,Tx}(f)} \cdot \sqrt{H_{RRC,Rx}(f)}$$

whereas, the frequency response of the RRC filter is given by:

$$H_{RRC}(f) = \sqrt{H_{RC}(f)} = \begin{cases} \sqrt{T_b}, & |f| \leq \frac{1-r}{2T_b} \\ \sqrt{\frac{T_b}{2}\left[1+cos\left(\frac{\pi T_b}{r}\left[|f|-\frac{1-r}{2T_b}\right]\right)\right]}, & \frac{1-r}{2T_b} < |f| \leq \frac{1+r}{2T_b} \\ 0, & otherwise \end{cases} \tag{3.27}$$

Fig.3.14(a) shows that the filter bandwidth is proportional to the roll-off factor, as is the spectrum of the filtered signal. Given a roll-off factor r and a symbol-rate F_b the signal bandwidth after RRC filtering is:

$$BW_{RRC} = F_b \cdot (1+r). \tag{3.28}$$

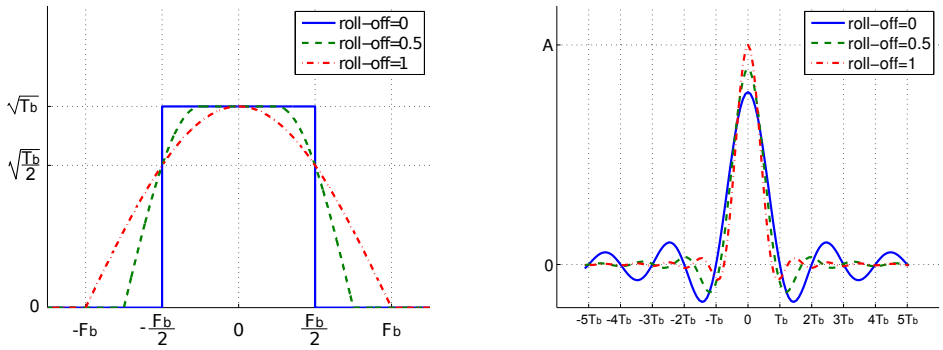

(a) Frequency-domain (b) Time-domain

Figure 3.14: Ideal frequency response (left) and impulse response (right) of the RRC filter for different roll-off factors.

The impulse response of the RRC filter is a sinc function, which ideally has an infinite time-domain representation, and as a result, an infinite attenuation stop-band. However, in a realistic implementation the filter is of finite length, resulting in a finite attenuation stop-band, particularly at lower roll-offs, as shown in Fig. 3.14(b). Since a lower attenuation stop-band translates into higher penalties due to ICI and spectral leakage, whilst a lower roll-off factor is desirable to achieve both a better ISI suppression and a higher spectral efficiency, a trade-off between spectral efficiency and performance thus needs to be attained.

As the RRC roll-off decreases the spectral correlation power and bandwidth decrease as well. Fig. 3.15 depicts the dependence of the bandwidth of the first cyclic spectrum $S_x^{\alpha=F_b}(f)$ on the roll-off factor and symbol-rate. For simplicity, assume that the cyclic spectrum is computed as the CPSD of two frequency shifted spectra (Eq. 3.16), obtained from the original signal spectrum $X(f)$.

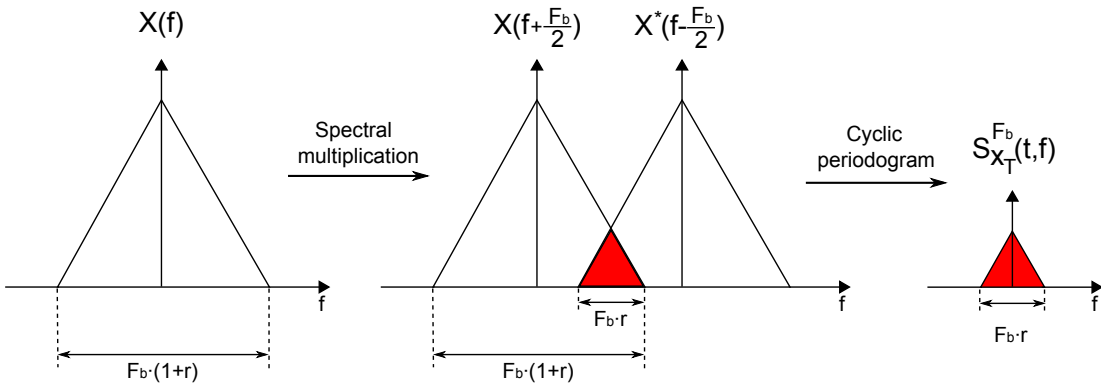

Figure 3.15: Bandwidth of the SCF at cyclic frequency equal to the symbol-rate (F_b) is the intersection of the two frequency-shifted FFTs. The triangles are abstractions of the signal spectrum with RRC filtering, which changes the spectral shape with roll-off.

Since the frequency separation between the two spectra is F_b, the bandwidth of $S_x^{\alpha=F_b}(f)$ can be deduced to be:

$$BW_{RRC}^{\alpha=F_b} = \frac{BW_{RRC}}{2} - \left(F_b - \frac{BW_{RRC}}{2}\right) = F_b \cdot r. \tag{3.29}$$

Eq. 3.28 and 3.29 can be translated into the graph of Fig. 3.16, which, by normalisation to the symbol-rate, shows the dependence of the bandwidth on the roll-off only. A roll-off of 0 maximises the spectral efficiency, but simultaneously nullifies the measure of spectral correlation. Conversely, when the roll-off is 1, the bandwidth of the cyclic spectrum is maximised, to the detriment of the spectral efficiency, which is reduced. Whilst these results are obtained under ideal assumptions, the impact of finite filter taps on the spectral correlation is treated in Chapter 5, Section 5.1.

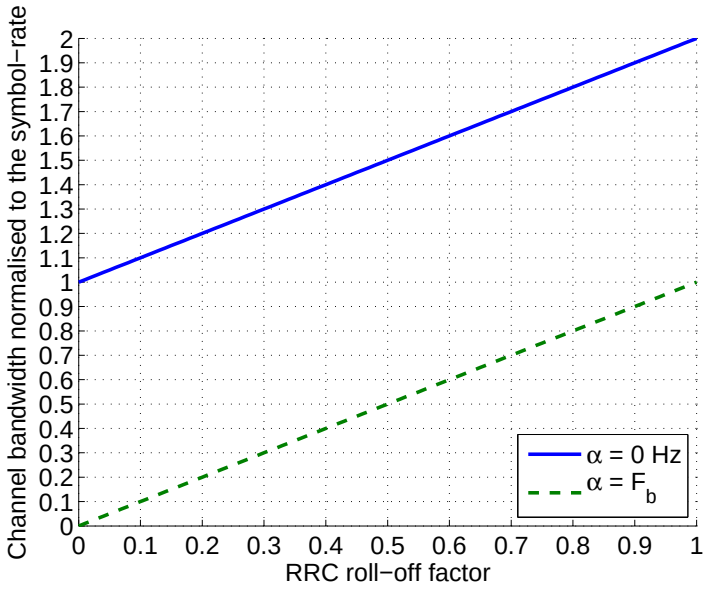

Figure 3.16: Bandwidth of the SCF as a function of RRC roll-off.

Fig. 3.17 shows that as the Nyquist bandwidth ($\left[-\frac{F_b}{2}, \frac{F_b}{2}\right]$) is approached, the power in the cyclic harmonics at $\alpha = F_b, 2 \cdot F_b, etc.$ is dissipated along the time lag, until they are completely filtered out, whilst the spectral efficiency is increased.

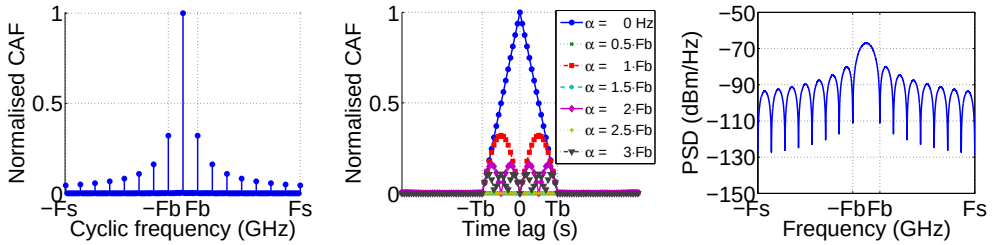

(a) NRZ signal

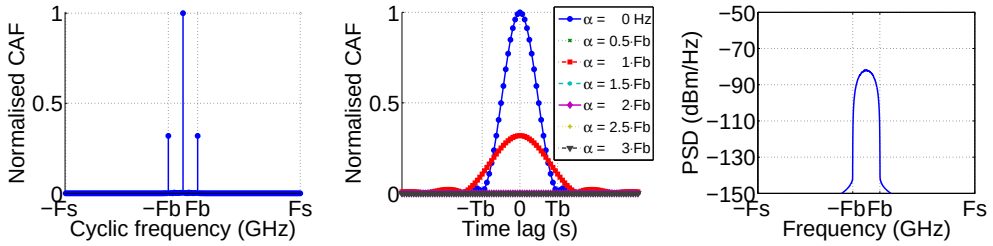

(b) roll-off = 1

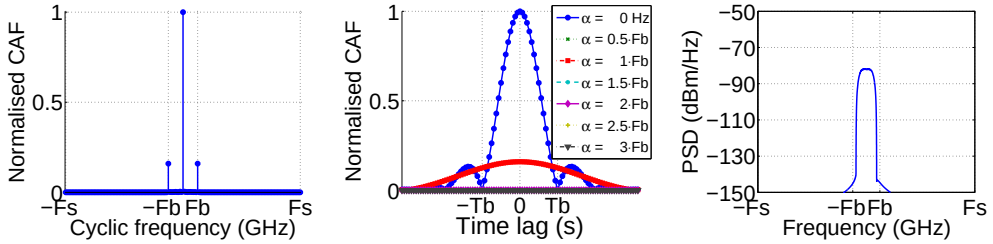

(c) roll-off = 0.5

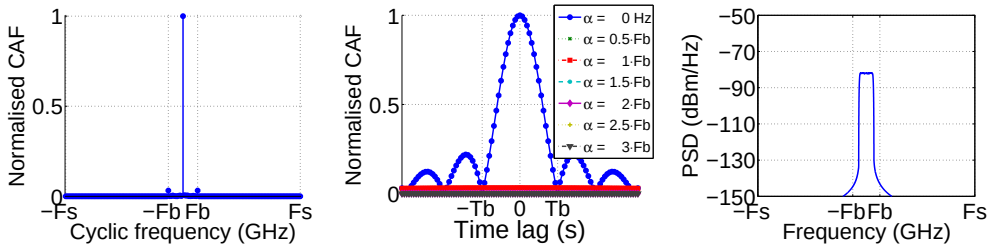

(d) roll-off = 0.1

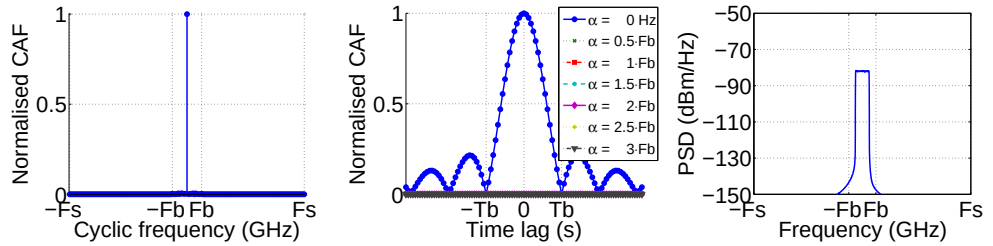

(e) roll-off = 0.01

Figure 3.17: CAF and PSD of NRZ signals with and without RRC filtering.

3.5 Summary

The computation of the PSD has so far been the established approach to characterise digitally modulated optical signals, in terms of their constituent frequencies. However, signal periodicities occurring due to modulation, filtering or coding are not evident from a conventional PSD analysis. Underlined in this chapter is a more appropriate model for such signals based on cyclostationarity, which takes into account these hidden periodicities.

Novel functions are defined in the realm of cyclostationarity theory. The SCF, which is a generalisation of the PSD, measures the correlation density between the constituent frequency components of the signal, separated by an arbitrary frequency difference (called cyclic frequency). Its time-domain counterpart is the CAF, as stated by the Cyclic Wiener Relation. Linearly modulated signals are cyclostationary in the wide-sense, as their cyclic autocorrelation and SCF are periodic with the symbol-rate along the cyclic frequency. AWGN, on the other hand, is stationary as it does not exhibit such a periodicity, its power being negligible for any non-zero cyclic frequencies. Stationary and cyclostationary processes can therefore be easily differentiated by means of their CAF or SCF.

A comparative table of the statistical and time-series interpretations of the cyclostationarity properties presented in this chapter are synthesised from [Gardner, 1986b] and [Gardner et al., 2006] in Table 3.3. The two definitions are equivalent, but from a practical perspective, the time-series approach is more appropriate.

Estimation methods of the conventional and cyclic spectra have also been presented in this chapter. The most basic approach is the periodogram, which suffers from low reliability. Improvements to the periodogram estimate can be made through either temporal or spectral smoothing techniques, and ensuring that a sufficient number of averages are performed to reduce the spectral variance due to random effects. In both conventional spectral analysis and spectral analysis of cyclostationary signals, there is a trade-off between the estimation reliability and temporal and spectral resolutions.

The correlation between spectral components is reduced when filtering is present. If RRC filtering is employed and the roll-off factor is the minimum of zero, the correlation characteristics of the modulated signal mimic those of stationary signals, as the spectral correlation periodicity is lost. As a result, consideration of the minimum roll-off must be made when designing cyclostationarity-based monitoring techniques, as high spectral correlation and high spectral efficiency are mutually exclusive.

The following chapters demonstrate novel performance monitoring techniques, that make use of the spectral and statistical properties of modulated signals and noise, and that can be implemented as part of the DSP stage of coherent transceivers. The limitation due to the RRC filtering on these techniques is investigated.

STOCHASTIC PROCESSES	**TIME-SERIES**
Autocorrelation function	
$R_x(t,\tau) \triangleq E\left\{x(t+\frac{\tau}{2}) \cdot x^*(t-\frac{\tau}{2})\right\}$	$R_x(t,\tau) \triangleq \frac{1}{\Delta t} \int_{-\Delta t/2}^{\Delta t/2} x(t+\frac{\tau}{2}) \cdot x^*(t-\frac{\tau}{2}) dt$
Second-order cyclostationarity in the wide-sense	
$x(t)$ is a cyclostationary process if its mean and autocorrelation are periodic: $E\{x(t+T_b)\} = E\{x(t)\}$ $R_x(t+T_b,\tau) = R_x(t,\tau)$	$x(t)$ is a cyclostationary signal if its *lag product* $z(t,\tau) = x(t+\frac{\tau}{2}) \cdot x^*(t-\frac{\tau}{2})$ contains finite-strength sine-wave components at $\alpha \in A$, the countable set: $A = \left\{\frac{k}{T_b}\right\}_{k\in\mathbb{Z}}$
Cyclic autocorrelation function	
Since periodic, the autocorrelation has a Fourier series decomposition: $R_x(t,\tau) = \sum_{n=-\infty}^{\infty} R_x^{\frac{n}{T_b}}(\tau) e^{j2\pi\frac{n}{T_b}t}$ where the Fourier coefficients $R_x^{\frac{n}{T_b}}(\tau)$ are the *Cyclic Autocorrelation Functions* $R_x^{\frac{n}{T_b}}(\tau) \triangleq \frac{1}{T_b} \int_{-T_b/2}^{T_b/2} R_x(t,\tau) \cdot e^{-j2\pi\frac{n}{T_b}t} dt$	The autocorrelation function is the summation of its sine-wave components: $R_x(t,\tau) = \sum_{\alpha\in A} R_x^{\alpha}(\tau) e^{j2\pi\alpha t}$ where $R_x^{\alpha}(\tau)$ are the *non-stochastic Cyclic Autocorrelation Functions* $R_x^{\alpha}(\tau) \triangleq \lim_{\Delta t\to\infty} \frac{1}{\Delta t} \int_{-\Delta t/2}^{\Delta t/2} z(t,\tau) \cdot e^{-j2\pi\alpha t} dt$
Spectral Correlation Density Function (or cyclic spectrum)	
The cyclic spectrum at cyclic frequency α is defined as the Fourier Transform of the cyclic autocorrelation function, property known as the *Cyclic Wiener Relation*: $S_x^{\alpha}(f) \triangleq \int_{-\infty}^{\infty} R_x^{\alpha}(\tau) e^{-j2\pi f\tau} d\tau$ or, the cross-spectral density of spectra frequency shifted by α from each other, giving the *Cyclic Periodogram* (the product inside the average) which can be either time-smoothed ($T = \frac{1}{\Delta f}$) or frequency-smoothed ($T = \Delta t$), for increased reliability: $S_x^{\alpha}(f) \triangleq \lim_{\Delta f\to 0} \lim_{\Delta t\to\infty} \left\langle \frac{1}{T} X_T(t, f+\frac{\alpha}{2}) X_T^*(t, f-\frac{\alpha}{2}) \right\rangle$ where $X_T(t,f) = \int_{-T/2}^{T/2} x(u) \cdot e^{-j2\pi f u} du$, is the *Short-time Fourier Transform*.	

Table 3.3: Summary of cyclostationarity properties and definitions.

4

Symbol-rate estimation based on the power spectral density

The method presented in this chapter uses the signal power spectrum to estimate the symbol-rate and is, as a result, CD and 1^{st} order PMD tolerant. It is also independent of the IF, as long as the signal spectrum does not fall outside of the receiver bandwidth. Having the advantage of being independent on CD, PMD and LO frequency offset, this method can be employed at the beginning of the DSP stage of the digital coherent receiver, as shown in Fig. 4.1. The main purpose of this estimator is to provide feedback information to the control plane, for spectral resource optimisation as discussed in Chapter 1. It can also be used as a control input to the timing recovery stage, for example.

The estimator is applicable to both M-PSK and M-QAM signals since their power spectral densities are identical [Couch, 1993, p.391]. Two methods are presented. Firstly, a MMSE approach with continuous ideal test spectra is proposed, but it is shown to be highly dependent on the moving-average filter applied. The second method is based on measuring the standard deviation of the spectrum, and is shown to operate from 4 to 25 GBaud QPSK signals with a maximum estimation error of 2% at the FEC limit of $3.8 \cdot 10^{-3}$, when a RRC filter with a roll-off of 0 is used.

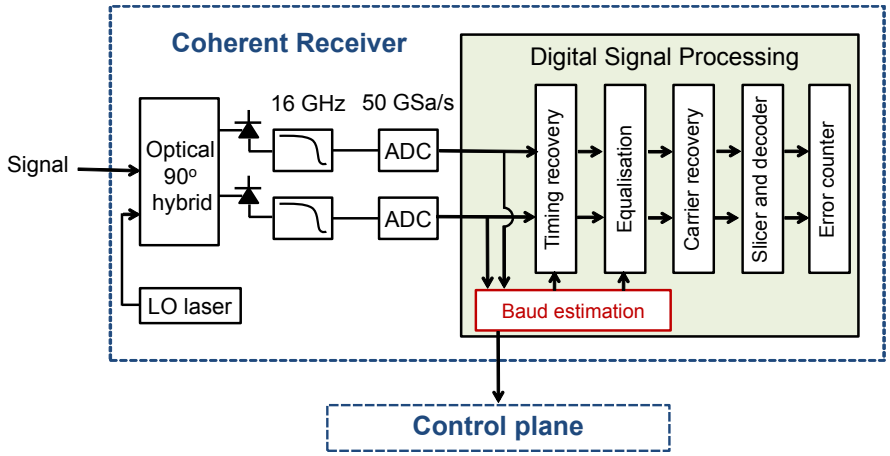

Figure 4.1: Digital coherent receiver including a symbol-rate estimation stage for QPSK signals.

4.1 MMSE with continuous ideal test spectra

4.1.1 Simulation setup

The symbol-rate estimation method depicted in Figure 4.2 is based on a MMSE approach. The method is based on spectral matching between the transmitted signal of unknown symbol-rate and an ideal signal of known symbol-rate. At the transmitter, a trapezoidal waveform is generated with a given symbol-rate to be estimated. AWGN is loaded onto the signal, before it is resampled at the receiver, at 50 GSa/s sampling rate.

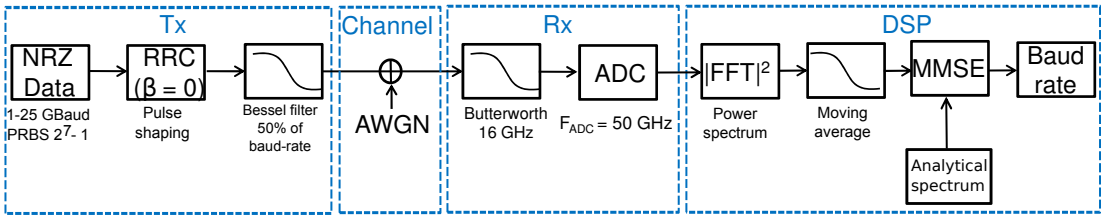

Figure 4.2: Simulation setup for MMSE with a large number of analytical test values.

The spectrum of the transmitted signal is then smoothed by a moving average filter. The length of the moving average filter (N_{MA}) is fixed based on the total number of samples captured (N_{ADC}):

$$N_{MA} = \frac{N_{ADC}}{2^5} \tag{4.1}$$

A range of ideal spectra is generated, assuming ideal trapezoidal waveforms of symbol-rates between 0.2 and 40 GHz, that are the test values of the symbol-rates to be estimated. The ideal spectra of the analytical model correspond to a trapezoidal signal, with the same frequency grid as the transmitted signal. The spectra of a trapezoidal waveform is given by [Paul, 2006, p.118]:

$$X(f) = \frac{2A}{\tau_r(2\pi f)^2}\left[cos\left(2\pi f\frac{\tau}{2}\right) - cos\left(2\pi f\left(\frac{\tau}{2}+\tau_r\right)\right)\right], \tag{4.2}$$

where:

A = maximum signal level,

τ = symbol length - sampling length,

τ_r = sampling length,

f = frequency grid.

The MMSE block estimates the symbol-rate by taking the minimum error corresponding to the difference between the spectra of the received signal and the generated ideal test spectra. The best value is determined through an unconstrained nonlinear optimisation.

The MSE is defined as:

$$mse(test) = |E_{test}(\omega)|^2 - |E_{measured}(\omega)|^2 \tag{4.3}$$

The MMSE is the minimum MSE value between all the test cases, which leads to the estimation of the symbol-rate:

$$\hat{F_b} = \arg_{test}\min\{mse(test)\}. \tag{4.4}$$

4.1.2 Performance analysis

The method's performance was evaluated as the signed estimation error with respect to different noise loading conditions (Fig. 4.3(a)) and number of captured samples (Fig. 4.3(b)). The method is independent of the SNR level, but depends on increasing the number of ADC captured samples in order to reduce the estimation error. While the estimator performs well for higher symbol-rates (<5% error), it results in high overestimation at low symbol-rates (approximately 20% error) due to the fact that the moving-average filter is not correctly optimised in those cases. More precisely, the moving-average length is too long at low symbol-rates, leading to a spreading of the spectrum, hence the overestimation. The dependence of the moving-average filter on the symbol-rate leaves this method inefficient for blind symbol-rate estimation.

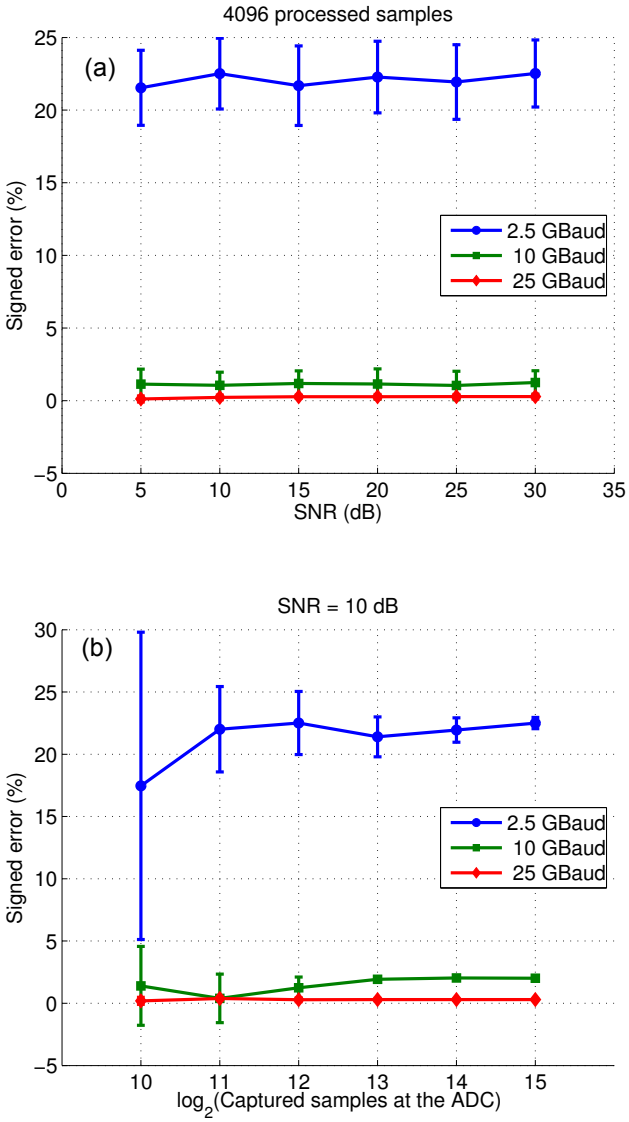

Figure 4.3: Signed estimation error of the MMSE approach verified by simulation of NRZ signals. (a) Impact of noise and (b) impact of captured samples.

4.2 Symbol-rate estimation based on the spectral standard deviation

4.2.1 Technique description

The metric of the proposed symbol-rate estimation technique uses the standard deviation of the received power spectrum. Regarding the spectrum as a probability density function, the spectral standard deviation can be defined as the second order non-central moment:

$$\sigma = \frac{\int (f-\mu)^2 S(f) df}{\int S(f) df} \tag{4.5}$$

where f is the frequency component, μ is the spectral mean measuring the intermediate frequency, and *S(f)* is the power spectral density measured at frequency f.

Assuming that the signal has been band-limited by pulse-shaping prior to transmission, with for example a RRC filter, the symbol-rate is directly proportional to the spectral width [Couch, 1993, p.180]:

$$F_b = \frac{B_T}{1+r} \tag{4.6}$$

where F_b denotes the symbol-rate, B_T the transmission bandwidth and r the RRC roll-off factor. The spectral width can be measured by the standard deviation of the spectrum. Thus, the symbol-rate can be estimated from the spectral standard deviation.

The QPSK signal spectrum is obtained by averaging the spectra of the in-phase and quadrature signal components, which reduces the noise contribution through averaging. In order to reduce the impact of noise even further, the maximum noise floor power is estimated using a band of frequencies outside the signal bandwidth as shown in Fig. 4.4. The signal spectrum is then limited by a threshold at the maximum noise power estimate in order to remove out-of-band noise.

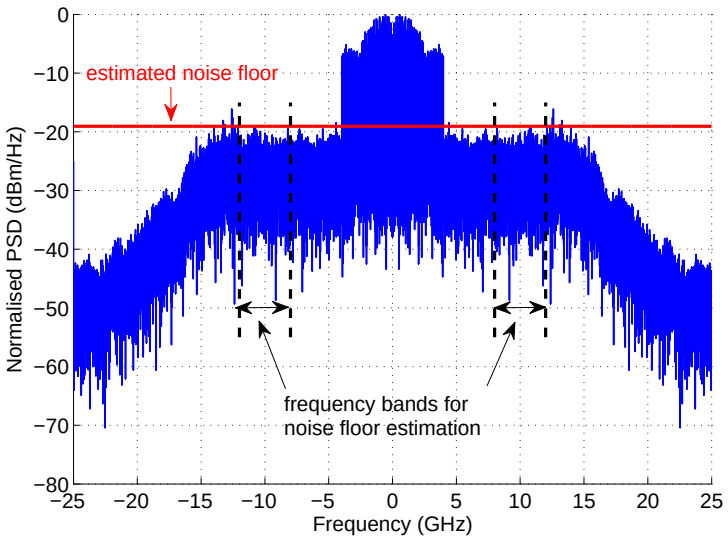

Figure 4.4: Simulated signal spectrum of a 8 GBaud pulse-shaped QPSK signal showing the frequency bands used for estimating the noise floor threshold, when the OSNR value is 3.9 dB.

A LUT is then used to convert the measured spectral standard deviation of a received signal into its symbol-rate. Different LUTs can be defined for different transmitter pulse shaping, as shown in Fig. 4.5. The LUT can be created in a pre-configuration step, requiring a minimum of two known symbol-rates with their corresponding measured spectral standard deviation values. In the absence of pulse shaping the relation between the spectral standard deviation and the symbol-rate will be non-linear, as demonstrated

in Fig. 4.5, because of the variation in the side-lobes of the spectrum at different symbol-rates, within a fixed receiver bandwidth.

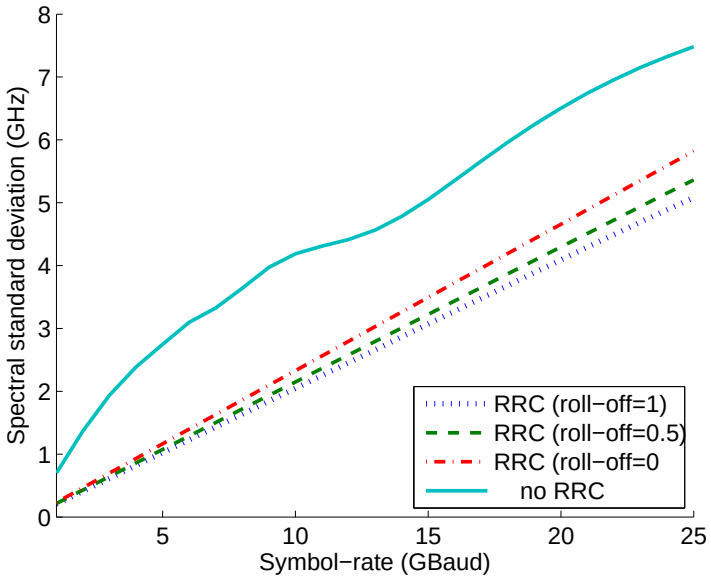

Figure 4.5: Look-up Table for different simulated pulse shaping cases.

The linearity between the spectral standard deviation and the symbol-rate is ensured not only by using Nyquist pulse shaping (Fig. 4.5), but also by applying a noise threshold (Fig. 4.6).

As expected, without noise thresholding, the noise-induced nonlinearity is higher for lower values of OSNR, as shown in Fig. 4.6(a). Additionally, at lower symbol-rates, there are a lot more noise components in the receiver bandwidth, contributing to the standard deviation value, since the receiver bandwidth is fixed to 25 GHz to allow the measurement of signals at symbol-rates up to 25 GBaud. Therefore, the estimation of lower symbol-rates is strongly limited by noise. Here lies the motivation for using a noise threshold. Fig. 4.6(b) shows a great improvement in the LUT when a noise threshold is applied. It is important to note here that, noise thresholding will be problematic in Nyquist WDM systems, where the channels can be contiguous.

4.2.2 Simulation setup

The method was tested by simulation under different noise loading conditions, as shown in Fig. 4.7. QPSK signals were generated from $2^7 - 1$ Pseudo-Random Binary Sequences (PRBSs), to simulate typical optical signals with line-coding. The intermediate frequency was set to be 500 kHz and the LO linewidth 100 kHz. Without loss of generality, the transmitter signal shape was trapezoidal with rise- and fall- times of 10% of the symbol-rate and a RRC filter with roll-off factor of 0. The two additional

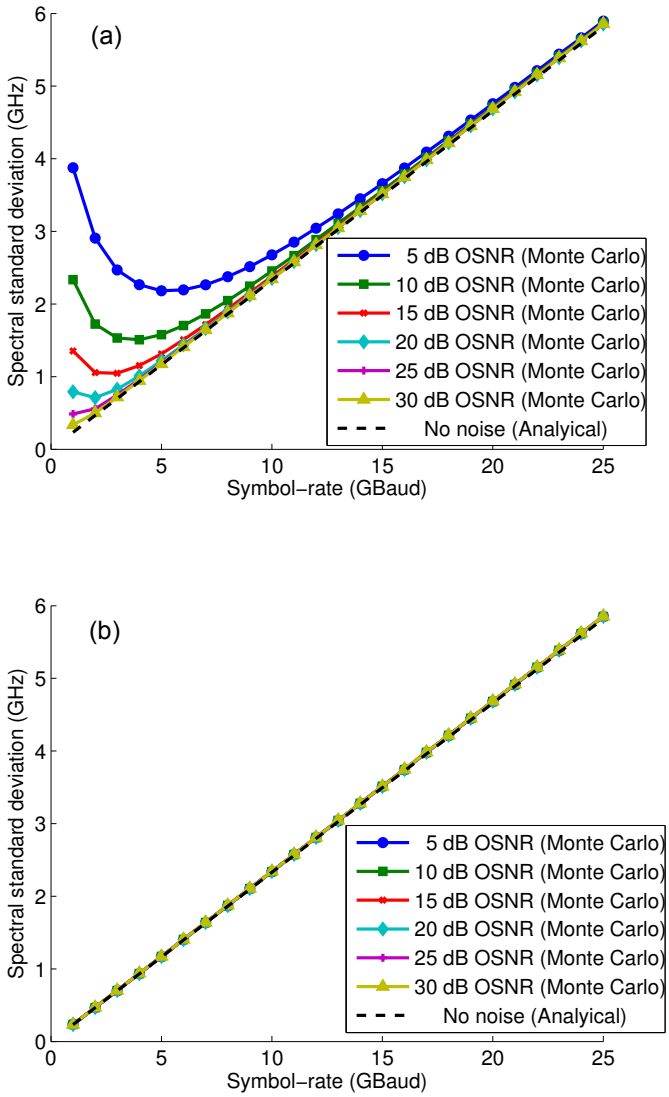

Figure 4.6: Impact of noise on the LUT verified by simulation of QPSK signals with 2^{15} captured samples, (a) without noise thresholding and (b) with noise thresholding.

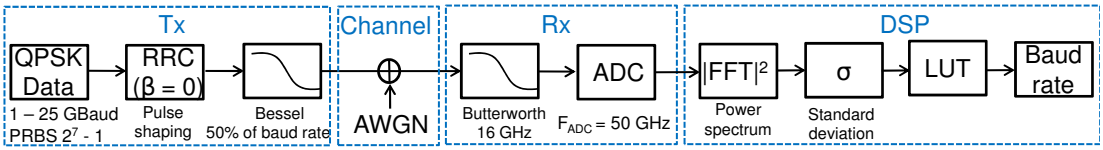

Figure 4.7: Simulation setup for testing the symbol-rate estimation technique for QPSK signals.

low-pass filters were used to account for the transmitter bandwidth limitations (5^{th} order Bessel filter with a cut-off frequency equal to 50% of the symbol-rate) and the receiver bandwidth (16 GHz 9^{th} order Butterworth filter, as shown in Fig. 4.8). The receiver sampling frequency was set to 50 GSa/s, allowing for symbol-rates up to 25 GBaud to be tested.

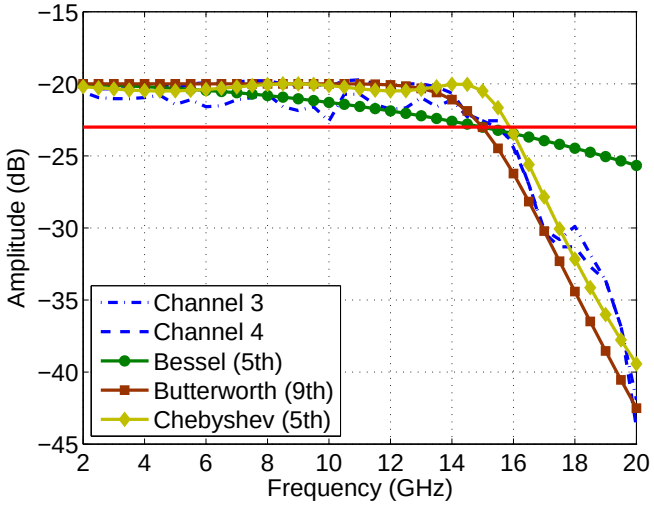

Figure 4.8: Tektronix Oscilloscope measured frequency characteristics. The filter giving the closest approximation is a 9^{th} order Butterworth filter.

4.2.3 Experimental setup

The technique was also tested experimentally for symbol-rates up to 14 GBaud. As in the simulations, the QPSK signals were generated with a PRBS length of $2^7 - 1$ and had a trapezoidal shape with rise- and fall-times of 10% of the symbol-rate and with 0 roll-off RRC. The in-phase and quadrature components of the signals are generated with a DAC-based Arbitrary Waveform Generator (AWG), as seen in Fig. 4.9, depicting the experimental setup. After modulation in the optical domain, the QPSK signals were noise loaded and subsequently converted back into the electrical domain using a coherent optical receiver with a sampling rate of 50 GSa/s. The symbol-rate estimation was subsequently carried out using offline processing [1].

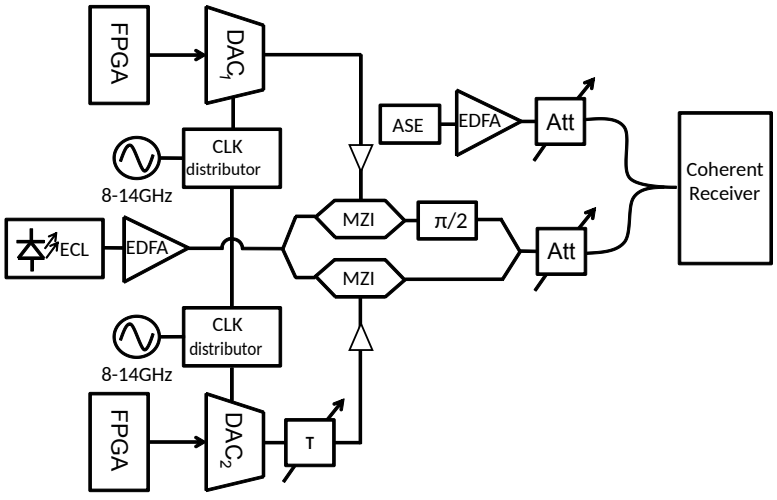

Figure 4.9: Optical back-to-back experimental setup for testing QPSK signals.

[1] The author is grateful to Sezer Erkılınç and Dr. Milen Paskov for their assistance with this experiment.

4.2.4 Performance analysis

Estimation accuracy

The estimation accuracy was measured by the signed percentage error:

$$\varepsilon = \frac{\hat{F}_b - F_b}{F_b} \cdot 100\%. \tag{4.7}$$

The mean and variance of the percentage signed errors were obtained from 100 different runs per symbol-rate. As shown in Fig. 4.10, the estimation accuracy increases with the number of captured samples. This is expected, since an increase in number of captured samples is equivalent to a higher frequency granularity, resulting in a more accurate spectral representation of the signal. Also, as more frequency components enter the computation of the spectral standard deviation, the lower the variance of the estimation accuracy becomes. Experimentally, a minimum of 2^{15} samples (corresponding to a capture time of 655 ns) for all symbol-rates are required to ensure an estimation accuracy of less than 2% at 5.9 dB OSNR, making this method suitable for fast acquisition and control. These results include noise reduction, described in the next section. The LUT was experimentally determined in order to include all spectral shaping that occurs in the system (RRC, Bessel and Butterworth filters as shown in Fig. 4.7).

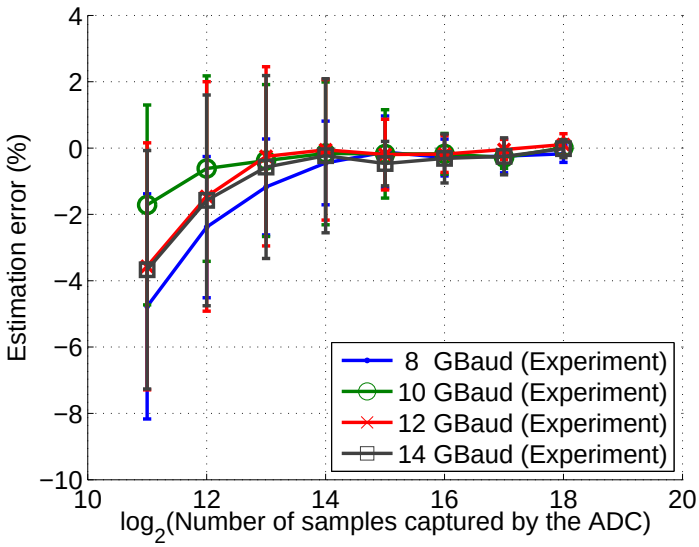

Figure 4.10: Estimation accuracy dependence on the number of captured samples, verified experimentally, at an OSNR of 5.9 dB.

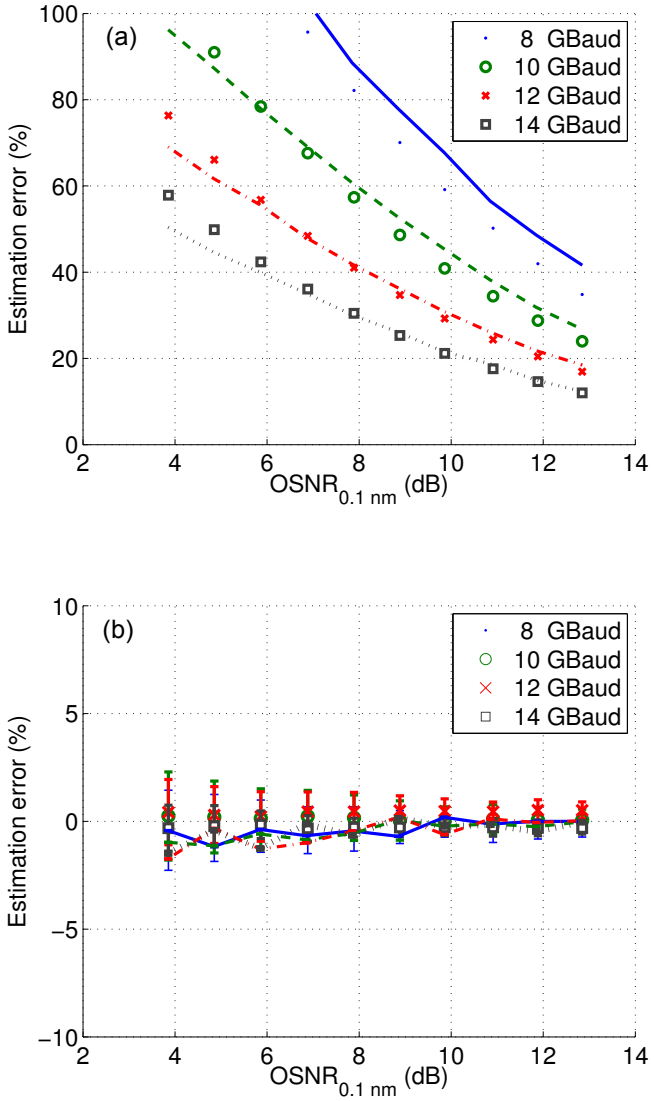

Figure 4.11: Impact of noise on the estimation verified by simulation (lines) and experiment (symbols) of QPSK signals with 2^{15} captured samples. (a) no noise threshold and (b) and applied noise threshold.

Impact of noise

The impact of OSNR on the estimation technique is shown in Fig. 4.11(a). At lower OSNRs the contribution of noise components to the value of the spectral standard deviation is higher, resulting in overestimation and high errors. These noise contributions become less significant for higher symbol-rates, as the signal bandwidth increases, whilst the noise bandwidth is fixed by the receiver sampling rate. The errors obtained by experimental verification are slightly different than those obtained by simulation due to the mismatch between the simulated spectra and the experimental spectra at the receiver.

The noise thresholding technique (described in 4.2.1) significantly improves the

performance of the estimator, especially at low symbol-rates where the signal bandwidth is much less than the acquisition bandwidth, as shown in Fig. 4.11(b). At low OSNRs, the estimation error increases due to the in-band noise not being completely removed by the threshold. For symbol-rates between 8 GBaud and 14 GBaud, at a minimum of 5.9 dB OSNR and 2^{15} samples, the spectral method results in estimation errors less than 2%.

Impact of filtering

The estimation of a wider range of symbol-rates was tested analytically, as well as via Monte-Carlo simulations, with results summarised in Fig. 4.12. The analytical investigation did not include any noise loading, in order to show the impact of the receiver bandwidth and pulse shaping alone.

The receiver bandwidth (16 GHz in this system) limits the estimation by filtering the higher frequency components and thus reducing the spectral width. At higher symbol-rates this results in an underestimation. The smallest symbol-rate at which underestimation starts occurring is dependent on the RRC roll-off. At more spectrally efficient roll-off values a wider range of symbol-rates can be correctly estimated.

The Monte Carlo simulations also show the impact of the noise threshold at different RRC filter roll-offs. In this instance, the noise threshold has been calculated by selecting the maximum noise level in the vicinity of the signal bandwidth. This is an idealised out-of-band noise measurement, assuming a rough knowledge of the symbol-rate. The purpose was of demonstrating that even an optimum out-of-band noise measurement has a great impact on the estimation. Conversely, the SNR level was set to give the same BER of $3.8 \cdot 10^{-3}$ at each symbol-rate, to show the estimation performance at the worst case operating point in terms of noise loading for each symbol-rate.

At higher RRC roll-offs the estimation of the out-of-band noise is less efficient, as the signal spectrum is broader and thus it is harder to distinguish the signal from noise. With an underestimated noise threshold, the high contribution of noise components within the estimation, results initially in overestimation (and the large overestimation peaks in Fig. 4.12(b)). The estimation error starts to gradually decrease when the signal bandwidth falls outside of the receiver bandwidth, leading ultimately to underestimation.

At the minimum RRC roll-off of 0, the estimation error is within 2% for symbol-rates between 4 GBaud and 32 GBaud, while for a roll-off of 1, the maximum error is 6% from 4 GBaud to 16 GBaud. For a typical RRC roll-off of approximately $0.05 - 0.1$, the method can perform well, however, a noise threshold based on the in-band noise is required for this technique to perform equally well at any RRC roll-off.

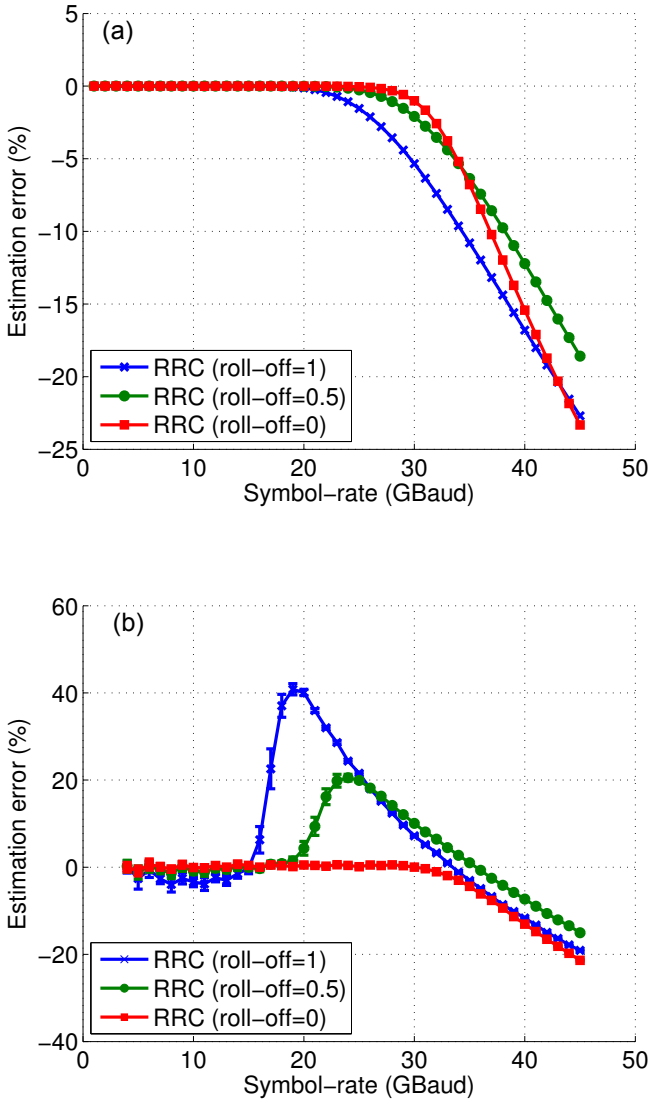

Figure 4.12: Receiver bandwidth impact on the estimation, for 2^{15} captured samples, (a) Analytical solution, noise free and (b) Monte Carlo simulation, with a fixed SNR equivalent to $BER = 3.8 \cdot 10^{-3}$ and applied noise threshold.

Impact of chromatic dispersion

Compared with two of the most common symbol-rate estimators, presented in 2.2, the estimation of the symbol-rate based on the spectral standard deviation is independent of chromatic dispersion, as shown in Fig. 4.13. These results were obtained by averaging over 100 Monte Carlo simulation and assuming the fibre dispersion parameter $17ps/nm/km$ and the fibre dispersion slope $0.09ps/nm^2$ [Buck, 2004]. The method proposed by [Kueckenwaitz et al., 2000] based on the non-linearity and peak search can be either very accurate or completely wrong due to the fact that although a high spectral peak corresponding to the symbol-rate is induced in the spectrum, it is not always the maximum peak. Through averaging over the 100 Monte Carlo runs, the estimation error

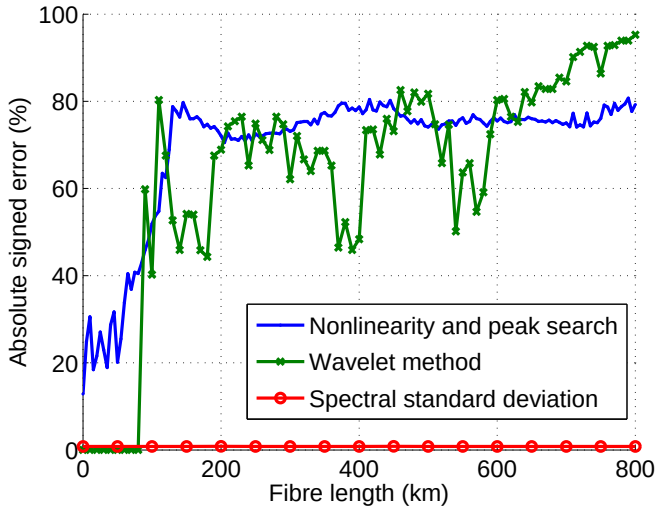

Figure 4.13: Impact of CD on symbol-rate estimation, by simulating and processing 2^{15} samples.

is non-zero, even in the absence of CD.

Impact of polarisation mode dispersion

The impact of PMD was investigated by simulation, for 2.5, 10, and 25 GBaud. The PMD-induced effects were simulated by concatenating 1 km long birefringent segments, connected by rotation Müler matrices of random rotation angles between 0 and $\frac{\pi}{2}$. The equation describing the total polarisation dispersion vector after the concatenation of the individual PMD segments is given by [Gordon and Hogelnik, 2000]:

$$\Omega_{n+1} = \Delta\Omega_{n+1} + R_{n+1}\Omega_n R_{n+1}^{-1} \tag{4.8}$$

where:
Ω_n is the polarisation dispersion vector of n concatenated segments
$\Delta\Omega_{n+1}$ is the polarisation dispersion contribution from the n+1 segment and
R_{n+1} is the Müler rotation matrix.

The method is independent on the 1^{st} order PMD as shown in Fig. 4.14. The estimator is dominated by deterministic errors, that decrease with the symbol-rate.

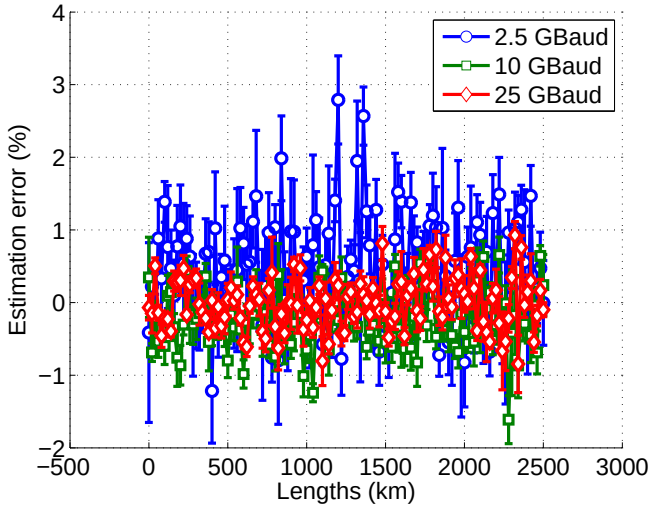

Figure 4.14: Impact of DGD on symbol-rate estimation, shown by simulation.

Impact of Local Oscillator intermediate frequency

The proposed estimator is independent of the IF, provided that the signal spectrum still fully falls within the receiver bandwidth, after being translated by IF. This effect can be seen in Fig. 4.15 for the 25 GBaud signal spectrum. As the frequency offset increases, more of the signal spectrum is being filtered out by the Butterworth filter at the receiver, decreasing the spectral standard deviation and therefore resulting in an increase in error with IF.

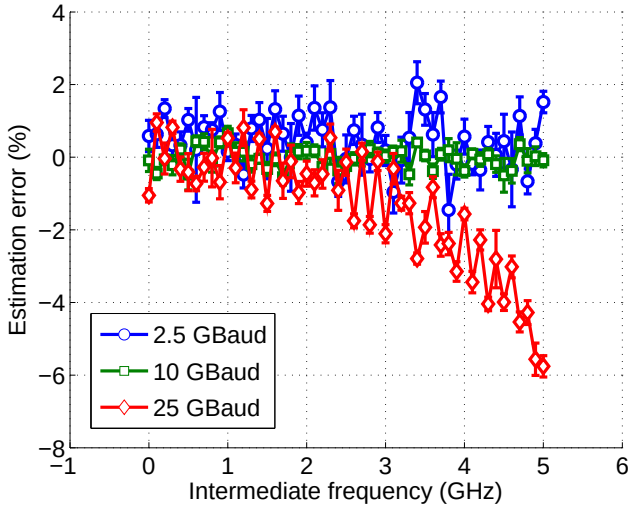

Figure 4.15: Impact of IF between the LO and transmitter lasers on the symbol-rate estimation, shown by simulation.

4.3 Conclusions

The presented method has the advantage of being CD and 1^{st} order PMD independent, as it relies on power spectrum of the signal. Additionally, by using 1^{st} and 2^{nd} order statistics of the spectrum, the method takes into account the intermediate frequency at the receiver. The method was verified experimentally and by simulation for QPSK signals, resulting in errors up to 2% for symbol-rates from 4 to 25 GBaud and a minimum of 2^{15} processed samples, at a fixed SNR corresponding to a BER of $3.8 \cdot 10^{-3}$ when pulse shaped by a RRC filter of 0 roll-off. The 2% error obtained is accurate enough to distinguish between a set of symbol-rates and the FEC level, where typical FEC overheads range between $6.69 - 25\%$ [Mizuochi, 2008]. When the roll-off is at the typical value of $0.05 - 0.1$, it is expected that the estimator will perform under similar error bounds, provided the corresponding look-up-table for the particular roll-off factor value is used. It was demonstrated that at excess bandwidths beyond 50%, the in-band contributions of AWGN severely degraded the estimation, in particular that of high symbol-rates.

5

Joint monitoring based on cyclostationarity

As outlined in Chapter 2, joint estimation of signal parameters and channel impairments is highly desirable in the design of autonomous reconfigurable optical networks. This chapter demonstrates a novel joint symbol-rate, roll-off, IF, CD and OSNR estimation method, based on the cyclostationary property of linearly modulated signals. This property is exploited either in the frequency domain, by making use of the SCF, or in the time domain, through the CAF. As Fourier pairs, both functions measure the correlation in amplitude and phase between frequency components of the signal, and are powerful analysis tools that can used in detecting signal features which are otherwise hidden within its PSD or autocorrelation function. A more thorough introduction on the theory of cyclostationarity is given in Chapter 3.

This work extends on the previously proposed symbol-rate estimator based on the CAF [Gardner, 1988] and OSNR estimator based on the SCF [Grupp, 2010], by investigating the impact of pulse shaping, number of samples, OSNR range and CD on the estimation accuracy. In addition, based on the same cyclostationarity approach, two novel highly accurate CD estimation techniques are proposed and demonstrated, preceded by novel RRC filter roll-off factor estimation and a coarse IF estimation. Also for the first time, the performance of the proposed techniques is experimentally validated, for Nyquist WDM signals modulated with DP-QPSK and 16-QAM formats, at 10 Gbaud, with varying amounts of linear ICI from a maximum of 0.5 dB to 0 dB.

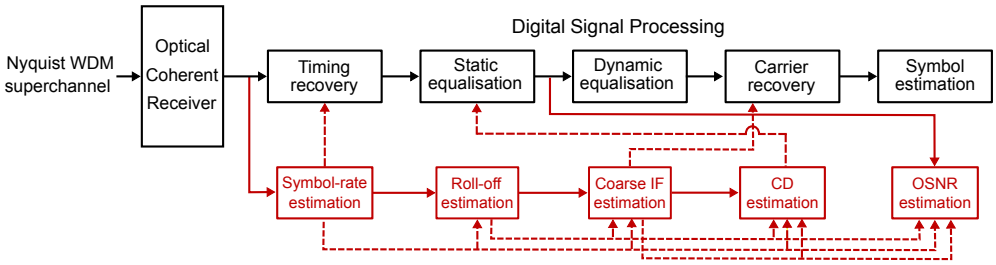

Figure 5.1: Digital coherent receiver setup including classic DSP stages (black), together with the proposed joint estimation blocks (red) based on cyclostationarity properties.

Fig. 5.1 shows how the monitoring techniques discussed in this chapter can be integrated within the coherent receiver DSP. The in-band OSNR estimation technique can be applied prior to the dynamic equalization stage, whilst the other four methods can be integrated prior to timing-recovery, at the very early stage of the receiver's DSP.

A highly accurate symbol-rate estimation is a strong requirement for all the subsequent estimation techniques to work. The OSNR and CD methods require knowledge of the symbol-rate, RRC roll-off factor and channel location, in order to limit the measurements to the bandwidth of interest. Tolerant to both PMD and non-linear distortions, the proposed OSNR monitoring technique presents the advantage of not requiring dynamic equalization or digital back-propagation processing, thus giving an improved estimation speed, compared to previously proposed in-band OSNR estimation techniques, presented in Chapter 2. However, CD compensation is necessary prior to the OSNR estimation, as discussed in more detail in Section 5.3.1. In the investigations of the OSNR estimator performance, an absolute error tolerance of 1.5 dB was chosen, to match the performance of the existing OSNR monitors, as proposed in the ITU-T standard G.697 [ITU, 2012]. All techniques are also tolerant to laser phase noise, therefore the signals do not require prior carrier phase recovery.

This chapter is structured as follows: Section 5.1 describes the simulation and experimental setups used for testing the proposed techniques, followed by Section 5.2 which describes the proposed digital implementations of the SCF and CAF. Section 5.3 describes and compares the two symbol-rate estimation techniques, based on the time domain and frequency domain approaches. A novel time domain roll-off estimator is proposed in Section 5.4. The proposed IF estimator from Section 5.5 is only implemented in the frequency domain, since the spectra shift with the value of the frequency offset. Cyclic correlation of signals propagating through dispersive paths is treated in Section 5.6, where we propose two new CD estimation methods, again based on the time domain and frequency domain, each with its advantages and disadvantages. Simulation and experimental results quantifying the performance of the in-band OSNR estimator are found in Section 5.7. Finally, Section 5.8 concludes the chapter.

5.1 Experimental and simulation setups

In testing the performance of the joint estimation techniques, simulation and experimental investigations were performed. The experimental setup is schematically illustrated in Fig. 5.2 [1]. Three PDM-QPSK/PDM-16QAM signals were generated with a PRBS length of $2^{15}-1$, at a fixed symbol-rate of 10 GBaud. The signals were Nyquist pulse shaped with a RRC filter of roll-offs between 0.01 and 0.5, then multiplexed and noise loaded, such that the OSNR values were between 4 and 28 dB. The channel spacing was fixed to 11.5 GHz for the QPSK signals and 12.5 GHz for the 16-QAM signals, giving a linear ICI Q^2-penalty of maximum 0.5 dB for the assumed roll-offs. The SSMF fibre dispersion parameter was $D = 16.78\frac{ps}{nm\cdot km}$ and the length per span, 80.7 km. At the receiver, intradyne coherent detection is assumed, with a combined transmitter and LO lasers linewidth of 100 kHz. The anti-aliasing filter of the receiver is approximately a 9th order Butterworth filter with a bandwidth of 24 GHz. The ADC sampling rate was fixed to 80 GHz, while the observation time was varied, in order to capture between 2^{15} and 2^{19} samples.

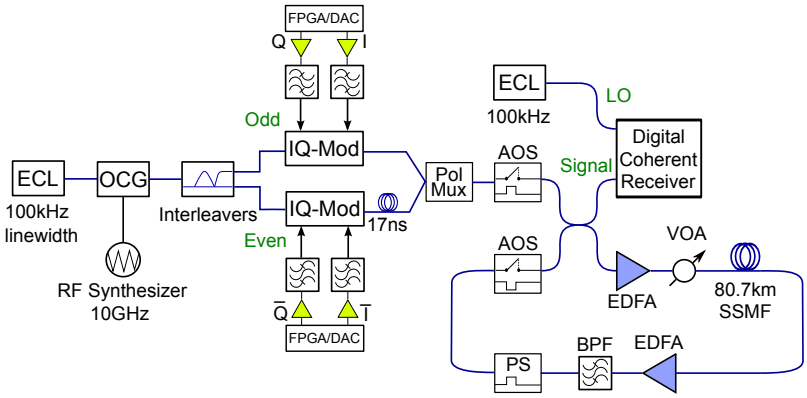

Figure 5.2: Experimental setup

Fig. 5.3 shows the OSNR range over which the experimental measurements were made, for both DP-QPSK and DP-16QAM modulation formats, including back-to-back transmission with noise loading at the receiver, as well as transmission over 10 and 25 spans of SSMF.

Monte Carlo simulations were performed to validate the experimental results, assuming a similar setup. The estimation results were averaged across independent simulation runs. The mean and standard deviation of the estimates were calculated over 100 averages, considering both polarisations separately. Initial results assume back-to-back propagation, while fibre propagation is considered subsequently.

When the estimation performance was investigated with respect to any other parameter than the OSNR, the amount of noise loading is fixed to correspond to the theoretical

[1] The author is grateful to Masaki Sato for his assistance with this experiment and to Dr. Robert Maher for providing additional experimental data.

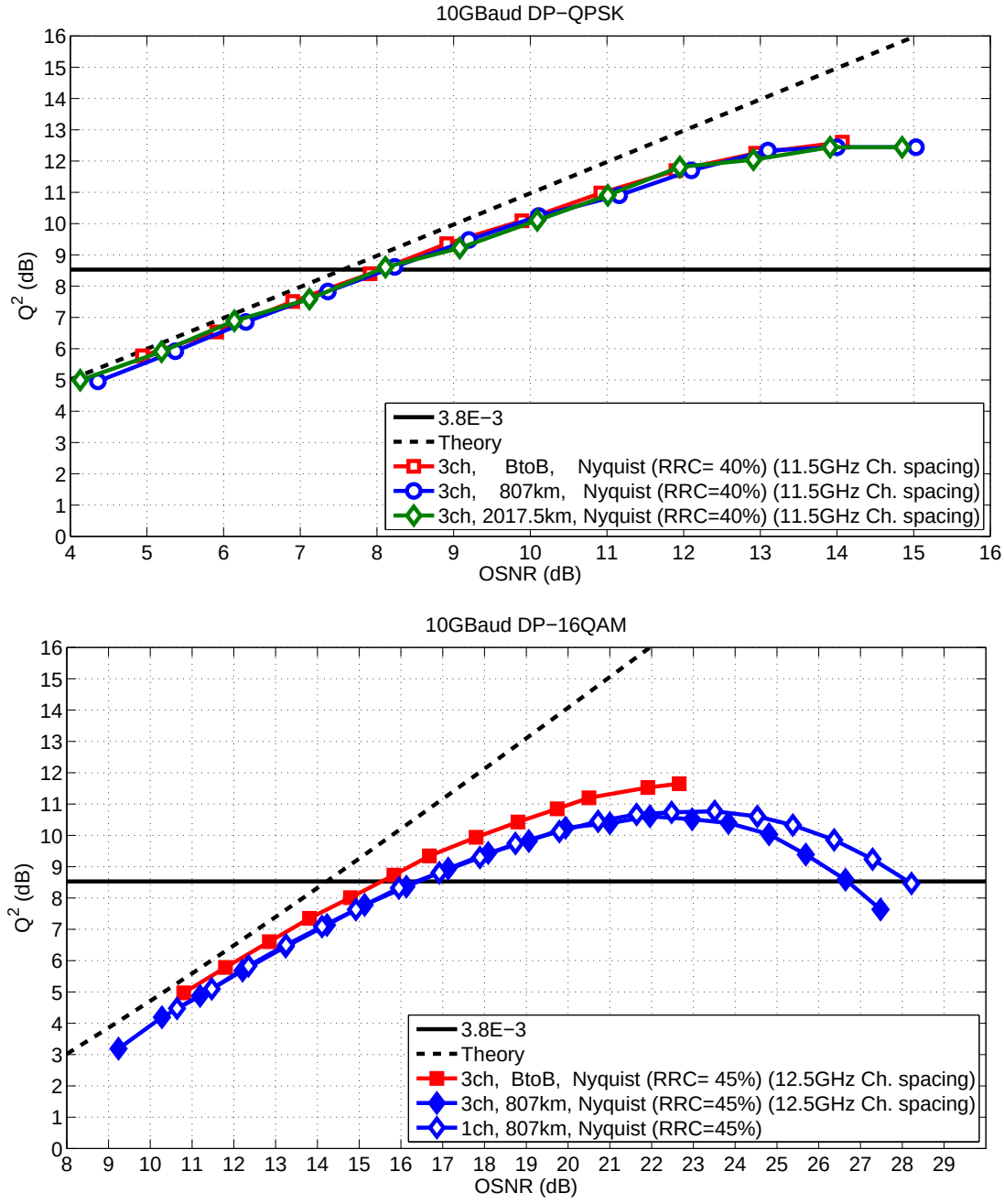

Figure 5.3: Experimental measurement of the Q-factor, obtained from the BER.

ROSNR for operating at a FEC limit of $3.8 \cdot 10^{-3}$. Fig. 2.3, illustrates how the value of the ROSNR increases with modulation format and symbol-rate.

Assuming a fixed RRC roll-off factor r, and a fixed symbol-rate F_b, two zero guard band scenarios are examined: with and without linear ICI. In this work, non-linear ICI is not quantified. When the channel spacing is equal to or greater than the channel bandwidth, given by $F_b \cdot (1+r)$, that simply means that there is zero linear ICI. When the channel spacing is less than the channel bandwidth, then a certain linear ICI penalty is expected. Fig. 5.4 shows what the channel spacing needs to be in order to limit this penalty to maximum 0.5 dB. The penalty here is measured as the OSNR penalty from

the theoretical limit, at a target BER of $3.8 \cdot 10^{-3}$. Higher order modulation formats have more stringent channel spacing requirements, due to the higher information spectral density, which manifests in an increase in the interference contributions from the adjacent channels. In this scenario, we find that the required channel spacing is linearly proportional to the symbol-rate. These simulation results are summarised in Table 5.1.

ICI	Modulation format	Channel spacing
0 dB	M-PSK, M-QAM	$(r + 1) \cdot Fb$
0.5 dB	QPSK	$(0.48 \cdot r + 0.97) \cdot Fb$
	16-QAM	$(0.64 \cdot r + 0.97) \cdot Fb$
	64-QAM	$(0.72 \cdot r + 0.97) \cdot Fb$

Table 5.1: Channel spacing as a function of modulation format, symbol-rate (F_b), RRC roll-off (r), which will induce 0 or 0.5 dB of linear ICI.

The design of the FIR filter, used to implement the RRC pulse shaping, both at the transmitter and at the receiver will induce an additional OSNR penalty unless a sufficiently large number of taps is employed. However, the longer the filter length, the higher the complexity of the filter design and the slower the response time of the transceiver. The results in Fig. 5.4 were obtained assuming a sufficiently long RRC filter length, of 256 symbols, in all cases. Fig. 5.5 shows how these requirements can be relaxed at no extra penalty and that they decrease exponentially with the roll-off factor.

The limited time-domain representation of the RRC filter, will induce spectral leakage, which can be particularly noticeable for the SCF at the cyclic frequency equal to the symbol-rate, as Fig. 5.6 shows. To clearly illustrate this, pulse shaping at a roll-off factor of 0 was chosen, because at this roll-off there should ideally be no spectral correlation. Sec. 3.4 offers a more detailed explanation on the impact of the RRC filter on the SCF. The ideal RRC is realised by complex multiplication in the frequency domain between the signal PSD and the RRC transfer function. In a practical implementation the spectral leakage becomes more pronounced as the number of symbols used in the realisation of the filter decreases. However, it can be inferred that, if the detectability of the cyclic spectrum is the problem to be solved, spectral leakage can be beneficial, provided that the maximum performance penalty is not exceeded.

In this section, the different parameters of both the simulation and experimental setups and the assumptions about the estimation parameters have been described. Throughout this chapter, wherever different assumptions than the aforementioned are made, this is explicitly stated in the respective section.

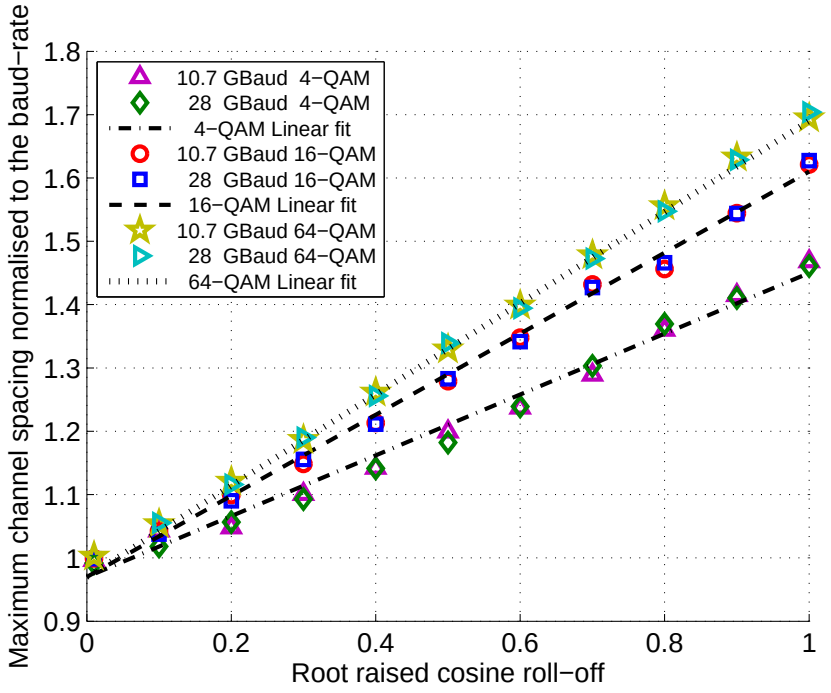

Figure 5.4: Required channel spacing as a multiple of the symbol-rate, in order to induce 0.5 dB linear ICI penalty. Simulations of three WDM channels.

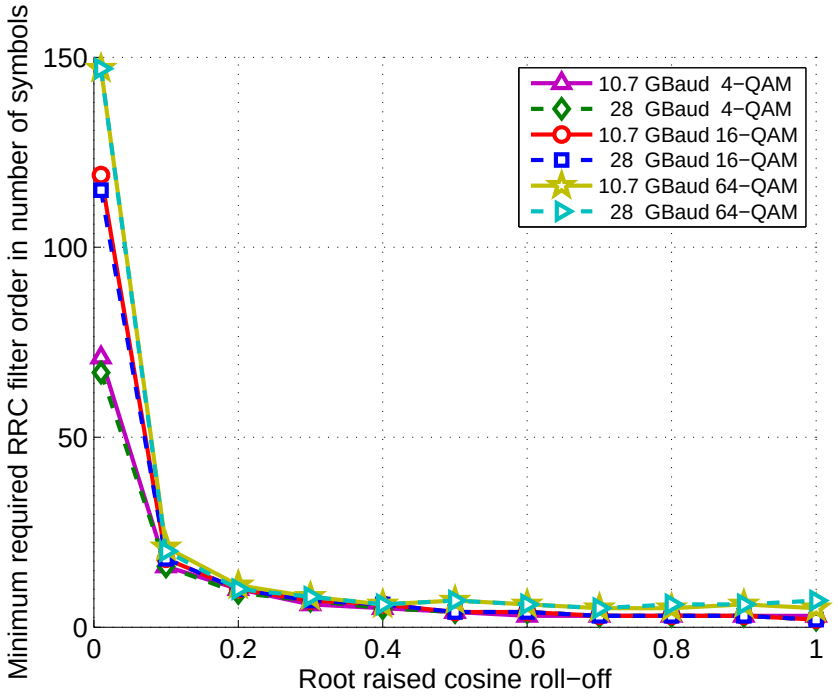

Figure 5.5: Minimum RRC filter order requirements in number of symbols, to ensure 0 dB penalty in a contiguous and homogeneous WDM signal, by simulation.

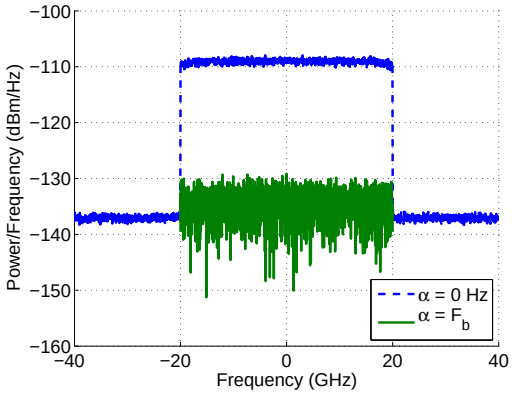

(a) Ideal RRC filter.

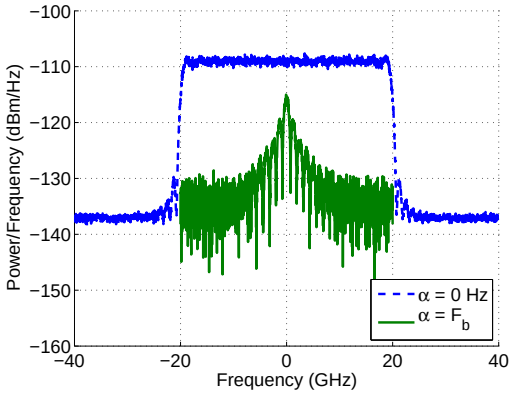

(b) 512 symbol-taps.

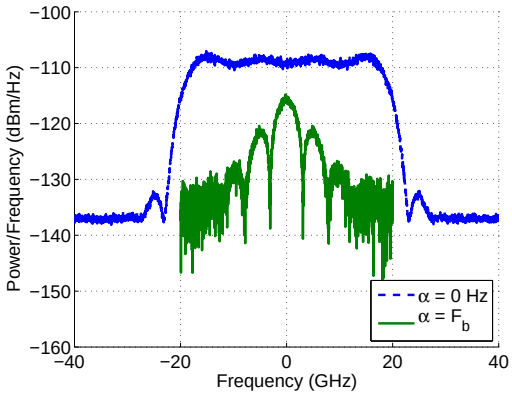

(c) 128 symbol-taps.

Figure 5.6: The limited number of taps in the design of the RRC filter induces spectral leakage in the frequency domain. The single channel 40 GBaud 16-QAM signal, was pulse shaped with a roll-off of 0 by simulation. α denotes the cyclic frequency.

5.2 Proposed digital implementations

The SCF was calculated here using the frequency-smoothing approach as depicted in Fig. 5.7, because it is more efficient when only requiring restricted cyclic frequencies values [Roberts et al., 1991]. Two time-domain copies of the incoming signals are created and frequency shifted such that the frequency difference between them is exactly α. These are then translated into the frequency domain for correlation, achieved through the complex multiplication between the two spectra. A frequency-smoothing operation on the product will further enhance the correlation. For the results presented in this chapter, a zero-phase response digital moving average filter has been used for frequency-smoothing, but a box-averaging filter can also be utilised for an increase in computation speed, as proposed in literature [Brown and Loomis, 1993], at the cost of a reduced spectral resolution. In addition, the implementation proposed here also differs from the previously proposed implementation (described in Chapter 3) by allowing a continuous cyclic frequency shift, instead of a sampling-dependent shift.

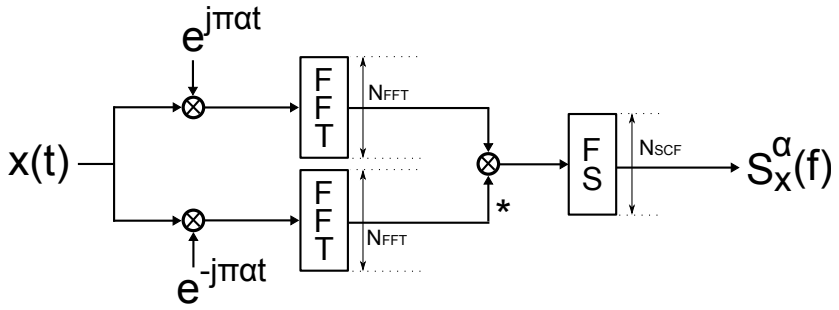

Figure 5.7: Proposed SCF implementation using two FFTs and frequency-smoothing (FS).

The two FFTs are performed over the entire captured signal of N_{FFT} size. The spectral averaging is performed over w samples and the resulting vector is N_{SCF} samples long, which needs to be adjusted to optimize the spectral resolution and correlation. When a moving average filter is employed, the averaging window is applied in single-sample steps, so the size of the resulting SCF will be equal to the size of the two FFTs, N_{FFT}. Box-averaging reduces this size to $N_{SCF} = \frac{N_{FFT}}{w}$, and will thus be more computationally efficient, but give a lower spectral resolution. As spectral resolution is important for observing the cyclostationary properties of the SCF, an optimised implementation of the moving average could provide a good trade-off between computational speed and performance.

A brute-force implementation of a moving average filter requires $w \cdot N_{FFT}$ additions. The complexity of a moving average filter can be vastly reduced by only obtaining the first average with w additions, and then re-utilising the current average to obtain the next one, with only one subtraction and one addition. The complexity is thus

reduced to approximately N_{FFT} complex multiplications, for large sample sizes, and the computational process is depicted in more detail in Figure 5.8.

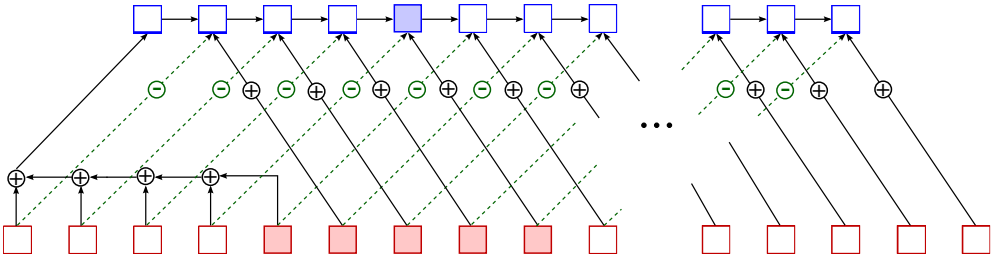

Figure 5.8: Moving average implementation of the frequency smoothing filter.

Whilst choosing the frequency smoothing approach, the SCF can be computed slice by slice, along a selection of cyclic frequencies, α. The complexity of computing a single slice of the three-dimensional function is $2\,N_{FFT}\,log_2 N_{FFT}$, dominated by the two FFT operations.

Operation	**Number of complex multiplications**
Frequency shift	$2\,N_{FFT}$
N_{FFT} - point FFT	$2\,N_{FFT}\,log_2 N_{FFT}$
Conjugate multiplication	N_{FFT}
Frequency moving average	$2\,N_{FFT}$
Overall	$N_{FFT}(2\,log_2 N_{FFT}+5) \approx$ $2\,N_{FFT}\,log_2 N_{FFT}$

Table 5.2: Implementation complexity of the frequency smoothed SCF. The number of samples of the SCF (N_{SCF}) is equal to the number of FFT points (N_{FFT}), and to the total number of captured samples (N_{ADC}).

The time domain reciprocal of the SCF is the CAF, which, as described previously in Chapter 3, is equivalent to the cross-correlation between two copies of the time domain signal $x(t)$, separated by a fixed frequency offset α. The proposed digital implementation of the CAF is depicted in the schematic of Fig. 5.9.

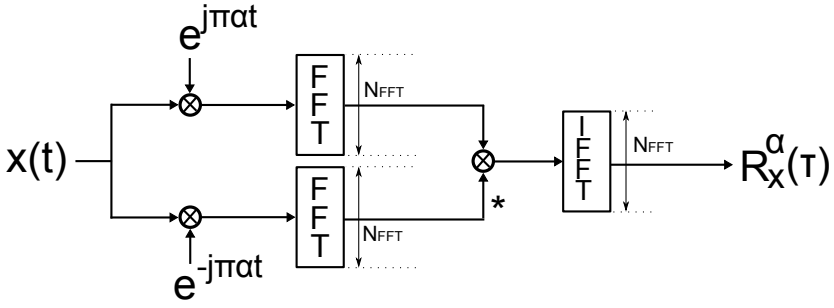

Figure 5.9: Proposed CAF implementation using two FFTs and one IFFT.

The cross-correlation between any two signals is more efficiently implemented in the frequency domain, as it corresponds to a element-by-element multiplication between the two shifted copies of the signal. However, the IFFT adds more complexity to the algorithm compared to the SCF computation. Table 5.3 summarises the computational cost of each operation required by the CAF, finally having an approximate complexity of $3\,N_{FFT}\,log_2 N_{FFT}$, when the sample size is very large.

Operation	**Number of complex multiplications**
Frequency shift	$2\,N_{FFT}$
N_{FFT} - point FFT	$2\,N_{FFT}\,log_2 N_{FFT}$
Conjugate multiplication	N_{FFT}
N_{FFT} - point IFFT	$N_{FFT}\,log_2 N_{FFT}$
Overall	$3\,N_{FFT}(log_2 N_{FFT}+1) \approx$ $3\,N_{FFT}\,log_2 N_{FFT}$

Table 5.3: Implementation complexity of the CAF. The number of FFT points (N_{FFT}) is equal to the total number of captured samples (N_{ADC}).

5.3 Symbol-rate estimation

Cyclostationary signals, such as those obtained through linear modulation, exhibit periodicity in their CAF and SCF, at symbol-rate intervals, as Chapter 3 explains. It is therefore possible to know the exact symbol-rates of a superchannel, by determining its cyclic frequencies. This section demonstrates symbol-rate estimation of both single channels and WDM superchannels, that can be implemented both in the time-domain (through the CAF) and in the frequency-domain (through the SCF). In both cases, the frequency offset between the transmitter and local oscillator lasers is randomly selected from the $[-1GHz, 1GHz]$ interval, to demonstrate the independence of the symbol-rate estimator on the IF. In order for both techniques to work, the data on each channel must be independent and identically distributed, but also there must be no correlation between the data transmitted on any two channels. Otherwise, the IF will constitute a strong correlation tone that will corrupt the symbol-rate estimation.

5.3.1 Spectral correlation function approach

In the frequency-domain, the symbol-rate estimation technique can be implemented as shown in Fig. 5.10. Initially, the SCF of the signal is computed for a range of selected cyclic frequencies α and for ordinary frequencies f within half the sampling frequency

$f \in \left[-\frac{F_{ADC}}{2}, \frac{F_{ADC}}{2}\right]$, then the SCF tones are defined as:

$$T_{y,SCF}(\alpha) = \max_{f} \left| S_y^{\alpha}(f) \right|, \tag{5.1}$$

and finally, the maximum spectral tone corresponding to a non-zero cyclic tone, gives the symbol-rate estimate:

$$\hat{F_b} = \arg_{\alpha \neq 0} \max T_{y,SCF}(\alpha). \tag{5.2}$$

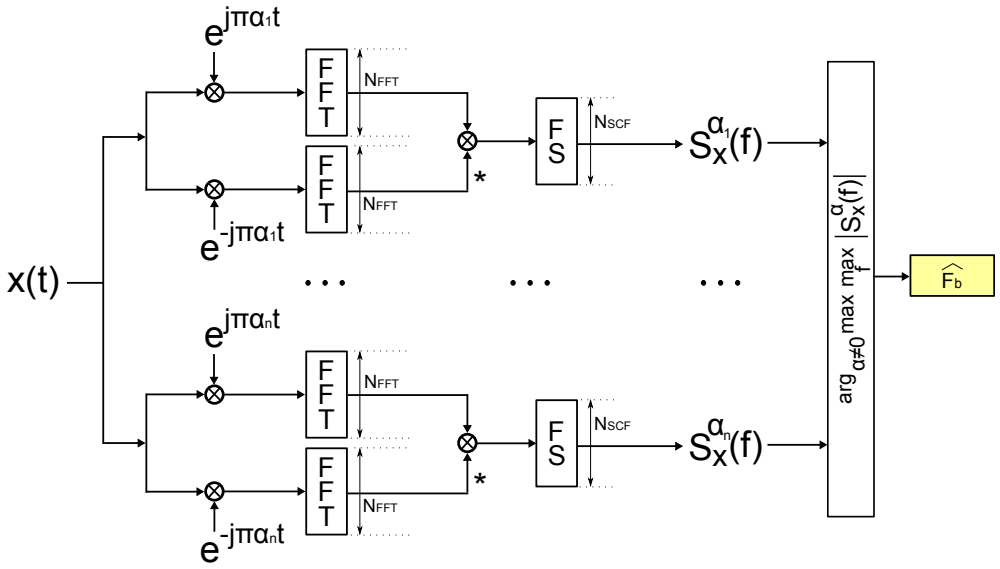

Figure 5.10: Implementation of the symbol-rate estimation technique based on the SCF. FFT = Fast Fourier Transform, FS = Frequency Smoothing, N_{FFT} = number of points in the FFT, N_{SCF} number of points after FS.

The estimation time increases proportionally with the number of cyclic frequencies under test and the complexity of this algorithm is thus given by: $2\,C\,N_{FFT}\,log_2 N_{FFT}$, where C is the total number of cyclic frequencies.

Symbol-rate scanning

Scanning the entire SCF can provide information about all the existing symbol-rates within the WDM superchannel, be it homo- or heterogeneous. To illustrate this affirmation, WDM signals formed of three channels were generated and pulse shaped with a RRC roll-off of 0.5. The channel spacing had been selected such that the three channels were contiguous − there was no linear ICI between any two adjacent channels. In this example, the transmission was dispersion and non-linearity free. The power of each channel was proportional to its bandwidth [Poggiolini et al., 2011]. Noise loading had been applied to match the average ROSNR across all sub-channels, assuming a FEC limit of $3.8 \cdot 10^{-3}$.

The Spectral Correlation Density of a homogeneous WDM signal, formed of three channels, each modulated with 10 GBaud DP-16QAM is displayed in Fig. 5.11(a). The spectral correlation clearly occurs at the symbol-rate, corresponding to a discrete peak along the cyclic frequency axis in Fig. 5.11(b).

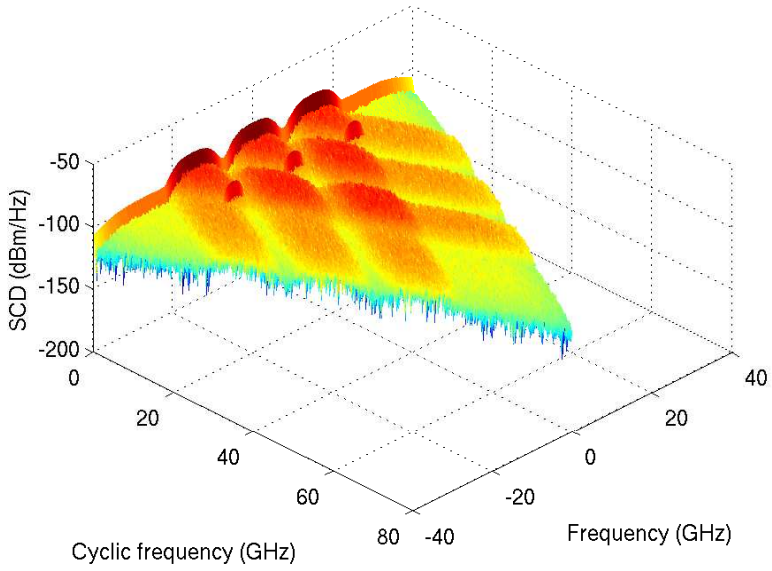

(a)

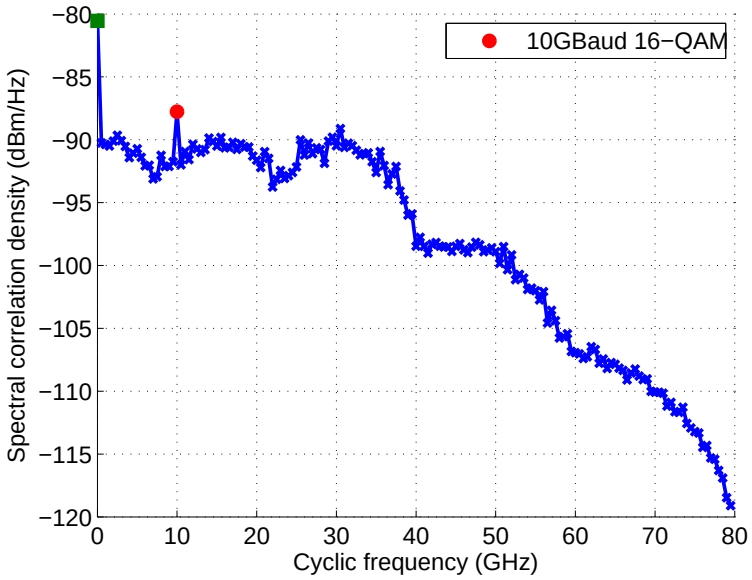

(b)

Figure 5.11: The Spectral Correlation Density Function of a simulated homogeneous WDM signal. 2^{18} samples are processed with a 256-points moving average window. The RRC roll-off factor was 0.5. (a) 3D plot, (b) profile along the cyclic frequencies.

Similarly, the symbol-rates of a heterogeneous WDM superchannel can be isolated from a single computation of the SCF, as shown in Fig. 5.12(a). Although the correspondence between the channel rate and channel location is lost, this information can potentially be recovered through further DSP techniques, which are not investigated here. It is interesting to note here that these spectral correlation peaks occur identically for all M-QAM and M-PSK formats of all orders.

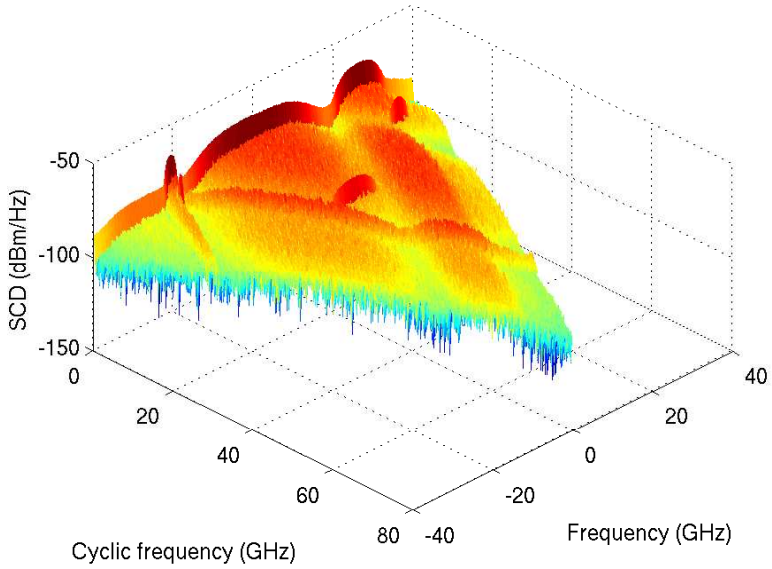

(a)

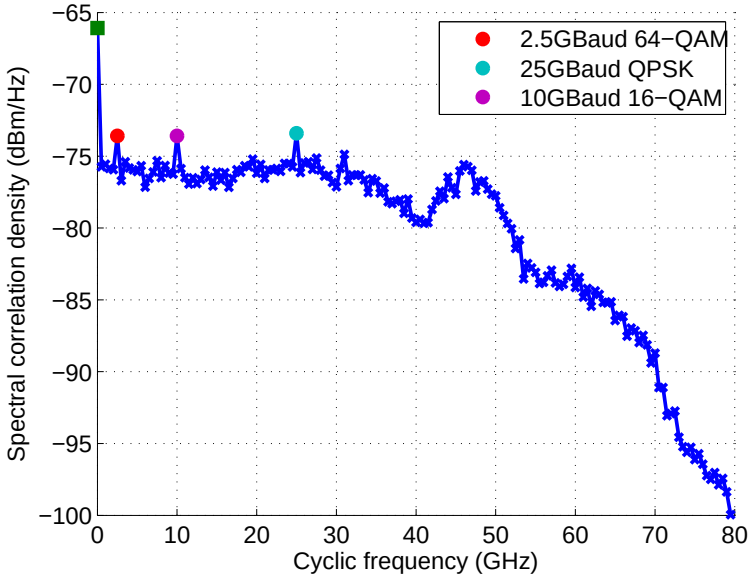

(b)

Figure 5.12: The Spectral Correlation Density Function of a simulated heterogeneous WDM signal. 2^{18} samples are processed with a 256-points moving average window. The RRC roll-off factor was 0.5. (a) 3D plot, (b) profile along the cyclic frequencies.

Arbitrary symbol-rates

The SCF is defined for cyclic frequencies between 0 and the ADC sampling-rate, and for an arbitrary cyclic frequency step, $\Delta\alpha$. Assuming that the symbol-rates of interest are within this range, the ideal step size is, of course, $\Delta\alpha = 0$, so that one of the cyclic frequencies is exactly equal to the symbol-rate. However, due to the discrete nature of the data, and time constraints, such precision is neither possible nor practical[2]. For any fixed symbol-rate, F_b, there is a maximum tolerable cyclic frequency deviation from the true symbol-rate value,

$$\Delta\alpha_{max} = \alpha - F_b \tag{5.3}$$

before the symbol-rate tone becomes undetectable by the scanning process. Herein, the estimation precision is defined by the power ratio between the spectral tone at an arbitrary cyclic frequency, α, and the spectral tone at the known symbol-rate:

$$T_{y,SCF}(\alpha)_{[dB]} - T_{y,SCF}(F_b)_{[dB]} = 10\,log_{10}\frac{\max_f \left|S_y^{F_b+\Delta\alpha}(f)\right|}{\max_f \left|S_y^{F_b}(f)\right|}. \tag{5.4}$$

The correlation noise floor, and as a consequence the symbol-rate estimation precision, are inversely proportional to the symbol-rate, as Fig. 5.13 depicts. The maximum alpha deviation can therefore be chosen to be 154.6 kHz, in order to ensure spectral correlation at the symbol-rate tone, across the range of 2.5-40 GBaud, for the lowest considered RRC roll-off of 0.01. When $\Delta\alpha$ exceeds $\Delta\alpha_{max}$, the phase correlation is lost and the detection of the symbol-rate tone cannot be guaranteed. The value of maximum alpha deviation is in fact equal to the frequency granularity of the measured PSD, which is given by the ratio between the receiver sampling rate and the number of captured samples, both fixed a priori. Provided the symbol-rate tone is detectable, the maximum cyclic frequency deviation from the true symbol-rate value constitutes the estimation error is given by the step size chosen. When this value is below 154.6 kHz, the timing-recovery stage that follows in the coherent receiver DSP, can further correct the sampling interval.

Conventional symbol-rates

Scanning the entire SCF is not feasible in fast-switching optical networks, as the computation time increases linearly with the number of cyclic-frequencies tested. The computation time can however be significantly reduced, considering that legacy systems only operate over a restricted set of possible symbol-rates, such as 2.5, 10 or 25 GBaud and the typical FEC overheads, ranging between $6.69 - 25\%$ Mizuochi [2008]. The

[2]This is only true for arbitrary symbol-rates. For a fixed set of conventional symbol-rates, the cyclic frequencies can be ideally selected, as explained further in this section.

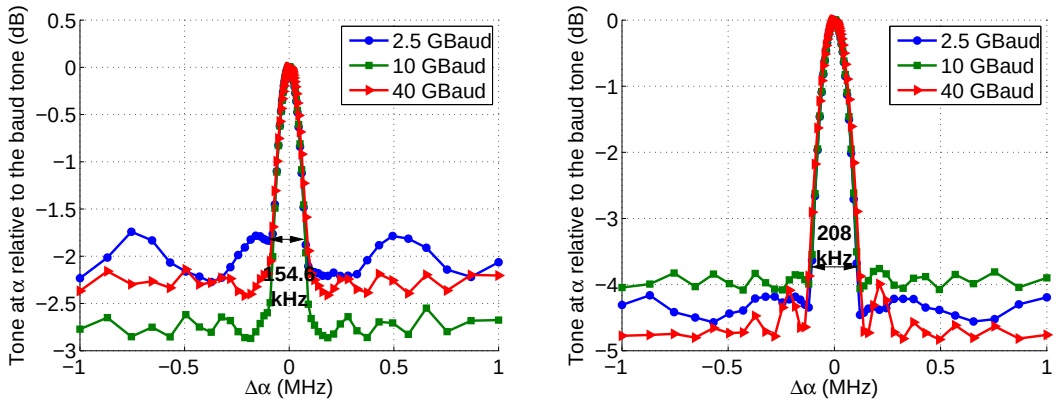

(a) 0.01 roll-off

(b) 0.1 roll-off

Figure 5.13: Precision of the symbol-rate estimation technique based on the SCF demonstrated by simulation for DP-16QAM. 2^{19} samples are processed and128 samples are averaged. Only AWGN is assumed as impairment.

precision of the estimator is sufficient to distinguish not only between different rates, but also different FEC overheads.

Range and accuracy

A symbol-rate estimator compatible with flex-grid optical transmission in future optical communications, requires an accurate estimation over a wide range of symbol-rates. Here, we test symbol-rates in the range between 1 and 50 GBaud, in steps of 1 GBaud. For simplicity and computational speed, it is sufficient to assume the same values and step size for the cyclic frequencies, which are the test symbol-rates. 2^{19} samples are processed with a moving average window of 128 taps. The following results show that the highest symbol-rate that can be estimated with 100% accuracy depends on the pulse-shaping and receiver bandwidths, as well as CD.

Fig. 5.14 reveals that for back-to-back transmissions, all symbol-rates up to approximately 45 GBaud can be correctly estimated, when the roll-offs are as high as 0.1 or 0.5, but this range decreases with the roll-off, since the spectral correlation tone power also decreases with the roll-off.

To further examine the impact of the roll-off factor and receiver bandwidth on the estimation range, the cyclic frequency granularity was lowered to 100 MHz. The findings are depicted in the contour plot, Fig. 5.15 showing the maximum achievable symbol-rates over the entire range of RRC roll-off factors. The back-to-back line constitutes the best-case scenario. Again, the symbol-rate estimation range increases with the roll-off, because of an increase in the tone SNR. The range of symbol-rate estimation extends across the entire receiver bandwidth, limited by its low pass filter, which is 48 GHz (or 24 GHz electrical bandwidth). For roll-offs higher than 0.01 and

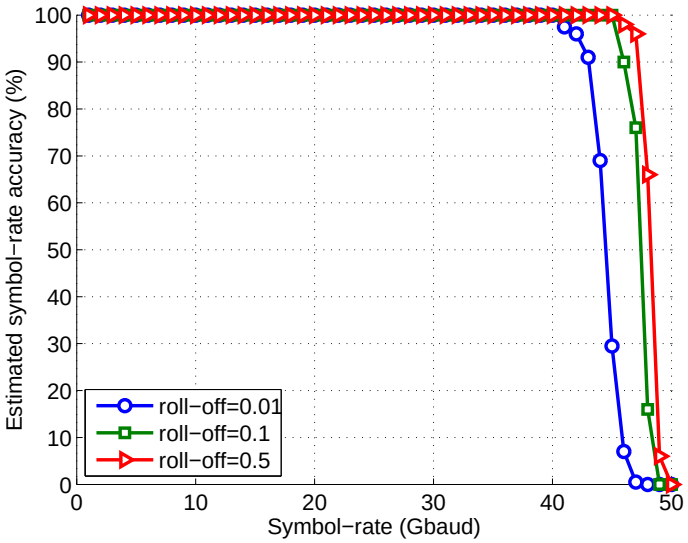

Figure 5.14: Range and accuracy of symbol-rate estimation, of 16-QAM signals in a back-to-back simulation.

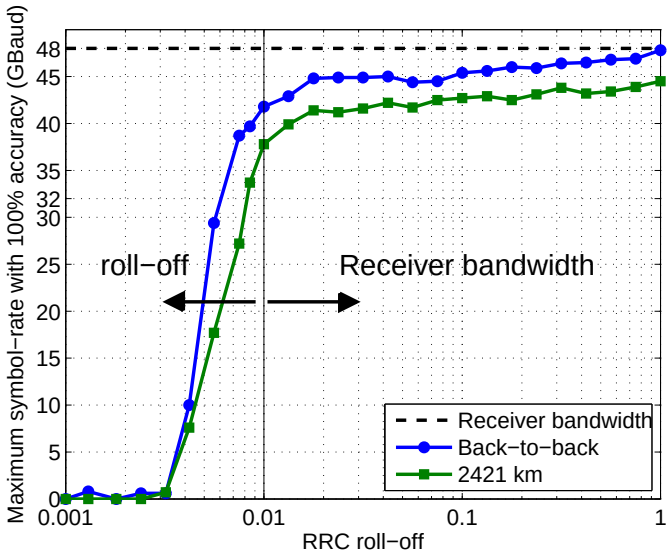

Figure 5.15: Maximum symbol-rate that can be estimated with 100% accuracy by simulation, for a 16-QAM WDM signal.

symbol-rates above 41.8 GBaud, the limitation due to the receiver bandwidth becomes dominant. For roll-offs below 0.01, the correlation is reduced insofar as the signal bandwidth is reduced by the transmitter pulse shaping filter, inducing more errors. This technique is not expected to work for roll-offs below 0.003.

Future 400G systems are more likely to operate at 28 GBaud, implemented as dual-carrier dual-polarisation 16-QAM with typical pulse shaping of 0.1 [Schmidt-Langhorst et al., 2013]. According to the findings presented in this chapter, at 28 GBaud, the minimum permissible roll-off is around 0.006 in order for this method to

function accurately for over 2400 km. This roll-off value is sufficiently low to approach the Nyquist bandwidth and simultaneously cover the typical values used in practice. Even though the generation and reception of rates higher than 40 GBaud is still very challenging with the currently available electronics, the maximum symbol-rate assumed in what follows is 40 GBaud, as an upper limit in the exploration of the capabilities of this estimation technique.

From this contour plot it can also be concluded that CD is another constraint to the estimation range, by limiting the accuracy of the higher baud-rates, through spectral correlation fading, which will be introduced and explained in detail in Section 5.3.1. As the transmission distance increases, the CD will limit the estimation range, to the point where, eventually, it will be impossible to estimate the symbol-rate, at any roll-off.

Spectral correlation optimisation

Both the number of captured samples and the size of the moving average window have a great impact on the symbol-rate estimation performance, as explored further herein.

Firstly, for determining the required total number of captured samples, the simulated data was processed with a fixed moving average window size of 128 samples. Since the implementation of the SCF is realised as a frequency-smoothing operation, the sample size coincides here with the FFT size. The number of samples is swept in powers of two, for the efficiency of the FFT operation, and the accuracy of the symbol-rate estimation is measured over 100 independent runs.

From Fig. 5.16 it is clear that the number of captured samples needs to be sufficiently high to allow a good spectral resolution, which, in turn, results in a good symbol-rate estimation. Based on these results, it can also be concluded that the minimum required FFT size depends on the channel bandwidth, which varied greatly from 2.53 GHz to 60 GHz. The worsening in performance at higher channel bandwidths is due to dispersion, whilst at lower bandwidths, due to reducing the spectral resolution. For the two extreme cases considered, and a transmission distance of 2421 km, a minimum of 2^{19} samples are necessary, which is the value assumed throughout the remainder of the chapter, such that a wide range of bandwidths are covered. Capturing 2^{19} samples with an ADC sampling at the rate of 80 GSa/s is equivalent to a capture time of 6.55 μs. In dynamic optical networks, reconfiguration times are of the order of *ns* [Maher et al., 2012], but the transmission roundtrip times are of the order of *ms*, and therefore, the acquisition time required for this estimation technique is acceptable.

In the absence of dispersion, as the roll-off factor becomes higher, less stringent requirements need to be imposed on the FFT size. This is because at the lowest roll-offs, the bandwidth of the signal decreases, and so does the amplitude of the cyclic spectrum at $\alpha = F_b$. The latter can be of the order of MHz, such as it is the case, for example, with 40 GBaud and r=0.01, when the cyclic spectrum bandwidth is 400 MHz. As a

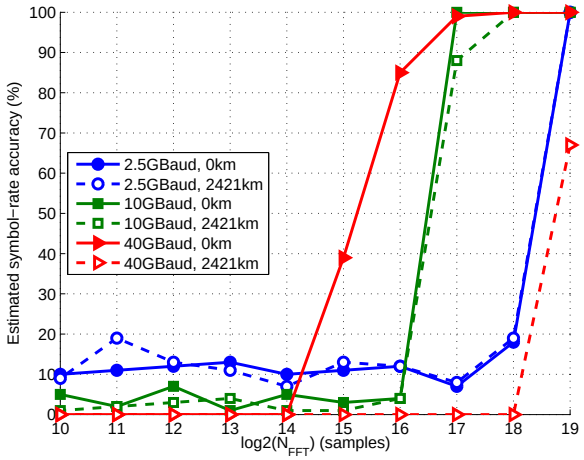

(a) RRC roll-off = 0.01.

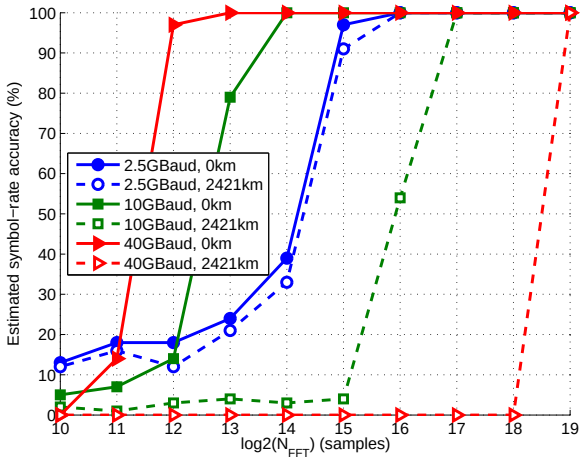

(b) RRC roll-off = 0.1.

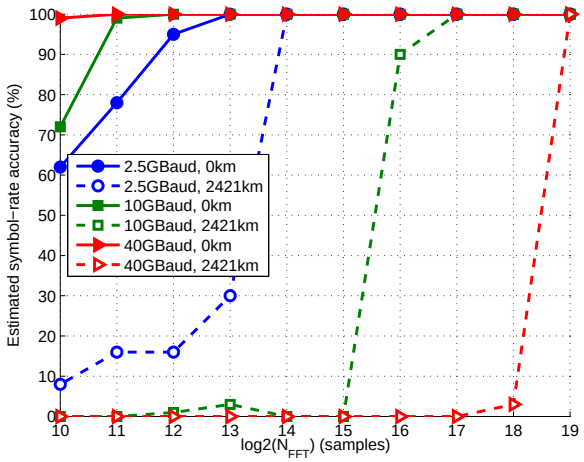

(c) RRC roll-off = 0.5.

Figure 5.16: Simulation results of the impact of FFT size on the symbol-rate estimation, for three contiguous channels modulated with 16-QAM. The size of the frequency smoothing window was 128 samples or, equivalently, 19.5 MHz.

result, we need a finer spectral resolution to represent the cyclic spectrum, compared to the ordinary spectrum. If we sample at 80 GSa/s, then, in order to have a frequency granularity much greater than 400 MHz, we need to capture a lot more than 3200 samples. But, if we were to consider a roll-off of 0.1 instead, the resolution restrictions are more relaxed, as the bandwidth of the cyclic spectrum is increased. When 2^{18} and 2^{19} samples are captured, the frequency resolution is 305.2 kHz and 152.6 kHz respectively, and more than sufficient in detecting the symbol-rate, for both r=0.01 and r=0.1. However, in the latter case, the number of samples can be further reduced down to 2^{13}, as shown in Fig. 5.16(b). Of course, there will be a limit to this spectral resolution tolerance as we increase the bandwidth, as well as an optimum averaging window with respect to the FFT size and the symbol-rate, presented in what follows.

When dispersion is present, the FFT size needs to be increased to compensate for the temporal pulse spread which reduces the cyclic spectrum power. CD has a higher impact on signals of wider bandwidths as the number of frequency components is higher, and thus the pulse spread under dispersion is wider, resulting in ISI after much shorter distances compared to lower bandwidths. By analogy, lower roll-offs mean lower bandwidths and therefore, a lower CD impact. When the signal bandwidth is approaching the Nyquist limit, such as in 5.16(a), CD is a prominent limitation only at high symbol-rates, such as 40 GBaud, which in fact, cannot be detected with 100% accuracy even when 2^{19} samples are processed. For lower symbol-rates, such as 10 GBaud or 2.5 GBaud, there is no significant difference between a back-to-back transmission and transmission over 2421 km. In such cases, the accuracy of the estimator is therefore dominated by the RRC pulse shaping filter.

The correct estimation of 40 GBaud is possible even at a roll-off of 0.01, for the FFT and averaging window sizes selected as above, if the transmission distance is reduced to limit the impact of CD. Otherwise, if the transmission distance has to be maintained, the roll-off has to be increased, resulting in a trade-off between spectral efficiency and transmission distance. This will be demonstrated further, for an optimised selection of the window size with distance. Alternatively, the transmission distance and the roll-off can be maintained, but at the cost of increasing the digitisation time and, therefore, the symbol-rate estimation time.

If the present symbol-rate estimation solution were to be used, these results could help to choose the best superchannel designs, as exemplified in the following case scenarios. Assume the transmission of 960 Gb/s over a fixed distance of 2421 km and the capturing of at most 2^{19} samples. Two design options are, for example, sending three channels each at 40 GBaud and roll-off equal to 0.1 or twelve 10 GBaud channels of roll-off equal to 0.01, both modulated with 16-QAM. Since both configurations are guaranteed 100% accuracy in estimating the symbol-rate, it would be advantageous to select the latter design as it has a better spectral efficiency compared to the former. These

types of design choices are likely to be made in core networks. If the reconfiguration time is more stringent, whilst the transmission distances shorter, such as it is the case in metro or regional networks, or in data centres, the 40 Gbaud channels with a roll-off of 0.1 may constitute a better option instead as it enables more relaxed requirements for the number of processed samples. Alternatively, the symbol-rate estimation could also be moved after the static CD compensation filter.

Once a sufficient number of samples has been captured, such as 2^{19}, the next question is what the optimum averaging window has to be in order to ensure a reliable spectral correlation measurement and, as a result, an accurate symbol-rate estimation. In what follows, a roll-off factor of 0.01 is considered in order to explore the worse-case scenario in terms of spectral correlation, whilst maintaining a high spectral efficiency. Three cases are considered: single-channel, three contiguous homogeneous channels and five contiguous heterogeneous channels. In order to explore a wide range of symbol-rates, three different values are illustrated here: 2.5 GBaud, 10 GBaud and 40 GBaud. The heterogeneous configurations varied the symbol-rates across five channels such that the central channel had been modulated at each of these values in turn. The three heterogeneous scenarios were: 10-40-2.5-40-10 GBaud, 2.5-40-10-40-2.5 GBaud and 2.5-10-40-10-2.5 GBaud. The SNR of the symbol-rate tone, defined as

$$SNR_{tone} = 10\,log_{10}\frac{\max\{S_y^{\hat{F}_b}(f)\}}{\max\{S_y^{\alpha\neq F_b}(f)\}}, \tag{5.5}$$

measures the power of the estimated symbol-rate tone relative to the power of the noise floor. This is different to the metric in Eq. 5.4, which measures the SCF tone power at cyclic frequencies around the symbol-rate, normalised to the actual symbol-rate tone power. The noise floor power is taken here, not as an average across multiple cyclic frequencies, but as the maximum power of the tone that is not the symbol-rate tone. This choice ensures that SNR>0 means that the symbol-rate tone is distinguishable from the noise floor and is equivalent to a correct estimation. The SNR is measured and averaged over 100 different realisations at different frequency smoothing window sizes, in order to show their impact on the measurement reliability of the spectral correlation. The results are illustrated in Fig. 5.17 (a), (b) and (c) for all three configurations respectively. The frequency smoothing operation mitigates the impact of the laser phase noise on the SCF and therefore the signals do not require prior carrier phase recovery.

A minimum *average* SNR_{tone} of approximately 0.95 dB is equivalent to 100% accuracy across all symbol-rates and multi-channel configurations. On average, there is an overall increase of approximately 0.4 dB in the SNR_{tone} of a single channel compared to three homogeneous channels. Firstly, this is because the neighbouring channels appear as noise to the central channel, as each encodes uncorrelated data with respect to the others. A second reason for the increased SNR with the reduced number

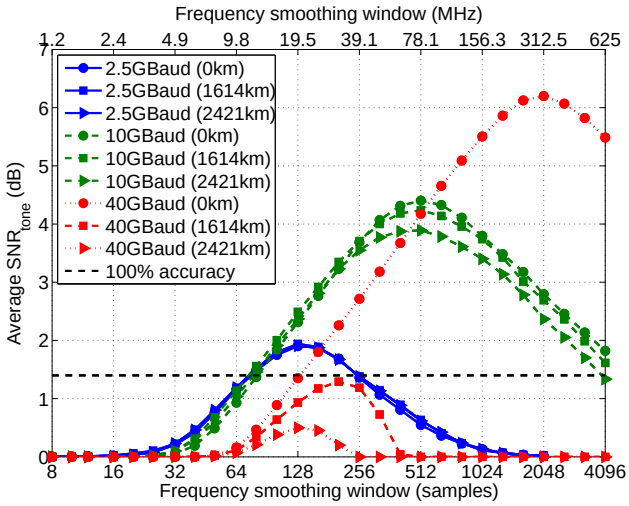

(a) Single channel 16-QAM signal.

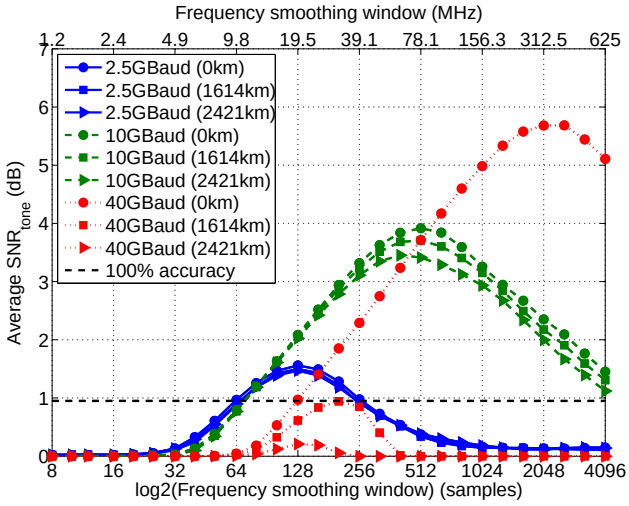

(b) Three homogeneous channels 16-QAM WDM signal.

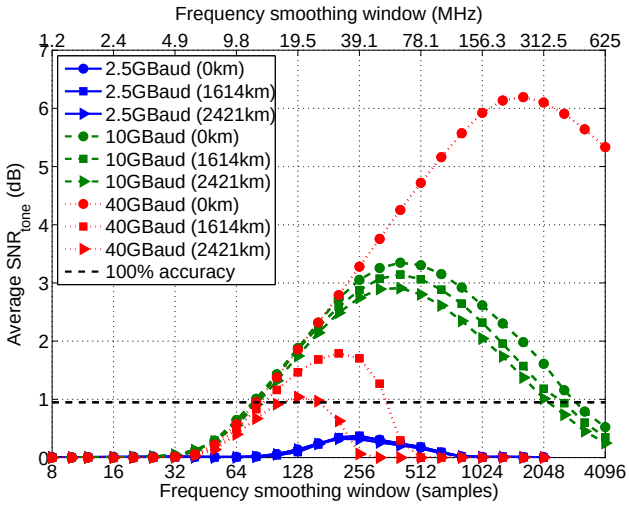

(c) Five heterogeneous channels 16-QAM WDM signal.

Figure 5.17: Impact of frequency smoothing window on the SNR of the symbol-rate tone. FFT size of 2^{19} samples and roll-off = 0.01.

of channels is the noise floor of the SCF with respect to the cyclic frequency, which increases proportionally with the signal bandwidth, as Fig. 5.18 demonstrates. Despite this SNR mismatch, there is no significant difference in terms of appropriate window size ranges, as the 100% accuracy threshold also increases proportionally by 0.4 dB. A heterogeneous WDM setup which has a narrow central channel surrounded by wider channels, such as 10-40-2.5-40-10 GBaud used in Fig. 5.17(c), will experience a shift in the optimum average window, under the influence of the faster phase changes of the neighbouring channels, which will completely 'overshadow' the symbol-rate tone corresponding to the central channel. At the intersection of all three cases, the optimum window size is 128 samples, which will cover a wide range of rates and configurations, at the longest transmission distances allowed by the present technique.

When computing the SCF, we first compute the cyclic periodogram, which is in itself an approximation to the analytical SCF (as explained in Section 3.3). Subsequently, a frequency smoothing stage reduces the inherent high variance of the periodogram and enhances the correlation between frequency components of the signal, by averaging out the contribution of the underlying random noise components - random in both amplitude and phase. These contributions are twofold: impairments such as AWGN or laser phase noise on one hand, and the randomness of the data on the other hand. Because of this randomness, when α is not a multiple of the symbol-rate, the symbols to be correlated are not in-phase and, this results in 'correlation noise', which is simply formed of random frequency components of the SCF.

A large smoothing window is required, such that through sufficient averaging, the SCF variation due to the presence of these noise components is reduced. The Grenader's reliability condition (Eq. 3.25) can be observed here, as the window size must be much greater than unity. However, a too large window size will reduce the spectral correlation, as the phase components making up the average are dominated by noise, eventually covering the entire phase range $(0, 2\pi]$. Spectrum broadening occurs, which means that its phase and amplitude information is lost. A larger averaging window also means a decrease in computation speed. Therefore, a trade-off between a low variance and a high reliability, or a low computational effort and a high reliability must be attained (Fig. 5.19).

In a back-to-back transmission, the optimum frequency-smoothing window is approximately equal to the bandwidth of the cyclic spectrum, as summarised in Table 5.4. Equivalently, the optimum number of symbols to be averaged by the moving average filter is equal to the number of symbols represented by the bandwidth of the cyclic spectrum, because that is the maximum number of symbols that can be correlated at one time when $\alpha = F_b$. The optimum window in number of symbols can be expressed as:

$$w_{opt(Symb)} = \frac{F_b \cdot r}{F_s} \cdot N_{symb}, \tag{5.6}$$

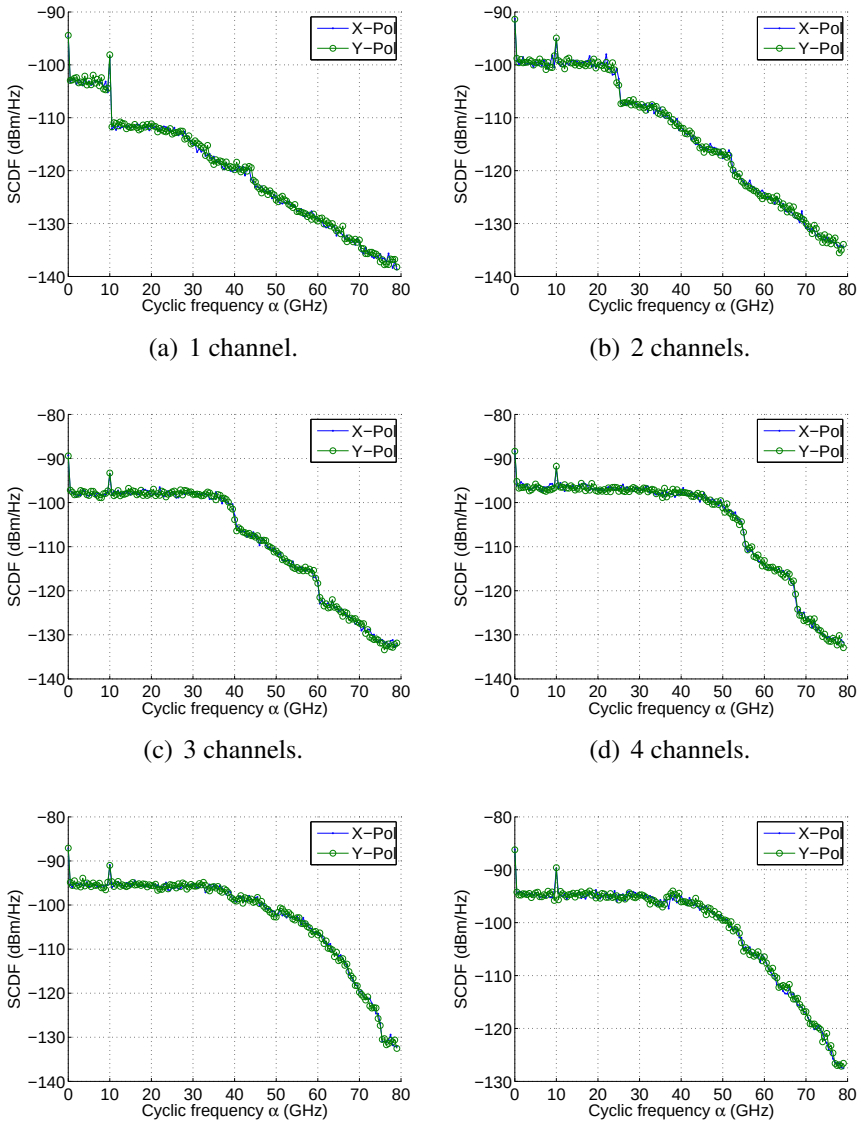

(a) 1 channel. (b) 2 channels.

(c) 3 channels. (d) 4 channels.

(e) 5 channels. (f) 6 channels.

Figure 5.18: The SCF noise floor broadens proportionally with the number of channels. In this example, the channels are modulated at 16-QAM at 10 GBaud, spaced with no guard-band and filtered with a RRC roll-off of 0.1. There is no significant difference in the simulated SCF profile with respect to the cyclic frequency after the number of channels is increased beyond 5, due to the receiver bandwidth (24 GHz electrical).

where F_b and F_s are the symbol-rate and the sampling rate respectively, r is the roll-off and N_{symb} is the total number of captured symbols.

If the capture time is restricted to say $3.28\mu s$, $1.64\mu s$ or $0.82\mu s$ (equivalent to $N_{FFT} = 2^{18}$, $N_{FFT} = 2^{17}$ or $N_{FFT} = 2^{16}$ FFT sample sizes respectively, when $F_s =$ 80 GSa/s), then the optimum window size (in number of samples) would change appropriately to match the cyclic spectrum bandwidth, as summarised in Table 5.5 and demonstrated in Figures 5.20 and 5.21. Whilst these latter results focus on the window size that maximises the tone *SNR*, a range of values around the optimum could

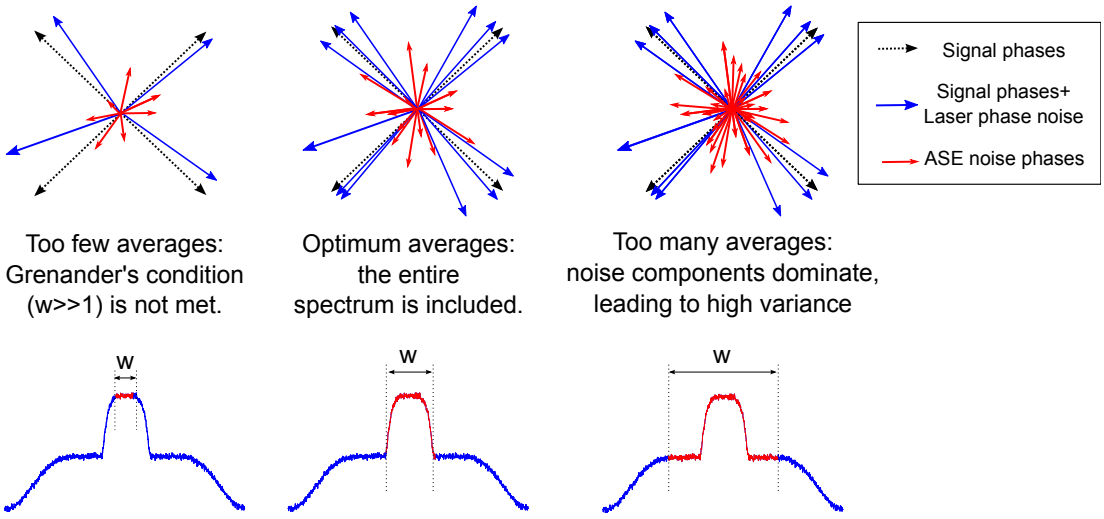

Figure 5.19: Phases (top row) and amplitudes (bottom row) of the frequency components of a QPSK signal and noise, within one window, centred around 0 Hz. Choosing an optimum number of averages is an important step in obtaining a reliable SCF estimate and therefore an accurate symbol-rate estimate.

Fb (GBaud)	2.5	10	40
w_{opt} (Samples)	2^7	2^9	2^{11}
w_{opt} (MHz)	19.53	78.13	312.5
Cyclic spectrum bandwidth (MHz)	25	100	400
Maximum distance before CD shifts the w_{opt} (km)	2,421	161.4	20
Maximum distance before ISI (km)	840	52.5	3.3

Table 5.4: Optimum averaging window in a back-to-back transmission, when 2^{19} samples are processed and the roll-off factor is 0.01.

Fb (GBaud)	2.5	10	40
w_{opt} (Samples)	2^6	2^8	2^{10}
w_{opt} (MHz)	19.53	78.13	312.5
Cyclic spectrum bandwidth (MHz)	25	100	400

Table 5.5: Optimum averaging window in a back-to-back transmission, when 2^{18} samples are processed and the roll-off factor is 0.01.

also allow 100% symbol-rate estimation accuracy. For instance, an FFT size of 2^{18} samples and an averaging window size of 256 samples could also be used to estimate 10 Gbaud and 40 GBaud. It becomes clear however, that lowering the number of captured samples has a great impact on the maximum transmission distance at 40 GBaud and the lowest symbol-rates, as this limits the number of correlated symbols. As a result, at least 2^{19} samples are required, in order to ensure that the technique proposed here can successfully estimate the symbol-rate for a wider range of rates and transmission distances.

The optimum averaging window size decreases with an increase in distance (Fig. 5.22), which is more noticeable for higher symbol-rates, more highly dependent on CD. By following the shift in optimum averaging window with distance, we can determine when the impact of CD becomes a limiting factor. The optimum window size cannot be selected per individual symbol-rate, as this is the unknown parameter to be estimated, thus a value that validates most cases must be selected.

In all of the following results in the remainder of this chapter, the investigation is restricted to a configuration of three homogeneous channels. In order to ensure operation at the best spectral efficiency (lowest roll-off and highest symbol-rate) and longest transmission distance, we assume 2^{19} samples for processing and 128 samples for performing frequency averaging. Additionally, in order to lower the complexity of the algorithm, we assume that the symbol-rate is being restricted to 2.5 GBaud, 10 GBaud and 40 GBaud, and typical FEC overheads ($6.69-25\%$ [Mizuochi, 2008]). By computing the SCF only for cyclic frequencies within these restrictions, the complexity of the estimator is greatly reduced. If very low symbol-rates, such as 2.5 GBaud, are unlikely, then averaging every 258 samples over a total 2^{18} captured samples would be more advantageous, such that longer distances and higher rates could be supported.

Impact of chromatic dispersion

In order to more thoroughly investigate the impact of chromatic dispersion on the proposed joint-estimation technique, we look at the SNR of the tone at the symbol-rate as a function of the traversed length of fibre. We find that the power of $S_y^{\alpha=F_b}(f)$ is strongly dependent on the amount of accumulated CD, as Fig. 5.23 shows.

As the different frequency components of the signal experience different propagation speeds through the fibre, their different arrival times at the receiver translates into the frequency domain as a frequency-dependent phase shift. The frequency components separated by the symbol-rate value are no longer in-phase, therefore their correlation is reduced. $S_y^{\alpha=F_b}(f)$ will fade with dispersion, eventually falling into the noise floor and the loss of periodicity in the SCF, can be coined as *'spectral correlation fading'*. As a result, the symbol-rate estimation based on the SCF approach is limited by the amount of cumulative dispersion present in the path of the signal, but will continue to

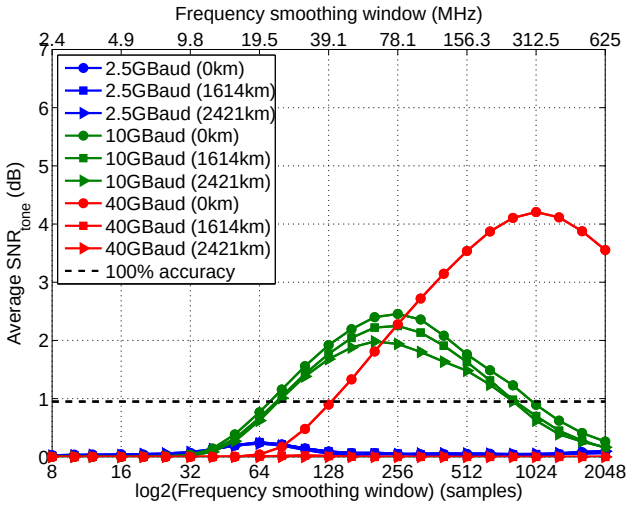

(a) $N_{FFT} = 2^{18}$ samples.

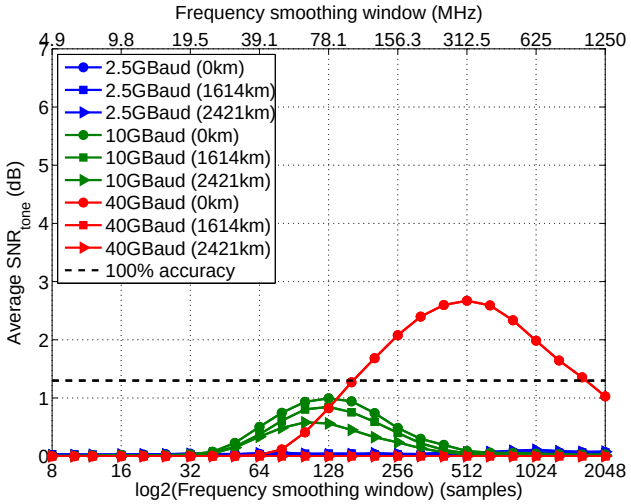

(b) $N_{FFT} = 2^{17}$ samples.

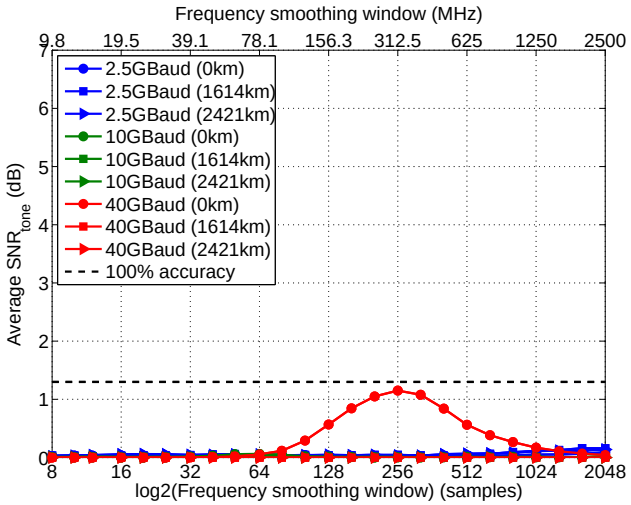

(c) $N_{FFT} = 2^{16}$ samples.

Figure 5.20: Impact of frequency smoothing window on the SNR of the symbol-rate tone for three 16-QAM channels, different FFT sizes and a fixed roll-off = 0.01.

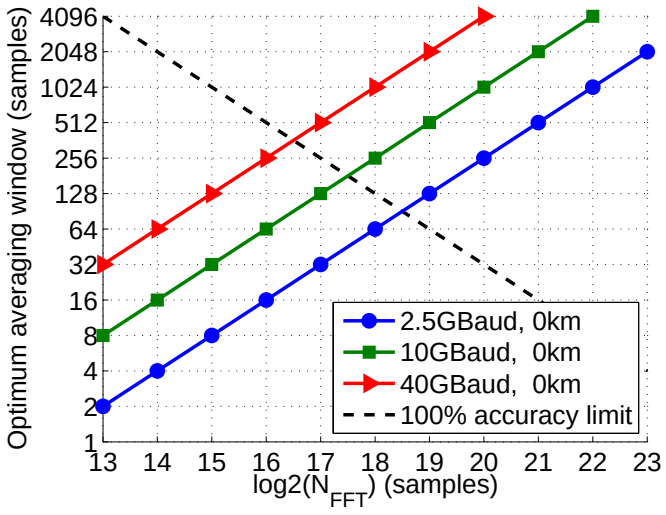

Figure 5.21: The optimum frequency-smoothing window for a maximum SNR of the symbol-rate tone, at different FFT sizes, a fixed roll-off of 0.01 and a sampling rate of 80 GSa/s. Back-to-back simulation of DP-16QAM signals.

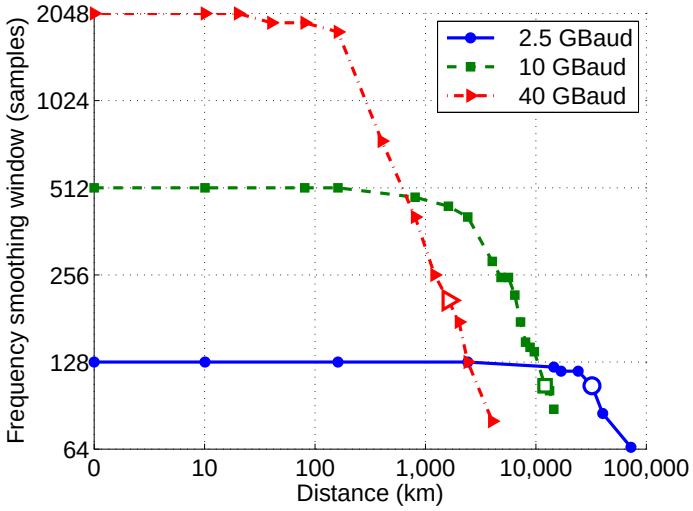

Figure 5.22: Optimum frequency smoothing window as a function of distance, in a simulated WDM signal formed of three homogeneous 16-QAM channels. The hollow markers indicate the maximum distance for which the estimation accuracy is 100%.

work without CD compensation until complete spectral correlation fading occurs, when the symbol-rate tone will no longer be distinguishable from the correlation noise floor. By contrast, in order to be able to apply the OSNR estimation technique effectively, CD estimation and compensation will be required a priori, because the signal power will fade with distance, leading to the OSNR to be underestimated. This aspect is discussed in more detail in the following Subsection 5.7.

Figure 5.24 shows the maximum achievable distances for estimating the symbol-rate with 100% accuracy, depending on the number of samples in the averaging window.

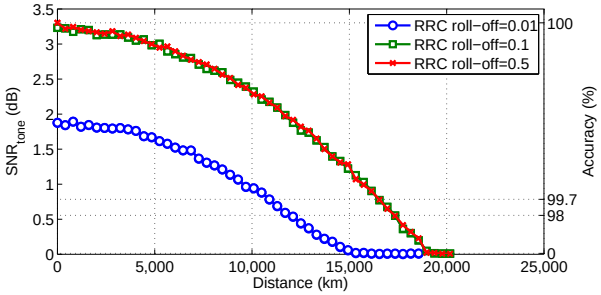

(a) 10 GBaud,16-QAM

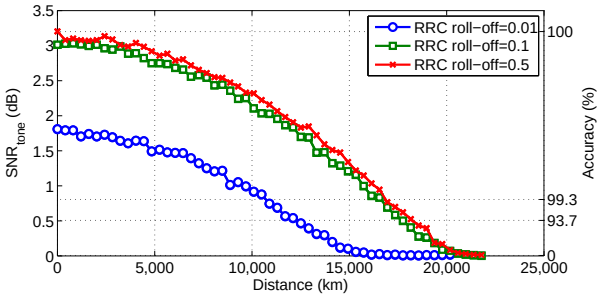

(b) 10 GBaud,QPSK

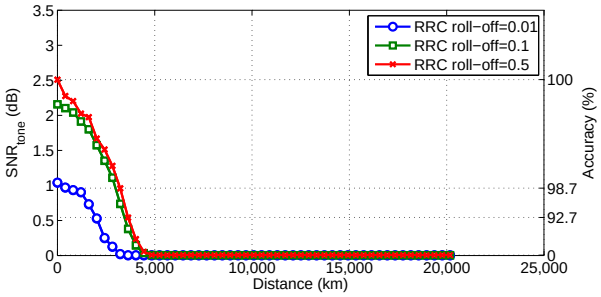

(c) 40 GBaud, 16-QAM

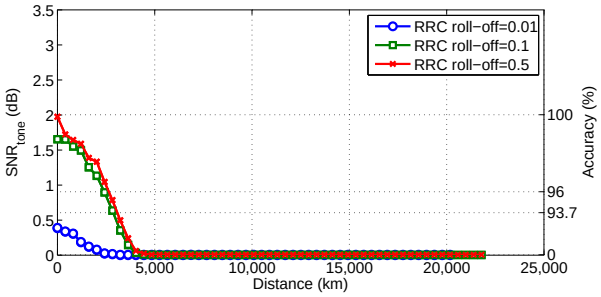

(d) 40 GBaud, QPSK

Figure 5.23: Impact of chromatic dispersion on the SCF tone SNR and symbol-rate estimation demonstrated by simulation.

At high values of the RRC roll-off, such as 0.1 or 0.5, the spectral correlation is more easily achieved, enabling high reach for various window sizes. As the roll-off factor decreases, the spectral correlation is reduced, limiting the range of acceptable averaging window sizes. For the maximum spectral efficiency case considered, when the roll-off is 0.01 and the symbol-rate is 40 GBaud, the optimum window size is approximately 203 samples, enabling the estimator to operate even after the superchannel has travelled over 1614 km of fibre. However, the reach can be at least doubled if a higher roll-off is used. There is therefore a trade-off between spectral-efficiency and reach in terms of the performance of this symbol-rate estimation method, just as it is in terms of the general DSP performance for such signals.

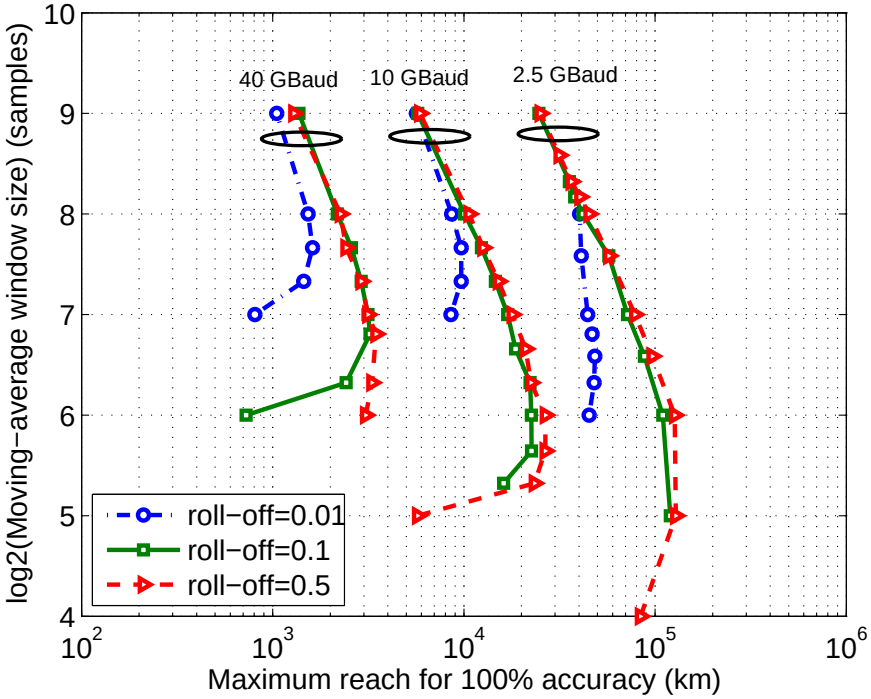

Figure 5.24: Maximum achievable distance limited by the accuracy of the symbol-rate estimation, by simulating three-channel 16-QAM WDM signals, without linear ICI.

Impact of Nyquist pulse shaping

Assuming that the transmission distance is fixed, we are then interested in maximising the spectral efficiency. Testing by simulation and experimentally, for both 16-QAM and QPSK, the minimum RRC roll-off for ensuring a perfect symbol-rate estimation has been determined. As Fig. 5.25 shows, higher transmission distances impose a more stringent requirement on the spectral efficiency with this estimation technique. Over 2017.5 km with QPSK modulation, the minimum roll-off factor is 0.008, while for the shorter distance of 807 km with 16-QAM, the minimum roll-off is 0.006.

Experimentally, when there is no dispersion, these results confirm that a roll-off as low as 0.01 allows a correct symbol-rate estimation. At even lower roll-offs the discrepancy between simulation and experimental results can be attributed to further signal power losses, present in the experiment, but unaccounted for in the simulation.

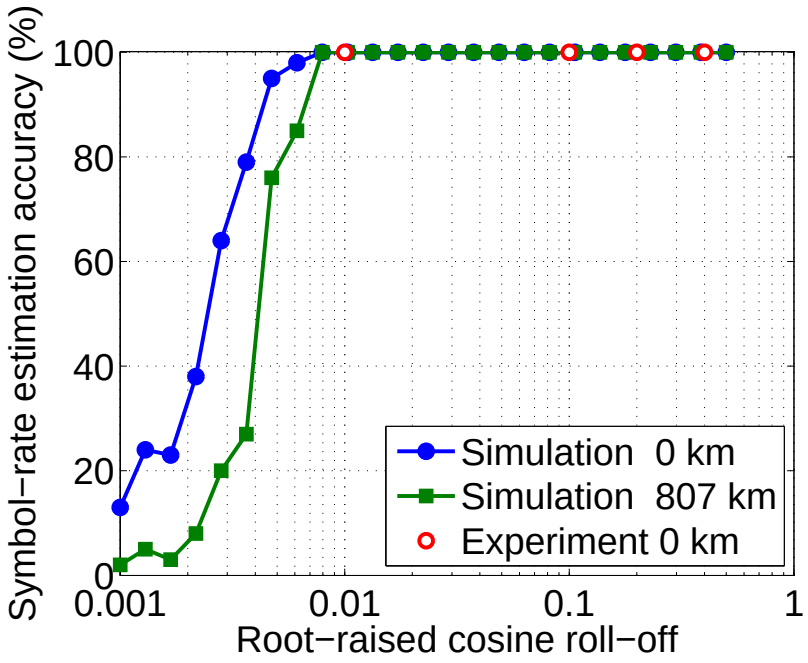

(a) QPSK.

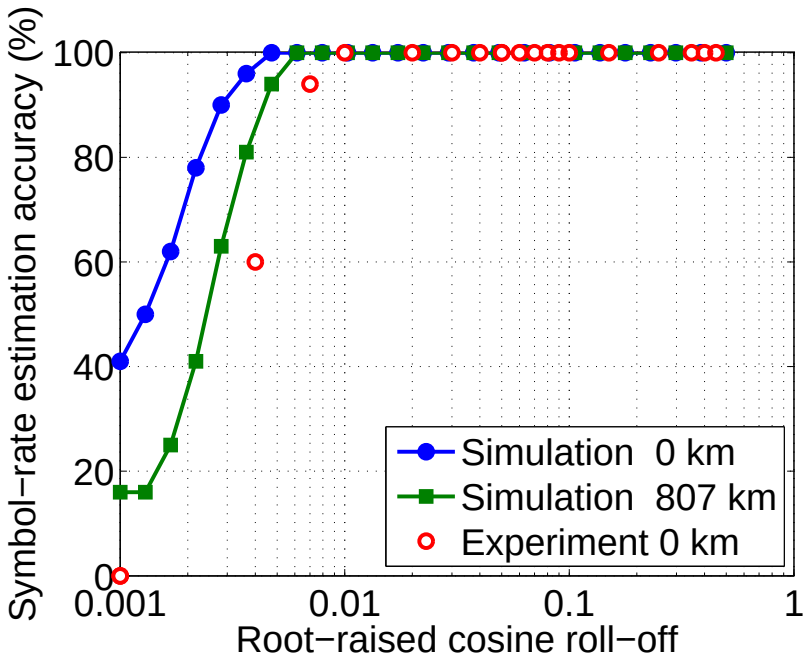

(b) 16-QAM.

Figure 5.25: Impact of RRC roll-off on the symbol-rate estimation, in a three channel WDM signal, modulated with 16-QAM at 10 GBaud.

Independence of OSNR

While the symbol-rate estimation limits have been investigated so far assuming linear regime operation, here we investigate the impact of highly linear and non-linear noise on the symbol-rate estimator. The simulations parameters assumed are described below.

λ [nm]	1550
α $[\frac{dB}{km}]$	0.2
D $[\frac{ps}{nm \cdot km}]$	16.78
S $[\frac{ps}{nm^2 \cdot km}]$	0.06
PMD parameter $[\frac{ps}{\sqrt{km}}]$	0.1
γ $[\frac{1}{W \cdot km}]$	1.2
Split step size [km]	0.5
Span length [km]	80.7
Number of spans	10 / 25

Table 5.6: Fibre parameters used in simulating the impact of OSNR on the symbol-rate estimation.

An important advantage of the SCF method for symbol-rate estimation is that it is completely independent of linear and non-linear noise, as demonstrated by simulation and experimentally in Fig. 5.26. This is due to the fact that noise can be modelled as a wide-sense stationary, but not cyclostationary, process which means that the spectral correlation of noise is not periodic and thus does not generate correlation peaks at non-zero cyclic frequencies.

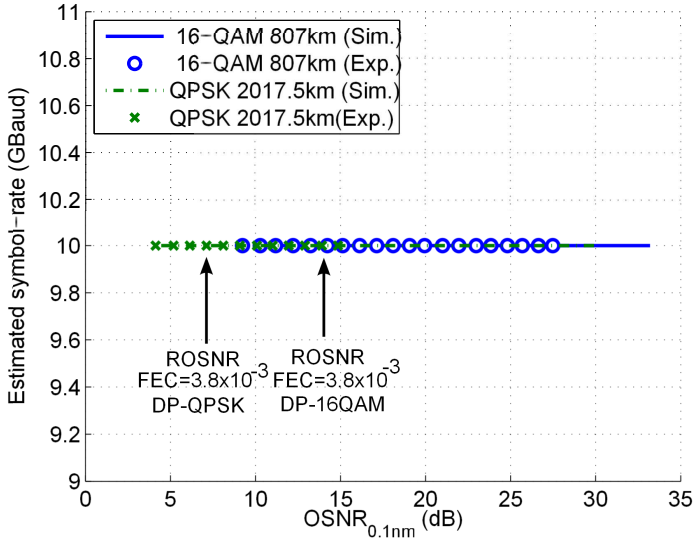

Figure 5.26: Symbol-rate estimation independence of the OSNR, in a three channel 10 GBaud WDM signal.

5.3.2 Cyclic autocorrelation function approach

The time-domain implementation of the cyclostationarity-based symbol-rate estimator utilises the CAF, as Fig. 5.27 depicts. Compared to the frequency-domain implementation of Fig. 5.10, to which it is almost identical, the time-domain implementation does not employ a moving average filter, but instead uses an IFFT to translate the spectral correlation back into the time-domain. For a given cyclic frequency α, the CAF of a received signal $y(t)$ is the IFFT of its cyclic periodogram at α:

$$R_y^{\alpha}(\tau) = \int_{-\infty}^{\infty} Y\left(f+\frac{\alpha}{2}\right) \cdot Y^*\left(f-\frac{\alpha}{2}\right) \cdot e^{j2\pi f\tau} df \tag{5.7}$$

A more detailed explanation of the relationship between the CAF and the cyclic periodogram as a Fourier Transform pair, can be found in Chapter 3. The IFFT is in itself a frequency-smoothing stage, because it is the average at time τ of all complex frequency components of the spectrum $Y(f)$, that are separated by α. This alternative time-domain implementation has a significant impact on the performance of the symbol-rate estimator as a function of dispersion, as well as roll-off factor, as it will be demonstrated next. In terms of processing speed, the replacement of the moving average operation by an IFFT operation does not change the complexity of the algorithm, as explained in Section 5.2.

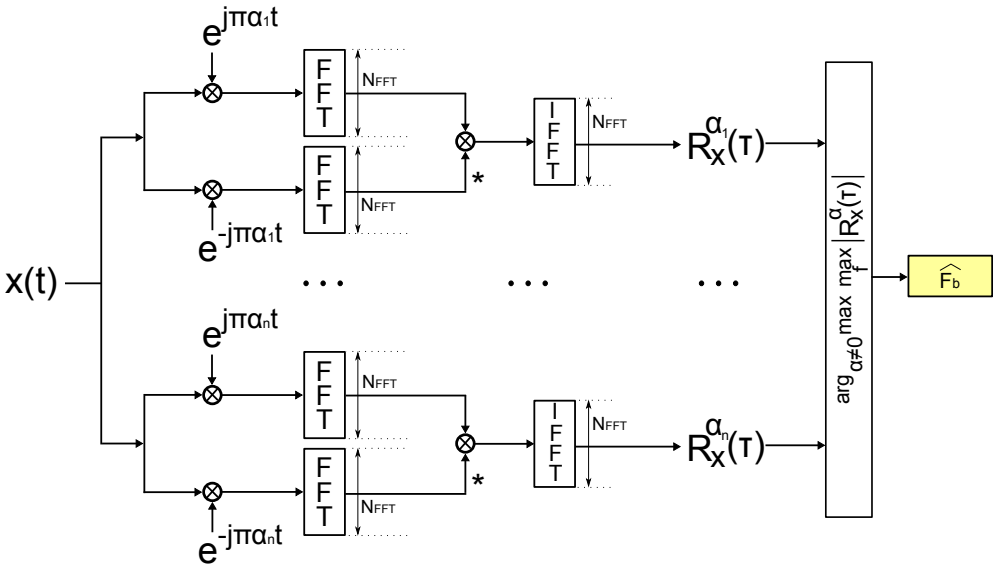

Figure 5.27: Implementation of the symbol-rate estimation algorithm based on the CAF.

After the CAF is computed for a selection of cyclic frequencies, its tones profile is obtained by taking the highest cyclic autocorrelation values along the time-lags τ for each cyclic frequency α. The result is a two-dimensional profile from the three-dimensional CAF, as in Fig. 5.28(b) for a homogeneous WDM signal or Fig. 5.28(d) for a heterogeneous WDM signal. The profile can be called the *CAF tones function* for

the received signal $y(t)$ and is defined with respect to the cyclic frequency as:

$$T_{y,CAF}(\alpha) = \max_{\tau \geq 0} \left| R_y^{\alpha}(\tau) \right|, \tag{5.8}$$

It is important to note that the causality condition $\tau \geq 0$ is imposed on this measurement. The symbol-rate estimate is then simply the non-zero cyclic frequency corresponding to the maximum tone:

$$\hat{F_b} = \arg_{\alpha \neq 0} \max T_{y,CAF}(\alpha). \tag{5.9}$$

Similarly to the symbol-rate estimation based on the SCF, single tones or multiple tones appear in the CAF of WDM signals, depending on whether they are homogeneous or multi-rate heterogeneous (Fig. 5.28).

As explained in Section 3.1, the CAF of linearly modulated signals, such as QPSK or 16-QAM, contains harmonics of a fundamental frequency equal to the symbol-rate. If any type of low pass filtering is applied on the signal, then the highest harmonics will reduce to zero and only the fundamental frequency will typically remain. These theoretical characteristics can be observed indeed in Fig. 5.28(b), showing the profile of the CAF with respect to the cyclic frequency α, for a WDM signal formed of three channels, each modulated with 16-QAM at 10 GBaud symbol-rate and RRC filtered with a roll-off factor of 0.5. The two highest peaks correspond to the cyclic frequencies equal to zero and the symbol-rate (the Direct Current (DC) and the fundamental frequency components respectively). The higher harmonics (20 GHz, 30 GHz, 40 GHz etc.) are not appearing, as they are strongly filtered by the RRC filter at the transmitter. At all other cyclic frequencies, not integer multiples of the symbol-rate $\alpha \neq k \cdot F_b$, $k \in \mathbb{Z}$, the CAF is approximately zero, as expected.

This proposed technique also works for heterogeneous WDM configurations, such as the one shown in Fig. 5.28(c), for three channels modulated with 2.5 GBaud 64-QAM, 25 GBaud QPSK and 10 GBaud 16-QAM respectively. The OSNR matches the average ROSNR across all channels, assuming a FEC limit of $3.8 \cdot 10^{-3}$. In these results, the launch power per channel is set out to be directly proportional to the symbol-rate, such that to maximise the individual transmission distances [Poggiolini et al., 2011]. Consequently, we find that the correlation tones increase in power with the channel bandwidth, suggesting that wider bandwidths correlate better under this technique. Even though the correspondence between the channel rate and channel location is lost, this information could be recovered through further DSP, but this aspect is not investigated in this thesis.

In this section, the time-domain approach to the cyclostationarity-based symbol-rate estimator is investigated with respect to ranges of rates that can be accurately estimated, the RRC excess bandwidth and CD.

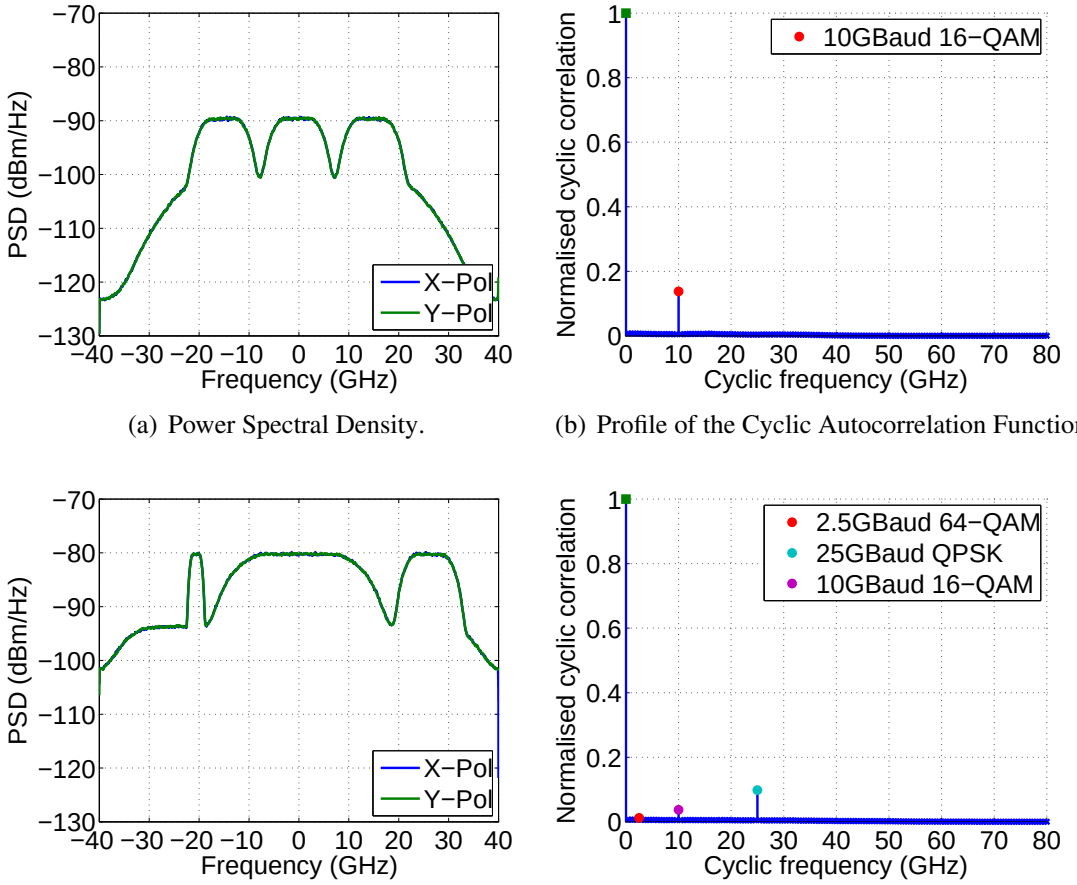

(a) Power Spectral Density.

(b) Profile of the Cyclic Autocorrelation Function.

(c) Power Spectral Density.

(d) Profile of the Cyclic Autocorrelation Function.

Figure 5.28: The Cyclic Autocorrelation Function of a homogeneous WDM signal spectrum (a) has a single tone (b), whilst a heterogeneous WDM signal spectrum (c) has multiple tones (d), one for each individual symbol-rate. Simulation and processing of 2^{19} samples; RRC roll-off factor of 0.5.

Range and accuracy

A robust symbol-rate estimator requires 100% accuracy over a wide range of values, such that it can be used with both established and future optical transmission system configurations. Fig. 5.29 depicts the estimation range for a configuration of three contiguous channels, modulated with 16-QAM and pulse shaped with a RRC filter of 1%, 10% and 50% excess bandwidths, in turn. After an ideal transmission (dispersion- and nonlinearity-free), the signals are noise-loaded at the receiver such that the OSNR matches the ROSNR for a FEC requirement of $3.8 \cdot 10^{-3}$ at the corresponding symbol-rate. These ROSNR values can be found in Fig. 2.3. Again, the IF between LO and transmitter lasers is randomly selected within the interval $[-1GHz, 1GHz]$, values as observed in practice, to justify the independence of this technique on typical frequency offset variations. The tested symbol-rate values are between 1 and 70 GBaud, in steps of 1 GBd, whilst the cyclic frequencies are between 0 and 80 GHz in steps of 500 MHz.

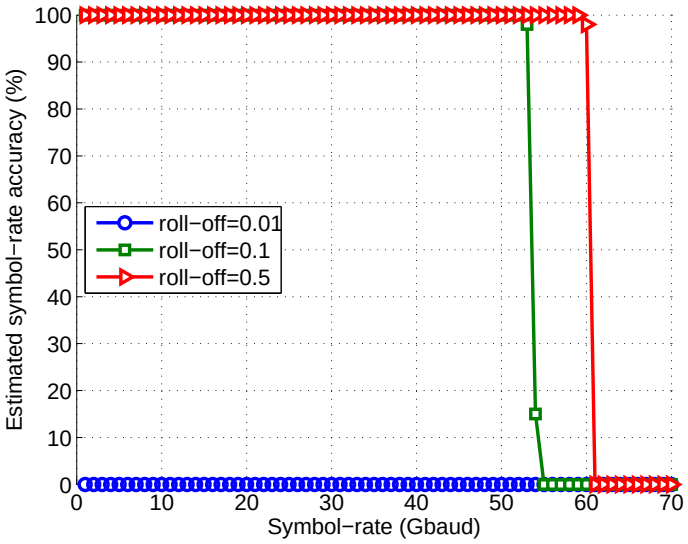

Figure 5.29: Range and accuracy of symbol-rate estimation based on the Cyclic Auto-correlation Function. Three channels modulated with 16-QAM, simulated back-to-back and sampled at 80 GSa/s for 6.55 μs (2^{19} captured samples).

The results show that the symbol-rate can be estimated over a wide range of values, even exceeding the receiver's cutoff and Nyquist frequencies. Such a performance can be better explained visually, by examining the shape of the tones profile at different symbol-rates in Fig. 5.31. Here, the CAF tones are normalised to the DC component and expressed in dBs:

$$T_{y,CAF}(\alpha)_{[dB]} - T_{y,CAF}(0)_{[dB]} = 10\,log_{10}\left(\frac{\max_{\tau\geq 0}\left|R_y^{\alpha}(\tau)\right|}{\max_{\tau\geq 0}\left|R_y^{0}(\tau)\right|}\right)[dB] \tag{5.10}$$

When the roll-off is 10% the maximum symbol-rate that can be estimated with 100% accuracy is 52 GBaud. Up to this value, the tone corresponding to the symbol-rate ($\alpha = F_b$), is easily detectable for this particular roll-off factor, as it lies above all other cyclic frequencies (with the exception of the DC) forming a *'correlation noise floor'*. The shape of the CAF profile is influenced by the signal configuration, but also by any type of filtering that the signal has undergone, including the RRC at the transmitter or the Low-Pass Filter (LPF) at the receiver, for instance. When the symbol-rate increases beyond 52 GBaud, the correlation is still achieved, but the tone power is lower as a result of low-pas filtering, which attenuates higher frequencies.

Fig. 5.30 demonstrates that for the same set of symbol-rates the tone power increases as the roll-off is increased to 0.5. For example, the tone at 52 GBaud has a much higher SNR when the roll-off is 0.5 compared to roll-off of 0.1. As a consequence, the estimation range extends up to 59 GBaud, because wider bandwidths increase the correlation at $\alpha = F_b$.

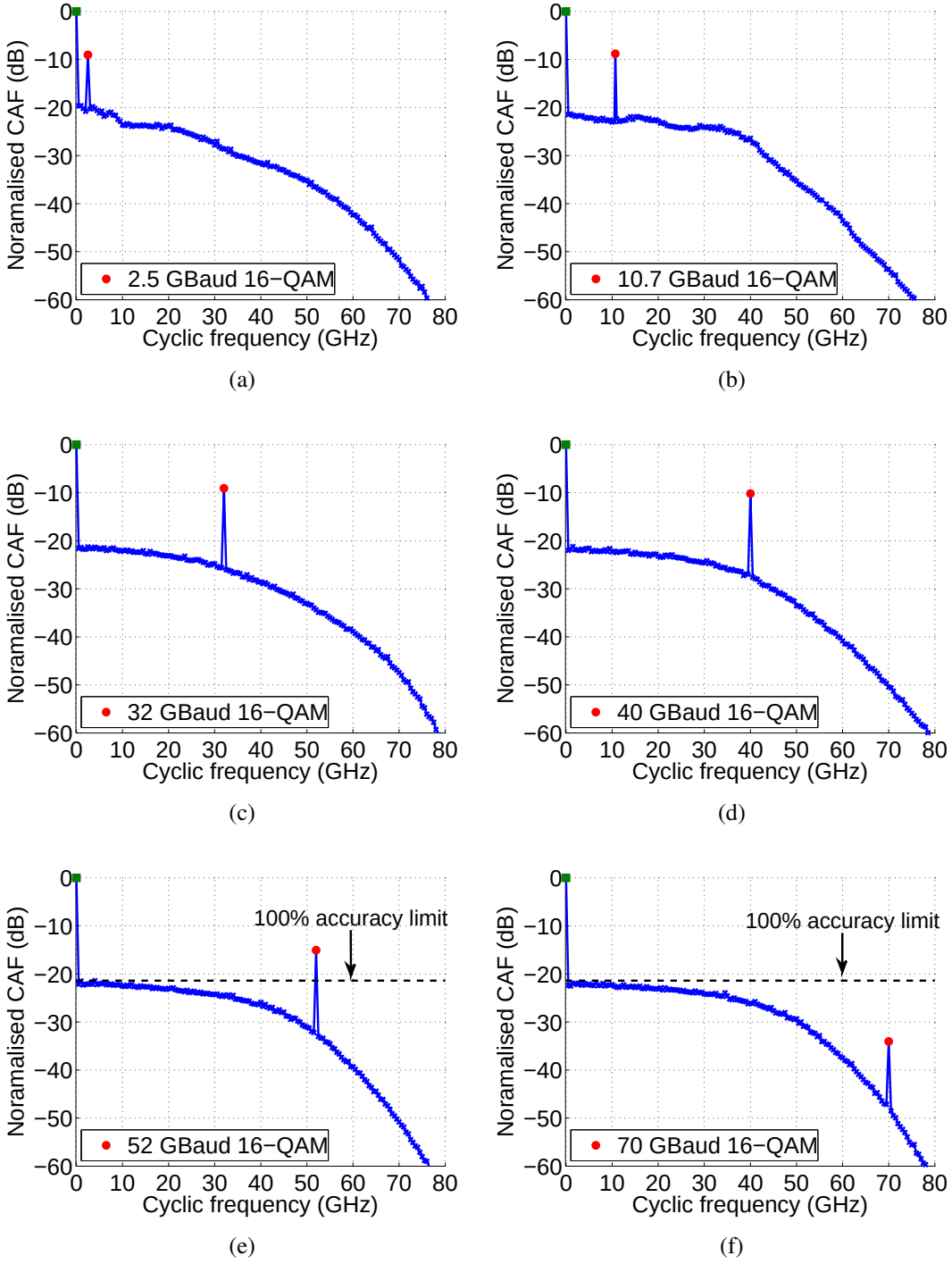

Figure 5.30: Normalised Cyclic Autocorrelation Function, for three contiguous WDM simulated channels, and a wide selection of symbol-rates (RRC roll-off factor is 0.5).

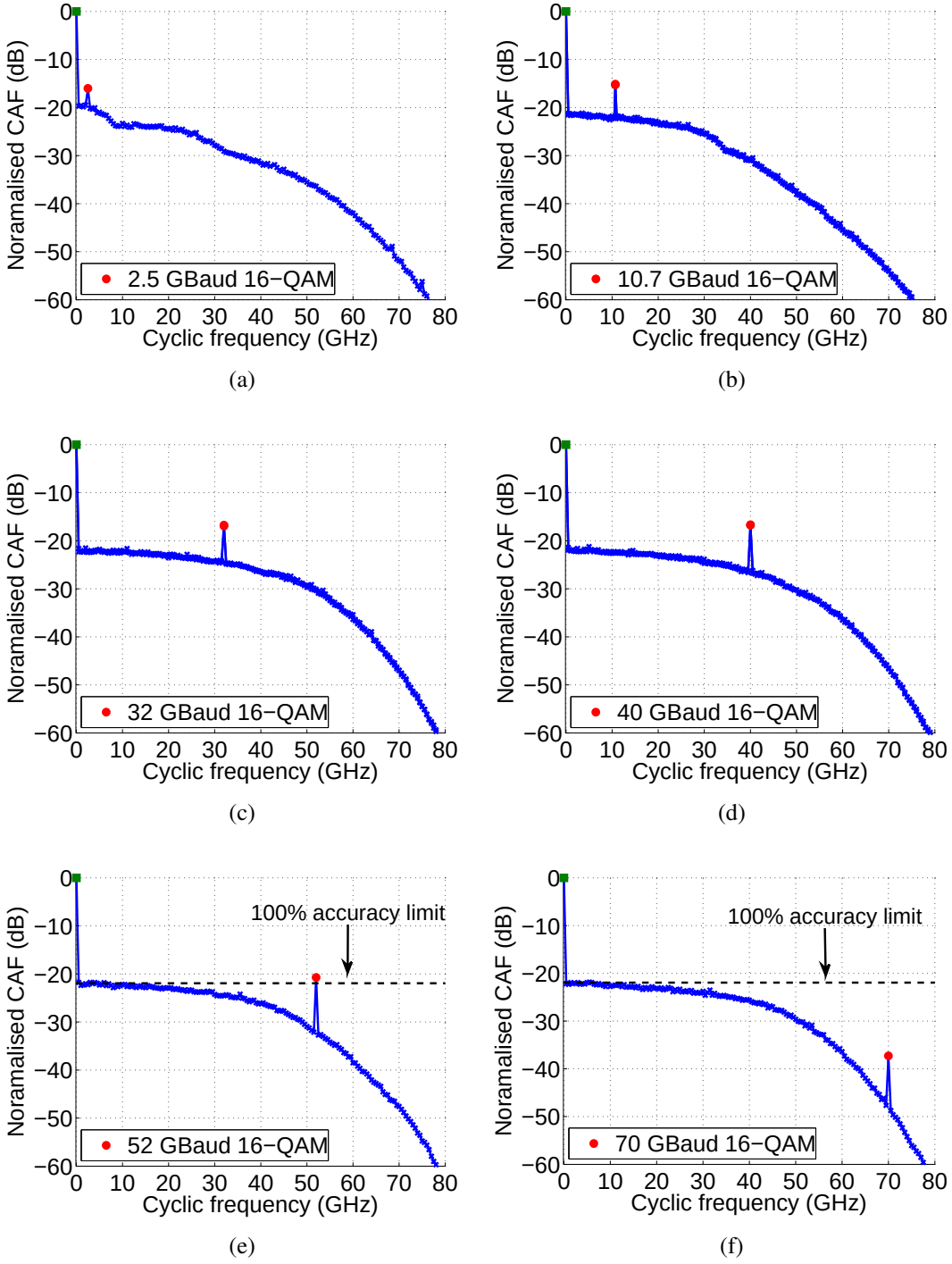

Figure 5.31: Normalised Cyclic Autocorrelation Function, for three contiguous WDM simulated channels, and a wide selection of symbol-rates (RRC roll-off factor is 0.1).

Conversely, for very low excess bandwidths such as 1%, the correlation peak disappears (Fig. 5.32), as the bandwidth is insufficient to obtain a strong overlap between the two shifted copies of the spectra. Referring back to Fig. 5.29, in this case, the technique completely fails for the entire range of symbol-rates. Therefore, the roll-off factor strongly limits this symbol-rate estimation approach, which is studied in more detail in the following section.

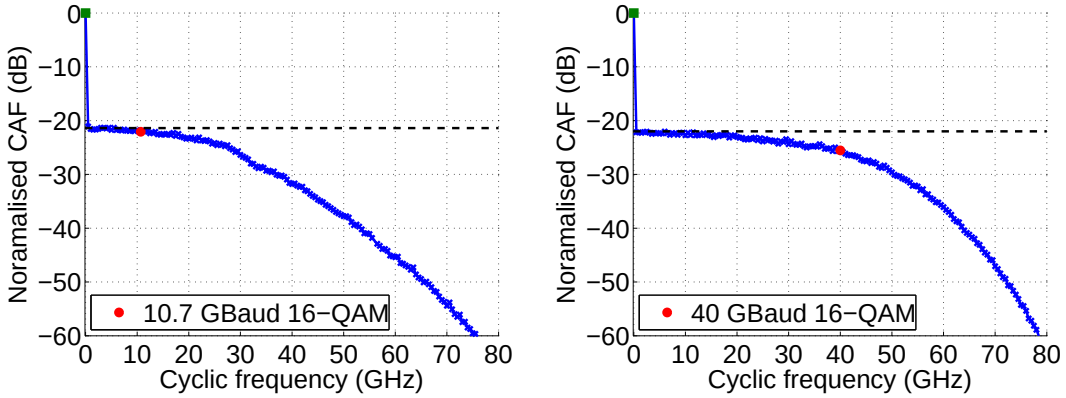

(a) (b)

Figure 5.32: Normalised Cyclic Autocorrelation Function, for three contiguous WDM simulated channels, and a wide selection of symbol-rates (RRC roll-off factor is 0.01).

Whilst in the previous example, the symbol-rate value was always found in the range of cyclic frequencies under test, in a real-time application assuming arbitrary symbol-rates, it may be necessary to scan the spectrum over even a finer cyclic frequency granularity, in order to ensure that the symbol-rate tone is correctly identified. It is not necessary to have an exact match between the set of possible symbol-rates and the set of tested values, as correlation can still occur even for a small offset of the order of kHz. If, F_b is the value to be estimated, let $\Delta\alpha_{max} = \alpha - F_b$ be the maximum cyclic frequency step size deviation from F_b, allowed before the correlation is lost. For any cyclic frequency granularity greater than $\Delta\alpha_{max}$, the symbol-rate tone can be undetectable, by the scanning process.

The measurement precision is thus quantified as the power ratio between the spectral tone at an arbitrary α and the spectral tone at the known symbol-rate:

$$T_{y,CAF}(\alpha)_{[dB]} - T_{y,CAF}(F_b)_{[dB]} = 10\,log_{10}\frac{\max_{\tau\geq 0}\left|C_y^{F_b+\Delta\alpha}(\tau)\right|}{\max_{\tau\geq 0}\left|R_y^{F_b}(\tau)\right|}. \tag{5.11}$$

Fig. 5.33 shows the precision measurements and that $\Delta\alpha_{max} = 208$ kHz for 10% excess bandwidth, an exact match with the SCF precision. If the roll-off is 0.01, then a careful selection of the cyclic frequency granularity is futile, as the estimation is inaccurate in all cases. For low symbol-rates, such as 2.5 GBaud or 10 GBaud, there

is no clear difference between the tone at exactly the symbol-rate and the tones within ± 1 MHz from it. When the symbol-rate is 40 GBaud, there is correlation between frequency components in a narrow range around F_b (or around $\Delta\alpha = 0$) because the increase in channel bandwidth, as previously discussed. However, this correlation does not yield a sufficiently high power tone to be detected by the estimator, as it is in fact clear from Fig. 5.32(b).

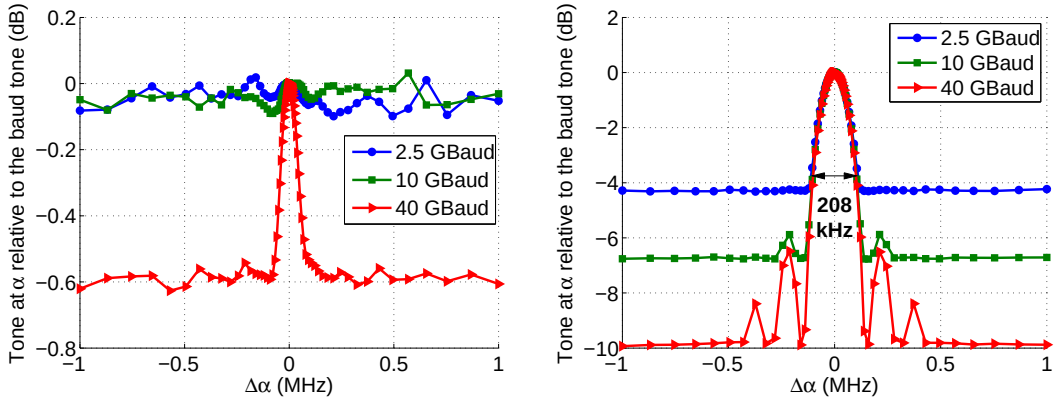

(a) 0.01 roll-off

(b) 0.1 roll-off

Figure 5.33: Precision of the symbol-rate estimation technique based on the CAF demonstrated by simulation for DP-16QAM. 2^{19} samples are processed and only AWGN is assumed as impairment.

Impact of Nyquist pulse shaping

The narrowing of the signal spectrum when employing Nyquist pulse shaping corresponds to the broadening of the pulse in the time domain. In turn, this broadening results in a lower CAF tone power, leading to a trade-off between the temporal correlation and spectral efficiency. Fig. 5.34(a), which depicts the measurement of the peak power in the estimated tone relative to the noise floor,

$$SNR_{tone} = 10\,log_{10}\frac{\max_{\tau}\{R_y^{\hat{F}_b}(\tau)\}}{\max\{R_y^{\alpha\neq F_b}(\tau)\}}, \tag{5.12}$$

demonstrates that the correlation changes proportionally with the roll-off, as well as the symbol-rate. For the three different symbol-rates considered, the SNR of the symbol-rate tone is identically zero for roll-offs of 0.018 and lower, when the temporal correlation cannot be achieved. However, on average, the tone power needs to exceed 0.7 dB in order for 100% estimation accuracy to be guaranteed.

As the symbol-rate increases, the range of roll-offs supported by the technique also increases. Fig. 5.34(b) confirms that the minimum roll-offs to correctly estimate 2.5 GBaud, 10 GBaud and 40 GBaud are approximately 0.056, 0.032 and 0.024 respec-

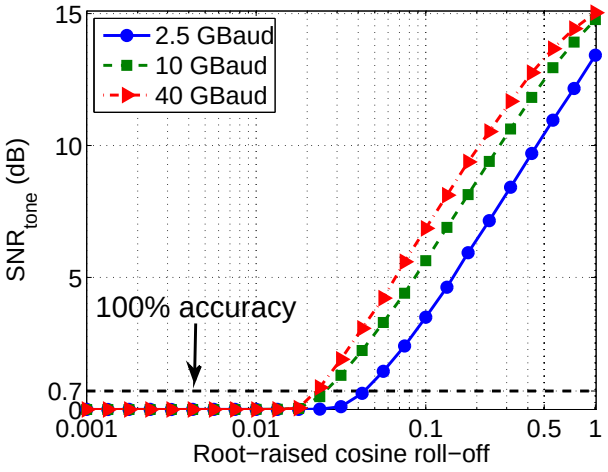

(a)

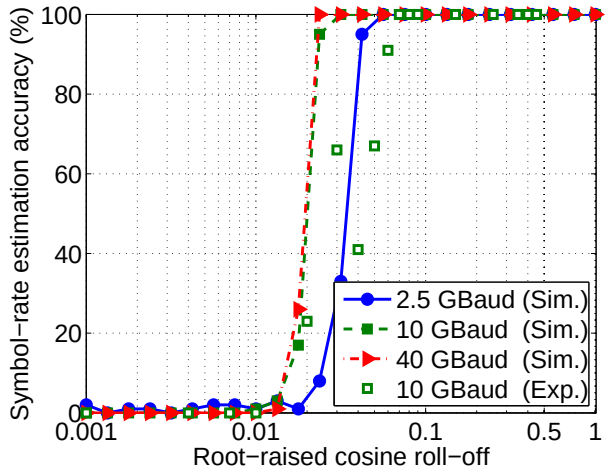

(b)

Figure 5.34: Impact of the RRC filter on the CAF-based symbol-rate estimation in terms of SNR of the estimated tone (a) and accuracy (b), when AWGN is the only impairment.

tively. When the roll-off approaches unity, the SNR_{tone} of 40 GBaud is lowered, as the bandwidth of the signal is more strongly filtered at the receiver compared to the lower rates. Experimentally it was found that the minimum roll-off for estimating 10 GBaud, in a back-to-back transmission, is in fact 0.07. The slight difference between the experimental and simulation findings can be attributed to further possible losses in the signal path, unaccounted for in simulation, which reduce the tone's SNR.

These results suggest that with the presented technique it is by far more advantageous to increase the spectral efficiency by increasing the symbol-rate, whilst keeping a roll-off factor greater than 0.07. This is in fact the opposite requirement to the predicted trend in the design of future fast optical networks.

Impact of chromatic dispersion

CD limits the maximum achievable transmission distances, as the pulses spread quadratically with the symbol-rate, leading to ISI. To limit this effect, a low RRC roll-off is preferred. However as described previously, a too low roll-off will limit the cyclic autocorrelation tone power, until complete fading when this value is approaching zero, as RRC filtering dissipates the energy in the CAF tones along the time-lag (Section 3.4, Figure 3.17).

In Figure. 5.35, we observe that the SNR of the fundamental cyclic frequency ($\alpha = F_b$) decreases slowly with distance, in particular for lower symbol-rates, and that a roll-off of 0.01 is detrimental to the estimation. As the symbol-rate is increased, the CD impact is higher, however the SNR tone is still decreasing at a slow rate. As the roll-off factor is increased, the method becomes even less affected by accumulated dispersion, because the tone SNR is higher.

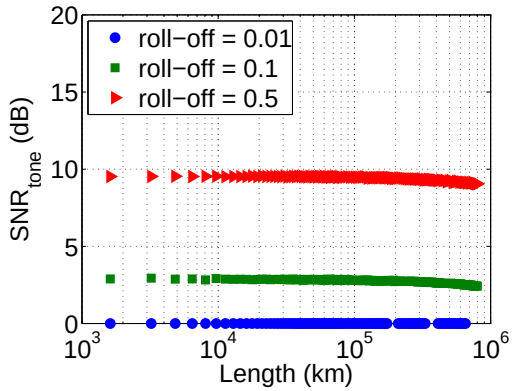

(a) 2.5 GBaud, 3 channels 16-QAM.

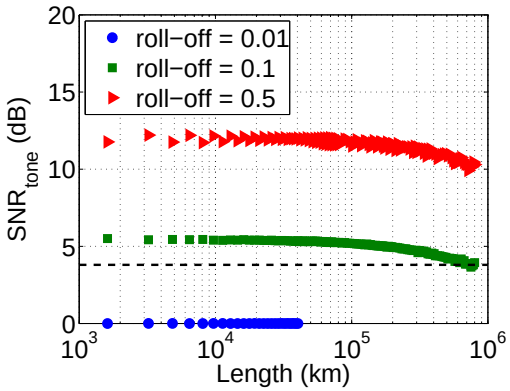

(b) 10 GBaud, 3 channels 16-QAM.

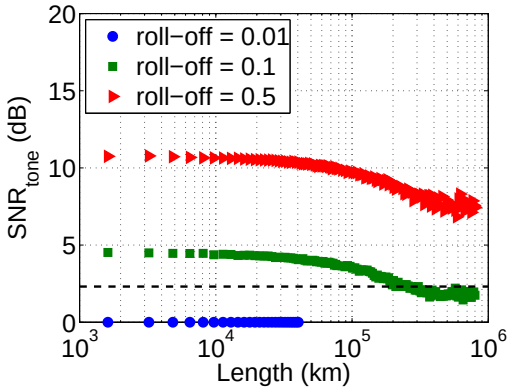

(c) 40 GBaud, 3 channels 16-QAM.

Figure 5.35: Impact of CD on the CAF-based symbol-rate estimation by simulation.

Due to this slow SNR decrease, the symbol-rate estimation based on the CAF appears as if it is CD independent, since it can function with 100% reliability for transmission distances of at least 173,500 km, as in Fig. 5.35(c) for instance when

the roll-of is 0.1 and the symbol-rate is 40 GBaud. From a practical point of view, as such high distances are not traversed without regeneration, it can be assumed that this estimator is indeed CD independent.

5.3.3 Comparison between the time domain and frequency domain symbol-rate estimators

Selecting the best between the two investigated techniques involves a few practical considerations. The optimum symbol-rate estimation technique performs with 100% accuracy for the highest transmission distance at the highest spectral efficiency and can allow a wide range of symbol-rates to be estimated. Ideally, fibre impairments should have minimal or no impact on the estimator. Between two estimators that are matching in performance, the one requiring the lowest computational effort is preferred.

The time-domain approach has a more stringent lower-bound limit on the excess bandwidth, imposing stricter requirements on the transmission configuration, such that this technique could be employed at the receiver. Although the IFFT employed to compute the CAF is a type of averaging operation, the moving-average filter is a much better frequency smoothing stage for enhancing the correlation when the signal bandwidth approaches Nyquist, as it has been demonstrated to work for roll-offs of 0.01.

On the other hand, since frequency-smoothing is not performed, the impact of CD on the CAF is reduced compared to the SCF. At sufficiently high roll-off factors, the SNR_{tone} is improved, as the peak at the cyclic frequency equal to the symbol-rate is better defined compared to the SCF method. For example, when the symbol-rate was 10 GBaud, the tones SNR of the CAF decrease at a much lower rate of approximately 0.05 dB in 21,793 km, compared to the tones of the SCF which decrease approximately exponentially, starting at only 3.2 dB above the noise floor and dropping to 0 dB in 20,000 km.

The spectral efficiency is defined as the capacity that can be transmitted in a unit bandwidth. For any M-arry dual-polarised modulation format, either single channel or contiguous superchannels configuration, it is given by:

$$SE = \frac{N_{ch} \cdot 2\log_2 M \cdot F_b}{N_{ch} \cdot Fb \cdot (1+r)} = \frac{2\log_2 M}{(1+r)}. \tag{5.13}$$

In other words, for these particular cases, the spectral efficiency is actually independent on the symbol-rate or number of channels, and can be maximised by increasing the modulation format order, decreasing the roll-off or both. Assuming DP-16QAM as the modulation format of choice, we compare the two cyclostationary symbol-rate estimation approaches in terms of the maximum spectral efficiency that they can support

and find a 0.4 b/s/Hz difference in the favour of the frequency domain approach.

Some of the performance limitations discussed thus far in this section, are summarised in Table 5.7.

Frequency-domain (SCF)				**Time-domain (CAF)**			
Maximum symbol-rate (GBaud)							
r=0.01	r=0.1	r=0.5		r=0.01	r=0.1	r=0.5	
41.8	45.4	45.65		0	52	59	
Maximum distance (km) as a function of the symbol-rate, F_b (GBd)							
F_b	r=0.01	r=0.1	r=0.5	F_b	r=0.01	r=0.1	r=0.5
2.5	48,420	129,120	128,474	2.5	0	>798,900	>798,900
10	9,684	22,596	26,712	10	0	782,800	>798,900
40	1,614	3,228	3,470	40	0	173,500	242,100
Minimum RRC roll-off when the symbol-rate is 10 GBaud							
r=0.01				r =0.07			
Maximum spectral efficiency (b/s/Hz)							
7.9 (M=16, r=0.01)				7.5 (M=16, r=0.07)			
Complexity							
$2CNADClog_2(NADC)$				$3CNADClog_2(NADC)$			

Table 5.7: Performance of the SCF- and CAF-based symbol-rates estimators, for three contiguous WDM channels, modulated with DP-16QAM.

Selecting which one the two estimators will be used, depends on the application. In terms of complexity they are comparable. The time-domain technique performs better in terms of CD to the detriment of limiting the lowest allowed roll-off. As a result, for most optical communications applications, the SCF approach would be preferred, as it allows the estimation of the symbol-rate over the widest range of roll-offs, and for reasonably high transmission distances.

5.4 Roll-off estimation

The RRC roll-off factor can be additionally estimated from the CAF computation, by looking at the power ratio between the tone at the symbol-rate and the DC. This ratio will be linear for a wide range of roll-offs, as shown in Fig. 5.36. Finding this linear approximation in a transceiver self-configuration stage, could thus enable the estimation of the roll-off factor with an acceptable performance [Yang et al., 2009] of $< 20\%$ Root Mean Squared Error (RMSE) down to a roll-off of 0.06, as demonstrated in Fig. 5.37.

These results have been investigated in a back-to-back transmission setup, in the presence of AWGN, loaded at the receiver to give the ROSNR for FEC = $3.8 \cdot 10^{-3}$. When pulse shaping is approaching the Nyquist limit, the symbol-rate tone becomes indistinguishable from the correlation noise floor, resulting in slight increases in errors

for roll-offs below 0.06. The discrepancy between the simulation and the experimental results in the low roll-off region arises from the additional noise sources that are present in the experiment but not accounted for in the simulation. On the other hand, when the signal bandwidth is higher than the receiver bandwidth, the tone power is also diminished, as the channel is being filtered out. The receiver bandwidth limitation is evident in particular at 40 GBaud, when the roll-off is greater than 0.3. As a consequence, this estimator will perform well, as long as the signal bandwidth is not strongly filtered.

The CAF of cyclostationary signals, computed as in Section 5.2, is only slowly fading with dispersion (Section 5.3.2). In fact, the SNR of the symbol-rate tone is approximately constant up to 18,000 km for a wide range of rates and roll-off factors (0.06-0.3), as it has been shown in Fig. 5.35. It is therefore expected that this technique should also work when the signal has traversed such significant distances.

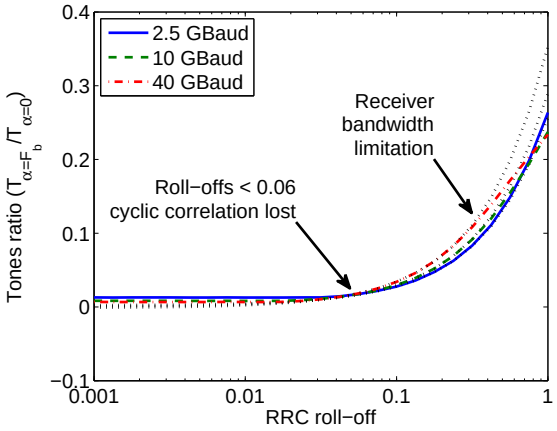

Figure 5.36: Power ratio between the CAF tones at $\alpha = F_b$ and $\alpha = 0$, with the RRC filter roll-off, obtained by simulation. The dotted black lines show the fitted linear approximations of the ratio.

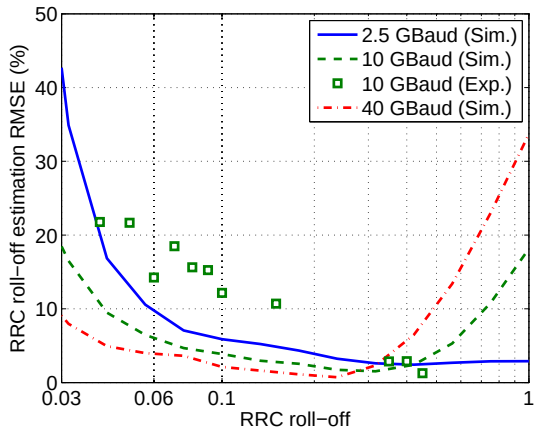

Figure 5.37: RRC filter roll-off estimation range.

5.5 Frequency offset estimation

Beating of the incoming optical signal with the LO at the coherent receiver optical front-end downconverts the signal to baseband. The frequency difference between the transmitter and receiver lasers is called the *'Intermediate Frequency'*, or IF, compensated for in a carrier recovery stage to enable data recovery.

Additionally, the CD and OSNR estimation stages of the proposed joint estimator require approximate knowledge of the IF, such that their measurements can be centred on the channel bandwidth of interest, prior to full carrier recovery. If the excess bandwidth of a 10 GBaud signal is 10%, a coarse estimate is sufficient for this task, since frequency offset errors as high as 125 MHz can be tolerated, as Section 5.6 will demonstrate. Narrower channels however, have a lower tolerance to frequency offset variations, when the channel deviation from the frequency grid needs to be known.

This section demonstrates a technique that can be used to recover the carrier frequency offset within an absolute error of the order of tens of MHz. This accuracy is sufficiently high to enable a subsequent correct estimation of the CD and OSNR parameters. Furthermore, the IF value obtained can be used as feedforward information for the carrier recovery stage that follows later in the receiver's DSP. It can be applied to the individual channels, or directly to the entire superchannel, enabling fast performance monitoring.

Just as the PSD of a signal experiences a shift in frequency equal to the IF value, so does its SCF (Fig. 5.38). We propose a technique for determining the IF value from the first cyclic spectrum, already measured during the symbol-rate estimation stage, thus utilising a single slice of the SCF, at cyclic frequency $\alpha = \hat{F}_b$. Analysis of the first cyclic spectrum is preferred, because compared to the PSD, the channels are fixed to the same frequency grid, but have reduced bandwidth, resulting in larger channel gaps. The constituent channels of a superchannel can thus be more easily distinguished, and this is the property upon which the proposed IF estimator depends.

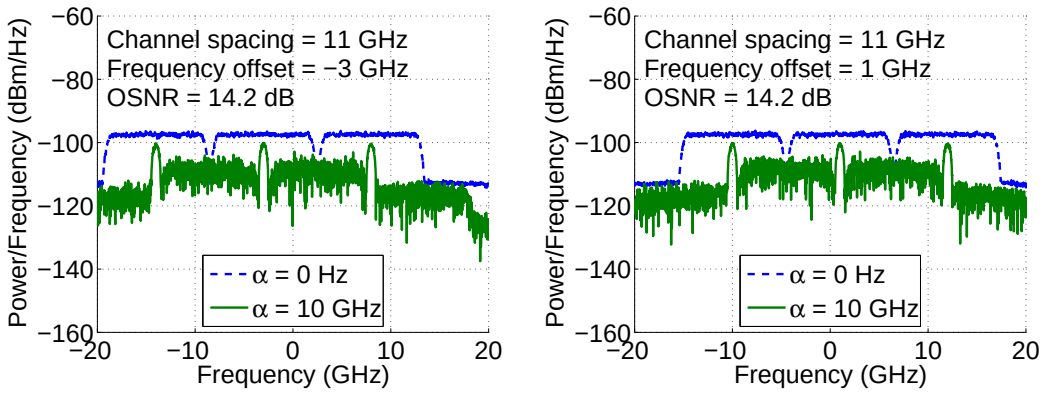

Figure 5.38: The PSD and SCF at $\alpha = F_b$ have the same IF. 10 Gbaud, roll-off=0.1.

Therefore, the proposed technique is not applicable to the traditional PSD where the guard interval between channels is absent or minimal. The basic principle of this proposed estimation method is to employ different mathematical operations on the cyclic spectrum, which will generate a frequency domain pulse that shifts with the channel position on the frequency grid. Identifying the pulse's frequency shift will thus indicate the frequency offset of the corresponding channel. If the receiver bandwidth is sufficient to capture multiple channels of the same superchannel, then it is sufficient to estimate the IF for one channel only, as this value will be shared between all of them. In the following investigation, we focus only on the central channel of a three channels configuration.

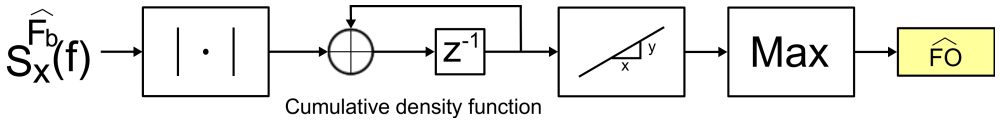

Figure 5.39: Implementation of the IF estimation technique based on the SCF.

The stages of the IF estimator are depicted in Fig. 5.39. Firstly, the Cumulative Density Function (CDF) of the magnitude cyclic spectrum is calculated, implemented as an addition operator with a one sample delay. For a 10 GBaud channel centred around 1 GHz, the CDF describes a trace as in Fig. 5.40. Outside the channel bandwidth, the slope increases slowly as the spectral correlation noise floor is approximately constant. Within the channel bandwidth, the higher amplitudes of the signal spectrum contribute to a higher change in slope. The channel bandwidth is proportional to the roll-off factor, and that can be clearly seen in this instance, in the change in slope centred at and around the 1 GHz frequency offset.

Provided that the channel spacing is such that the neighbouring channels are not contiguous or overlapping in the cyclic spectrum, there will be a clear change in slope in the measured CDF, corresponding to the channel location. Note that contiguity in the cyclic spectrum can only occur for extreme cases of faster-than-Nyquist superchannels as depicted in Fig. 5.41. If the channel spacing is approximately equal to the cyclic spectrum bandwidth $F_b \cdot r$, then this technique fails, because the slopes of the individual channels cannot be distinguished in the CDF analysis. Nevertheless, such extreme channel spacings are unlikely to be practical in optical communications, as data recovery would prove difficult [Sato et al., 2014]. Since the slope change indicates the presence of a channel, the problem of estimating the IF reduces to finding the central point (in frequency) where this change has occurred.

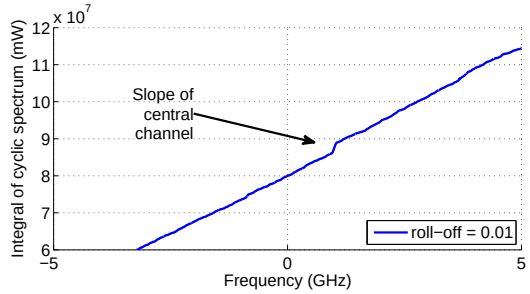

(a) RRC roll-off of 0.01

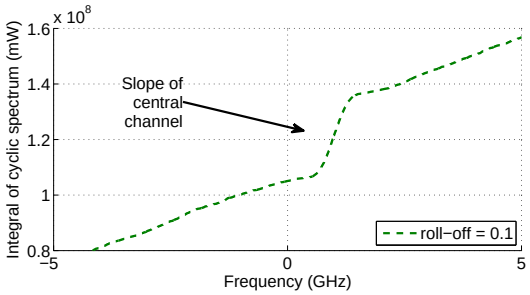

(b) RRC roll-off of 0.1

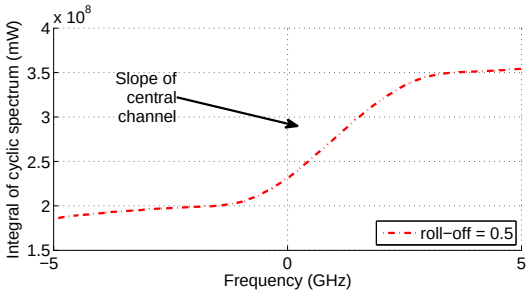

(c) RRC roll-off of 0.5

Figure 5.40: Cumulative density function of the cyclic spectrum for a simulated 10GBaud signal at a 1GHz frequency offset, which can be identified by the slope increase. The slope also increases with the roll-off, as the bandwidth of the SCF decreases.

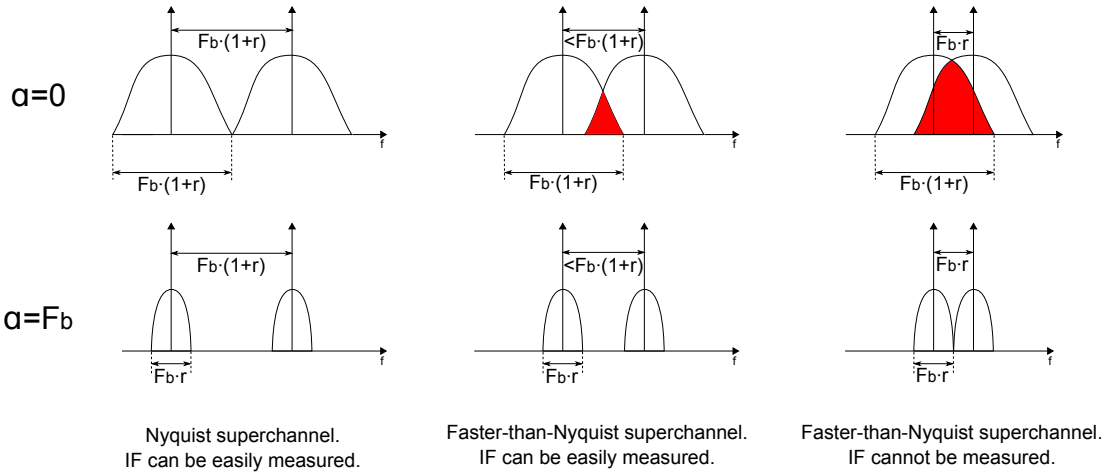

Figure 5.41: The IF estimator works for faster-than-Nyquist superchannels if the channel spacing is much greater than the symbol-rate – roll-off product.

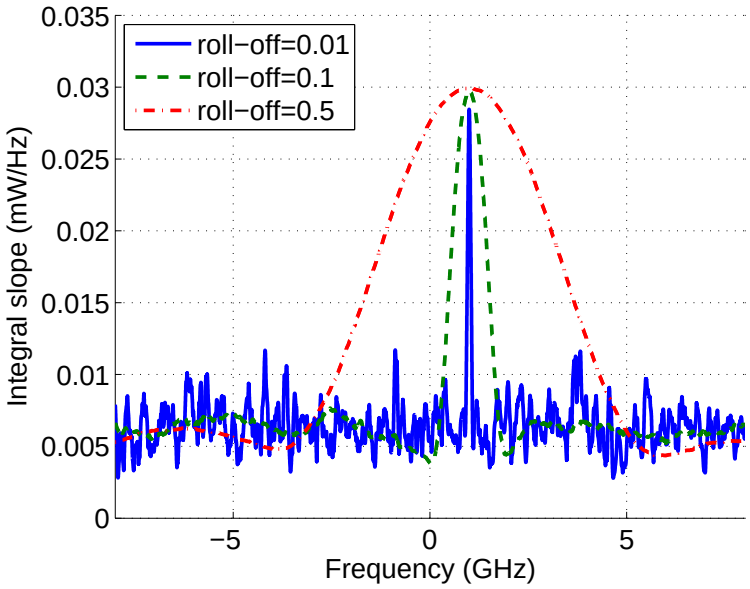

Figure 5.42: Slope of the cumulative density function around the central channel. The peak is located at the IF. Here, the slope was measured over a bandwidth half the channel's bandwidth in the cyclic spectrum, more precisely $\frac{1}{2}F_b \cdot r$, where F_b=10GBaud.

To solve this newly formulated problem, in the second stage of the estimator the slope is measured within a fixed sliding window, over which the CDF is approximately linear with respect to frequency. The measured slope will be maximum when the frequency equals the IF, as seen in Fig. 5.42. These measurements form the frequency-domain pulses, as previously mentioned.

Fig. 5.43 demonstrates that the optimum sliding window is around 70% of the total cyclic spectrum bandwidth, to minimise the absolute IF estimation error. When the measurement bandwidth is too short, it becomes difficult to distinguish sudden slope changes. The frequency-domain pulses are flattened out, and, with no clear maximum at any given frequency, higher estimation errors are obtained. On the other hand, when the slope bandwidth is close to or larger than the actual bandwidth of the channel, the function is no longer linear over this bandwidth, again leading to higher IF estimation errors. Because the slope measurement bandwidth is dependent on the channel bandwidth, knowledge of the symbol-rate and roll-off are required prior to applying this technique, both of which have previously been estimated within the proposed joint estimator.

All simulation results in this section were obtained for three contiguous channels modulated with 16-QAM and transmitted over 30 spans (2421 km) of SSMF, but the conclusions hold for any linear modulation and fibre length, as limited by the performance of symbol-rate and roll-off estimators. In what follows, the slope measurement bandwidth will be fixed to 70% of the of cyclic spectrum bandwidth, namely $0.7 \cdot F_b \cdot r$, which gives the minimum estimation errors across all considered symbol-rates.

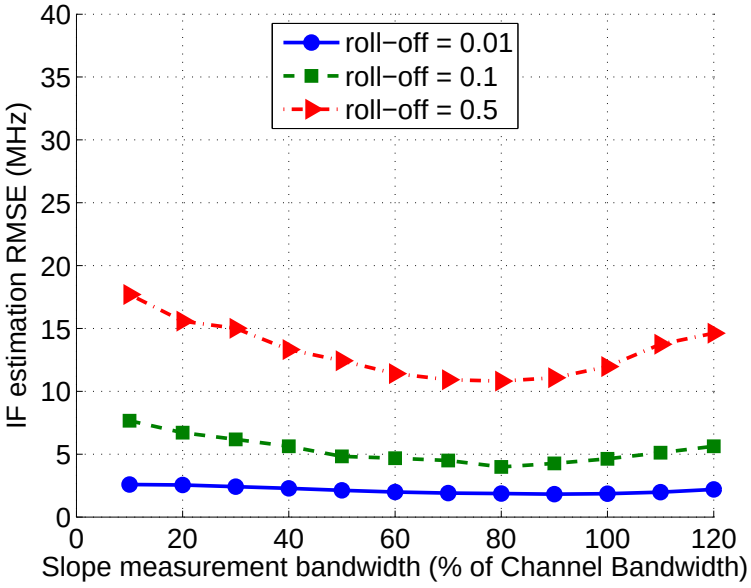

Figure 5.43: Impact of the slope measurement bandwidth on the IF estimation (simulation of a 10 GBaud DP-16QAM WDM signal formed of three channels).

Range and accuracy

From a practical perspective, typical IF absolute values are less than 300 MHz. The performance of this estimator in terms of accuracy is depicted in Fig. 5.44(a) for simulation (16-QAM over 2421 km) and experimental data (16-QAM over 807 km). The RMSE is under 14 MHz, for a maximum roll-off considered of 0.5 and 4 MHz for the typically used roll-off of 0.1. The maximum absolute errors are below 40 MHz in Fig. 5.44(b), dominated by the ambiguity of the maximum peak at the highest roll-offs. The maximum IF estimation error decreases at lower roll-offs, because they give rise to a steeper CDF slope and thus, the spectral peak giving the frequency offset

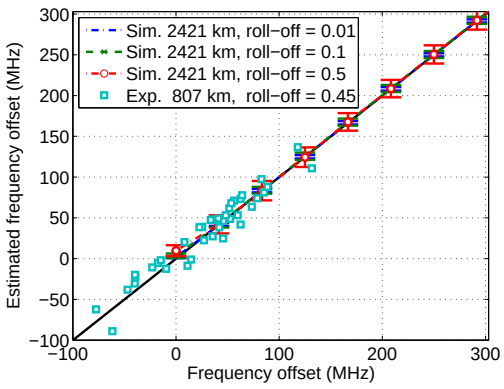

(a) Estimation accuracy.

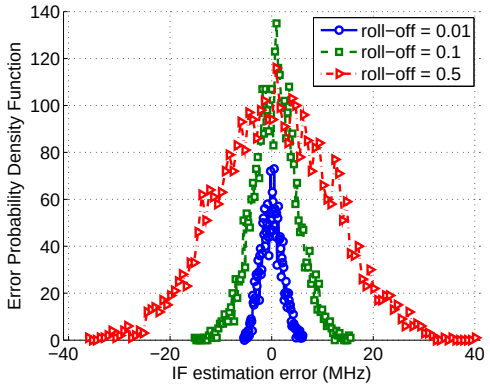

(b) Error probability distribution by simulation.

Figure 5.44: Estimation of IF applied to 10 GBaud homogeneous WDM signals.

estimation is more easily determined. Experimentally, there is no significant difference between QPSK and 16-QAM when estimating the IF. Exact knowledge of the IF was not possible experimentally. Instead, the estimated values obtained with this proposed technique are compared to the estimated values obtained with the DSP carrier recovery stage. The OSNR was fixed to 14.2 dB by simulation and varied between 9.2 and 27.5 dB experimentally, demonstrating the independence of the technique on AWGN.

Impact of chromatic dispersion

As demonstrated in Fig. 5.45, the algorithm presented here is independent of the transmission length, provided correlation fading due to CD does not occur. If operating independently of the symbol-rate estimator, when the roll-offs are 0.01, 0.1 and 0.5 and at 10 GBaud, the IF estimator can work up to 13,720 km, 19,370 km and 20,180 km respectively, making this technique attractive for long-haul high-capacity optical communication systems.

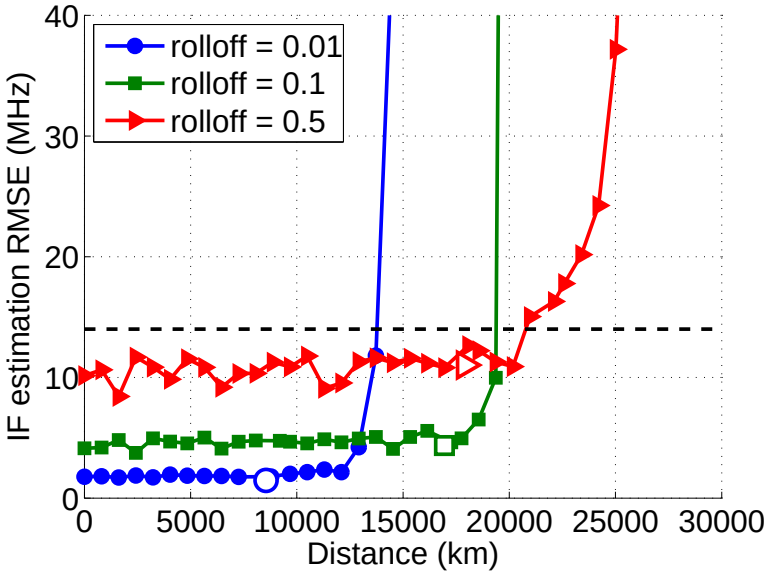

Figure 5.45: IF estimation for different transmission distances (simulation of three 10 GBaud DP-16QAM WDM channels). The hollow marks show the maximum length up to which the symbol-rate can be estimated with 100% accuracy

As fading starts occurring, the symbol-rate estimator will fail before the IF estimator, therefore if the latter depends on feedback from the former, the transmission distances that can be achieved are limited to 8,554 km, 16,950 km and 17,920 km for the same roll-offs of 0.01, 0.1 and 0.5 respectively.

Dependence on channel bandwidth

Fig. 5.46 shows that as the channel bandwidth increases, either by increasing the symbol-rate, the roll-off or both, the performance of the IF estimator degrades. This is a direct consequence of the broadening of the frequency pulses which results in an ambiguity around the maxima at the channel frequency offset. Another limitation here is the receiver bandwidth, which will limit the detection of the channel as its bandwidth broadens.

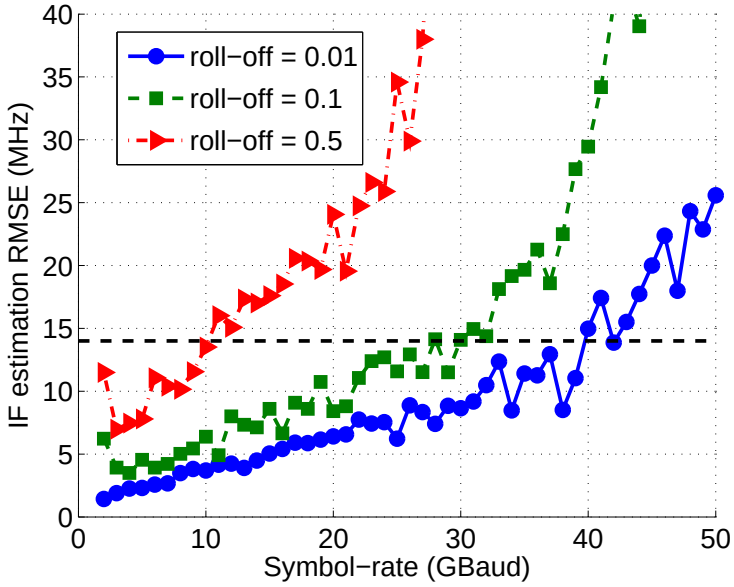

Figure 5.46: IF estimation improves for lower channel bandwidths, as changes in slope can be more precisely estimated (simulation of three 10 GBaud DP-16QAM WDM channels).

These results are depicted under the assumption that the symbol-rate and the roll-off factor have been ideally known a priori. In such applications where this is possible, if the IF estimation RMSE is targeted at 14 MHz, then the maximum permissible symbol-rate values are 39 GBaud, 28 GBaud and 10 GBaud, for roll-offs of 0.01, 0.1 and 0.5 respectively, in order for this technique to work. If perfect knowledge of the channel bandwidth is not possible, the limitation will be imposed by the maximum detectable symbol-rate, which depends on the technique used to estimate it and the distance the signal has travelled under the CD limitations.

The 14 MHz RMSE is sufficiently low to be utilised by the carrier phase recovery within the coherent receiver DSP, at high excess bandwidths. Indifferent to the target error limit, the main advantage of the IF estimator is that its performance improves as the roll-off factor decreases. In conclusion, the proposed IF estimator supports superchannel configurations of the highest spectral efficiency, making it an ideal candidate for future fast optical networks.

5.6 Chromatic dispersion estimation

Through cyclostationarity analysis of signals affected by dispersion, we demonstrate in this section that CD corresponds to a linear phase offset in the frequency domain and a delay in the time domain. Two novel CD estimation techniques are thus deduced, one which is based on the SCF and the other on the CAF. We investigate the limits of these techniques with respect to the RRC filter bandwidth, averaging window size, symbol-rate, as well as amount of cumulative dispersion. The amount of residual dispersion resulting from the imperfect estimation of CD at this stage and thus incomplete CD compensation at the static equaliser stage, has to be sufficiently reduced such that it can be further corrected within the digital coherent receiver DSP by the dynamic equaliser based on the CMA at no significant extra cost. As the number of taps within the dynamic equaliser needs to increase as the residual dispersion increases, we analyse the performance of the two CD estimators within a target RMSE of 200 ps/nm, which would limit the CMA number of taps required to compensate for it, to 2 for 10 GBaud and 12 for 40 GBaud, when the roll-off is 0.1. If this limit is relaxed to 400 ps/nm, then the required number of taps remains the same (2 taps) for 10 GBaud but more than doubles (22 taps) for 40 GBaud, leading to an undesired increased computational cost at higher data rates. Thus, in the following, we have restricted our requirements for the CD estimators to a RMSE of 200 ps/nm.

5.6.1 Spectral correlation function approach

The implementation of the proposed frequency-domain CD estimator is shown in Figure 5.47. Subsequent to the symbol-rate, roll-off and IF estimation, phase analysis of the first cyclic spectrum, as shown for example in Fig. 5.48, is used to estimate the amount of cumulative dispersion on the channel of interest. The classical PSD, when $\alpha = 0$, is real and therefore caries no phase information. The PSD when $\alpha = F_b$, on the other hand, is complex and its phase response is linear within the channel bandwidth. The slope of the phase is linearly proportional to the dispersion within the channel, and it is thus used to estimate the cumulative dispersion.

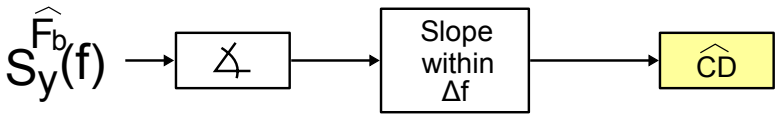

Figure 5.47: Implementation of the CD estimation technique based on the SCF.

CD is a linear fibre impairment which has a quadratic phase response, described by the transfer function:

$$H_{CD}(f) = e^{j\Psi f^2}, \tag{5.14}$$

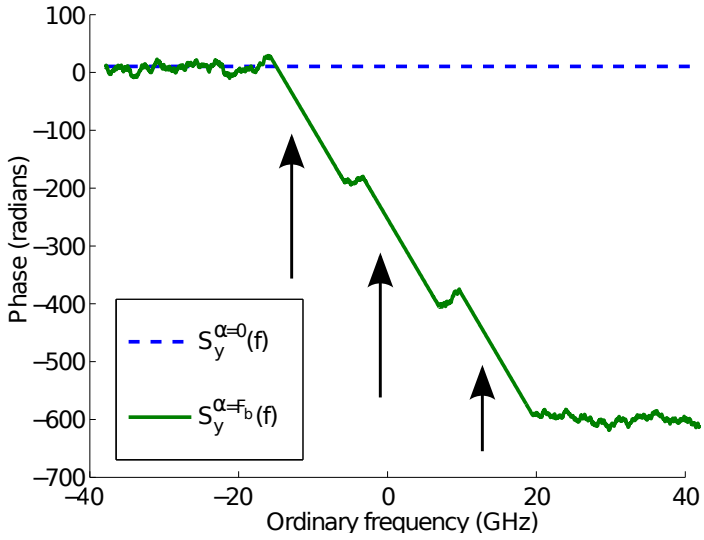

Figure 5.48: Phase measurement of the SCF of three 10 GBaud DP-16QAM channels, showing a linear response within the channel bandwidth when α equals the symbol-rate.

where $\psi = -\frac{\pi\lambda^2 DL}{c}$, with D dispersion coefficient, λ the reference wavelength, L fibre length and c the speed of light in vacuum.

The phase response of the cyclic spectrum when $\alpha = F_b$ is linear, as the transfer function of the channel (according to Gardner [1987] and as demonstrated in Appendix B) is given by:

$$\hat{H}_{CD}^{\alpha=F_b}(f) = H_{CD}(f+\frac{\alpha}{2}) \cdot H_{CD}^{*}(f-\frac{\alpha}{2}) = e^{j2\psi\alpha f} \tag{5.15}$$

The SCF of the signal is calculated as the frequency-smoothing cyclic periodogram:

$$\hat{S}_y^{\alpha}(f) = \lim_{\Delta f \to 0} \lim_{\Delta t \to \infty} \frac{1}{\Delta f} \int_{f-\frac{\Delta f}{2}}^{f+\frac{\Delta f}{2}} e^{j2\psi\alpha\nu}\ \hat{S}_{x_{\Delta t}}^{\alpha}(t,\nu)\, d\nu \tag{5.16}$$

where $y(t)$ is the received signal, after propagating through L km of fibre, $x(t)$ is the transmitted signal and $\hat{S}_{x_{\Delta t}}^{\alpha}(t,f)$ its cyclic periodogram.

Let m be the slope of the phase response of $\hat{S}_y^{\alpha=F_b}(f)$. In a back-to-back transmission, the slope m is zero. Otherwise, it increases proportionally with the amount of accumulated dispersion. The cumulative dispersion can thus be estimated as:

$$\hat{DL} = -\frac{m \cdot c}{2\pi\lambda^2\alpha} \tag{5.17}$$

In the following, unless otherwise stated, $N_{ADC} = 2^{19}$ samples and $w = 128$ samples are used as the total captured sample size and the moving-average size, in order to calculate the SCF, as these values enable a good performance of the SCF estimator. In the following subsections, the optimisation of the CD estimate is investigated.

Impact of phase slope measurement bandwidth

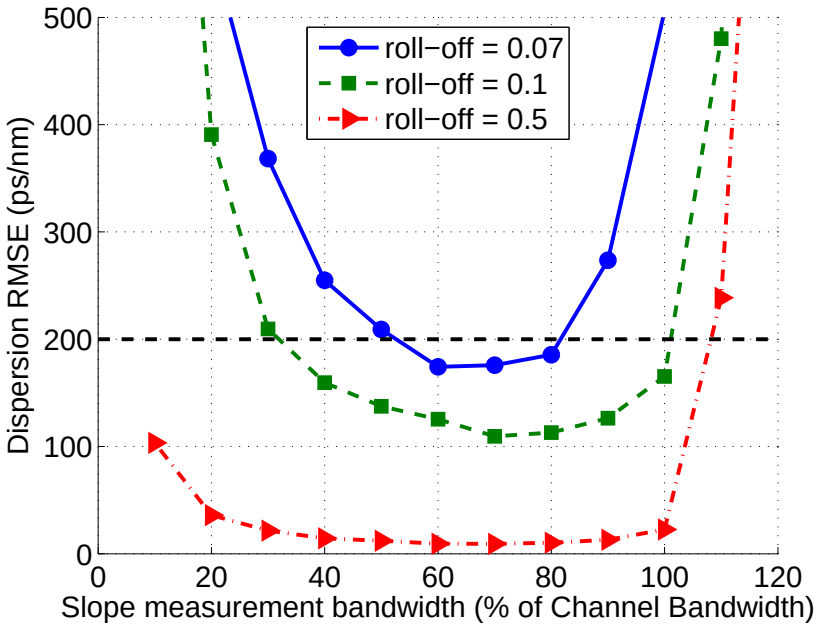

Figure 5.49: Impact of the slope measurement bandwidth on the CD estimation (simulation of three-channel 10 GBaud DP-16QAM WDM signal).

The phase measurement is ideally centred around the channel bandwidth, and for that reason the frequency offset information is required. However, because the proposed IF estimator presented in the previous section is coarsely accurate, the phase measurement is restricted over a fraction of the bandwidth of the cyclic spectrum. This choice enables the tolerance of higher frequency offset errors, but limits the performance of the CD estimator at very low symbol-rates or pulse shaping bandwidths.

For a fixed transmission distance of 2421 km or fixed cumulative dispersion of 40,624 ps/nm, we investigated the impact of the slope bandwidth on the CD estimation. Fig. 5.49 demonstrates that the optimum bandwidth over which the slope is measured for the estimation of dispersion is between $60\% - 80\%$ of the channel bandwidth measured in the cyclic spectrum (which is given by the symbol-rate – roll-off product). Such a setup will impose a limit of 200 ps/nm residual dispersion RMSE for roll-offs of at least 0.07. As the RRC excess bandwidth tends towards zero, the CD estimator based on the SCF fails to perform within this error margin. For all of the following results, the estimation slope will be restricted to 70% of the cyclic spectrum bandwidth, namely: $0.7 \cdot F_b \cdot r$.

Impact of frequency offset

Previously, in Section 5.5, a novel method for coarsely estimating the frequency offset between the transmitter laser and local oscillator has been proposed and demonstrated. One principal motivation for it was to aid the CD estimator, by giving an approximation of the deviation from the expected frequency grid of the channel, such that the slope measurement can be correctly confined to the channel bandwidth.

The benefit of the proposed IF estimation on the CD estimator is evident in Fig. 5.50. If frequency offset estimation is absent, and the SCF phase slope is measured around DC, the CD estimation will be strongly influenced by the IF value. In particular for the lower roll-off factors, the larger frequency offsets will easily shift the channels away from the 70% slope measurement bandwidth centred at DC, making it impossible for the algorithm to measure the slope correctly. In fact, when the roll-off is 0.07, frequency offsets of more than approximately 25 MHz will increase the CD estimation's RMSE above 200 ps/nm. A coarse knowledge of the IF value is thus required, as it enables the estimation of dispersion, within the target error limit of 200 ps/nm, for IF values even as high as 1 GHz.

It is interesting to note here that, at higher bandwidths, the IF estimation errors increase, but the CD estimator becomes more tolerant. This is a consequence of restricting the bandwidth of measurements over 70% of the channel bandwidth, which allows more variability along the frequency axis, as induced by higher frequency offset errors.

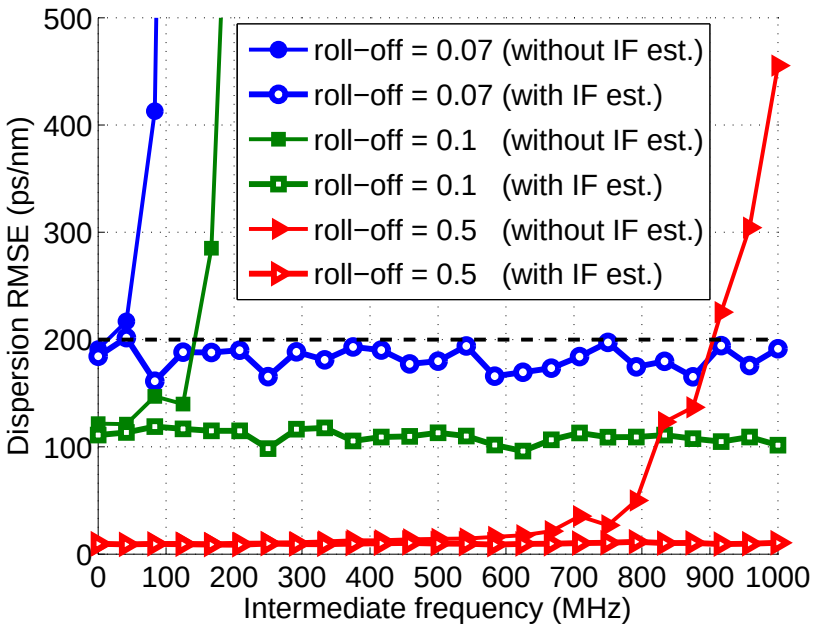

Figure 5.50: Impact of frequency offset on the CD estimation (simulation of 10 GBaud WDM signals formed of three channels and modulated with DP-16QAM).

Impact of signal bandwidth

Unlike the IF estimation, the errors of the CD estimation decrease as the channel bandwidth increases, because more points can be used in measuring the dispersion slope, leading to a more accurate measurement. The minimum roll-offs to ensure a RMSE of 200 ps/nm are approximately 0.066 and 0.01, for 10 GBaud and 40 GBaud respectively. At lower symbol-rates, such as 2.5 GBaud, even a roll-off factor of 0.5 is not sufficiently high to ensure operation within the same error limit.

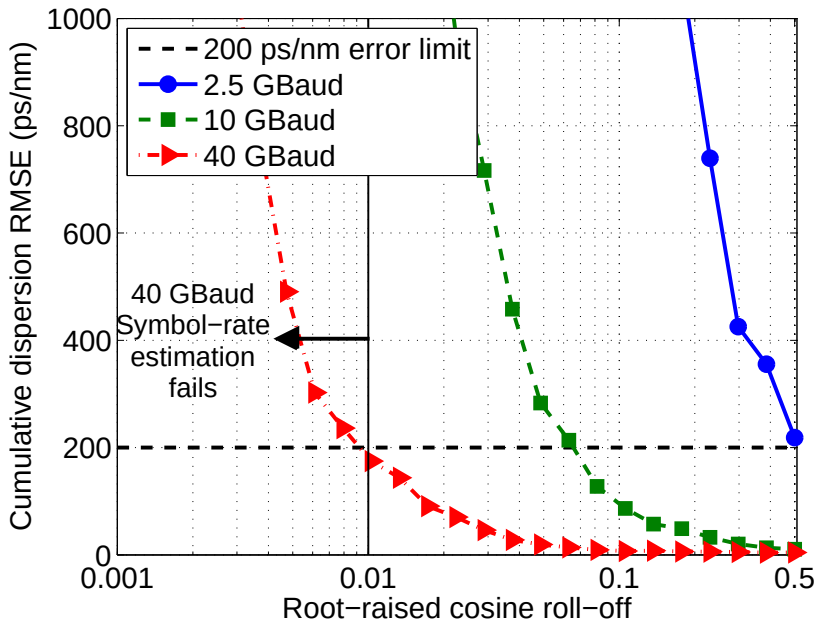

Figure 5.51: Simulation of impact of RRC filter roll-off on the CD estimation (DP-16QAM).

Impact of the frequency smoothing window

The frequency smoothing stage within the SCF measurement, enhances the correlation between frequency components at a difference equal to the symbol-rate from each other, by averaging the phase noise contributions of the cyclic periodogram.

Figures 5.52 − 5.54 show the impact of different frequency smoothing window sizes on the CD estimator for three symbol-rates (2.5 GBaud, 10 GBaud and 40 GBaud) and three roll-offs (0.01, 0.1 and 0.5). All cases show a similar trend, that the CD can be closely tracked, before the correlation between frequencies that are separated by exactly $\alpha = F_b$ walk off from each other, under the impact of dispersion, slowly reducing the correlation power. This concept has been introduced in Section 5.3.1 as *spectral correlation fading*, which explains here the sudden drops in dispersion estimation performance, when the phase offset introduced by dispersion is so high that it completely de-correlates the otherwise correlating frequencies.

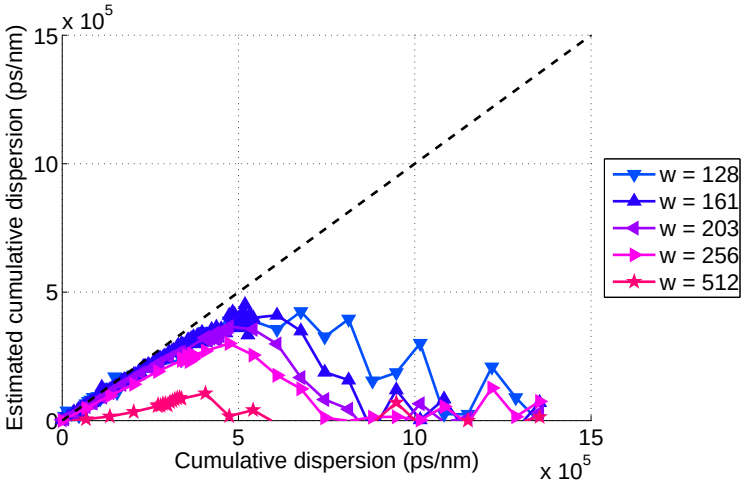

(a) 2.5 GBaud, roll-off = 0.01.

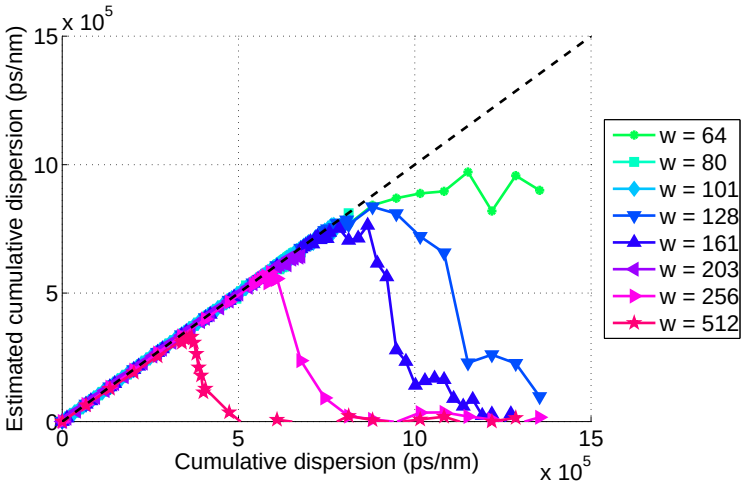

(b) 2.5 GBaud, roll-off = 0.1.

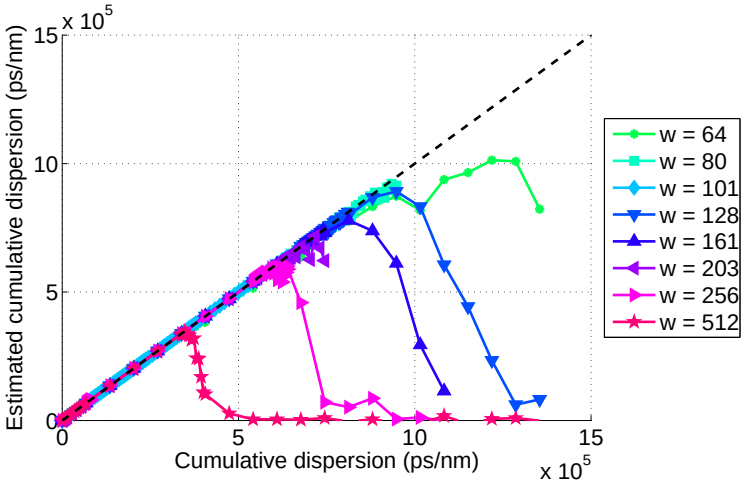

(c) 2.5 GBaud, roll-off = 0.5.

Figure 5.52: Impact of frequency smoothing window on the CD estimation, when simulating three 16-QAM channels, each of 2.5 GBaud symbol-rate.

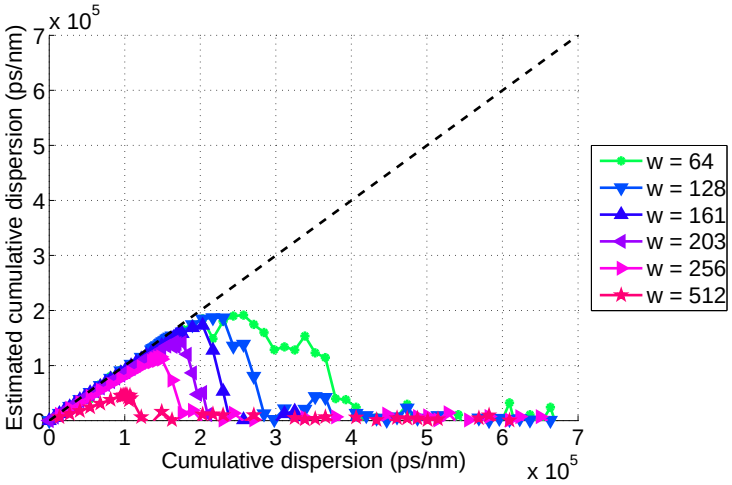

(a) 10 GBaud, roll-off = 0.01.

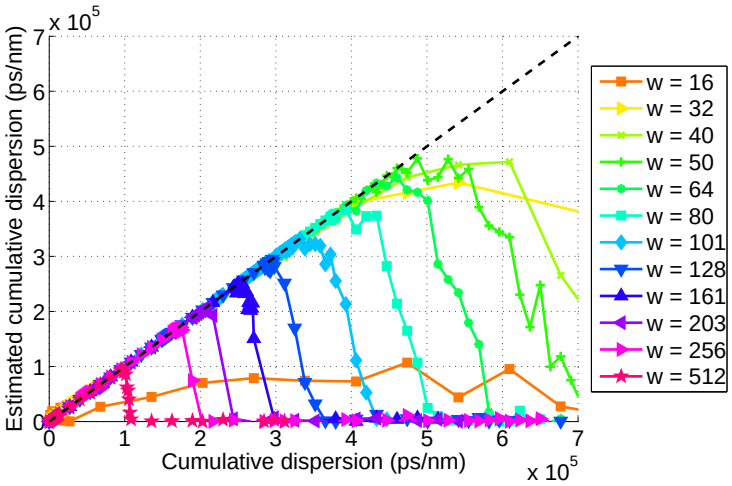

(b) 10 GBaud, roll-off = 0.1.

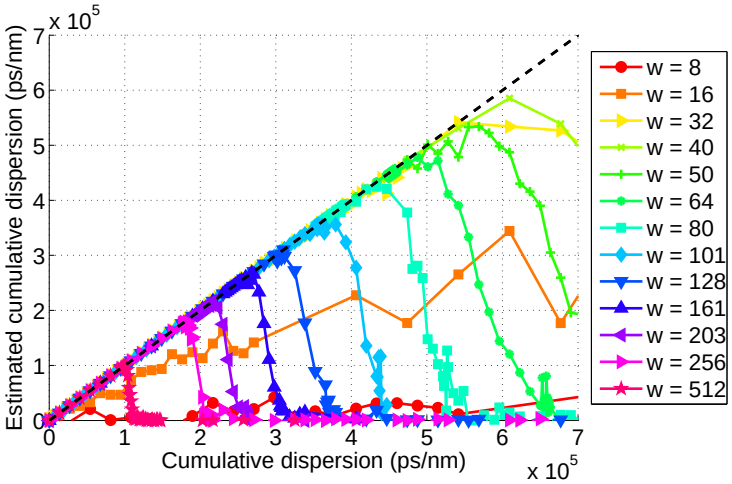

(c) 10 GBaud, roll-off = 0.5.

Figure 5.53: Impact of frequency smoothing window on the CD estimation, when simulating three 16-QAM channels, each of 10 GBaud symbol-rate.

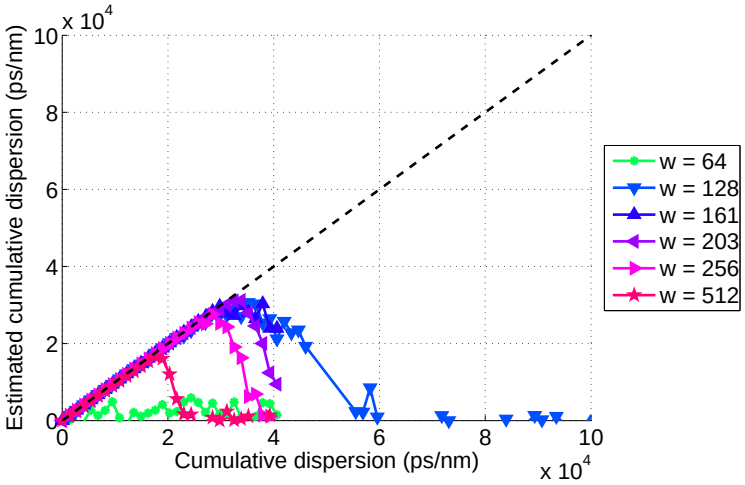

(a) 40 GBaud, roll-off = 0.01.

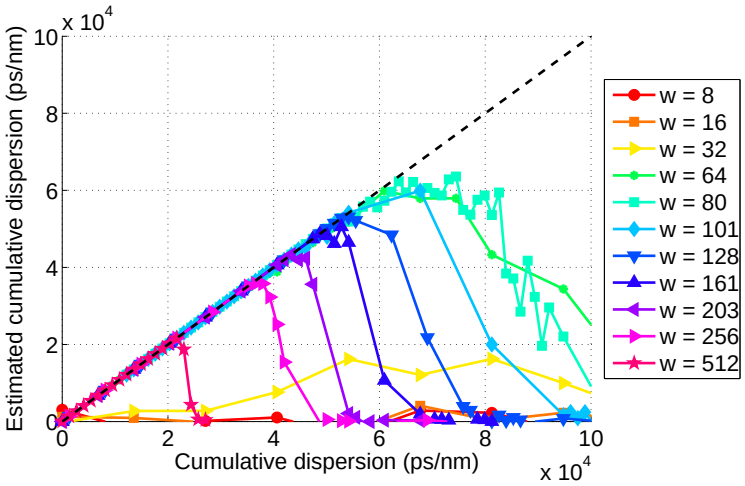

(b) 40 GBaud, roll-off = 0.1.

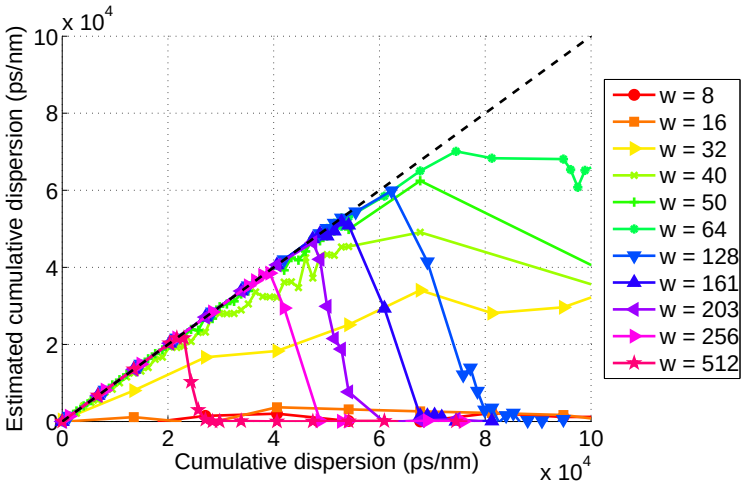

(c) 40 GBaud, roll-off = 0.5.

Figure 5.54: Impact of frequency smoothing window on the CD estimation, when simulating three 16-QAM channels, each of 40 GBaud symbol-rate.

For each combination of symbol-rates and roll-offs there is an optimum range of window sizes that can ensure CD tracking capability with a RMSE below 200 ps/nm, shown in Figure 5.55. These results have been obtained assuming knowledge of symbol-rate and roll-off. If these two parameters are estimated within the proposed joint estimator, the upper distance limits will be given by the interposition with those in Figure 5.24.

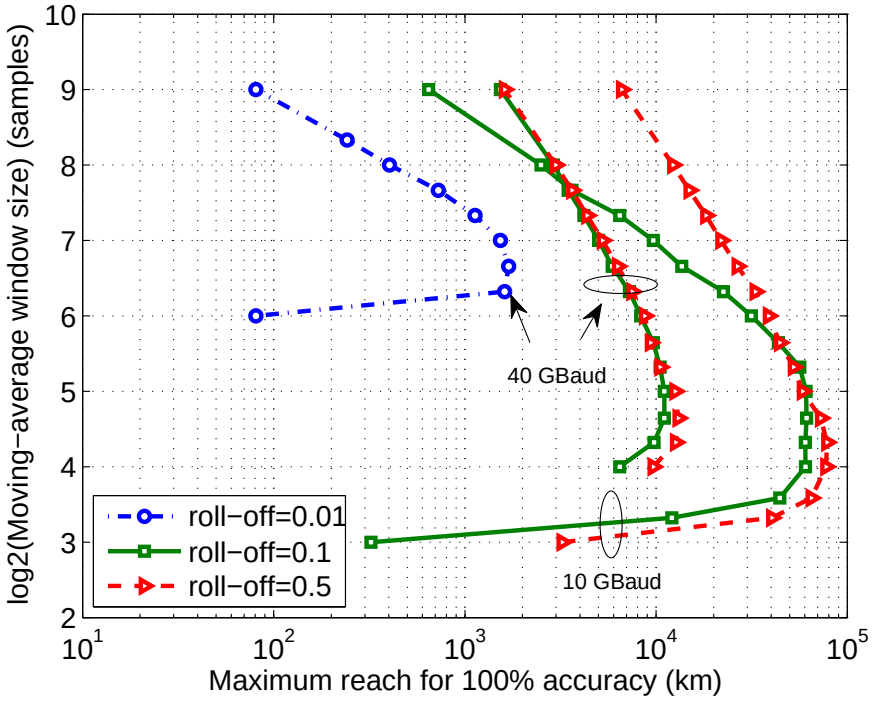

Figure 5.55: Maximum achievable distance limited by the accuracy of the CD estimation, after simulating three-channel 16-QAM WDM signals, without any linear ICI.

The number of averages must greatly exceed unity, to satisfy Grenander's condition (Eq. 3.25) for a good spectral estimate. As the window size increases, more averages are performed within the channel bandwidth, giving an improved slope measurement, and therefore an increased CD estimation range. However, if the moving average is too high, it will include more noise components than signal phase components, and thus the cyclic correlation will be lost, reducing the maximum CD value that can be correctly estimated. This effect is more obvious for narrower channel bandwidths, for example 40 GBaud signals with 0.01 roll-off and 10 GBaud signals with 0.1 roll-off. A trade-off must be attained, for optimising the correlation of symbol phases.

If the symbol-rate and the roll-off factor are either known or estimated a priori, then the SCF can be recalculated with the optimum frequency smoothing window, such that the CD estimation performance is optimal, based on these results. However, for a reduced computation speed, it is preferable to use the pre-computed SCF from the symbol-rate estimation stage. Averaging 128 samples (or equivalently, 19.53 MHz

for an 80 GSa/s sampling rate), is optimal in terms of the maximum reach across all considered combinations of symbol-rates and roll-offs, matching well with the frequency smoothing requirements of the symbol-rate estimator.

CD estimation with 200 ps/nm is completely unreliable for the lowest considered bandwidths, when the symbol-rate is 2.5 GBaud or the symbol-rate is 10 GBaud and the roll-off 0.01. The cumulative dispersion estimation range increases proportionally with the signal bandwidth, as shown in Fig. 5.55.

Estimation range

The errors increase with distance, Fig. 5.56, as a result of the fixed frequency smoothing filter. For an increased estimation range, the filter length should decrease to adapt to the phase slope increase. However, this is not possible, as the filter size is fixed without a priori knowledge of the distance. Alternatively, the estimation range can be further increased if the error margin is relaxed. For example, for a dispersion error margin of 400 ps/nm, a roll-off factor of 0.1 and 10 GBaud symbol-rate, approximately 338,620 ps/nm (20,180 km) of cumulative dispersion can be estimated with this technique. With the same configuration, the 200 ps/nm residual dispersion target is achieved only up to a total cumulative dispersion of 162,498 ps/nm (9,684 km).

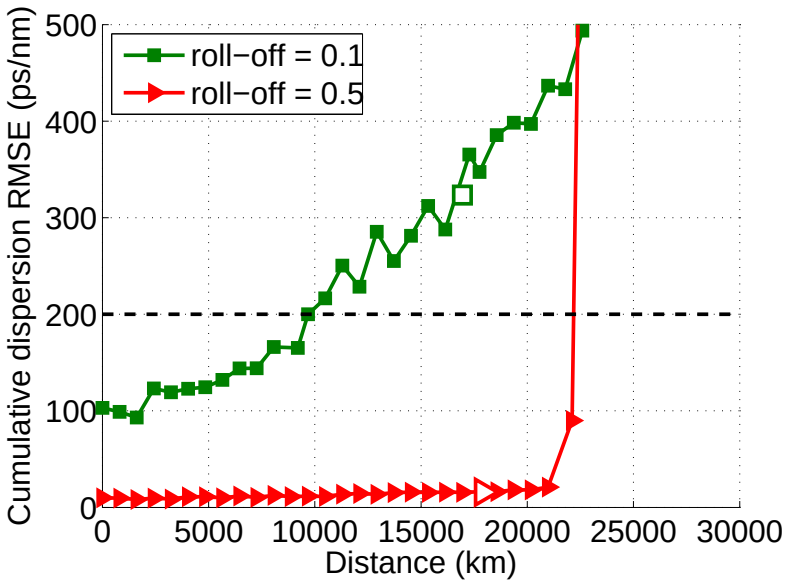

Figure 5.56: Estimation range limitations of the CD estimation, for three channels modulated with 10 GBaud 16-QAM. The hollow marks indicate the maximum length up to which the symbol-rate can be estimated by simulation with 100% accuracy.

Independence of OSNR

The experimental investigation of Fig. 5.57 shows that AWGN does not have an impact on the CD estimator. The residual CD resulting from the estimator is less than 200 ps/nm for the QPSK signal transmitted over 25 spans of fibre, compared to 140 ps/nm for 16-QAM over 10 spans. The reason for the higher errors for the former case can be accounted for by the higher CD estimation errors at longer transmission distances and lower roll-offs. The residual errors correspond to 14.9 km and 10.1 km of uncompensated fibre respectively, less than 1.3% of the considered fibre lengths. Such low residual CD values can be compensated for by the adaptive equaliser stage which follows the CD static equaliser.

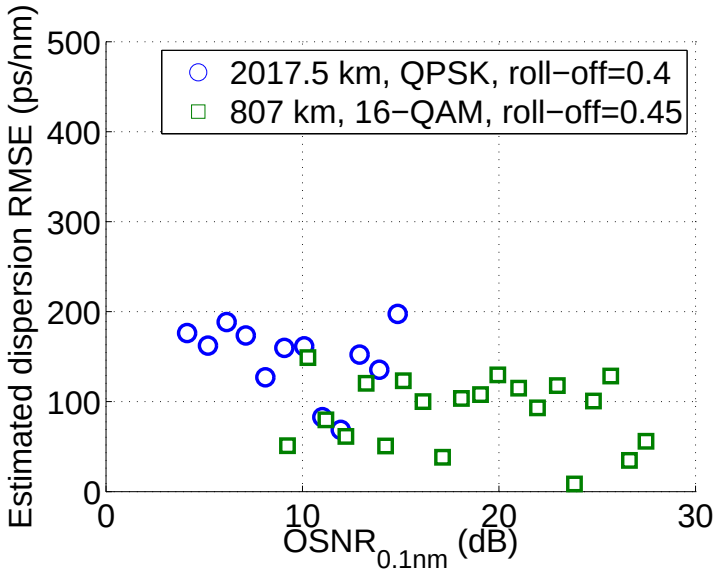

Figure 5.57: Experimental estimation of CD applied to a 10 GBaud homogeneous WDM signal, under different levels of noise loading.

In this section it has been demonstrated that the proposed frequency-domain CD estimation technique yields a better performance as the channel bandwidth increases, which more easily enable a correct slope measurement of the phase response. In order to deal with RRC filtering effects and the impact of IF, the bandwidth over which the phase slope is measured was optimally selected as 70% of the cyclic spectrum's channel bandwidth. $N_{ADC} = 2^{19}$ samples and 128 moving average taps, which give a good symbol-rate estimation as seen previously in Subsection 5.3, can also give a good CD estimate up to 162,498 ps/nm (9,684 km of SSMF), for 10 GBaud and 0.1 roll-off factor, limited by 200 ps/nm RMSE. With this technique, it is possible to increase the symbol-rate whilst minimising the roll-off factor, thus allowing operation at an improved spectral efficiency. As shown here, 40 GBaud WDM channels, filtered with a RRC roll-off of 0.01, allow a CD estimation of up to 27,083 ps/nm (1614 km of SSMF), within a RMSE margin of 200 ps/nm.

5.6.2 Cyclic autocorrelation function approach

Subsequent to symbol-rate estimation, the CAF at the cyclic frequency equal to the symbol-rate measures a pulse, which has a time-lag delay proportional to the amount of dispersion the signal has accumulated on its path. The pulse measured at cyclic frequency of zero, does not experience such a shift and it therefore does not provide useful information for the CD estimation technique. The examples in Figure 5.58 show the two pulses without any dispersion and after the signal has travelled over 2421 km. The time domain CD estimation problem thus reduces to estimating the time delay of the cyclic autocorrelation pulse. Lowering the RRC excess bandwidth reduces the cyclic autocorrelation tone peak power as the pulse spreads. Nyquist pulse shaping is a major limitation of this proposed CD estimation technique.

The proposed time-domain cyclostationarity approach for the estimation of dispersion is illustrated in Fig. 5.59. The cyclic autocorrelation at $\alpha = F_b$ is easily extracted as once slice of the cyclic periodogram, followed by an IFFT operation along the ordinary frequency. The details of this implementation can be found in Section 5.2.

The time delay is approximated as follows: the pulse peak location gives an initial coarse delay estimate, which is dependent on the sampling rate of the receiver. To refine this estimate, a brick wall filter is applied around the peak to limit the sample size to 1001 samples, for an enhanced processing speed. These selected samples are then further filtered with a moving average filter which will result in a smoothed pulse. Finally, the quadratic fit of the central 150 samples are used to obtain an improved time delay approximation, which is then used to estimate the cumulative dispersion as:

$$\hat{DL} = \frac{\hat{\Delta\tau} \cdot c}{\hat{F_b} \cdot \lambda^2}. \tag{5.18}$$

where $\hat{\Delta\tau}$ is the estimated time delay, c is the speed of light in vacuum, $\hat{F_b}$ is the symbol-rate estimate and λ is the reference wavelength. The mathematical proof of the time-domain cyclostationarity properties under the impact of dispersion can be found in Appendix C. The number of samples used in this process have been empirically selected when investigating the performance of the CD estimation technique, for the ranges of symbol-rates and roll-offs considered. As a result, this estimator is independent of the roll-off factor and IF, but it will be shown further that it depends on the symbol-rate.

A moving average window of approximately 64 samples is optimal for estimating the dispersion within the target error, but only for roll-offs higher than 0.1, as shown in Fig. 5.61. As the cyclic autocorrelation pulse is lost for roll-offs of 0.01 or lower, the CD estimation cannot be performed in those instances.

Fig. 5.62 shows that the pulse time delay, as deducible from Eq. 5.18, is indeed proportional to dispersion and that it can be correctly measured by simulation, by means of the technique just described.

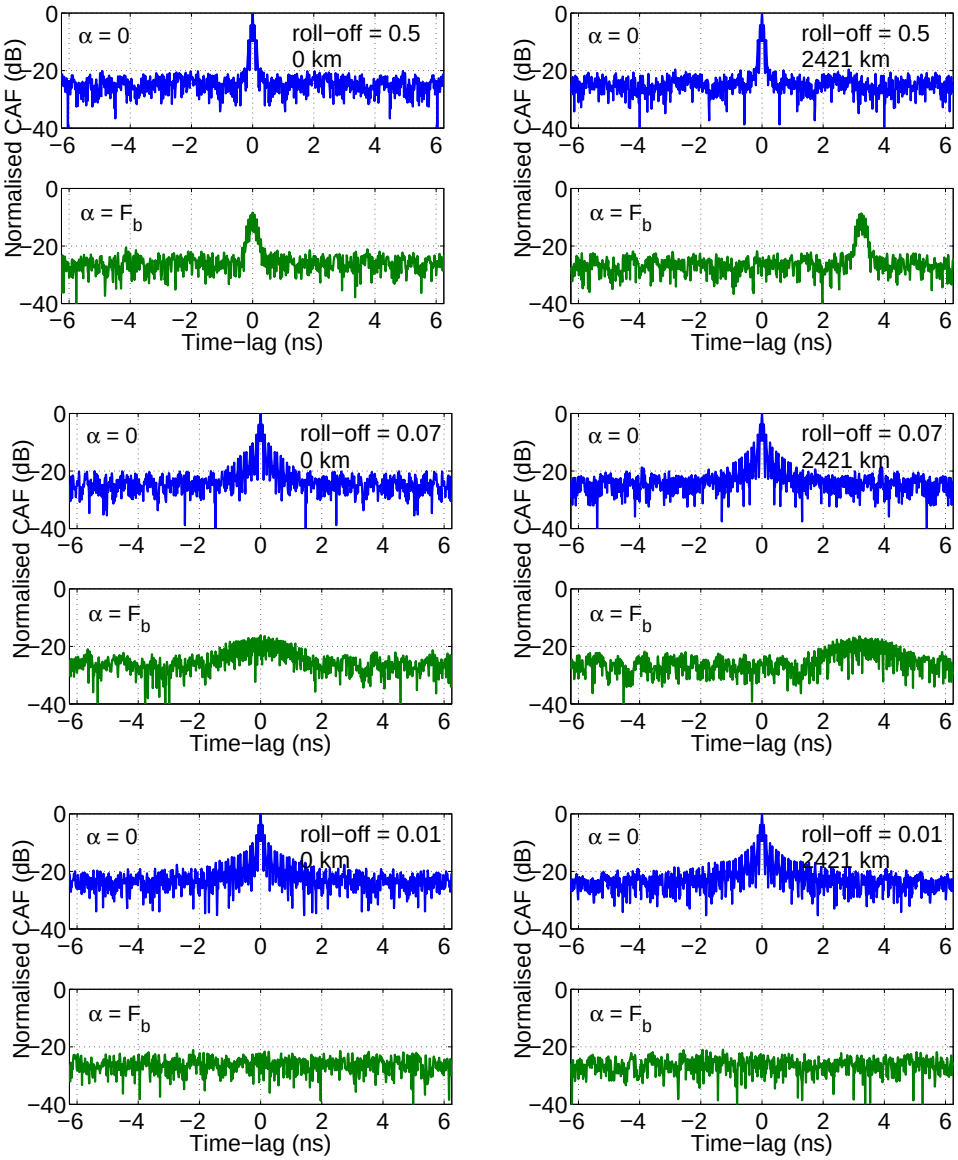

Figure 5.58: CD induces a time-shift in the CAF when $\alpha = F_b$. 10 GBaud for all three simulated 16-QAM channels. Correlation does not occur for a roll-off of 0.01.

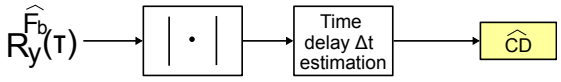

Figure 5.59: Implementation of the time-domain CD estimator.

Dependence on signal bandwidth

Fig. 5.63 shows the dependence of the estimator on the Nyquist pulse shaping bandwidth. 2.5 GBaud is the lowest symbol-rate considered and can only enable CD estimation within the proposed error limit, if the roll-off factor is larger than 0.41. As the symbol-rate is increased, the tolerance and performance of the CD estimator with respect to the roll-off factor improves. This is because signals of higher bandwidths have sharper

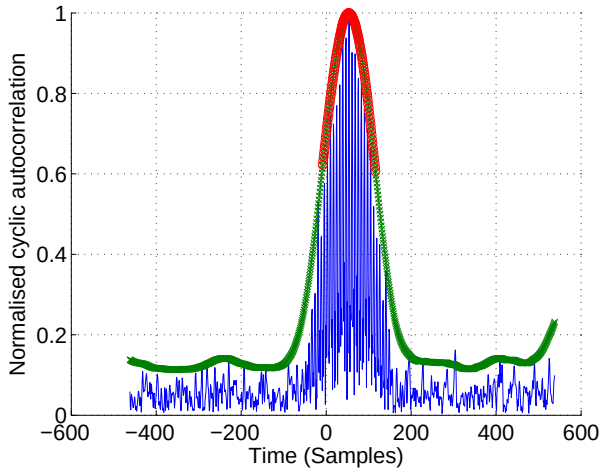

Figure 5.60: The CAF at the symbol-rate is a pulse that shifts in time with dispersion. Here, for a 10 GBaud signal and a roll-off of 0.1, a 500 km transmission is equivalent to a delay of 53.752 samples. In (blue) actual measured pulse limited to 1001 samples, (green) temporal smoothing with a moving average filter, (red) quadratic fit.

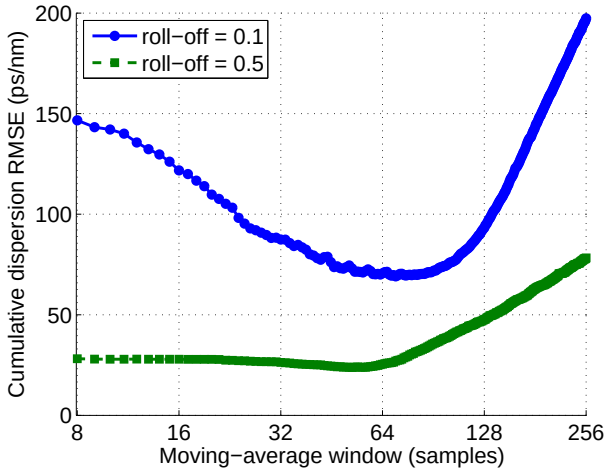

Figure 5.61: Simulation of the impact of the time-domain moving average filter window on the CD estimation. Low roll-offs, such as 0.01, render the method impractical at any window.

pulses in the time-domain, for which the time delay can be more easily determined. Additionally, the same time-delay errors translate into smaller CD estimation errors at higher symbol-rates, as Eq. 5.18 and Figure 5.64 suggest.

At 10 GBaud, the minimum roll-off is approximately 0.069, for a RMSE of 200 ps/nm. Under the same conditions, 40 GBaud signals could allow roll-offs as low as 0.0178, the lowest roll-off compared to the other two considered rates, so it can be concluded that this technique becomes more efficient as the information spectral density of the signal increases.

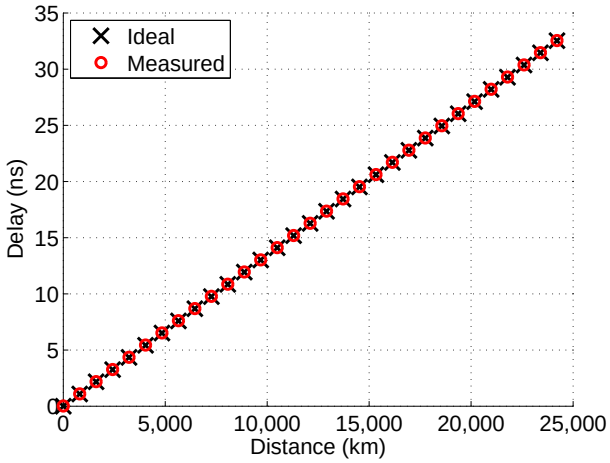

Figure 5.62: The time-domain cyclic correlation pulse experiences a time delay proportional to the amount of cumulative dispersion present in the signal. Simulations of 10 GBaud signals, modulated with 16-QAM and filtered with a RRC of roll-off of 0.1.

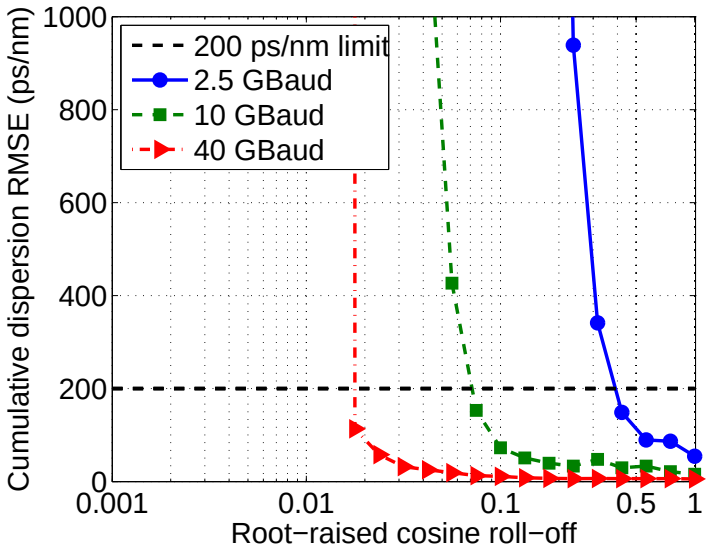

Figure 5.63: Impact of the RRC filter on the estimation of 40,624 ps/nm dispersion (simulations of three channels modulated with DP-16QAM).

Estimation range

As CAF pulses shift in time proportionally with the amount of dispersion accumulated by the signal, the CD estimation range is only limited by the capture time at the receiver, provided that the symbol-rate is correctly estimated. The estimation does not exceed 200 ps/nm RMSE across a wide range of fibre lengths, roll-offs as Figure 5.65 shows. The maximum cumulative dispersion values that can be correctly estimated with this technique ranges between 10^6 and 10^7 ps/nm, which are equivalent to over 60,000 km to 600,000 km of SSMF respectively. These distances are by far exceeding the practically achievable distances at the respective transmission configurations.

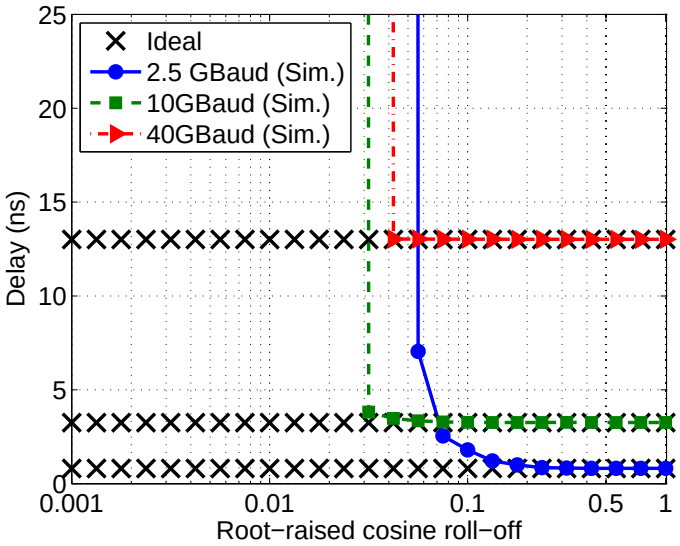

Figure 5.64: The estimation accuracy of the pulse time delay is impacted by the roll-off factor. The amount of cumulative dispersion is fixed to 40,624 ps/nm (2421 km of SSMF), but the time delay changes with the symbol-rate.

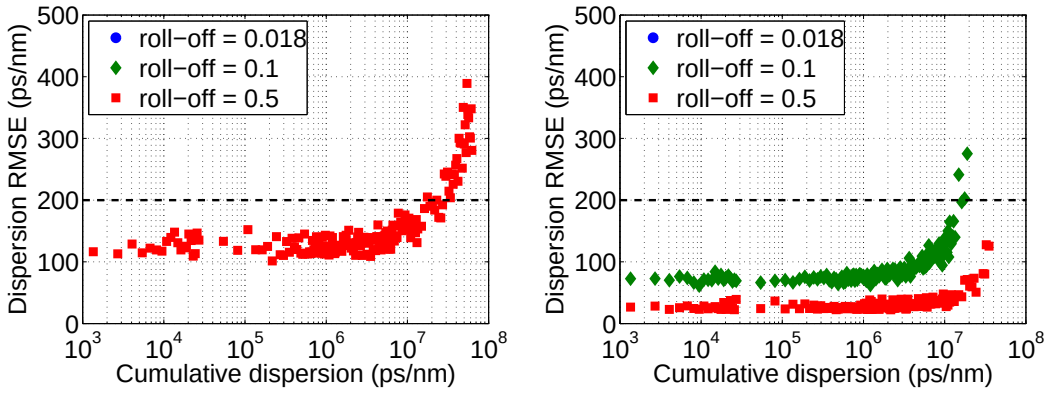

(a) 2 GBaud, 3 channels 16-QAM.

(b) 10 GBaud, 3 channels 16-QAM.

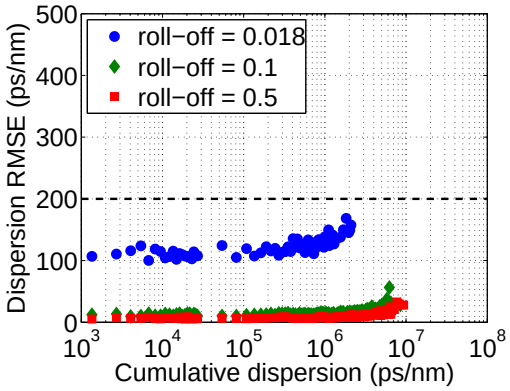

(c) 40 GBaud, 3 channels 16-QAM.

Figure 5.65: Estimation of CD by means of CAF, applied to homogeneous WDM signals traversing different lengths of SSMF fibre, by simulation.

Figure 5.66 shows that the technique works experimentally for 16-QAM and QPSK modulation formats, independent of the OSNR value at the receiver. The errors are not exceeding 200 ps/nm when transmitting over 2018 km of fibre and 807 km (QPSK and 16-QAM respectively), but these could in essence be compensated for by the dynamic equaliser.

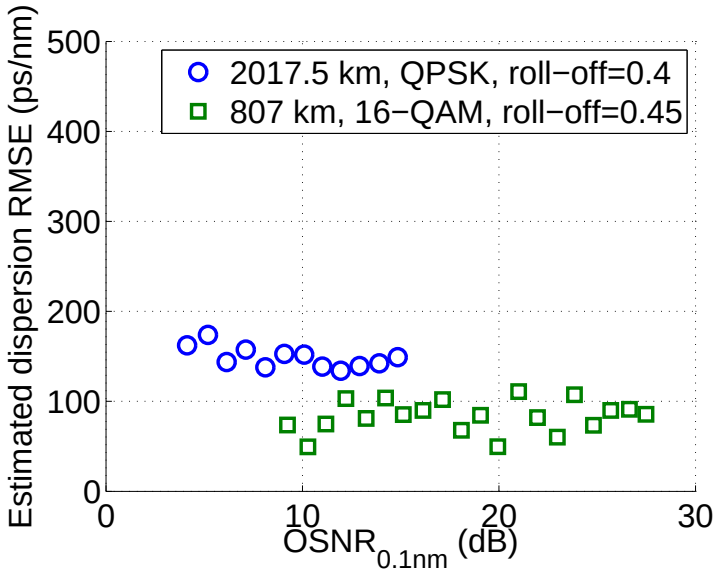

Figure 5.66: Experimental estimation of CD applied to a 10 GBaud homogeneous WDM signal, under different levels of noise loading.

5.6.3 Comparison between the time domain and frequency domain chromatic dispersion estimators

This section demonstrated by simulation and experimentally the feasibility of time and frequency domain CD estimators, based on the cyclostationarity properties of modulated signals. Although based on the same statistical properties, the differing implementation approaches between the two functions result in performance differences in terms of dispersion estimation range or bandwidth requirements.

The SCF is computed as the frequency averaged cyclic periodogram, whilst the CAF is the IFFT of the cyclic periodogram. Frequency averaging performed with a moving average filter introduces correlation fading and therefore a decrease in performance with an increase in dispersion. Unlike the CD estimator based on the SCF, the CAF implementation can allow under 200 ps/nm RMSE up to 2,098,926 ps/nm cumulative dispersion (equivalent to 125,085 km of SSMF) when the symbol-rate is 40 GBaud and the roll-off factor is 0.018, This is a consequence of the robustness of the CAF, which is practically CD independent as Section 5.3.2 demonstrated. The maximum cumulative dispersion that can be estimated with either technique varies with signal bandwidth, as

listed in Table 5.8.

The preceding symbol-rate, roll-off and frequency offset estimates are needed for this CD estimation stage, when the SCF is used. The CAF approach requires only knowledge of the symbol-rate.

The two techniques show a similar behaviour with respect to channel bandwidth, both requiring larger bandwidths for an increased estimation accuracy, as summarised in Table 5.9. The SCF performs slightly better as the symbol-rate increases, allowing slightly lower roll-off values.

Computationally, the two approaches are very similar, as the dominating complexity comes from the correlation functions, which both require $N_{ADC} \log_2 N_{ADC}$ complex multiplications. Both techniques are independent of impairments such as AWGN, transmitter and LO phase offset and phase noise.

It can be concluded that the frequency-domain implementation of the CD estimator is preferable, as its performance improves with respect to pulse shaping excess bandwidth limitations, as the symbol-rate increases.

Spectral Correlation Function

Symbol-rate (GBaud)	Maximum achievable range (ps/nm)		
	roll-off = 0.01	roll-off = 0.1	roll-off = 0.5
2.5	–	–	–
10	–	1,313,522	1,027,797
40	27,083	185,518	219,372

Cyclic Autocorrelation Function

Symbol-rate (GBaud)	Maximum achievable range (ps/nm)		
	roll-off = 0.0178	roll-off = 0.1	roll-off = 0.5
2.5	–	–	1,614,000
10	–	16,249,752	35,207,796
40	2,098,926	8,531,120	9,343,607

Table 5.8: Maximum achievable cumulative dispersion estimation with RMSE under 200 ps/nm, for the two proposed chromatic dispersion estimators, based on the Spectral Correlation and on the Cyclic Autocorrelation Functions.

Symbol-rate	Minimum allowable RRC roll-off	
	SCF-CDE	CAF-CDE
2.5 GBaud	>0.5	0.4121
10 GBaud	0.066	0.0692
40 GBaud	0.0092	0.0178

Table 5.9: Bandwidth requirements for the two proposed chromatic dispersion estimators, based on the Spectral Correlation and on the Cyclic Autocorrelation Functions.

5.7 In-band OSNR estimation

Using the different statistical properties of linearly modulated signals, which are wide-sense cyclostationary, and AWGN, which is wide-sense stationary, it is possible to estimate the in-band OSNR, as demonstrated herein.

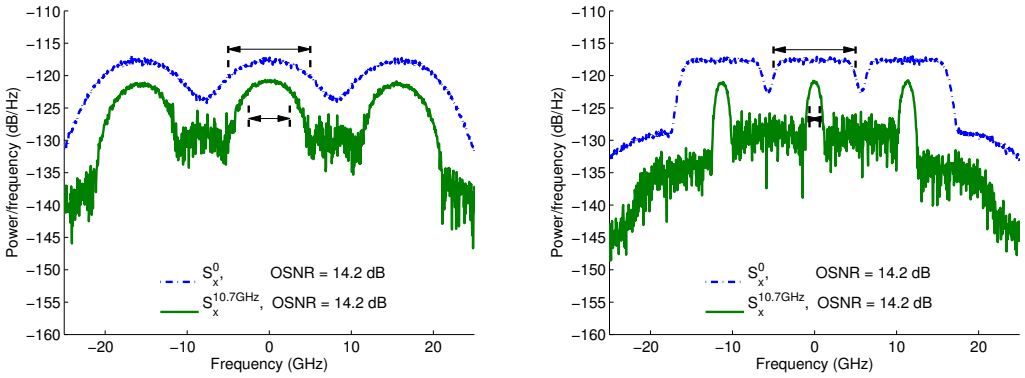

(a) roll-off of 1 (b) roll-off of 0.25

Figure 5.67: Spectral Correlation Functions calculated for three simulated WDM channels, modulated at 10GBaud with DP-16QAM and Nyquist pulse-shaping. The arrows delimit the bandwidths over which the powers are integrated.

As Fig. 5.67 shows, when $\alpha = 0$ the SCF is the traditional power spectral density of the signal with additive noise. Conversely, the cyclic spectral density when $\alpha = F_b$ measures the signal power only, since AWGN is not a cyclostationary process and it will not correlate at this cyclic frequency. The OSNR can thus be estimated from the two SCFs: $\hat{S}_x^{\alpha=0}(f)$ and $\hat{S}_x^{\alpha=F_b}(f)$. In a noise-free measurement, the two cyclic spectra will differ by a scaling factor k, which needs to be pre-calculated as part of a calibration stage. When the signal is noise-loaded, the average powers $P_{ave}^{\alpha=0}$ and $P_{ave}^{\alpha=F_b}$ are calculated over fixed bandwidths, corresponding to both SCFs.

Assuming a fixed signal launch power, but varying optical paths and therefore varying accumulated noise levels, $P_{ave}^{\alpha=0}$ decreases with OSNR, whilst $P_{ave}^{\alpha=F_b}$ is approximately constant over the entire OSNR interval. At lower OSNRs, there is however a slight increase in $P_{ave}^{\alpha=F_b}$ with noise. This is due to the fact that both $S_x^{\alpha=0}(f)$ and $S_x^{\alpha=F_b}(f)$ scale with noise power, in the same proportion that the autocorrelation of noise scales with noise power. When the OSNR is very low, below 5 dB, the high noise power becomes a significant term in $S_x^{\alpha=F_b}(f)$.

These power measurements finally lead to the OSNR estimate:

$$OSNR = 10log_{10}\left(\frac{kP_{ave}^{\alpha=F_b}}{kP_{ave}^{\alpha=0} - kP_{ave}^{\alpha=F_b}}\frac{B_{res}}{B_{ref}}\right). \tag{5.19}$$

B_{res} and B_{ref} are the resolution and reference bandwidths respectively.

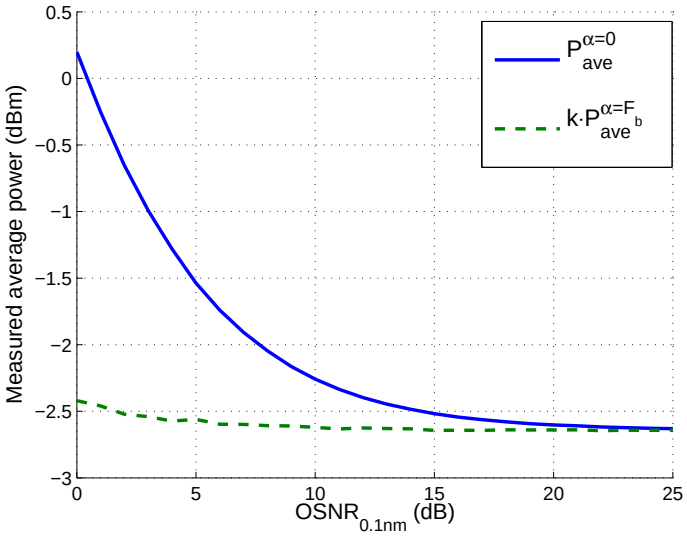

Figure 5.68: SCF power measurements at cyclic frequencies of 0 and symbol-rate.

A correct estimation of the OSNR is thus directly dependent on a correct estimation of the two average powers $P_{ave}^{\alpha=0}$ and $P_{ave}^{\alpha=F_b}$. In order to improve the estimate, the OSNR is averaged between the two polarizations. A schematic of the digital implementation of this technique is depicted in Fig. 5.69. After CD compensation, which is required to avoid power fading, the SCF is recalculated for only two cyclic-frequencies, at 0 and at the estimated symbol-rate.

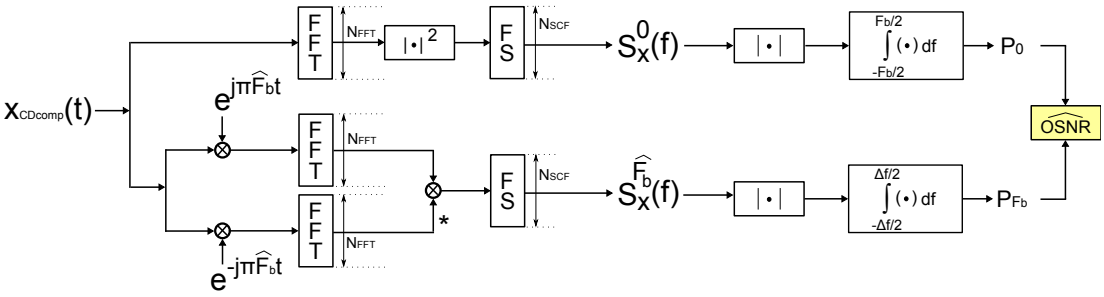

Figure 5.69: Single polarisation implementation of the SCF-based OSNR estimation.

In the two examples of Fig. 5.67, three 10 GBaud 16-QAM WDM channels are spaced at 12.5 GHz and are Nyquist pulse-shaped with a RRC filter of roll-off of 0.25 and 1 respectively. When ICI is present, as in this case, the powers are measured over restricted bandwidths, less than the entire bandwidth of the channel of interest, in order to avoid power measurements of the adjacent channels, which would in turn result in an overestimation of the signal power. At higher symbol-rates, if the bandwidth of the channel would exceed the receiver bandwidth, then the powers would be integrated over the entire receiver bandwidth. The average powers $P_{ave}^{\alpha=0}$ and $P_{ave}^{\alpha=F_b}$ were measured over F_b and $F_b\frac{roll-off}{2}$ bandwidths respectively. Finally, the OSNR was estimated according to Eq. (5.19), with a 10 GHz resolution bandwidth and 0.1 nm reference bandwidth.

5.7.1 Back-to-back Transmission

Figures 5.70 and 5.71 show the range over which the OSNR can be estimated within the acceptable error margin, for a fixed RRC roll-off, in a back-to-back setup. At higher OSNRs, low noise powers are more difficult to estimate, resulting in a limited estimation accuracy for higher OSNRs. A correct estimation is achieved up to 12 dB OSNR for DP-QPSK and up to 16 dB OSNR for DP-16QAM. Since the ROSNR is 7.6 dB for 10 GBaud DP-QPSK and 14.2 dB for 10 GBaud DP-16QAM, the range of correct estimation includes the ROSNR by a margin.

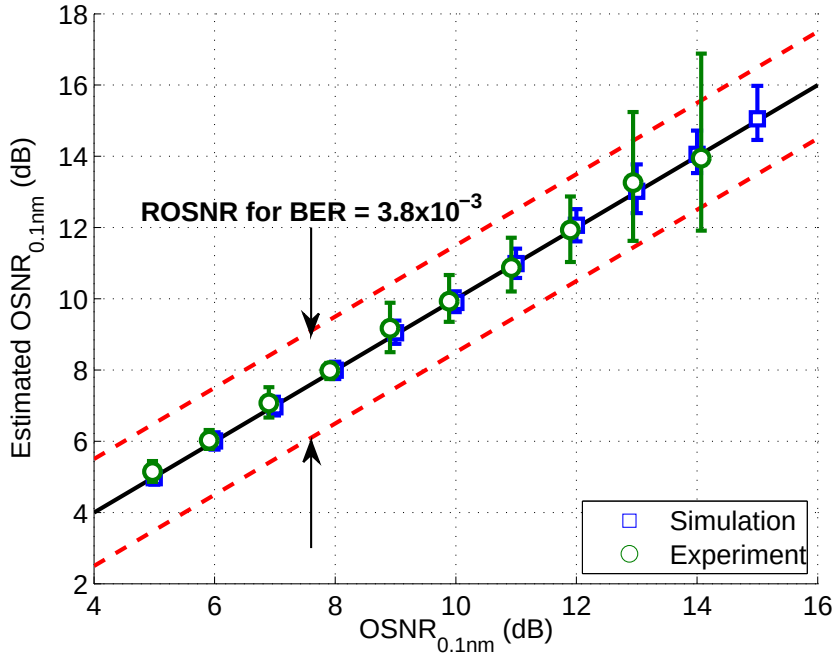

Figure 5.70: OSNR estimation for DP-QPSK in a back-to-back setup and a RRC roll-off of 0.4.

Since 16-QAM operates at higher OSNRs, the receiver's noise starts to become limiting from around 19 dB OSNR. The calibration of noise-free estimation is more sensitive for 16-QAM compared to QPSK, and in estimating the same OSNR, the errors will be higher than in the case of QPSK, despite the fact that the method is independent of modulation format. In both cases, there is a good agreement between simulation and experimental results. Additionally, the probability density function of the OSNR estimation errors is not necessarily a symmetric Gaussian distribution, but it can be skewed, as Fig. 5.72 shows for example. The upper bound on the OSNR estimation range highly depends on the number of samples processed, the roll-off factor and CD, which are treated next.

Fig. 5.73 shows the dependency of the estimation on the number of samples, based on experimental results, for a fixed symbol-rate of 10 GBaud and its corresponding

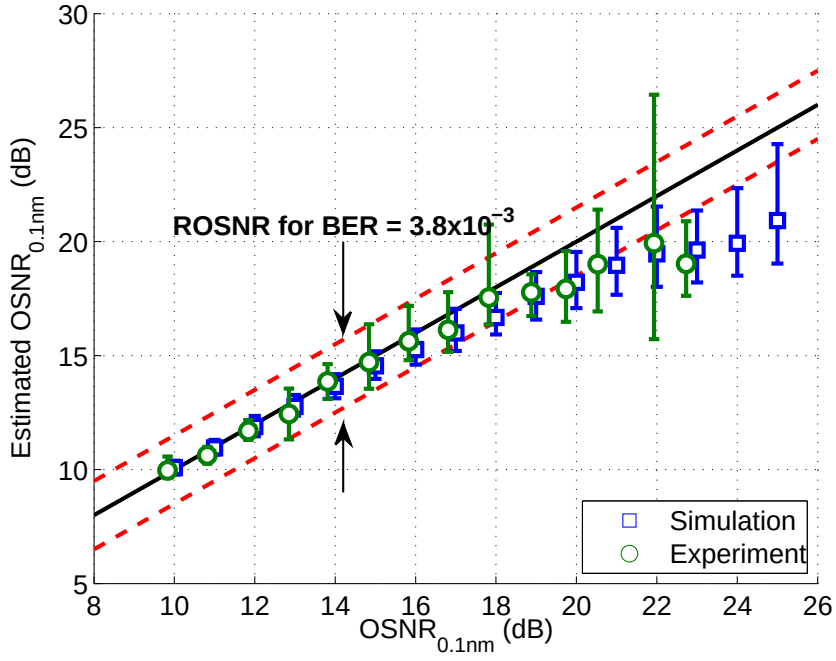

Figure 5.71: OSNR estimation for DP-16QAM in a back-to-back setup and a RRC roll-off of 0.45.

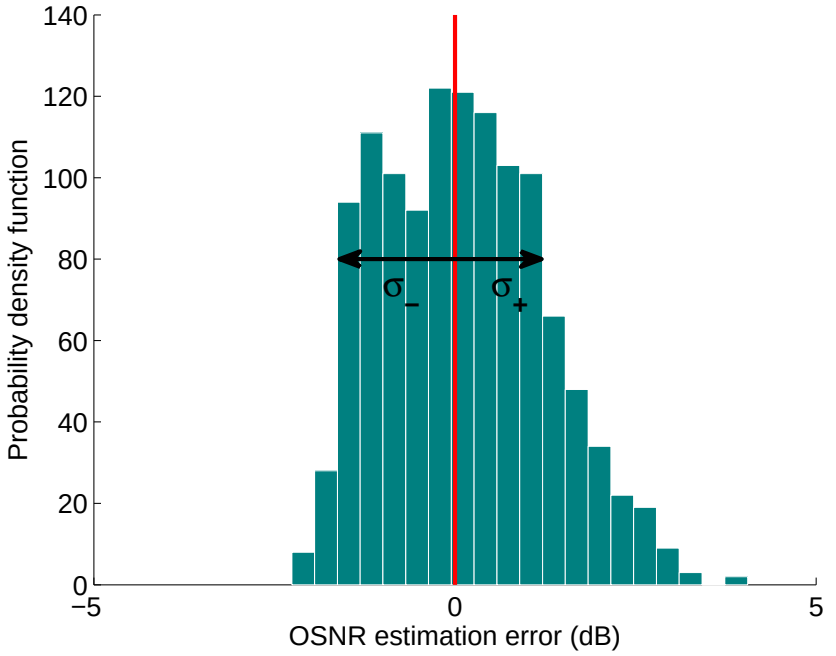

Figure 5.72: Estimation of the ROSNR for DP-16QAM in a back-to-back experimental setup and a RRC roll-off of 0.45.

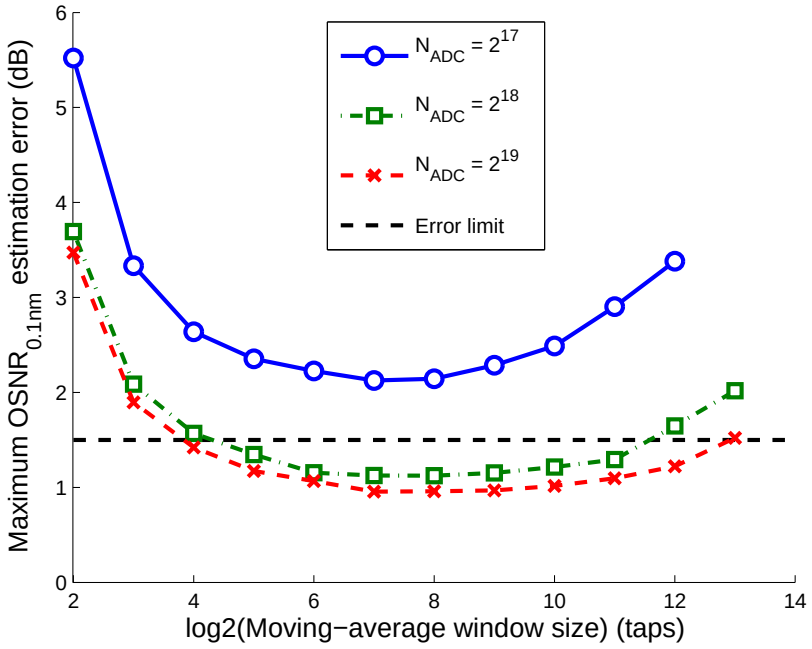

Figure 5.73: Impact of frequency smoothing window on the in-band OSNR estimation, for a three channel DP-16QAM WDM in a back-to-back simulated transmission.

ROSNR, to ensure a BER of $3.8 \cdot 10^{-3}$. The accuracy increases with a higher number of samples captured by the ADC, because that is equivalent to an increase in the number of points over which the STFT is computed, leading to a better SCF estimate. At least 2^{18} samples are required for correct power estimations that would result in errors less than 1.5 dB, as required by ITU [2012] standard.

The spectral smoothing window is also essential in optimizing the estimation. When the window size is too low, the absolute errors increase as the number of spectral averages is not sufficient in obtaining an accurate approximation of the SCF in Eq. 3.23. On the other hand, when the window size is high and close in value to N_{ADC}, the errors increase as a result of the reduced resolution of the SCF. The optimum averaging window size when $N_{ADC} = 2^{18}$ samples is between $128 - 512$ samples.

The RRC roll-off is a limiting factor for the in-band OSNR estimation as shown in Fig. 5.74. At lower roll-offs the signal bandwidth is reduced, as depicted in Fig. 5.67, for both $\alpha = 0$ and $\alpha = F_b$. Because the power integration bandwidth is even lower when $\alpha = F_b$, the measurement accuracy of $P_{ave}^{\alpha=F_b}$ will be reduced under the low roll-offs conditions and thus leading to higher OSNR estimation errors. The performance here is evaluated in terms of the standard deviation of the measured error, across all 100 estimations. Roll-offs higher than 0.1 induce higher errors also in the measurement of the IF, which the OSNR estimator relies on.

Increasing the order of the modulation format, will result in more stringent limitations of the presented technique in terms of achievable roll-offs. For DP-QPSK,

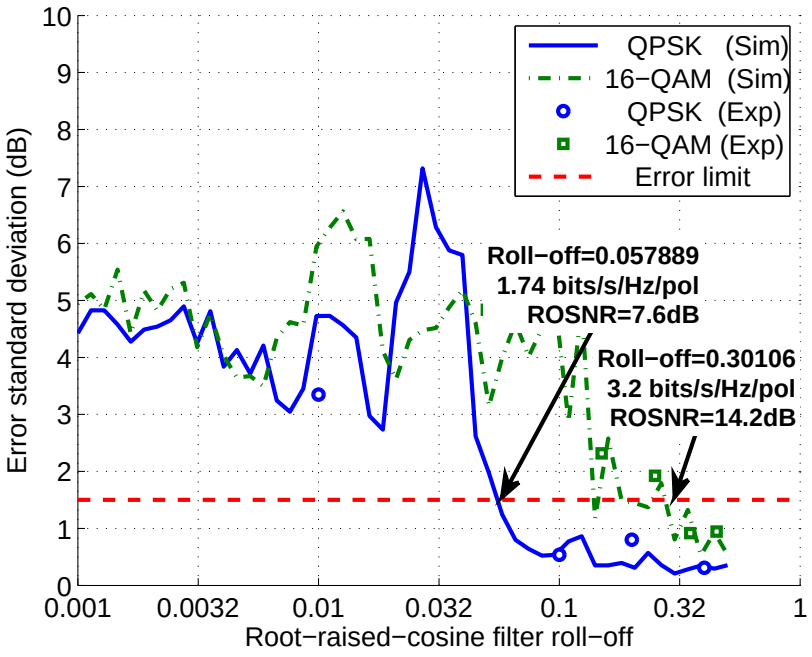

Figure 5.74: Impact of RRC roll-off factor on the in-band OSNR estimation, for a three channel WDM signal in a back-to-back transmission.

the minimum roll-off of 0.06 gives the maximum acceptable error of 1.5 dB, while for DP-16QAM this value is 0.3. The difference in the roll-off tolerance for the two modulation formats comes from their different ROSNRs. Depending on the modulation format used, the roll-off limitation also imposes constraints on the maximum achievable spectral efficiency. Although the requirements on the maximum roll-off are more stringent for 16-QAM compared to QPSK, the achievable spectral efficiency is still increased almost two-fold when using 16-QAM modulation format. Again, there is a good match between simulation and experimental results.

5.7.2 Standard Single Mode Fiber Transmission

Fig. 5.75 and 5.76 show that the OSNR estimation can be performed over distances of 2017.5 km for DP-QPSK and 807 km in the case of DP-16QAM. The power fluctuations in the experimental setup, due to the instability of the Acusto-Optic Switch (AOS) and PDL, which cause fluctuations in the OSNR measurement. However, the errors are still within the 1.5 dB imposed error margin, at the ROSNR. The receiver noise starts to dominate at around 19 dB OSNR, and it is the only source of error at high OSNRs.

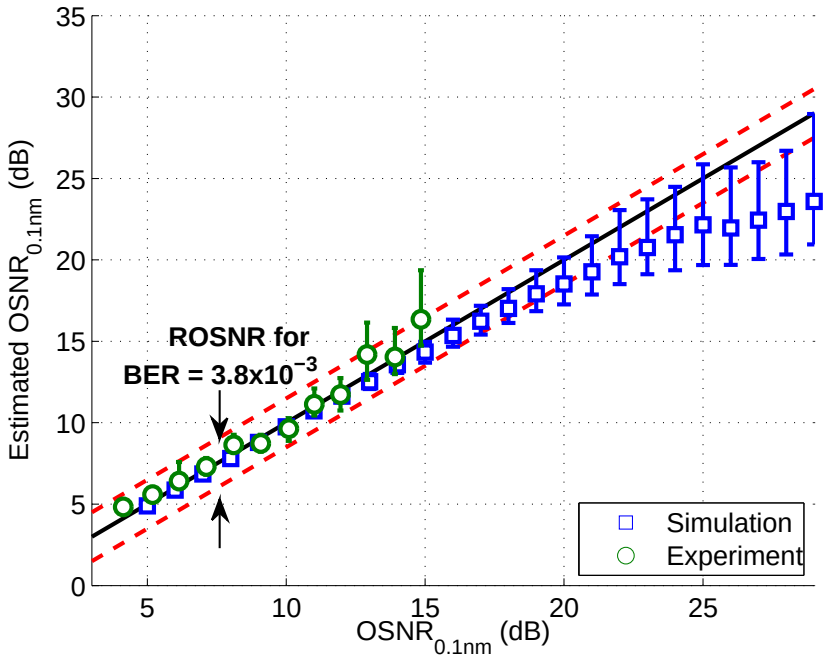

Figure 5.75: OSNR estimation for DP-QPSK and a transmission distance of 2017.5 km and a RRC roll-off of 0.4.

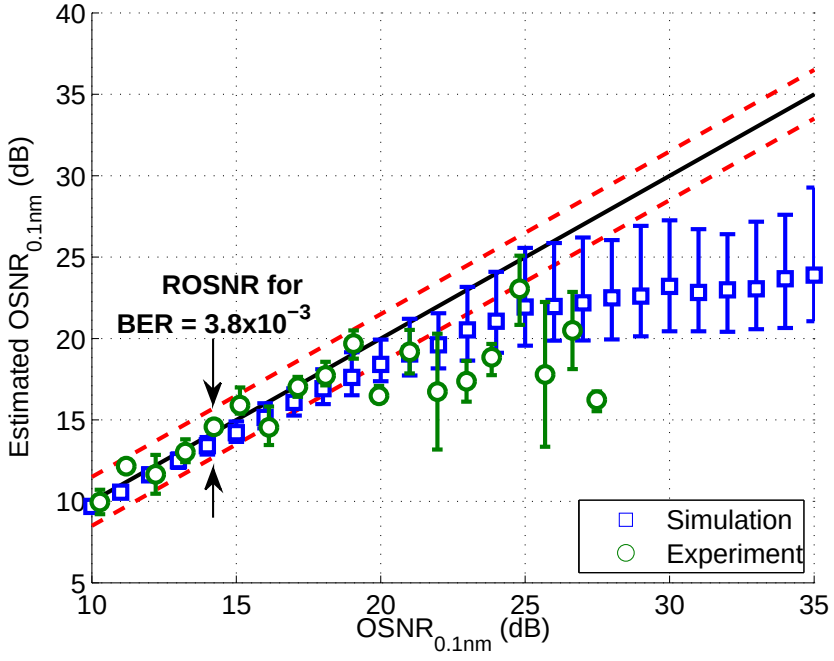

Figure 5.76: OSNR estimation for DP-16QAM and a transmission distance of 807 km and a RRC roll-off of 0.45.

5.8 Conclusions

This chapter demonstrated novel joint estimation techniques, based on the cyclostationarity properties of linearly modulated signals, that can efficiently be implemented within the digital coherent receiver DSP for monitoring purposes in SDONs. The stages of the joint monitor consist of symbol-rate, roll-off IF, CD and OSNR estimations, consecutively applied in this order.

A correct symbol-rate estimation is essential for the reliability of the entire joint estimator. The conditions under which the symbol-rate estimation can perform with 100% accuracy have been investigated in detail, including the impact of acquisition time, symbol-rate range, pulse shaping, as well as chromatic dispersion and noise. Time-domain and frequency-domain implementations have been discussed and compared in terms of their performance.

The frequency-domain implementation, based on the SCF, employs a frequency-smoothing filter for enhancing the spectral correlation through noise averaging. The main limitation of this technique is its dependence on CD, which results in correlation fading as demonstrated for the first time in this chapter. The optimum frequency-smoothing window changes with distance and signal bandwidth, but in order to cover a wide range of possible required capacity – spectral-efficiency – reach combinations, a window size of 128 – 256 samples is sufficient for a reliable symbol-rate estimation. Although limited by dispersion, the method allows the accurate estimation of 40 GBaud up to 1,614 km at a roll-off of 0.01 or 3,228 km at a roll-off of 0.1. On the other hand, the time-domain implementation, based on the CAF, does not employ a moving-average filter and is as a result almost completely independent of CD. The main limitation of both the time-domain and frequency-domain approaches is that they cannot perform well when the excess bandwidth of the Nyquist pulse shaping filter tends to zero. When the symbol-rate is 10 GBaud, the SCF-based estimator allows a 1% minimum roll-off, whilst the CAF approach requires at least 7% excess bandwidth. The frequency domain approach is thus preferred for symbol-rate estimation.

The CAF is more sensitive to the RRC roll-off and can therefore be used to estimate it, from the power ratio between the CAF tone at the cyclic frequency equal to the symbol-rate and its DC component. Roll-off factors down to 0.06 can be estimated within a RMSE of $< 20\%$, independently of IF, noise or CD.

From the spectral correlation at the symbol-rate estimate, a new IF estimation technique has been demonstrated. Contrary to the CD estimation stage that succeeds it, a lower roll-off factor is of benefit to the IF estimation. For three channels at 10 GBaud, the RMSE is 14 MHz for a roll-off of 0.5 and 4 MHz for a roll-off of 0.1, sufficient for the following CD and OSNR estimation stages.

Time-domain and frequency-domain cyclostationarity-based CD estimation tech-

niques have been proposed and demonstrated here for the first time. The former measures the time delay of the CAF pulse, while the latter measures the phase of the cyclic spectrum within the channel bandwidth, both giving an estimate of the amount of cumulative dispersion in the signal. A sufficiently low RMSE limit of 200 ps/nm residual uncompensated CD is imposed, as it can be corrected for by the dynamic equaliser at the very low cost of employing 2 extra taps at 10 GBaud. For a more reliable performance, both techniques require high channel bandwidths, achievable either by increasing the symbol-rate or the roll-off factor. At 40 GBaud, the time-domain implementation functions for roll-offs as low as 0.018, whilst the frequency-domain method can achieve the same performance for a minimum roll-off of 0.01. In terms of spectral efficiency this means an 8% improvement, which becomes siginificant when moving to data-rates of 400 Gb/s and beyond. The SCF-based approach is thus preferred, as it improves the CD estimation with respect to roll-off limitations, with an increase in the symbol-rate. However, if a longer transmission distance is desirable, then the time-domain implementation enables the estimation of up to 2,098,926 ps/nm, at a RMSE of 200 ps/nm, outperforming the frequency-domain approach. For a faster processing speed, the CAF-based CD estimator can be applied simultaneously with the IF and the roll-off estimators, as it is independent from them.

The in-band OSNR can be estimated by using the cyclostationarity property of linearly modulated signals, with certain constraints. This method is particularly useful for Nyquist WDM systems, when the roll-off factor is larger than 0.06 for DP-QPSK and 0.3 for DP-16QAM, but results in errors higher than 1.5 dB otherwise, even when 2^{19} samples are processed. The accuracy can be improved by capturing more samples at the receiver, at the cost of a longer estimation time, and from a correct selection of the spectral smoothing window size. The ROSNR of 10 GBaud DP-QPSK and DP-16QAM for BER of $3.8 \cdot 10^{-3}$ falls within the range of OSNRs that can be correctly estimated within 1.5 dB of error. The method requires knowledge of the symbol-rate, RRC roll-off factor and CD, but as demonstrated these parameters can be also estimated using the same cyclostationarity approach.

To enhance the cyclic correlation features of the signal, 2^{19} samples are processed which requires an acquisition time of 6.55 μs when the sampling rate is 80 GSa/s. In current dynamic optical networks reconfiguration and the DSP data recovery algorithm operate on a μs time-scale, which makes the proposed joint estimator suitable for practical implementation. For a faster processing time, a compromise between transmission capacity-distance product and accuracy is needed. Finally, the linear or non-linear noise components have no impact on the joint estimator.

6

Conclusions and future work

As the evolution of electronics speed seems to have reached a halt, capacity increases in future optical networks will no longer be able to meet traffic demands, by simply increasing the symbol-rate. Increasing the modulation format order limits the transmission distance, and this approach also fails when aiming to increase the channel capacity. Moreover, legacy systems are inherently over-engineered, as they support only static signal configurations. In response to this capacity crunch, optical networks are becoming more software-defined in order to optimise spectral utilisation, and define transmission parameters according to existing demands and channel impairments. For instance, data-rates exceeding 1 Tb/s can be achieved by employing flexible grid Nyquist WDM superchannels, which enable flexibility in the spectral domain, as well as capacity and reach to be customised to specific application requirements. Whilst optical networks become more dynamic and reconfigurable, they require monitoring for maintenance purposes. In addition, SDON could reach autonomy, required for optimised reconfigurability, through persistent and continuous self-observation. It is thus equally important to enable sensing of both future superchannels, but also legacy channels operating at lower symbol-rates and OOK or BPSK formats.

The introduction of coherent detection with DSP enabled programmable receivers, capable of adaptively monitoring and compensating fibre impairments. As such, sensing integrated within the digital domain of coherent receivers is currently the most cost-effective solution, given the increased sampling speed of existing ADCs and Complementary Metal-Oxide-Semiconductor (CMOS) scalability, together with the

employment of digital coherent receivers on a large scale. Future digital monitoring techniques require to be as independent as possible of the data-recovery algorithms, such that monitoring can be performed at the beginning stages of the DSP, for increased feedback response towards the control plane.

The most common parameters that would change dynamically are: symbol-rate, FEC, roll-off, modulation format, reach, OSNR and wavelength. In particular, the reach depends on transmitted power, symbol-rate, superchannel configuration and existing fibre impairments. The following sections explain how this work meets the aforementioned goals and how it compares with monitoring techniques existing in literature, which have already been presented and discussed in Chapter 2.

6.1 Research summary

The work that forms the body of this thesis focused on the estimation of symbol-rate, CD, and OSNR, which are some of the main parameters to be employed in decision-making regarding transmission reconfiguration. The roll-off factor of the transmitter RRC pulse shaping filter and the IF between the transmitter and LO lasers have also been estimated, as enablers to the proposed CD and OSNR techniques. All techniques presented here have been demonstrated for M-PSK and M-QAM modulation formats, but are also applicable to OOK.

Symbol-rate estimation

Three different signal-transforming symbol-rate estimation techniques have been demonstrated, all based on spectral properties of modulated signals. Chapter 3 provides the basic theory required for the understanding of these techniques.

A novel symbol-rate estimator, based on measuring the spectral variance, that works well at Nyquist pulse shaping of zero excess bandwidth, is demonstrated in Chapter 4. The extent of its independence of IF, dispersion and AWGN has been demonstrated. The absolute error is of the order of MHz, which may be slightly high for timing recovery algorithms that require an accuracy of the order of kHz. However, the accuracy is sufficient to distinguish between different FEC levels, from a known set of values. The main drawback of this algorithm is that it would not function for WDM systems, as its performance depends on the measurement of the individual channel bandwidth. This technique is therefore applicable only to single-channel legacy systems.

In Chapter 5, two different approaches for estimating the symbol-rate are additionally investigated, based on the time-domain and frequency-domain properties of cyclostationarity signals, by measuring their CAF and SCF respectively. Whilst the two functions are Fourier pairs, their implementation differed by additionally employing

a moving-average filter to reduce the spectral variance for the SCF approach. Thus, their complexities are comparable, but their performances slightly different. The main difference brought by the inclusion of the frequency domain smoothing filter, is that it limits the transmission distance achievable with this technique due to spectral correlation fading. On the other hand, in the absence of this filter the CAF symbol-rate estimator is virtually CD independent.

Both are limited by Nyquist pulse shaping of reduced excess bandwidths, which reduces the cyclic correlation. The CAF approach has been previously proposed in literature, but a significant improvement has been brought to it herein by employing a finer spectral resolution. Whilst a RRC roll-off of only 0.2 was permitted in previous results, here it is possible to go to roll-offs as low as 0.07, enabling Nyquist superchannel operation. Nonetheless, the novel SCF approach, proposed here for the first time, is preferred, as it allows roll-offs as low as 0.01.

In the literature, it is found that the reconfiguration time of coherent transceivers is less than 150 ns and the time required for the DSP to recover the data is less than 200 ns. The single-channel symbol-rate estimator requires a comparable amount of time, 655 ns, for collecting sufficient data for the estimation. On the other hand the cyclostationarity-based symbol-rate estimators are limited by a 6.55 μs digitisation time. This latter value is still acceptable, as the amount of time to transfer the information over 1000 km of SSMF, if data-aided estimation was employed instead, is 10 ms.

Whilst three orders of magnitude slower than the single-channel technique, the possibilities of the cyclostationarity estimation are greater by comparison. The accuracy is much higher, of the order of kHz, it enables estimation across the entire WDM signal without need for demultiplexing, and the estimation of other parameters is enabled subsequently, from the same technique.

Roll-off estimation

The estimation of the roll-off factor is a rare subject in the literature and it is briefly touched upon in this thesis. The applicability of such an estimator lies both in the update of the match-filter at the receiver, but also of the subsequent CD and OSNR estimators investigated in this work. Based on the time-domain CAF, the proposed roll-off estimator performs within RMSE of 20% for roll-offs between 0.06 and 0.3, which is an acceptable performance [Yang et al., 2009].

Frequency offset estimation

A spectrum-based IF estimator was also demonstrated here, in order to aid the CD and OSNR estimators, by centering their measurements around the channel location. There is a good correspondence between this estimator and the estimator based on the fourth

power measurement, followed by an iterative spectral search of the carrier, typically employed in the coherent receiver's DSP. The RMSE of 4 MHz has been demonstrated for a roll-off of 0.1, and this value improves as the roll-off factor decreases.

Chromatic dispersion estimation

Two novel algorithms are proposed for the estimation of CD, based on the same SCF and CAF functions. Similarly to the symbol-rate estimation, the frequency domain approach is limited by correlation fading. By contrast, the CAF allows the estimation of 2,098,926 ps/nm cumulative dispersion (equivalent to 125,085 km of SSMF) when the symbol-rate is 40 GBaud and the roll-off factor is 0.018. This by far exceeds the performance of the existing CD estimators implemented within the coherent receiver and requires only $Nlog_2N$ computations, where N is the total number of samples. The main limitation of this technique is the narrow pulse shaping performed at the receiver. The SCF-based approach is thus preferred as it improves the CD estimation down to roll-offs as low as 0.01, giving a 8% improvement in terms of spectral efficiency, which becomes siginificant when moving to data-rates of 400 Gb/s and beyond. The target residual dispersion error proposed here was a RMSE of 200 ps/nm, which is sufficiently low to limit the number of taps of the dynamic equaliser, required to compensated for it.

Optical signal-to-noise ratio estimation

In recent years, there has been an increased focus on in-band OSNR monitors that could be integrated within the coherent receiver DSP, motivated by their wide employment with high data-rate systems, which means that these monitors could be cheaply incorporated into their design. The ITU-T recommendation is of 1.5 dB maximum allowable OSNR estimation error. It is desirable to implement OSNR estimation that is independent of other DSP steps.

A previously proposed OSNR estimator based on cyclostationarity properties of signals, has been further investigated in this thesis. It was confirmed both by simulation and experimentally the the performance of this estimator is within the 1.5 dB error limit, and in addition, does not require PMD compensation, nor symbol recovery. It is however dependent on CD, and requires approximate knowledge of the channel location and bandwidth, which have all been made possible with the previously presented estimators. The OSNR estimation algorithm also requires a calibration stage, which can be appropriate for burst-mode switching networks where a period of receiver training is already employed.

Joint parameter estimation

Jointly monitoring of any of the required parameters is a faster and more computationally efficient solution. In the literature, the majority of the joint estimation techniques focus either on the transmission parameters or the channel parameters. In this thesis, joint estimation of both classes has been demonstrated, which is of particular significance, when the changing of the signal configuration and transmission path at the transceiver nodes are both inter-dependent.

Compared to the joint estimator based on the FIR filter coefficients [Hauske et al., 2008], the cyclostationarity technique can be executed in approximatelly the same amount of time (of the order of μs). In the absence of DGD, both OSNR estimators perform similarly with maximum 1 dB and 1.5 dB absolute errors for the FIR filter taps and cyclostationarity approaches respectively. In this work, a RMSE of 200 ps/nm was self-imposed for the CD estimation performance, which allows an esimation range up to 27,083 ps/nm when the roll-off is 0.01 and the symbol-rate is 40 GBaud. The equaliser approach on the other hand allows a more precise CD estimation of 63 ps/nm standard deviation, but was only tested for up to 2000 ps/nm. Furthermore, the FIR filter technique requires demultiplexing and timing recovery, and it has not been tested for Nyquist pulse shaped signals.

As Nyquist WDM superchannels are becoming ubiquitous, joint performance monitors will need to focus more on signals that have undergone pulse-shaping approaching the Nyquist limit, since not so many have been given consideration in the literature so far. In this thesis such a joint estimator has been demonstrated. Its operation is limited by the narrowest pulse shaping, when the RRC roll-off is less than 0.3, and could also benefit of higher ADCs and processors speeds. Since it has a high potential, more work is required to further investigate and improve this joint estimator, as proposed in what follows.

6.2 Proposed future work

Further work could be performed in investigating the potential of the proposed cyclostationarity-based joint estimator. Whilst the work in this thesis demonstrated the applicability of the frequency offset, CD and OSNR estimators only for the central channel, the same approach can also be applied to the individual subchannels of the entire superchannel. Moreover, the linear CD phase response of the SCF computed at the symbol-rate, for channels that have travelled on different optical paths, could be estimated individually, from a single computational effort. Such signals are not superchannels by definition, but they are a common occurrence in networks employing ROADMs, where channels are added and dropped at different nodes within the network,

and therefore also need consideration.

As demonstrated in this thesis, symbol-rate estimation can be performed on heterogeneous WDM superchannels, where tones linking to each unique symbol-rate can be detected. However, the correspondence between the channel rate and channel location is lost, and this information could be recovered through further DSP techniques. One proposed approach is to perform spectral scanning, and use the already estimated parameters in doing so. Subsequent to symbol-rate and roll-off estimation, the analytical spectrum can be generated on a per-channel basis. From the frequency offset estimator, the location of existing channels can be identified. Further, it may then be possible to correlate the spectrum of the superchannel with the analytical spectrum of the channel to be searched for, and finally identify which channel corresponds to which bandwidth.

More work needs to be done to reduce the number of samples required in the computation of the SCF, and thus improve the response time of the estimate to similar time-scale as the network elements switching time (ns order). Using weighing windows other than rectangular windows, as assumed throughout this thesis, usually decreases spectral leakage of the conventional PSD. However, when computing the SCF, spectral leakage increases the spectral correlation and it is desirable. It is thus expected that apodisation limits the cyclostationarity of modulated signals, and more tests are required to confirm this.

One possible alternative approach to the Welch's method, that has been left unexplored so far, is to employ the Multi-taper method for computing the SCF. Whilst both methods aim at reducing the variance of the periodogram, the Multi-taper approach can give a better trade-off between low variance and high resolution, and thus has the potential to operate with a lower number of samples.

Finally, better pulse delay estimators need to be investigated, as having the potential to improve the time-domain CD estimator even further.

References

S. Abbott, "Review of 20 years of undersea optical fiber transmission system development and deployment since TAT-8," in *Optical Communication, 2008. ECOC 2008. 34th European Conference on*, 2008, pp. 1–4. 12

T. Anderson, A. Kowalczyk, K. Clarke, S. Dods, D. Hewitt, and J. Li, "Multi impairment monitoring for optical networks," *Lightwave Technology, Journal of*, vol. 27, no. 16, pp. 3729–3736, Aug 2009. 38, 39

L. Baker-Meflah, B. Thomsen, J. Mitchell, and P. Bayvel, "Multi-impairment WDM optical performance monitoring for burst switched networks," *Lightwave Technology, Journal of*, vol. 28, no. 23, pp. 3417–3426, Dec 2010. 38, 39

W. Barnes, N. LaSorte, H. Refai, and M. Yeary, "Symbol rate classification of PSK/QAM signals using direct frequency estimators," in *Instrumentation and Measurement Technology Conference, 2009. I2MTC '09. IEEE*, 2009, pp. 943–946. 30

J. Berthold, A. Saleh, L. Blair, and J. M. Simmons, "Optical networking: Past, present, and future," *Lightwave Technology, Journal of*, vol. 26, no. 9, pp. 1104–1118, 2008. 13

N. M. Blachman and S. Mousavinezhad, "The spectrum of the square of a synchronous random pulse train," *Communications, IEEE Transactions on*, vol. 38, no. 1, pp. 13–17, Jan 1990. 30

G. Bosco, A. Carena, V. Curri, P. Poggiolini, and F. Forghieri, "Performance limits of Nyquist-WDm and CO-OFDM in high-speed PM-QPSK systems," *Photonics Technology Letters, IEEE*, vol. 22, no. 15, pp. 1129–1131, Aug 2010. 26

G. Bosco, A. Carena, V. Curri, P. Poggiolini, E. Torrengo, and F. Forghieri, "Investigation on the robustness of a Nyquist-WDM terabit superchannel to transmitter and receiver non-idealities," in *Optical Communication (ECOC), 2010 36th European Conference and Exhibition on*, Sept 2010, pp. 1–3. 26

G. Bosco, V. Curri, A. Carena, P. Poggiolini, and F. Forghieri, "On the performance of Nyquist-WDM terabit superchannels based on PM-BPSK, PM-QPSK, PM-8QAM or PM-16QAM subcarriers," *Lightwave Technology, Journal of*, vol. 29, no. 1, pp. 53–61, Jan 2011. 26

W. Brown and H. Loomis, "Digital implementations of spectral correlation analyzers," *Signal Processing, IEEE Transactions on*, vol. 41, no. 2, pp. 703–720, Feb 1993. 57, 59, 89

F. Buchali, K. Schuh, D. Rosener, E. Lach, R. Dischler, W. Idler, L. Schmalen, A. Leven, R.-P. Braun, A. Ehrhardt, C. Gerlach, and L. Schurer, "512-Gb/s DP-16-QAM field trial over 734 km installed SSMF with co-propagating 10 Gb/s NRZ neighbors incorporating soft-FEC decoding," in *Optical Fiber Communication Conference and Exposition (OFC/NFOEC), 2012 and the National Fiber Optic Engineers Conference*, March 2012, pp. 1–3. 26

J. A. Buck, *Fundamentals of optical fibers*. Wiley, 2004. 78

J.-X. Cai, Y. Sun, H. Batshon, M. Mazurczyk, H. Zhang, D. Foursa, and A. Pilipetskii, "54 Tb/s transmission over 9,150 km with optimized hybrid Raman-EDFA amplification and coded modulation," in *Optical Communication (ECOC), 2014 European Conference on*, Sept 2014, pp. 1–3. 28

C. C. K. Chan, *Optical Performance Monitoring. Advanced Techniques for Next-Generation Photonic Networks*. Elsevier, 2010. 33

Y. Chan, J. W. Plews, and K. Ho, "Symbol rate estimation by the wavelet transform," in *Circuits and Systems, 1997. ISCAS '97., Proceedings of 1997 IEEE International Symposium on*, vol. 1, 1997, pp. 177–180 vol.1. 30

S. Chandrasekhar, X. Liu, B. Zhu, and D. Peckham, "Transmission of a 1.2-Tb/s 24-carrier no-guard-interval coherent OFDM superchannel over 7200-km of ultra-large-area fiber," in *Optical Communication, 2009. ECOC '09. 35th European Conference on*, vol. 2009-Supplement, Sept 2009, pp. 1–2. 27, 28

H.-C. Chien, J. Yu, Z. Jia, Z. Dong, and X. Xiao, "512-Gb/s quad-carrier PM-QPSK transmission over 2400-km SMF-28 subject to narrowing 100-GHz optical bandwidth," in *Optical Communications (ECOC), 2012 38th European Conference and Exhibition on*, Sept 2012, pp. 1–3. 26

P. Ciblat, P. Loubaton, E. Serpedin, and G. Giannakis, "Asymptotic analysis of blind cyclic correlation-based symbol-rate estimators," *Information Theory, IEEE Transactions on*, vol. 48, no. 7, pp. 1922–1934, Jul 2002. 32

Ciena, "Enabling a bigger and smarter network with Ciena's WaveLogic 3," Ciena, Tech. Rep., 2012. 24

L. K. I. Couch, *Digital and Analog Communication Systems*, 4th ed. New York: MacMillan, 1993. 67, 71

C. Do, A. Tran, C. Zhu, D. Hewitt, and E. Skafidas, "Data-aided OSNR estimation for QPSK and 16-QAM coherent optical system," *Photonics Journal, IEEE*, vol. 5, no. 5, pp. 6 601 609–6 601 609, Oct 2013. 34

Z. Dong, A. Lau, and C. Lu, "OSNR monitoring for PM-QPSK systems in presence of fiber nonlinearities for digital coherent receivers," in *Opto-Electronics and Communications Conference (OECC), 2012 17th*, July 2012, pp. 763–764. 27, 28, 34

M. Eiselt, B. Teipen, K. Grobe, A. Autenrieth, and J. P. Elbers, "Programmable modulation for high-capacity networks," in *Optical Communication (ECOC), 2011 37th European Conference and Exhibition on*, 2011, pp. 1–3. 19

J.-P. Elbers and A. Autenrieth, "From static to software-defined optical networks," in *Optical Network Design and Modeling (ONDM), 2012 16th International Conference on*, April 2012, pp. 1–4. 20

E. Escalona, Y. Qin, G. Zervas, J. Triay, G. Zarris, N. Amaya-Gonzalez, R. Nejabati, C. Cervelló-Pastor, and D. Simeonidou, "Experimental demonstration of a novel QoS-aware hybrid optical network," in *Optical Communication (ECOC), 2010 36th European Conference and Exhibition on*, Sept 2010, pp. 1–3. 13

R. Essiambre and R. Tkach, "Capacity trends and limits of optical communication networks," *Proceedings of the IEEE*, vol. 100, no. 5, pp. 1035–1055, 2012. 13

M. Faruk, Y. Mori, and K. Kikuchi, "In-band estimation of optical signal-to-noise ratio from equalized signals in digital coherent receivers," *Photonics Journal, IEEE*, vol. 6, no. 1, pp. 1–9, Feb 2014. 34

I. Fatadin and S. Savory, "Compensation of frequency offset for 16-qam optical coherent systems using qpsk partitioning," *Photonics Technology Letters, IEEE*, vol. 23, no. 17, pp. 1246–1248, Sept 2011. 23

I. Fatadin, S. Savory, and D. Ives, "Compensation of quadrature imbalance in an optical QPSK coherent receiver," *Photonics Technology Letters, IEEE*, vol. 20, no. 20, pp. 1733–1735, Oct 2008. 21

C. Fludger, T. Duthel, D. van den Borne, C. Schulien, E.-D. Schmidt, T. Wuth, J. Geyer, E. de Man, G.-D. Khoe, and H. De Waardt, "Coherent equalization and POLMUX-RZ-DQPSK for robust 100-GE transmission," *Lightwave Technology, Journal of*, vol. 26, no. 1, pp. 64–72, Jan 2008. 13

D. Foursa, H. Batshon, H. Zhang, M. Mazurczyk, J.-X. Cai, O. Sinkin, A. Pilipetskii, G. Mohs, and N. Bergano, "44.1 Tb/s transmission over 9,100 km using coded modulation based on 16QAM signals at 4.9 bits/s/Hz spectral efficiency," in *Optical Communication (ECOC 2013), 39th European Conference and Exhibition on*, Sept 2013, pp. 1–3. 27, 28

Y. Gao, Y. Wan, L. Li, and J. Men, "Baud rate estimation of FSK signals based on Wavelet Transform," in *Intelligent System Design and Engineering Application (ISDEA), 2012 Second International Conference on*, 2012, pp. 181–184. 30

F. M. Gardner, "Interpolation in digital modems. I fundamentals," *Communications, IEEE Transactions on*, vol. 41, no. 3, pp. 501–507, Mar 1993. 22

W. A. Gardner, "Representation and estimation of cyclostationary processes," Ph.D. dissertation, Department of Electrical and Computer Engineering, University of Massachussetts, 1972. 45

——, "The spectral correlation theory of cyclostationary time-series," *Signal Process.*, vol. 11, no. 1, pp. 13–36, Jul. 1986. 48, 50

——, "Measurement of spectral correlation," *Acoustics, Speech and Signal Processing, IEEE Transactions on*, vol. 34, no. 5, pp. 1111–1123, Oct 1986. 54, 60, 61, 65

——, *Statistical Spectral Analysis: A Non-probabilistic Theory*. Prentice-Hall, N.J, 1987. 51, 134

——, "Signal interception: a unifying theoretical framework for feature detection," *Communications, IEEE Transactions on*, vol. 36, no. 8, pp. 897–906, Aug 1988. 31, 82

——, "Two alternative philosophies for estimation of the parameters of time-series," *Information Theory, IEEE Transactions on*, vol. 37, no. 1, pp. 216–218, Jan 1991. 43

——, *Cyclostationarity in communications and signal processing*, ser. Electrical engineering, communications and signal processing. IEEE Press, 1994. 48

W. A. Gardner, A. Napolitano, and L. Paura, "Cyclostationarity: Half a century of research," *Signal Process.*, vol. 86, no. 4, pp. 639–697, Apr. 2006. 43, 65

D. Gariépy and G. He, "Measuring OSNR in WDM systems – Effects of resolution bandwith and optical rejection ratio," EXFO, Tech. Rep., 2009. 32

G. Gavioli, E. Torrengo, G. Bosco, A. Carena, S. Savory, F. Forghieri, and P. Poggiolini, "Ultra-narrow-spacing 10-channel 1.12 Tb/s D-WDM long-haul transmission over uncompensated SMF and NZDSF," *Photonics Technology Letters, IEEE*, vol. 22, no. 19, pp. 1419–1421, Oct 2010. 28

C. Glingener, "Optical networking trends and evolution," in *Optical Fiber Communication Conference and Exposition (OFC/NFOEC), 2011 and the National Fiber Optic Engineers Conference*, 2011, pp. 1–3. 18

J. P. Gordon and H. Hogelnik, "PMD fundamentals: Polarization mode dispersion in optical fibers," *Proceedings of the National Academy of Sciences*, vol. 97, April 2000. 79

S. Gringeri, N. Bitar, and T. Xia, "Extending software defined network principles to include optical transport," *Communications Magazine, IEEE*, vol. 51, no. 3, pp. 32–40, March 2013. 19

W. Grupp, "In-band OSNR measurement based on spectral correlation," in *Photonic Networks, 2010 ITG Symposium on*, 2010, pp. 1–4. 34, 82

F. Hauske, J. Geyer, M. Kuschnerov, K. Piyawanno, T. Duthel, C. Fludger, D. van den Borne, E.-D. Schmidt, B. Spinnler, H. de Waardt, and B. Lankl, "Optical performance monitoring from fir filter coefficients in coherent receivers," in *Optical Fiber communication/National Fiber Optic Engineers Conference, 2008. OFC/NFOEC 2008. Conference on*, Feb 2008, pp. 1–3. 38, 40, 164

F. Hauske, M. Kuschnerov, B. Spinnler, and B. Lankl, "Optical performance monitoring in digital coherent receivers," *Lightwave Technology, Journal of*, vol. 27, no. 16, pp. 3623–3631, 2009. 36, 40

F. Hauske, Z. Zhang, C. Li, C. Xie, and Q. Xiong, "Precise, robust and least complexity CD estimation," in *Optical Fiber Communication Conference and Exposition (OFC/NFOEC), 2011 and the National Fiber Optic Engineers Conference*, March 2011, pp. 1–3. 35

S. Haykin, *Cognitive Dynamic Systems: Perception-Action Cycle, Radar and Radio*. Cambridge University Press, 2012. 18

K. L. Holladay, "Experimental analysis of Wavelet Transforms for estimating PSK symbol rate," in *IASTED International Conference on Communication Systems and Applications*, 2004. 31

Y.-K. Huang, E. Ip, T. Xia, G. Wellbrock, M.-F. Huang, Y. Aono, T. Tajima, and M. Cvijetic, "Mixed line-rate transmission (112-gb/s, 450-gb/s, and 1.15-tb/s) over 3560 km of field-installed fiber with filterless coherent receiver," *Lightwave Technology, Journal of*, vol. 30, no. 4, pp. 609–617, Feb 2012. 26

H. L. Hurd, "An investigation of periodically correlated stochastic processes," Ph.D. dissertation, Duke University, 1969. 45

J.-C. Imbeaux, "Performances of the delay-line multiplier circuit for clock and carrier synchronization in digital satellite communications," *Selected Areas in Communications, IEEE Journal on*, vol. 1, no. 1, pp. 82–95, Jan 1983. 30

M. Ionescu, M. Erkilinc, M. Paskov, S. Savory, and B. Thomsen, "Novel baud-rate estimation technique for M-PSK and QAM signals based on the standard deviation of the spectrum," in *Optical Communication (ECOC 2013), 39th European Conference and Exhibition on*, Sept 2013, pp. 1–3. 15

M. Ionescu, M. Sato, and B. Thomsen, "In-band OSNR estimation for Nyquist WDM superchannels," in *Optical Communication (ECOC), 2014 European Conference on*, Sept 2014, pp. 1–3. 15

E. Ip and J. Kahn, "Digital equalization of chromatic dispersion and polarization mode dispersion," *Lightwave Technology, Journal of*, vol. 25, no. 8, pp. 2033–2043, Aug 2007. 22

E. Ip, A. P. T. Lau, D. J. F. Barros, and J. M. Kahn, "Coherent detection in optical fiber systems," *OPTICS EXPRESS*, vol. 16, no. 2, pp. 753–791, JAN 21 2008. 21

ITU-T G.697 : Optical monitoring for dense wavelength division multiplexing systems, ITU Telecommunication Standardization Sector Std., February 2012. 32, 83, 155

ITU-T G.709: Interfaces for the optical transport network, ITU Telecommunication Standardization Sector Std. 12

D. J. Ives, B. C. Thomsen, R. Maher, and S. Savory, "Estimating OSNR of equalised QPSK signals," in *37th European Conference and Exposition on Optical Communications*. Optical Society of America, 2011, p. Tu.6.A.6. 34

P. Ji, "Software defined optical network," in *Optical Communications and Networks (ICOCN), 2012 11th International Conference on*, 2012, pp. 1–4. 19

M. Jinno, H. Takara, B. Kozicki, Y. Tsukishima, Y. Sone, and S. Matsuoka, "Spectrum-efficient and scalable elastic optical path network: architecture, benefits, and enabling technologies," *Communications Magazine, IEEE*, vol. 47, no. 11, pp. 66–73, 2009. 25

I. P. Kaminow, *Optical Fiber Telecommunications*. Elsevier, 2013, vol. VIB - Systems and Networks. 24

F. N. Khan, Y. Zhou, Q. Sui, and A. P. T. Lau, "Non-data-aided joint bit-rate and modulation format identification for next-generation heterogeneous optical networks," *Optical Fiber Technology*, vol. 20, no. 2, pp. 68 – 74, 2014. 38, 39

M. Kueckenwaitz, F. Quint, and J. Reichert, "A robust baud rate estimator for noncooperative demodulation," in *MILCOM 2000. 21st Century Military Communications Conference Proceedings*, vol. 2, 2000, pp. 971–975 vol.2. 78

M. Kuschnerov, F. Hauske, K. Piyawanno, B. Spinnler, M. Alfiad, A. Napoli, and B. Lankl, "DSP for coherent single-carrier receivers," *Lightwave Technology, Journal of*, vol. 27, no. 16, pp. 3614–3622, 2009. 14, 35

M. Kuschnerov, M. Chouayakh, K. Piyawanno, B. Spinnler, E. de Man, P. Kainzmaier, M. Alfiad, A. Napoli, and B. Lankl, "Data-aided versus blind single-carrier coherent receivers," *Photonics Journal, IEEE*, vol. 2, no. 3, pp. 387–403, June 2010. 35

J. Lee, H. Choi, S. K. Shin, and Y. Chung, "A review of the polarization-nulling technique for monitoring optical-signal-to-noise ratio in dynamic WDM networks," *Lightwave Technology, Journal of*, vol. 24, no. 11, pp. 4162–4171, 2006. 33

K. Lee and T. Aprille, "SONET evolution: the challenges ahead," in *Global Telecommunications Conference, 1991. GLOBECOM '91. 'Countdown to the New Millennium. Featuring a Mini-Theme on: Personal Communications Services*, 1991, pp. 736–740 vol.2. 12

L. Li, H. Xu, and J. Wu, "Simultaneous monitoring of first-order polarization mode dispersion and chromatic dispersion based on RF power detection technique," *Optics Communications*, vol. 317, no. 0, pp. 45 – 52, 2014. 38

X. Liu and S. Chandrasekhar, "Superchannel for next-generation optical networks," in *Optical Fiber Communications Conference and Exhibition (OFC), 2014*, March 2014, pp. 1–33. 24, 26

X. Liu, S. Chandrasekhar, P. J. Winzer, T. Lotz, J. Carlson, J.Yang, G. Cheren, and S. Zederbaum, "1.5-Tb/s guard-banded superchannel transmission over 56x100-km (5600-km) ULAF using 30-Gbaud pilot-free OFDM-16QAM signals with 5.75-b/s/Hz net spectral efficiency," in *Optical Communication (ECOC), 2012 38th European Conference and Exhibition on*, 2012. 28

R. Maher, D. Millar, S. Savory, and B. Thomsen, "Fast switching burst mode receiver in a 24-channel 112Gb/s DP-QPSK WDM system with 240km transmission," in *Optical Fiber Communication Conference and Exposition (OFC/NFOEC), 2012 and the National Fiber Optic Engineers Conference*, 2012, pp. 1–3. 24, 98

L. Mazet and P. Loubaton, "Cyclic correlation based symbol rate estimation," in *Signals, Systems, and Computers, 1999. Conference Record of the Thirty-Third Asilomar Conference on*, vol. 2, Oct 1999, pp. 1008–1012 vol.2. 32

T. Mizuochi, "Next generation FEC for optical communication," in *OFC/NFOEC2008, Tutorial OTuE, FEC and Capacity*, 2008. 29, 81, 95, 106

I. Monroy, D. Zibar, N. Gonzalez, and R. Borkowski, "Cognitive heterogeneous reconfigurable optical networks (CHRON): Enabling technologies and techniques," in *Transparent Optical Networks (ICTON), 2011 13th International Conference on*, 2011, pp. 1–4. 13, 14, 29

M. Morelli and U. Mengali, "Feedforward carrier frequency estimation with MSK-type signals," *Communications Letters, IEEE*, vol. 2, no. 8, pp. 235–237, Aug 1998. 23

T. Ng, J. Blows, and B. Eggleton, "In-band OSNR monitoring using cascaded four-wave mixing in a fibre optical parametric amplifier," in *Lasers and Electro-Optics, 2005. (CLEO). Conference on*, vol. 2, 2005, pp. 977–979 Vol. 2. 33

A. Oppenheim and R. Schafer, *Discrete-Time Signal Processing*, ser. Pearson Custom Library. Pearson Education, Limited, 2010. 50

J. Pan, C. Liu, T. Detwiler, A. Stark, Y.-T. Hsueh, and S. Ralph, "Inter-channel crosstalk cancellation for Nyquist-WDM superchannel applications," *Lightwave Technology, Journal of*, vol. 30, no. 24, pp. 3993–3999, Dec 2012. 25

C. R. Paul, *Introduction to Electromagnetic compatibility*, 2nd ed. Wiley, 2006. 68

P. Poggiolini, G. Bosco, A. Carena, V. Curri, V. Miot, and F. Forghieri, "Performance dependence on channel baud-rate of PM-QPSK systems over uncompensated links," *Photonics Technology Letters, IEEE*, vol. 23, no. 1, pp. 15–17, Jan 2011. 26, 92, 114

G. Raybon, S. Randel, A. Adamiecki, P. Winzer, L. Salamanca, R. Urbanke, S. Chandrasekhar, A. Konczykowska, F. Jorge, J. Dupuy, L. Buhl, S. Draving, M. Grove, and K. Rush, "1-Tb/s dual-carrier 80-GBaud PDM-16QAM WDM transmission at 5.2 b/s/Hz over 3200 km," in *Photonics Conference (IPC), 2012 IEEE*, Sept 2012, pp. 1–2. 28

G. Raybon, S. Randel, A. Adamiecki, and P. Winzer, "High symbol rate transmission systems for data rates above 400 Gb/s using ETDM transmitters and receivers," in *Optical Communication (ECOC), 2014 European Conference on*, Sept 2014, pp. 1–3. 28

D. Reed and M. Wickert, "Minimization of detection of symbol-rate spectral lines by delay and multiply receivers," *Communications, IEEE Transactions on*, vol. 36, no. 1, pp. 118–120, 1988. 30

J. Renaudier, O. Bertran-Pardo, H. Mardoyan, P. Tran, G. Charlet, S. Bigo, A. Konczykowska, J. Dupuy, F. Jorge, M. Riet, and J. Godin, "Spectrally efficient long-haul transmission of 22-tb/s using 40-gbaud pdm-16qam with coherent detection," in *Optical Fiber Communication Conference and Exposition (OFC/NFOEC), 2012 and the National Fiber Optic Engineers Conference*, March 2012, pp. 1–3. 28

K. Roberts, "100G and beyond," in *Opto-Electronics and Communications Conference (OECC), 2012 17th*, 2012, pp. 144–145. 13

R. Roberts, W. Brown, and H. Loomis, "Computationally efficient algorithms for cyclic spectral analysis," *Signal Processing Magazine, IEEE*, vol. 8, no. 2, pp. 38–49, April 1991. 57, 61, 89

S. Ryu, *Coherent Lightwave Communication Systems*. Artech House, 1995. 21

M. Sato, R. Maher, D. Lavery, K. Shi, B. Thomsen, and P. Bayvel, "Frequency diversity MIMO detection for dual-carrier DP-16QAM transmission," in *Optical Communication (ECOC), 2014 European Conference on*, Sept 2014, pp. 1–3. 127

S. J. Savory, "Digital filters for coherent optical receivers," *Opt. Express*, vol. 16, no. 2, pp. 804–817, Jan 2008. 22

S. Savory, "Digital coherent optical receivers: Algorithms and subsystems," *Selected Topics in Quantum Electronics, IEEE Journal of*, vol. 16, no. 5, pp. 1164–1179, 2010. 21, 23

C. Schmidt-Langhorst, F. Frey, M. Nölle, R. Elschner, C. Meuer, P. Wilke-Berenguer, and C. Schubert, "Optimization of subcarrier spacing of 400-Gb/s dual-carrier Nyquist PDM-16QAM in a flexgrid scenario," in *Optical Communication (ECOC 2013), 39th European Conference and Exhibition on*, Sept 2013, pp. 1–3. 97

M. Seimetz, "Laser linewidth limitations for optical systems with high-order modulation employing feed forward digital carrier phase estimation," in *Optical Fiber communication/National Fiber Optic Engineers Conference, 2008. OFC/NFOEC 2008. Conference on*, 2008, pp. 1–3. 23

M. Selmi, Y. Jaouen, and P. Ciblat, "Accurate digital frequency offset estimator for coherent PolMux QAM transmission systems," in *Optical Communication, 2009. ECOC '09. 35th European Conference on*, Sept 2009, pp. 1–2. 23

T. Shen, K. Meng, A. Lau, and Z.-Y. Dong, "Optical performance monitoring using artificial neural network trained with asynchronous amplitude histograms," *Photonics Technology Letters, IEEE*, vol. 22, no. 22, pp. 1665–1667, Nov 2010. 38

J. Sills and J. J. Wood, "Optimal baud-rate estimation," in *Military Communications Conference, 1996. MILCOM '96, Conference Proceedings, IEEE*, vol. 3, 1996, pp. 1015–1019 vol.3. 29

R. Soriano, F. Hauske, N. Gonzalez, Z. Zhang, Y. Ye, and I. Monroy, "Chromatic dispersion estimation in digital coherent receivers," *Lightwave Technology, Journal of*, vol. 29, no. 11, pp. 1627–1637, June 2011. 36, 37

H. Takara, T. Mizuno, H. Kawakami, Y. Miyamoto, H. Masuda, K. Kitamura, H. Ono, S. Asakawa, Y. Amma, K. Hirakawa, S. Matsuo, K. Tsujikawa, and M. Yamada, "120.7-Tb/s (7 SDM/180 WDM/95.8 Gb/s) MCF-ROPA un epeatered transmission of PDM-32QAM channels over 204 km," in *Optical Communication (ECOC), 2014 European Conference on*, Sept 2014, pp. 1–3. 27, 28

M. Taylor, "Phase estimation methods for optical coherent detection using digital signal processing," *Lightwave Technology, Journal of*, vol. 27, no. 7, pp. 901–914, April 2009. 23

B. Thomsen, R. Maher, D. Millar, and S. Savory, "Burst mode receiver for 112 gb/s dp-qpsk," in *Optical Communication (ECOC), 2011 37th European Conference and Exhibition on*, Sept 2011, pp. 1–3. 21, 40

C. Tom, "Investigation and implementation of computationally-efficient algorithm for cyclic spectral analysis," Master's thesis, Carleton University, 1995. 56, 59

A. Wegener, "Practical techniques for baud rate estimation," in *Acoustics, Speech, and Signal Processing, 1992. ICASSP-92., 1992 IEEE International Conference on*, vol. 4, 1992, pp. 681–684 vol.4. 29

W. Wei, C. Wang, and J. Yu, "Cognitive optical networks: key drivers, enabling techniques, and adaptive bandwidth services," *Communications Magazine, IEEE*, vol. 50, no. 1, pp. 106–113, 2012. 13, 18

H. Wen, L. Cheng, X. Zheng, H. Zhang, Y. Guo, and B. Zhou, "Simultaneous clock recovery and dispersion, OSNR monitoring for 112Gbit/s NRZ-DQPSK using frequency down-conversion electro-optical phase-locked loop," in *Optical Communication (ECOC), 2011 37th European Conference and Exhibition on*, Sept 2011, pp. 1–3. 38

M. Wickert and W. Staton, "The effect of multipath on the detection of symbol-rate spectral lines by delay and multiply receivers," *Selected Areas in Communications, IEEE Journal on*, vol. 10, no. 3, pp. 545–549, 1992. 30

P. Winzer, "High-spectral-efficiency optical modulation formats," *Lightwave Technology, Journal of*, vol. 30, no. 24, pp. 3824–3835, 2012. 13

T.-H. Wo, D. Kolar, and R. Cardwell, "High-speed self-healing ring architectures for future interoffice networks," in *Global Telecommunications Conference, 1989, and Exhibition. Communications Technology for the 1990s and Beyond. GLOBECOM '89., IEEE*, 1989, pp. 801–807 vol.2. 12

Y. Yamamoto and T. Kimura, "Coherent optical fiber transmission systems," *Quantum Electronics, IEEE Journal of*, vol. 17, no. 6, pp. 919–935, 1981. 14

H. Yang, L. Zhu, and T. Wu, "The effects of mismatched roll-off factor on the receiving performance of qam signals," in *Communications, Circuits and Systems, 2009. ICCCAS 2009. International Conference on*, July 2009, pp. 86–90. 124, 162

Y. Yi and C. Yu, "Simultaneous OSNR and CD monitoring for NRZ-DPSK and DQPSK signals by single-channel sampling technique," in *Communications (APCC), 2013 19th Asia-Pacific Conference on*, Aug 2013, pp. 577–578. 38

G. Zervas and D. Simeonidou, "Cognitive optical networks: Need, requirements and architecture," in *Transparent Optical Networks (ICTON), 2010 12th International Conference on*, 2010, pp. 1–4. 14, 18

D. Zhao, L. Xi, X. Tang, W. Zhang, Y. Qiao, and X. Zhang, "Periodic training sequence aided in-band OSNR monitoring in digital coherent receiver," *Photonics Journal, IEEE*, vol. 6, no. 4, pp. 1–8, Aug 2014. 34

Z. Zheng, R. Ding, F. Zhang, and Z. Chen, "1.76Tb/s Nyquist PDM 16QAM signal transmission over 714km SSMF with the modified SCFDE technique," *Opt. Express*, vol. 21, no. 15, pp. 17 505–17 511, Jul 2013. 27, 28

C. Zhu, A. Tran, S. Chen, L. Du, C. Do, T. Anderson, A. Lowery, and E. Skafidas, "Moments-based OSNR monitoring for QPSK and QAM coherent optical systems," in *Opto-Electronics and Communications Conference (OECC), 2012 17th*, July 2012, pp. 747–748. 34

A
Acronyms

ADC	Analog-to-Digital Converter
AOS	Acusto-Optic Switch
ASE	Amplified Spontaneous Emission
AWG	Arbitrary Waveform Generator
AWGN	Additive White Gaussian Noise
BER	Bit Error Rate
BPF	Band-Pass Filter
BPSK	Binary Phase-Shift Keying
CAF	Cyclic Autocorrelation Function
CD	Chromatic Dispersion
CDF	Cumulative Density Function
CMA	Constant Modulus Algorithm
CMOS	Complementary Metal-Oxide-Semiconductor
CO-OFDM	Coherent Optical Orthogonal Frequency-Division Multiplexing
CPE	Carrier Phase Estimation
CPSD	Cross-Power Spectral Density
DAC	Digital-to-Analog Converter
DC	Direct Current

DFT Discrete Fourier Transform

DGD Differential Group Delay

DPSK Differential Phase-Shift Keying

DSP Digital Signal Processing

DP Dual-polarised

DP-QPSK Dual-polarised Quadrature Phase-Shift Keying

DWDM Dense Wavelength Division Multiplexing

EDFA Erbium Doped Fibre Amplifier

EVM Error Vector Magnitude

FAM FFT Accumulation Method

FEC Forward Error Correction

FFT Fast Fourier Transform

FIR Finite Impulse Response

FSK Frequency-Shift Keying

FWM Four-Wave Mixing

ICI Inter-Channel Interference

IF Intermediate Frequency

IP Internet Protocol

IFFT Inverse Fast Fourier Transform

ISI Inter-Symbol Interference

ITU International Telecommunication Union

LMS Least Mean Square

LO Local Oscillator

LPF Low-Pass Filter

LTI Linear Time-Invariant

LUT Look-up Table

M-PSK M-ary Phase-Shift Keying

M-QAM M-ary Quadrature Amplitude Modulation

MIMO Multiple-Input Multiple-Output

MMSE Minimum Mean Squared Error

MZM Mach-Zehnder Modulator

NRZ Non-Return-to-Zero

OADM Optical Add-Drop Multiplexer

O-E-O Optical-Electrical-Optical

OOK On-Off Keying

OPM Optical Performance Monitoring

OSA Optical Spectrum Analyser

OSNR Optical Signal-to-Noise Ratio

OFDM Optical Frequency Division Multiplexing

OTN Optical Transport Network

PD Photodiode

PDF Probability Density Function

PDL Polarisation Dependent Loss

PDM Polarisation Division Multiplexing

PMD Polarisation Mode Dispersion

PRBS Pseudo-Random Binary Sequence

PSD Power Spectral Density

QAM Quadrature Amplitude Modulation

QoS Quality of Service

QPSK Quadrature Phase-Shift Keying

RC Raised Cosine

RF Radio Frequency

RMSE Root Mean Squared Error

ROADM Reconfigurable Optical Add/Drop Multiplexer

ROSNR Required Optical Signal-to-Noise Ratio

RRC Root-Raised Cosine

RZ Return-to-Zero

SCDF Spectral Correlation Density Function

SCF Spectral Correlation Function

SDH Synchronous Digital Hierarchy

SDON Software-Defined Optical Network

SE Spectral Efficiency

SNR Signal-to-Noise Ratio

SONET Synchronous Optical Networking

SONET/SDH Synchronous Optical Networking/Synchronous Digital Hierarchy

SSCA Strip Spectrum Correlation Algorithm

SSMF Standard Single Mode Fibre

STFT Short-Time Fourier Transform

WDM Wavelength Division Multiplexing

WSS Wavelength Selective Switch

XPM Cross-Phase Modulation

B

Spectral correlation function of signals affected by chromatic dispersion

A coherent transmission system, where chromatic dispersion is the only source of fibre impairment, can be modelled as an Linear Time-Invariant (LTI) system as the one represented in Fig. B.1. A general analytical solution to the SCF of the output signal of an LTI system is given and then the impact of CD on the newly obtained SCF is investigated.

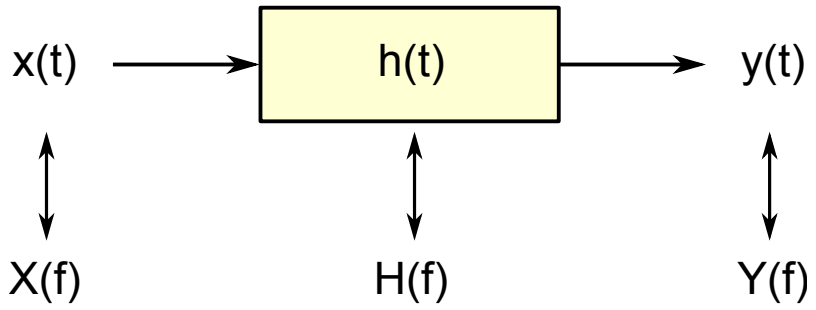

Figure B.1: LTI system, with input $x(t)$ and output $y(t)$ measured in the time-domain. The capital letters indicate frequency domain representation.

The output signal $y(t)$ is the result of the convolution between the input signal $x(t)$ and the inpulse response of the channel $h(t)$:

$$y(t) = h(t) * x(t) \triangleq \int h(\tau)x(t-\tau)d\tau = \int x(\tau)h(t-\tau)d\tau \tag{B.1}$$

The cyclic autocorrelation, is defined as the time average of the autocorrelation lag product weighted by a frequency α:

$$\hat{R}_y^{\alpha}(\tau) = \overline{y\left(t+\frac{\tau}{2}\right) y^*\left(t-\frac{\tau}{2}\right) e^{-j2\pi\alpha t}} \tag{B.2}$$

For linearly modulated signals, the cyclic frequency α is defined over a set $A_y = \{\frac{m}{T_b} \mid m \in \mathbb{Z}\}$, where T_b is the symbol period. Over this set, the cyclic autocorrelation constitutes the Fourier coefficients of the autocorrelation:

$$\begin{aligned}
\hat{R}_y^{\alpha}(t,\tau) &\stackrel{\Delta}{=} \sum_{\alpha\in A_y} \hat{R}_y^{\alpha}(\tau)\cdot e^{j2\pi\alpha t} \\
&\stackrel{B.2}{=} \sum_{\alpha\in A_y} \overline{y\left(t+\frac{\tau}{2}\right) y^*\left(t-\frac{\tau}{2}\right) e^{-j2\pi\alpha t}}\cdot e^{j2\pi\alpha t} \\
&\stackrel{B.1}{=} \sum_{\alpha\in A_y} \overline{\left[\int h(\lambda_1) x\left(t+\frac{\tau}{2}-\lambda_1\right) d\lambda_1\right]\cdot\left[\int h(\lambda_1) x\left(t-\frac{\tau}{2}-\lambda_2\right) d\lambda_2\right]^* e^{-j2\pi\alpha t}}\cdot e^{j2\pi\alpha t} \\
&\stackrel{B.1}{=} \sum_{\alpha\in A_y} \overline{\left[\int h(\lambda_1) x\left(t+\frac{\tau}{2}-\lambda_1\right) d\lambda_1\right]\cdot\left[\int h^*(\lambda_1) x^*\left(t-\frac{\tau}{2}-\lambda_2\right) d\lambda_2\right] e^{-j2\pi\alpha t}}\cdot e^{j2\pi\alpha t} \\
&\stackrel{LTI}{=} \sum_{\alpha\in A_y} \int\int h(\lambda_1) h^*(\lambda_2) \overline{x\left(t+\frac{\tau}{2}-\lambda_1\right)\cdot x^*\left(t-\frac{\tau}{2}-\lambda_2\right) e^{-j2\pi\alpha t}}\cdot e^{j2\pi\alpha t} d\lambda_1 d\lambda_2 \\
&= \sum_{\alpha\in A_y} \int\int h(\lambda_1) h^*(\lambda_2) \left(\hat{R}_x^{\alpha}(\tau-\lambda_1+\lambda_2) e^{-j2\pi\alpha\frac{\lambda_1+\lambda_2}{2}}\right)\cdot e^{j2\pi\alpha t}\ d\lambda_1 d\lambda_2 \\
&= \int\int h(\lambda_1) h^*(\lambda_2) e^{-j2\pi\alpha\frac{\lambda_1+\lambda_2}{2}} \left(\sum_{\alpha\in A_y} \hat{R}_x^{\alpha}(\tau-\lambda_1+\lambda_2)\cdot e^{j2\pi\alpha t}\right) d\lambda_1 d\lambda_2 \\
&= \int\int \left[h(\lambda_1) e^{-j2\pi\alpha\frac{\lambda_1}{2}}\right]\cdot\left[h^*(\lambda_2) e^{-j2\pi\alpha\frac{\lambda_2}{2}}\right]\cdot \hat{R}_x^{\alpha}(t,\tau-\lambda_1+\lambda_2)\ d\lambda_1 d\lambda_2 \\
&= \int\int \left[h(\lambda_1) e^{-j2\pi\alpha\frac{\lambda_1}{2}}\right]\cdot\left[h(\lambda_2) e^{j2\pi\alpha\frac{\lambda_2}{2}}\right]^*\cdot \hat{R}_x^{\alpha}(t,\tau-\lambda_1+\lambda_2)\ d\lambda_1 d\lambda_2.
\end{aligned}$$

Here, $\bar{x}$ indicates the mean of x, and x^* the complex conjugate. The previous result can be simplified by defining the following functions:

$$\begin{aligned}
g_1(t) &= h(t) e^{-j2\pi\frac{\alpha}{2}t} \\
g_2(t) &= h(t) e^{j2\pi\frac{\alpha}{2}t}
\end{aligned}$$

which have the corresponding Fourier transforms:

$$G_1(f) = \mathcal{F}\{g_1(t)\} = H\left(f+\frac{\alpha}{2}\right) \tag{B.3}$$

$$G_2(f) = \mathcal{F}\{g_2(t)\} = H\left(f-\frac{\alpha}{2}\right). \tag{B.4}$$

Which leads to:

$$\begin{aligned}
\hat{R}_y^{\alpha}(t,\tau) &= \int\int g_1(\lambda_1)\cdot g_2^*(\lambda_2)\cdot \hat{R}_x^{\alpha}(t,\tau-\lambda_1+\lambda_2)d\lambda_1 d\lambda_2 \\
&= \int g_2^*(\lambda_2)\cdot\left[\int g_1(\lambda_1)\cdot \hat{R}_x^{\alpha}(t,\tau-\lambda_1+\lambda_2)d\lambda_1\right]d\lambda_2 \\
&= \int g_2^*(\lambda_2)\cdot\left[g_1 * \hat{R}_x^{\alpha}\right](t,\tau+\lambda_2)d\lambda_2 \\
&= g_2(\tau)\star\left[g_1 * \hat{R}_x^{\alpha}\right](t,\tau) \\
&= g_2^*(-\tau) * g_1(\tau) * \hat{R}_x^{\alpha}(t,\tau).
\end{aligned} \tag{B.5}$$

The $\star$ denotes the correlation operation, which relates to the convolution operation as follows:

$$x(t)\star y(t) \stackrel{\Delta}{=} \int x^*(\tau)x(t+\tau)d\tau = x^*(-t) * y(t). \tag{B.6}$$

Correlation in the time domain corresponds to multiplication in the frequency domain, and Eq. B.5 becomes:

$$\mathcal{F}\left\{\hat{R}_y^{\alpha}(t,\tau)\right\} = \mathcal{F}\left\{g_2^*(-\tau)\right\}\cdot\mathcal{F}\left\{g_1(\tau)\right\}\cdot\mathcal{F}\left\{\hat{R}_x^{\alpha}(t,\tau)\right\} \tag{B.7}$$

According to the *Wiener-Khinchine relation*, the periodogram of a signal is obtained as the Fourier Transform of its autocorrelation function, and similarly the cyclic periodogram is obtained from the Fourier Transform of its cyclic correlogram, as given by Eq: B.8 below. The index Δt represents the measurement time interval of the signal.

$$\hat{S}_{x_{\Delta t}}^{\alpha}(t,f) = \mathcal{F}\left\{\hat{R}_{x_{\Delta t}}^{\alpha}(t,\tau)\right\} = \int_{-\infty}^{\infty}\hat{R}_{x_{\Delta t}}^{\alpha}(t,\tau)e^{-j2\pi f\tau}d\tau. \tag{B.8}$$

The Fourier Transform of the time reversed and conjugated $g_2^*(-\tau)$ is $G_2^*(f)$:

$$\begin{aligned}
\mathcal{F}\left\{g_2^*(-\tau)\right\} &= \int_{-\infty}^{\infty} g_2^*(-\tau)e^{-j2\pi f\tau}d\tau \\
&\stackrel{-\tau=u}{=} -\int_{\infty}^{-\infty} g_2^*(u)e^{j2\pi fu}du \\
&= \int_{-\infty}^{\infty} g_2^*(u)e^{j2\pi fu}du \\
&= \left[\int_{-\infty}^{\infty} g_2(u)e^{-j2\pi fu}du\right]^* \\
&= G_2^*(f).
\end{aligned} \tag{B.9}$$

Thus, eq. B.7 becomes:

$$\hat{S}_{y_{\Delta t}}^{\alpha}(t,f) = G_2^*(f)\cdot G_1(f)\cdot\hat{S}_{x_{\Delta t}}^{\alpha}(t,f) \tag{B.10}$$

Finally, using B.3 and B.4, the cyclic periodogram of the output of an LTI system, which has a transfer function $H(f)$, is:

$$\hat{S}_{y_{\Delta t}}^{\alpha}(t,f) = H^*(f-\frac{\alpha}{2})\cdot H(f+\frac{\alpha}{2})\cdot\hat{S}_{x_{\Delta t}}^{\alpha}(t,f) \tag{B.11}$$

This solution applies in general to any LTI system, however in Eq. B.11 can be further simplified if we consider the system to be a CD element only. The frequency response of the dispersive fibre is:

$$H(f) = e^{-j\frac{\pi\lambda^2 DL}{c}f^2} = e^{j\psi f^2}, \tag{B.12}$$

where $\psi = -\frac{\pi\lambda^2 DL}{c}$, with D dispersion coefficient, λ the reference wavelength, L fibre length and c the speed of light in vacuum. The periodogram for this particular case becomes:

$$\hat{S}^{\alpha}_{y_{\Delta t}}(t,f) = e^{j2\psi\alpha f} \cdot \hat{S}^{\alpha}_{x_{\Delta t}}(t,f) \tag{B.13}$$

The SCF is more accurately estimated by frequency-smoothing or time-smoothing the cyclic periodogram. For illustration here, assume frequency-smoothing, although the same result can be obtained in the limit with time-smoothing. Let Δf be the frequency-smoothing window. The SCF of a signal affected by CD is thus:

$$\begin{aligned}\hat{S}^{\alpha}_{y}(f) &= \lim_{\Delta f\to 0}\lim_{\Delta t\to\infty}\frac{1}{\Delta f}\int_{f-\frac{\Delta f}{2}}^{f+\frac{\Delta f}{2}} \hat{S}^{\alpha}_{y_{\Delta t}}(t,\nu)\,d\nu \\ &= \lim_{\Delta f\to 0}\lim_{\Delta t\to\infty}\frac{1}{\Delta f}\int_{f-\frac{\Delta f}{2}}^{f+\frac{\Delta f}{2}} e^{j2\psi\alpha\nu}\ \hat{S}^{\alpha}_{x_{\Delta t}}(t,\nu)\,d\nu\end{aligned} \tag{B.14}$$

When $\alpha = 0$ Eq. B.14 reduces to the classic PSD, which does not change with dispersion:

$$\hat{S}^{\alpha=0}_{y}(f) = \lim_{\Delta f\to 0}\lim_{\Delta t\to\infty}\frac{1}{\Delta f}\int_{f-\frac{\Delta f}{2}}^{f+\frac{\Delta f}{2}} \hat{S}^{\alpha=0}_{x_{\Delta t}}(t,\nu)\,d\nu = \hat{S}^{\alpha=0}_{x}(f) \tag{B.15}$$

When $\alpha \neq 0$ however, the exponential term together with the frequency-averaging operation in Eq. B.14 induces correlation fading of the SCF.

C

Cyclic autocorrelation function of signals affected by chromatic dispersion

The Cyclic Autocorrelation Function of a signal affected by dispersion shows a dependency on the amount of dispersion it has accumulated on its path, as a a delay along the time-lag parameter. In this appendix, it is demonstrated that this delay is proportional to the cumulative dispersion and the cyclic frequency.

Let $y(t)$ be the received signal, after propagating the transmitted signal $x(t)$ through L km of fibre. As CD is a linear time-invariant transformation, the Fourier transform of the a signal at the output of the fibre channel is equal to the product of the channel transfer function and the Fourier transform of the input signal:

$$Y(f) = H(f) \cdot X(f). \tag{C.1}$$

Assuming chromatic dispersion as the only impairment of the fibre, then the transfer function of the fibre channel is:

$$H(f) = H_{CD}(f) = e^{j\psi f^2} = e^{-j\frac{\pi\lambda^2 DL}{c} f^2},$$

where D is the fibre dispersion coefficient, λ the reference wavelength, L is the fibre length and c the speed of light in vacuum.

Let $\hat{S}^{\alpha}_{x_{\Delta t}}(t,f)$ be the cyclic periodogram of the input signal, measured over Δt at α cyclic frequency. Under the impact of dispersion the cyclic periodogram of the signal $y(t)$, at the input of the coherent receiver:

$$\hat{S}^{\alpha}_{y_{\Delta t}}(t,f) = Y\left(f+\frac{\alpha}{2}\right) \cdot Y\left(f-\frac{\alpha}{2}\right) \tag{C.2}$$

$$= H_{CD}\left(f+\frac{\alpha}{2}\right) \cdot H^{*}_{CD}\left(f-\frac{\alpha}{2}\right) \cdot X\left(f+\frac{\alpha}{2}\right) \cdot X^{*}\left(f-\frac{\alpha}{2}\right) \tag{C.3}$$

$$= e^{j2\psi\alpha f} \cdot \hat{S}^{\alpha}_{x_{\Delta t}}(t,f) \tag{C.4}$$

The CAF of the dispersed signal is calculated as the IFFT of its cyclic periodogram:

$$\hat{R}_y^{\alpha}(\tau) = \int_{-\infty}^{\infty} \hat{S}_{y_{\Delta t}}^{\alpha}(t,f)\ e^{j2\pi f\tau} df \tag{C.5}$$

$$= \int_{-\infty}^{\infty} e^{j2\psi\alpha f} \cdot \hat{S}_{x_{\Delta t}}^{\alpha}(t,f)\ e^{j2\pi f\tau} df \tag{C.6}$$

$$= \int_{-\infty}^{\infty} \hat{S}_{x_{\Delta t}}^{\alpha}(t,f)\ e^{j2\pi f(\tau+\psi\alpha/\pi)} df \tag{C.7}$$

$$= \hat{R}_x^{\alpha}(\tau + \frac{\psi\alpha}{\pi}). \tag{C.8}$$

Therefore, the CAF of the output of the fibre is equal to the CAF of the input to the fibre, with a time-lag delay of:

$$\Delta\tau = \frac{\psi\alpha}{\pi} = -\frac{\lambda^2 DL\alpha}{c}. \tag{C.9}$$

where the product between the fibre dispersion parameter D and fibre length L is the cumulative dispersion.

The CAF of a linearly modulated signal contains harmonics at the fundamental frequency equal to the symbol-rate, therefore this time-shift will be found only when α is an integer multiple of the symbol-rate, as the function is ideally zero otherwise. In the special case when $\alpha = 0$, the CAF is not influenced by CD, as $\Delta\tau = 0$ as well.

D
Definitions

Autocorrelation	Function that measures the correlation of a signal with itself, or the similarity between the different samples of a measured signal, at a given time-lag from each other.
Cyclic autocorrelation	Function that measures the presence of a period or a tone in the autocorrelation function of a signal. This function is dependent on two parameters: the time-lag and cyclic frequency, which is the tone at which the periodicity is measured.
Cyclostationary (in the wide-sense)	The property of a random process whereby its first and second order statistics are periodic in time, and stationary within the period interval.
Ergodicity	The property of stationary signals whereby the expectation value of a random process is equal to the time average in the limit of the time-series representation of the process.
Spectral correlation	Function that measures the correlation between two frequency components of a signal separated by a fixed frequency difference. The function is defined by two parameters: the ordinary frequency centred around the two frequency components to be correlated and the cyclic frequency, which is the difference between them.
Stationary (in the wide-sense)	The property of a process whereby its first and second order statistics are time-invariant.